BACTERIAL CELL DIVISION IN-SIGHT: A SUPER-RESOLUTION STUDY OF THE ESCHERICHIA COLI DIVISOME

by

Jackson Buss

"A dissertation submitted to Johns Hopkins University in conformity with the requirements for the degree of Doctor of Philosophy"

Baltimore, Maryland

October, 2013

ABSTRACT

The polymerization of FtsZ into an annular structure (Z-ring) at midcell is the first recognized step in *E. coli* cell division, and is required for the recruitment of the remaining essential division proteins. Further studies suggest that the Z-ring itself may provide the force that drives constriction. Despite its importance, the in-vivo structure of the Z-ring remains unknown.

Given the small size of bacteria, visualizing a cytoplasmic structure within an intact cell is technically challenging. Conventional fluorescence microscopy lacks the resolution needed for molecular insight, while electron microscopy fails to unambiguously identify subcellular structures in whole bacteria. To circumvent these challenges, we applied a single molecule-based super-resolution imaging technique, photoactivated localization microscopy (PALM), and determined the in-vivo structure of the Z-ring with a resolution of ~30nm. We found that in contrast to the homogenous, ring-like structure expected from previous studies, the Z-ring adopted a heterogeneous configuration with dimensions indicative of a loose, multi-layered protofilament arrangement.

To further investigate the structural composition of the Z-ring, we determined the effect of two FtsZ-associated proteins, ZapA and ZapB, on the assembly dynamics and structure of the Z-ring. In cells deleted of *zapA* or *zapB*, we observed abnormal septa and highly dynamic FtsZ structures that resolve into disordered arrangements of FtsZ clusters via PALM. Quantitative analyses found these clusters were larger and contained more molecules than a single FtsZ protofilament, and likely represented a distinct polymeric species that is inherent

to the assembly pathway of the Z-ring. Our results suggest that ZapA/B function to promote the alignment of FtsZ clusters into a ring-like arrangement and further propose that the FtsZ cluster, not the protofilament, is the basic structural unit of the Z-ring. Complimentary studies employing a variety of two-color and three-dimensional high-resolution imaging methods were applied to elucidate the spatial arrangement of FtsZ, ZapA and ZapB. Our results are consistent with a layered model whereby ZapB forms a stable, cytoplasmic raft upon which clusters of FtsZ protofilaments are anchored through ZapA.

AKNOWLEDGEMENTS

First and foremost, I would like to thank my family and friends. To my parents, William and Denise Buss, your unwavering support and encouragement have provided the foundation for all of my successes. Although rarely voiced, I truly appreciate everything that you have done for me. To my sister, Dr. Sarah Mannon, thank you for your guidance. I'm grateful to have such a fearless and headstrong individual blaze ahead of me. To my girlfriend, Janice Lee, thank you for your patience. You selflessly endured the long hours and late nights by my side, and to that I owe a great deal. To my friends, your joyful distractions kept me both grounded and sane. I love you all.

Next, I would like to thank my advisor, Dr. Jie Xiao. You have taught me a great deal, not only about science, but about myself, as your strength and perseverance are without equal. I hope to bring pride to your lineage.

This work would not have been possible without the help and tutelage from my coworkers, Carla Coltharp, Dr. Zach Hensel and Dr. Tao Huang. Additionally, I acknowledge the contributions of our collaborators, Dr. Harald Hess and Dr. Gleb Shtengel, at the HHMI Janelia Farm Campus for use of their iPALM setup and custom analysis software. Thanks are also in order for the guidance received from members of my thesis committee, Dr. Erin Goley, Dr. Jin Zhang, and Dr. Jon Lorsch. Lastly, I would like to thank all of the staff that I have relied on at the School of Medicine and Homewood campuses, specifically Kathy Kolish and Ranice Crosby.

Table of Contents

FIGURE & TABLE LIST

Chapter 1

E. coli Cell Division

The Divisome

Reproduction is essential to life, as it is the propagation of information that drives evolution. In the primordial world, membrane encapsulation of self-replicating entities is believed to have produced the first cell (Witken, 1976, Monnard & Deamer, 2002). This event represented a major step in evolution, as the level of organization offered by an enclosed environment provided a significant fitness advantage. The presence of a lipid bilayer, however, also presented new challenges, including the requirement of membrane fission for procreation.

Today, in addition to a lipid bilayer, most bacteria possess a rigid cell wall (peptidoglycan). This structure provided further advantage, primarily through resistance to deleterious changes in osmotic pressure, but also represented a substantial energetic obstacle that could not be overcome by the passive constriction mechanisms employed by early cells (Errington, 2013). Division of walled cells now required membrane invagination against a constant (3-15 atm) turgor pressure (Woldringh, 1994, Lan *et al.*, 2007), and the directed hydrolysis and synthesis of peptidoglycan. Furthermore, these two processes had to be temporally and spatially coordinated so as to efficiently utilize energy and prevent lysis. Although bacteria evolved numerous ways to achieve this degree of coordination, this study will focus on the mechanism employed by the γ-proteobacteria *Escherichia coli*.

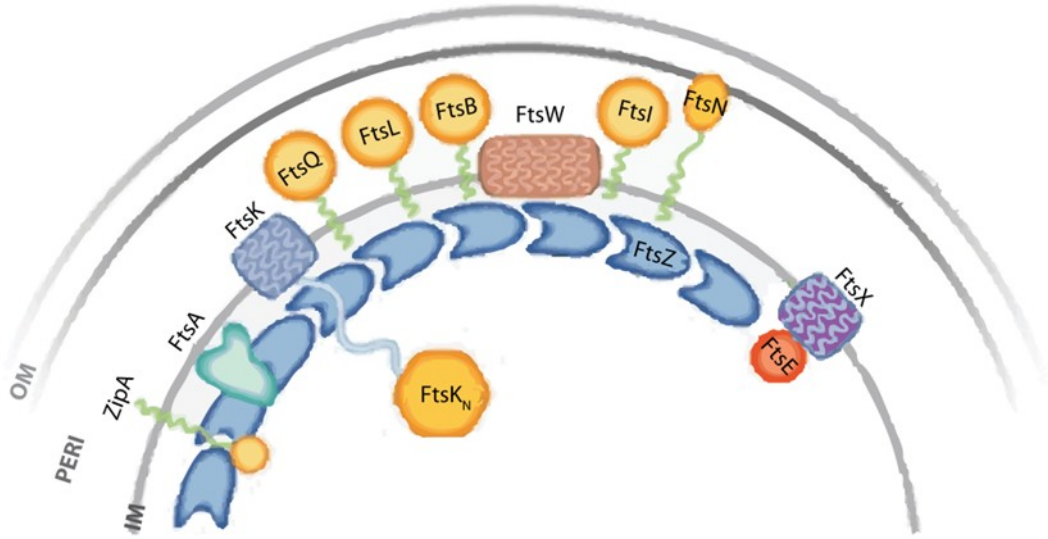

Figure 01.1 - Division protein topology. The primary structural features and appropriate membrane associations of the essential division proteins are depicted (modified from Vicente and Löwe, 2003).

Early efforts to characterize cell division in *E. coli* identified a number of DNA loci that when mutated resulted in temperature-sensitive filamentous phenotype (Van De Putte *et al.*, 1964, Hirota *et al.*, 1968). Since filamentation represents a failure to divide, the proteins produced from these mutated genes were identified as essential division proteins and given the moniker *Fts*, for filamentous temperature sensitive. Later studies showed that only a subset of the *Fts* proteins are truly required for cell division (Caldas *et al.*, 2000, de Leeuw *et al.*, 1999, Tomoyasu *et al.*, 1993) and that a number of additional proteins also participate, including the essential FtsZ-interacting protein, ZipA (Hale & de Boer, 1997). On first inspection, it is clear that these proteins span the various

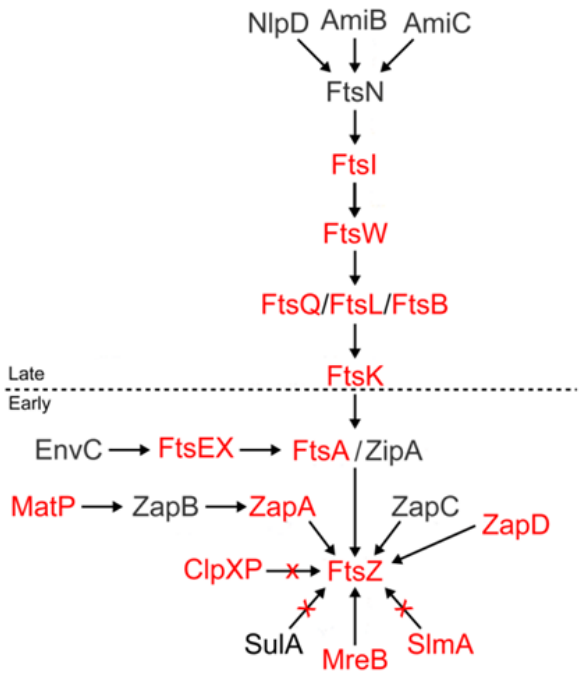

Figure 1.3 – Divisome Recruitment Pathway. Conditional lethal mutants coupled with fluorescence imaging were used to identify the recruitment pathway for the division proteins. Arrows point towards the most downstream protein required for recruitment. Conserved proteins are shown in red and 'x' signifies a negative regulator (modified from Egan and Vollmer, 2013). The dotted line separates the early and late division proteins.

compartments of *E. coli*, from cytoplasm to outer membrane (Figure 1.1), and may offer the spatial coordination required for division.

All division proteins are recruited to midcell and, based on the complex interaction network, are believed to loosely associate into a large complex termed the divisome (Figure 1.2) (Karimova *et al.*, 2005, Di Lallo *et al.*, 2003, Maggi *et al.*, 2008, Alexeeva *et al.*, 2010). Recruitment to the divisome is initiated in the cytoplasm and follows a largely linear pathway (Egan & Vollmer, 2013), in which components are added sequentially in a specified order (Figure 1.3). Recent studies have shown that this recruitment process is temporally segregated with the late division proteins arriving tens of minutes after the early division proteins

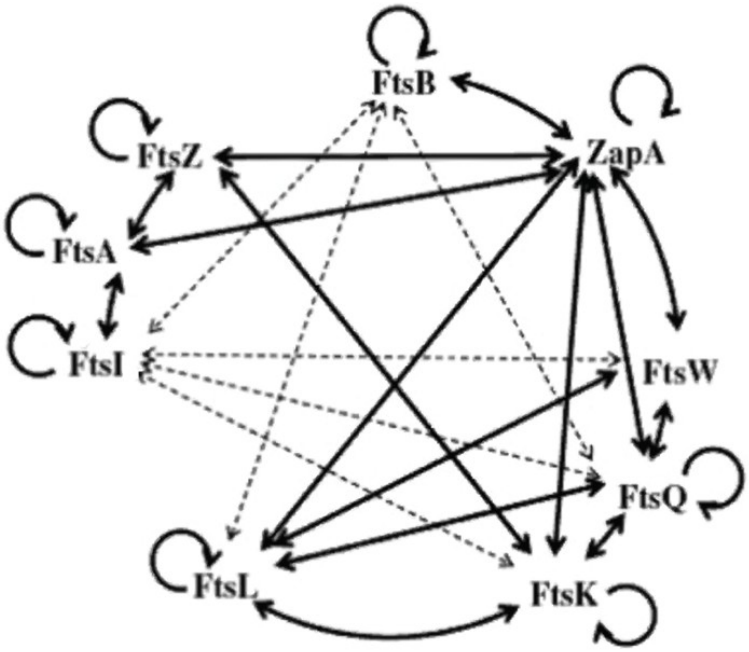

Figure 1.2– Divisome interaction network. Bacterial two-hybrid analyses illustrate the potential interactions between the various division proteins (modified from Maggi *et al.*, 2008). The bold arrows indicate conserved interactions found in both *S. pneumoniae* and *E. coli*, while the dotted arrows indicated species-specific interactions.

(Aarsman *et al.*, 2005). It is unclear how simple diffusion can support such a complex recruitment pathway.

Despite decades of work, the process of cell division, namely divisome organization and force propagation, remain unknown. The aim of this work was to provide a detailed look at cell division in *E. coli* using the new high-resolution fluorescence microscopy techniques and ultimately provide a quantitative description of the divisome in its native environment. It is our belief, that by understanding the structural arrangement of the divisome, we can gain insight into how it functions.

ftsZ

The *ftsZ* (*sfiB*, *sulB*) locus is located in the highly conserved *dcw* gene cluster (Figure 1.4) and encodes a 40.3 kDa globular protein with four structural domains: 1) an N-terminal domain of unknown function 2) a central nucleotide-binding domain, 3) a flexible C-terminal spacer region, 4) a highly conserved C-terminal (7aa) peptide (Figure 1.5A) (Lutkenhaus *et al.*, 1980, Cordell *et al.*, 2003, Erickson *et al.*, 2010). The globular central domain of FtsZ displays high structural homology to the GTP-binding and second domain of eukaryotic tubulin (Erickson, 1995). Like tubulin, FtsZ is capable of polymerization (de Boer *et al.*, 1992a, RayChaudhuri & Park, 1992), which in turn is required for GTPase activity, as the synergy (T7) loop of one FtsZ monomer activates the GTPase activity of an adjacent monomer (Figure 1.5A). FtsZ assembles into a ring-like structure (Z-ring) at midcell (Bi & Lutkenhaus, 1991, Sun & Margolin, 1998) and is required for the recruitment of all other division proteins to the divisome (Figure 1.3) (Addinall *et al.*, 1996, Buddelmeijer & Beckwith, 2002). Given its integral role, it is not surprising that FtsZ is conserved across most bacteria (Vaughan *et al.*, 2004) and archaea (Wang *et al.*, 2003), as well as select chloroplasts and mitochondria (Osteryoung *et al.*, 1998, Beech & Gilson, 2000, Gilson *et al.*, 2003).

The Z-ring undergoes rapid FtsZ subunit turnover *in vivo* ($t_{½}$ ≈ 9 s) (Stricker *et al.*, 2002, Anderson *et al.*, 2004). This dynamic behavior is believed to be a product of its intrinsic GTPase activity, as FtsZ84, a variant with reduced GTPase activity, displays much slower turnover ($t_{½}$ ≈ 30 s). Although initial

hypotheses invoked the nucleotide-dependent conformations or dynamics of FtsZ as possible mechanisms for constriction, the fact that FtsZ84 can serve as a functional replacement suggests against FtsZ-driven constriction (Stricker et al., 2002). Whether or not the Z-ring utilizes the turnover of GTP to drive or support constriction *in vivo* remains unknown.

The C-terminal linker (~50 aa) between the globular domain and the conserved C-terminal peptide exists as an intrinsically disordered protein (Oliva *et al.*, 2004, Oliva *et al.*, 2007, Gardner *et al.*, 2013). It possesses little sequence conservation, requires no charge specification and can be functionally replaced (Gardner et al., 2013). A functional linker needs only be flexible and of a specified length (~43-95 aa) (Gardner et al., 2013) suggesting that it functions as a flexible tether allowing interactions between membrane-bound proteins and itself.

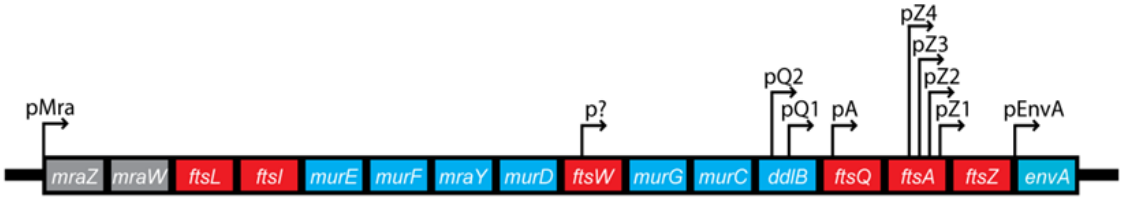

Figure 1.4 – Conserved *dcw* gene cluster. The division and cell wall gene cluster in *E. coli* (modified from Vicente *et al.,* 2006 and Joseleau-Petit *et al.*, 1999) encode essential genes involved in peptidoglycan precursor synthesis or translocation (blue) and cell division processes (red), as well as proteins of unknown functions (grey).

FtsZ expression, turnover and polymerization are highly regulated. Transcription from *ftsZ* occurs from at least 6 promoters located upstream or within the adjacent *ftsQA* genes (Robinson *et al.*, 1984, Robinson *et al.*, 1986, Yi *et al.*, 1985, Joseleau-Petit *et al.*, 1999). Notably, FtsZ expression is upregulated by SdiA and RcsB, both members of the LuxR family of transcription factors that may be involved in responding

to external stimuli (Wang *et al.*, 1991, Sitnikov *et al.*, 1996, Yamamoto & Ubukata, 2001, Gervais *et al.*, 1992). Distal upstream elements and their corresponding regulators have not been fully characterized (Takada *et al.*, 2005, de la Fuente *et al.*, 2001, Flardh *et al.*, 1998). FtsZ turnover is carried out by ClpXP (~13 % per generation) and is independent of cell cycle (Camberg *et al.*, 2009). Under wt conditions, even though *ftsZ* transcription may oscillate according to the cell cycle (Garrido *et al.*, 1993, Robin *et al.*, 1990, Smith *et al.*, 1993), protein levels were found to remain constant (Rueda *et al.*, 2003). Consequently, as the spatial and temporal regulation of cell division is directed through FtsZ, this process is likely carried out through the modulation of FtsZ polymerization.

In vitro FtsZ polymerizes into single-stranded protofilaments (Figure 1.5B) (Rivas *et al.*, 2000, Romberg *et al.*, 2001). These protofilaments can further associate into a variety of higher-ordered structures depending on the applied conditions (Figure 1.5C-D) (Erickson & Stoffler, 1996, Rivas *et al.*, 2001, Popp *et al.*, 2009). Although the high expression level of FtsZ (3,000-15,000 molecules $cell^{-1}$, 3-10 μM) (Rueda et al., 2003), suggests that protofilaments or higher-

ordered structures are likely the predominant species *in vivo*, the physiological relevant polymer species remains unclear. To further complicate matters, a large number of conserved proteins (FtsA, ZipA, ZapA, ZapC, ZapD, SulA, SlmA, MinC, ClpX) directly associate with FtsZ and appear to modulate its *in vivo* structure (Pichoff & Lutkenhaus, 2002, Hale *et al.*, 2011, Mosyak *et al.*, 2000, Gueiros-Filho & Losick, 2002, Durand-Heredia *et al.*, 2012, Durand-Heredia *et al.*, 2011, Bi & Lutkenhaus, 1992, Bernhardt & de Boer, 2005). Elucidating the *in vivo* structure of FtsZ and how it changes according to cell cycle is critical to understanding bacterial cell division.

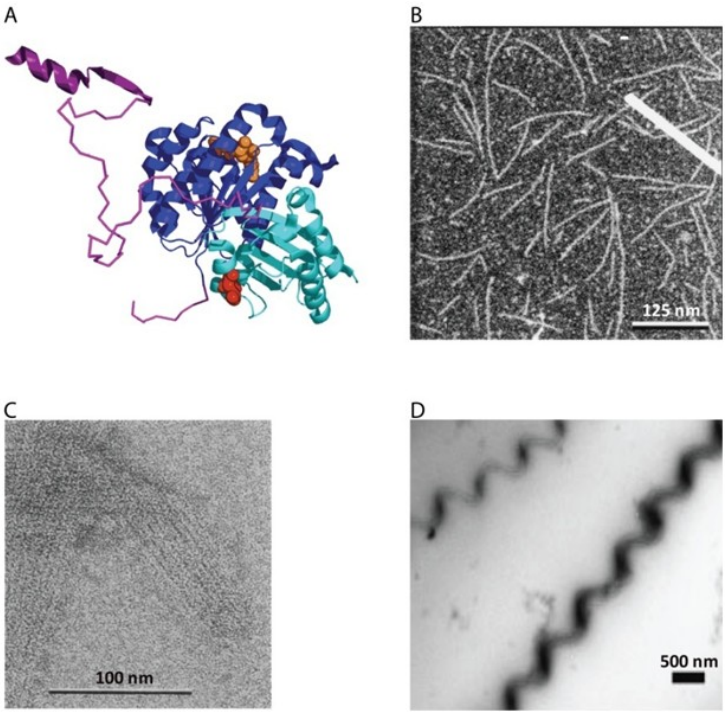

Figure 1.5 – FtsZ structure and protofilament arrangements. (A) Crystal Structure of FtsZ from *Pseudomonas aeruginosa*. The globular domain comprises two independently subdomains: 1) the N-terminal nucleotide-binding domain (blue; GDP, orange), and 2) the C-terminal domain containing the T7 loop (red). The flexible, unstructured termini (purple) have been modeled. The C-terminal conserved helix (purple) is responsible for interaction with FtsA, ZipA, MinC, ZapD, and ClpX (modified from Gardner *et al.*, 2013) (B) Single-stranded protofilaments (modified from Romberg *et al.*, 2001). (C-D) Higher-ordered arrangements of FtsZ protofilaments associating via lateral interactions to sheets and helical bundles (modified form Erickson *et al.*, 1996 and Popp *et al.*, 2009)

ftsA

ftsA (*divA)* is located immediately upstream of *ftsZ* and encodes a highly conserved 45 kDa protein that belongs to the actin/Hsp70 superfamily of ATP-binding proteins (Lutkenhaus *et al.*, 1979, Dewar *et al.*, 1992, Bork *et al.*, 1992, Addinall & Lutkenhaus, 1996a). This cytoplasmic protein contains a conserved, C-terminal amphipathic helix that enables peripheral association with the inner membrane (van den Ent & Lowe, 2000, Pichoff & Lutkenhaus, 2005). FtsA binds the C-terminal tail of FtsZ and likely functions in cell division by tethering the dynamic polymers of FtsZ to the membrane (Ma & Margolin, 1999). This hypothesis is supported by the observation of a required ratio of FtsA:FtsZ (~1:10, ~740 FtsA molecules cell^{-1}) (Dai & Lutkenhaus, 1992, Dewar et al., 1992, Rueda et al., 2003). Like actin and its bacterial homolog, MreB, FtsA was recently shown to polymerize into protofilaments (Szwedziak *et al.*, 2012). This self-interaction is believed to be essential for its function and begs the question of what is the physiological relevant polymer species of FtsA and how does it interact with FtsZ polymers.

FtsA is recruited to the divisome early and is required for the recruitment of FtsK, FtsQLB, FtsW, FtsI and FtsN (Figure 1.3). A single point mutation in FtsA (R286W, FtsA*) bypasses the need for ZipA or FtsK recruitment, and illustrates its importance in cell division. FtsA*, however, has reduced self-interaction, questioning the importance of FtsA polymers (Pichoff *et al.*, 2012). Since FtsA has been shown to interact directly with FtsN (Dai *et al.*, 1993, Goehring *et al.*, 2006, Busiek *et al.*, 2012) , it is possible that FtsA's main

function may not be to stabilize the Z-ring but to recruit downstream proteins and provide an indirect link between FtsZ and the murein synthases (Pichoff et al., 2012, Muller *et al.*, 2007).

FtsA shares many similarities with the well-characterized MinD protein. Both polymerize, associate peripherally with cytoplasmic face of the IM via an amphipathic helix, and possess poor intrinsic ATPase activity. Furthermore, the membrane targeting sequences of FtsA and MinD can be functionally swapped (Pichoff & Lutkenhaus, 2007). From extensive *in vitro* studies we know that MinD's nucleotide-bound state dictates its membrane association and self-polymerization. A similar characterization of FtsA has been complicated by its poor behavior *in vitro*, but recent successes suggest that ATP binding and hydrolysis may be unnecessary for FtsA function (Sanchez *et al.*, 1994, Martos *et al.*, 2012). It will be interesting to see what role, if any, ATP binding and hydrolysis play in FtsA function.

ZipA

The FtsZ-interacting protein, ZipA, is a 36.5 kDa integral membrane protein possessing a rare type 1b topology comprising three structural domains: 1) single N-terminal transmembrane anchor, 2) flexible Glutamine/Proline-rich linker, and 3) globular C-terminal cytoplasmic domain (Hale & de Boer, 1997, Ohashi *et al.*, 2002). The C-terminal domain (143 aa) binds the conserved C-terminal peptide of FtsZ and promotes the assembly of higher-ordered structures

in vitro (Hale *et al.*, 2000). Although the stoichiometry of the FtsZ-ZipA interaction is believed to be 1:1 (Mosyak et al., 2000), ZipA likely homodimerizes (Skoog & Daley, 2012), enabling cross-linking between protofilaments. The self-interaction of ZipA is likely mediated through $ZipA_N$, as $ZipA_C$ is monomeric in solution (Martos *et al.*, 2010).

Together with the unstructured linker domain and membrane anchor, ZipA provides a flexible tether for initial Z-ring development (Hale et al., 2000, Ohashi et al., 2002, Lopez-Montero *et al.*, 2013). ZipA's integral tether, however, may be abnormal as ZipA-GFP displays as similar dynamic turnover as FtsZ ($t_{½}$ ≈ 26 s) (Stricker et al., 2002). Binding of ZipA to FtsZ may also function to protect FtsZ from ClpXP degradation (Pazos *et al.*, 2013).

Although ZipA is only conserved in γ-proteobacteria, in *E. coli* it is required for recruitment of FtsK, FtsEX, FtsQLB, FtsW, FtsI and FtsN (Figure 1.3) (Hale & de Boer, 2002, Chen *et al.*, 2002, Ghigo *et al.*, 1999, Liu *et al.*, 1999, Pichoff & Lutkenhaus, 2002, Schmidt *et al.*, 2004). Determining ZipA's function has been complicated by its rare membrane topology, which makes in vitro analyses difficult and is incompatible with most two-hybrid approaches (Hale & de Boer, 1997, Skoog & Daley, 2012). Much is to be learned of ZipA's function, however, as it was recently implicated in the PBP3-independent peptidoglycan synthesis (PIPS) (Potluri *et al.*, 2012) and shown to potentially complex with EptA (YjdB), an enzyme involved in lipopolysaccharide synthesis (Stenberg *et al.*, 2005).

FtsK

ftsK encodes an inner membrane-targeted, 146.7 kDa (1329 aa) multi-functional protein with three main structural domains: 1) an N-terminal ($FtsK_N$, 1-202 aa) division domain, 2) a long variable linker ($FtsK_L$, 203-818 aa), and 3) a cytoplasmic C-terminal ($FtsK_C$, 819-1329 aa) helicase domain (Bigot *et al.*, 2004). In total, six transmembrane helices are predicted for FtsK with the first periplasmic loop containing a zinc metalloprotease sequence motif (HEXXH) (Dorazi & Dewar, 2000a).

The C-terminal helicase domain is a member of the AAA^+ superfamily of ATPases. This domain forms a homohexamer that enables directional DNA translocase via interaction with FtsK orienting polar sequences (KOPS) (Bigot *et al.*, 2005, Levy *et al.*, 2005). Ultimately, this domain functions in chromosome dimer resolution by rapidly translocating to the dif sites within the Ter MDs of the replicated E. coli chromosomes and loading XerCD (Aussel *et al.*, 2002, Graham *et al.*, 2010).

The $FtsK_N$ domain is sufficient to localize FtsK to the divisome and support cell division (Yu *et al.*, 1998, Draper *et al.*, 1998, Buddelmeijer & Beckwith, 2002). Although functional, the morphology of cells rescued by $FtsK_N$ were observed to be abnormal, providing the first evidence that $FtsK_C$ also functions in division, likely by providing association with other late proteins (Yu et al., 1998, Dubarry *et al.*, 2010).

FtsK is the first late division protein to arrive at midcell and its recruitment is significantly delayed with respect to FtsA and ZipA (Aarsman et al., 2005). Neither the purpose nor the mechanism underlying this delay in recruitment is understood. An attractive explanation is that FtsK localization is dictated in part by $FtsK_C$, in that its translocation towards Ter would drive FtsK to midcell only during late stages of DNA replication. In this context, it will be interesting to see if FtsK also associates with ZapB or MatP, two proteins known to participate in Ter segregation and condensation, respectively (Espeli *et al.*, 2012, Mercier *et al.*, 2008).

The function of FtsK in cell division has yet to be resolved. Hints along these lines exist, as FtsK recruitment can be bypassed completely by FtsA* and Δf*tsK* can be rescued by overproduction of FtsN (Draper et al., 1998) or FtsQAZ (Geissler & Margolin, 2005). Most interestingly, a temperature-sensitive FtsK mutant can be rescued by deletion of *dacA* (Begg *et al.*, 1995, Draper et al., 1998), implicating FtsK in peptidoglycan remodeling and providing a potential function for FtsK's metalloprotease.

ftsEX

FtsEX is an ATP-binding cassette (ABC) transporter of unknown substrate(s) (de Leeuw et al., 1999). FtsE, the 24 kDa ATPase domain, is associated to the inner membrane by FtsX (de Leeuw et al., 1999). FtsEX recruitment to the divisome is dependent on the early essential division

proteins—FtsZ, FtsA and ZipA (Schmidt et al., 2004). The FtsEX null mutant, although typically filamentous, is suppressed by high concentrations of K^+, suggesting that the preferred substrate for FtsEX translocation may be K^+-pumps (Ukai *et al.*, 1998). FtsEX has also been shown to support Z-ring formation under low salt conditions (Schmidt et al., 2004). One of their hypotheses suggested that the ionic conditions could affect the folding of a late division protein and that FtsEX may function as stabilizing factor. In support of this hypothesis, high-throughput assays have identified a number of chaperone proteins that may be associated with FtsE that could assist in folding (HchA, SlyD, GroEL-GroES, IbpA) (Butland *et al.*, 2005, Arifuzzaman *et al.*, 2006, Hu *et al.*, 2009).

FtsE and X are transcribed from *ftsYEX*. Both proteins likely dimerize. FtsX expression has been measured at ~30 molecules per cell (Taniguchi *et al.*, 2010). FtsY is the receptor of the signal recognition particle (SRP) that functions in targeting various inner membrane proteins (Angelini *et al.*, 2005).

ftsQLB

ftsQ and *ftsL* are within the conserved *dcw* gene cluster and encode essential bitopic proteins that traverse the inner membrane (Carson *et al.*, 1991, Guzman *et al.*, 1992). The *ftsB* locus is outside *dcw*, yet it remains conserved across bacteria (Gonzalez *et al.*, 2010). All proteins are likely produced in small quantities (~20 molecules $cell^{-1}$) and likely form a subcomplex, regardless of their midcell localization (Carson et al., 1991, Guzman et al., 1992, Buddelmeijer &

Beckwith, 2004). For all three proteins, a general tripartite topology is conserved: 1) short N-terminal cytoplasmic domain, 2) single transmembrane domain, and 3) a relatively large periplasmic domain (Carson et al., 1991, Guzman et al., 1992, Gonzalez & Beckwith, 2009).

The periplasmic domain of FtsQ (31.4 kDa) is required for its recruitment to the divisome by FtsK and mediates a number of other essential interactions (FtsA, FsK, FsX, FsL, FtsB, FtsW, FtsI, FtsN and YmgF), including a potential self-interaction (D'Ulisse *et al.*, 2007). The N-terminal cytoplasmic domain and long transmembrane domain also appear to function in divisome localization, though functional swaps suggest otherwise (Scheffers *et al.*, 2007, Guzman *et al.*, 1997).

The C-terminal periplasmic domain of FtsL is required for its recruitment to the divisome via FtsQ (Gonzalez et al., 2010, Ghigo et al., 1999). Its transmembrane domain and large periplasmic domain, which contains a leucine zipper motif, are required for interaction with FtsB ().The short cytoplasmic domain of FtsL (13.6 kDa) is involved in the recruitment of downstream proteins (Gonzalez et al., 2010).

FtsB self-oligomerizes via its transmembrane domain and interacts with FtsL through its periplasmic domain likely via a coiled-coil interaction (LaPointe *et al.*, 2013). The oligomerization species of this interaction is unknown. The FtsB-FtsL interaction is required for the divisome recruitment of both proteins, as well as FtsW (Gonzalez & Beckwith, 2009). FtsB is degraded in the absence of

FtsQL, suggesting that interaction with these proteins may stabilize some aspect of FtsB possibly the Glycine-rich periplasmic domain (LaPointe et al., 2013).

The function of FtsQLB is poorly understood. Given the stable, tripartite nature of FtsQLB and the range interactions suggested for FtsQ, the currently theory is that FtsQLB provides a structural link between the early-arriving cytoplasmic proteins, and the late-arriving periplasmic proteins.

ftsW

ftsW is located within the *dcw* cluster and encodes a highly conserved, integral membrane protein (46 kDa) with 10 predicted transmembrane helices (Khattar *et al.*, 1994, Boyle *et al.*, 1997, Wang *et al.*, 1998, Lara & Ayala, 2002). FtsW is recruited late to the divisome by FtsQLB and consequently does not likely function to stabilize the Z-ring (Mercer & Weiss, 2002). As a member of the SEDS protein family, FtsW forms a subcomplex with its cognate transpeptidase, FtsI (Fraipont *et al.*, 2011). This interaction is required for the recruitment of FtsI to the divisome (Mercer & Weiss, 2002). FtsW also reportedly associates with FtsN, the late essential division protein, and MtgA, a monofunctional peptidoglycan glycosyltransferase (Alexeeva et al., 2010, Derouaux *et al.*, 2008).

The essential function of FtsW is undoubtedly concerned with facilitating peptidoglycan synthesis, however its specific role is unclear. One hypothesis states that FtsW simply functions to recruit FtsI to midcell (Mercer & Weiss, 2002). Recent evidence, however, supports a more direct role, suggesting that

FtsW is the enigmatic Lipid II flippase that transports lipid-linked peptidoglycan precursors across the inner membrane (Mohammadi *et al.*, 2011). Given the identification of another potential Lipid II flippase, MurJ, and the proposal that RodA functions as a non-septal Lipid II flippase, it is clear more work is needed to resolve this issue.

ftsI (PBP3)

ftsI is a conserved gene that encodes a 63.9 kDa bitopic protein with three essential structural domains: 1) an N-terminal cytoplasmic domain, 2) a transmembrane helix, and 3) a C-terminal periplasmic domain (Spratt, 1975, Nguyen-Disteche *et al.*, 1998, Bowler & Spratt, 1989). The C-terminal domain ($FtsI_{240-588}$) can be further dissected into a penicillin-binding domain, which functions as a transpeptidase in septal peptidoglycan synthesis, and a noncatalytic domain that is required for the recruitment of FtsN to the divisome (Botta & Park, 1981, Hedge & Spratt, 1984, Pisabarro *et al.*, 1986, Guzman et al., 1997, Wissel & Weiss, 2004). The transmembrane helix is required for recruitment of FtsI to the divisome by FtsW (Weiss *et al.*, 1999, Wissel *et al.*, 2005).

FtsN

ftsN encodes an poorly conserved 35.8 kDa bitopic protein that predicted at 3.000-6,000 molecules cell^{-1} and is essential for cell division in *E. coli* (Dai et al., 1993, Dai *et al.*, 1996, Ursinus *et al.*, 2004). Although its sequence conservation is poor, functional equivalents are thought to exist in most Gram-negative bacteria (Moll & Thanbichler, 2009). FtsN possesses a similar tripartite topology as FtsQLB: 1) a short N-terminal cytoplasmic domain ($FtsN_{1-33}$), 2) a single transmembrane helix ($FtsN_{34-53}$), and 3) a large C-terminal periplasmic domain ($FtsN_{54-319}$) (Dai et al., 1996). The C-terminal domain can be further separated into three structural components: 1) a short membrane proximal region containing three α-helices ($FtsN_{62-123}$), (2) a long, unstructured glutamine-rich region ($FtsN_{124-242}$), and 3) a peptidoglycan-binding SPOR domain that adopts a RNP-like fold ($FtsN_{243-319}$) (Yang *et al.*, 2004, Gerding *et al.*, 2009).

ftsN was initially identified as a multicopy suppressor of $ftsA12_{Ts}$, and later discovered to suppress $ftsK44_{Ts}$, $ftsQ1_{Ts}$ and $ftsI23_{Ts}$ (Dai et al., 1993, Draper et al., 1998). These observations suggest that FtsN may function to stabilize these proteins in the divisome. In support of this hypothesis, FtsN has been shown to associate with FtsA, FtsQ and FtsI (Busiek et al., 2012, Karimova et al., 2005). Although non-essential for cell division, the N-terminal cytoplasmic domain mediates binding to FtsA and is required for suppression of $FtsK_{Ts}$ and $FtsQ_{Ts}$, implicating this region as the stabilizing factor (Busiek et al., 2012, Goehring *et al.*, 2007, Gerding *et al.*, 2007).

FtsN is the last essential division protein recruited to midcell (Addinall *et al.*, 1997a, Hale & de Boer, 2002, Wissel & Weiss, 2004). Its recruitment and essential function is only dependent on a small region (~35 aa) within the membrane-proximal region of its periplasmic domain (Gerding et al., 2009). The non-essential SPOR domain also is capable of localizing to the midcell constriction site and likely enhances FtsN's recruitment.

The function of FtsN is still unknown, but given its interaction with the peptidoglycan enzymes, FtsI (PBP3), PBP1b, and MtgA (Derouaux et al., 2008), its recruitment of the peptidoglycan hydrolases, AmiB and AmiC (Bernhardt & de Boer, 2003), and its direct interaction with peptidoglycan, it likely is involved in directing septal cell wall synthesis/hydrolysis.

Z-ring Associated Proteins

Within the last decade a number of small, cytoplasmic proteins have been identified that appear to modulate the polymerization of FtsZ. These non-essential factors often display synergistic or even synthetic lethal defects when combined with the deletion of other regulatory factors. In *E. coli*, these proteins have been assigned to the FtsZ-associated protein family (Zap). The characteristic common to all Zap proteins is that Zap null mutants display abnormal, extended Z-rings, implicating these proteins in the conformational regulation of FtsZ. Given the degree of functional overlap apparent between these proteins, identifying their specific roles remains a challenge.

zapA (ygfE)

zapA was initially identified in a genetic screen for factors that stabilized the Z-ring in the presence of excess MinCD (Gueiros-Filho & Losick, 2002). A complimentary screen for the localization of *E. coli* ORF's C-terminally labeled with GFP (Table 1.1) also identified ZapA as a midcell associating factor (Kitagawa *et al.*, 2005).

ZapA is a small (12.6 kDa), conserved protein expressed at ~5000 molecules per cell (Small *et al.*, 2007). ZapA dimerizes via its N-terminal globular domain and likely tetramerizes through its C-terminal coiled-coil domain (Figure 1.6A) (Low *et al.*, 2004). Based on the intracellular concentration, the dimer is favored *in vivo* (Low et al., 2004).

ZapA binds FtsZ directly through its N-terminal domain and this interaction is required for ZapA's recruitment to midcell (Galli & Gerdes, 2012). *In vitro* ZapA promotes FtsZ assembly into the higher-ordered arrangements (Figure 1.6B) (Gueiros-Filho & Losick, 2002, Small et al., 2007). This effect is dependent on ZapA tetramerization (Pacheco-Gómez *et al.*, 2013), and may involve a cross-linking interaction (Dajkovic *et al.*, 2010). The ZapA null mutant displays a mild filamentous phenotype accompanied by abnormal, extended Z-ring structures (Dajkovic et al., 2010). ZapA may promote FtsZ polymerization through an effect on FtsZ GTPase, but his mechanism is still disputed (Small et al., 2007, Mohammadi *et al.*, 2009). $ZapA_C$ also directly associates with ZapB (Ebersbach *et al.*, 2008), and this interaction may be more important than previously thought (Buss *et al.*, 2013a), as no physiological relevance has been ascribed to ZapA's *in vitro* effect on FtsZ protofilaments.

zapB (yiiU)

The poorly conserved ZapB was originally identified in a screen for plasmid partitioning factors (Ebersbach et al., 2008). Its role in DNA segregation, however, remains unclear. Recent evidence showed that ZapB associates with MatP, a DNA-binding protein known to condense the Ter MD (Espeli et al., 2012, Mercier et al., 2008, Thiel *et al.*, 2012). The ZapB-MatP interaction results in a direct linkage between the replicated chromosomes and the division machinery. Loss of the ZapB-MatP interaction leads to early segregation of the Ter MD

(Espeli et al., 2012). Unless tethering of DNA-binding proteins to the divisome via ZapB offers a general mechanism for faithful DNA segregation, these results do not explain ZapB's role in plasmid segregation.

ZapB is a small (9.6 kDa) α-helical protein that forms an anti-parallel dimer (Figure 1.6C) (Ebersbach et al., 2008). This dimer further self-assembles into large fibrils *in vitro* (Figure 1.6D) that are likely mediated through extensive coiled-coil interactions (Ebersbach et al., 2008).

In the absence of ZapB, the Z-ring adopts an abnormal, extended morphology. However, ZapB does not bind FtsZ directly (Galli & Gerdes, 2010) and imparts no effect on FtsZ polymerization *in vitro* (Galli & Gerdes, 2012). Therefore it is unclear how ZapB promotes Z-ring in vivo. The only proposal comes from a recent study conducted by the Gerdes group, which showed that ZapB may form a concentric ring inside the Z-ring (Galli & Gerdes, 2010). Therefore, while ZapB appears to have little effect on the polymerization of FtsZ into protofilaments, the internal arrangement of ZapB may offer stability to the protofilament organization of the Z-ring.

zapC (*ycbW*)

ZapC is a small (20.6kDa), cytoplasmic protein that is only conserved in a subset of γ-proteobacteria (Durand-Heredia et al., 2011, Hale et al., 2011). Its function in cell division was first alluded to in the GFP localization screen described previously (Kitagawa et al., 2005). Follow-up studies showed that the

midcell localization of ZapC is dependent on a direct interaction with FtsZ (Hale et al., 2011), and that like ZapA, ZapC promotes the polymerization of FtsZ i*n vitro* (Durand-Heredia et al., 2011). ZapC likely promotes Z-ring assembly by reducing the FtsZ GTPase activity ~ 40% (Durand-Heredia et al., 2011).

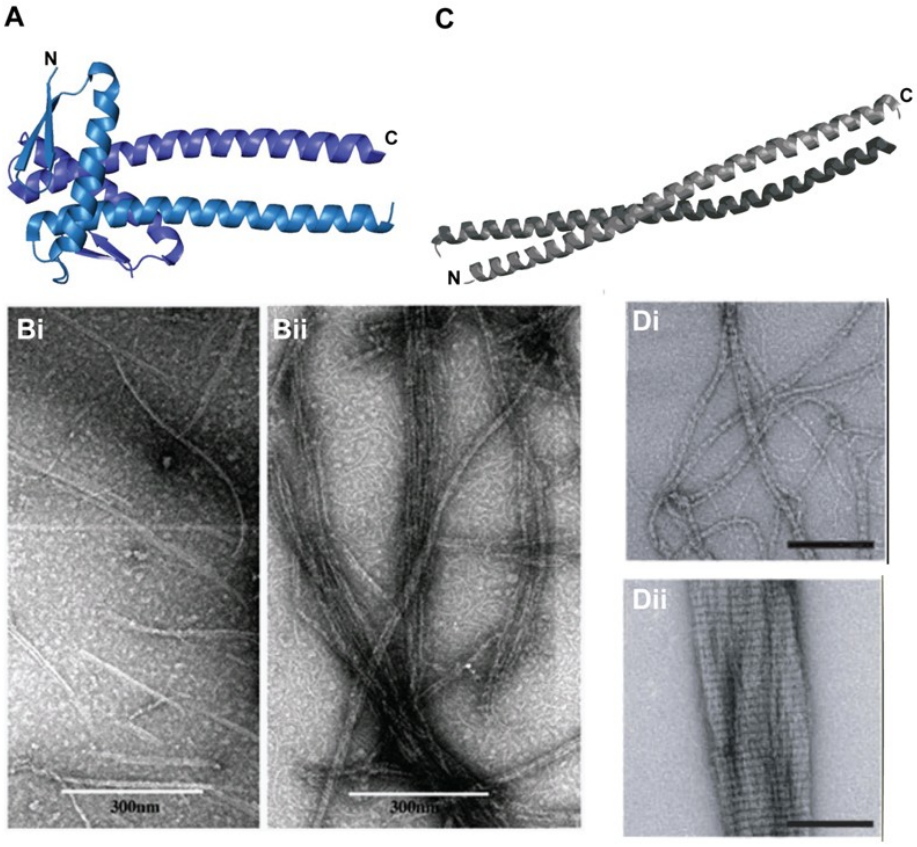

Figure 1.6 – FtsZ-associated proteins (Zap) *in vitro*. (A) Crystal Structure of ZapA dimer from *Pseudomonas aeruginosa* (PDB 1W2E) with N- and C-terminus labeled. (B) EM micrographs of FtsZ protofilaments polymerized *in vitro* in the absence (i) and presence (ii) of ZapA (modified from Low *et al*., 2004) The single-stranded protofilaments associate into higher-ordered fibers upon the addition of ZapA. (C) Crystal structure of the antiparallel ZapB dimer from E. coli (PDB 2JEE) with the N- and C-terminus labeled. (D) EM micrographs of ZapB fibrils polymerized in vitro in the absence (i) and presence (ii) of ZapA (modified from Galli and Gerdes, 2012). Scale Bars, 300nm (B) and 100nm (D).

zapD (*yacF*)

zapD is adjacent to the *dcw* cluster and encodes a small (28.3 kDa), cytoplasmic protein that is present at ~230 molecules per cell (Ishihama *et al.*, 2008). ZapD was identified in the GFP localization screen as being recruited to midcell (Kitagawa et al., 2005). Later it was found that ZapD's recruitment is dependent only on FtsZ and that ZapD binds the conserved C-terminal peptide of FtsZ (Durand-Heredia et al., 2012). This association results in a decrease in FtsZ GTPase by ~70% and an enhanced bundling of FtsZ protofilaments *in vitro* (Durand-Heredia et al., 2012). Given that ZapD is known to dimerize and potentially exist in a number of higher-ordered associations, it will be interesting to see how its mechanism differs from that of the other Zap proteins.

Division Site Selection

Division site selection is required for proper proliferation. Localization of the septum precisely to midcell ensures the production of equal-sized daughter cells, and thus an equal partition of the diffusive cytoplasmic molecules. In the rod-shaped *E. coli*, division sites are typically localized to within ~5% of the midcell plane (Trueba, 1982, Yu & Margolin, 1999, Sun & Margolin, 2001). FtsZ, however, possesses no inherent spatial preference. Consequently, in the absence of some regulatory system, the Z-ring could assemble at any place along the membrane. Understanding how the Z-ring is faithfully positioned precisely at the midcell plane has garnered much attention and two complimentary systems were identified, MinCDE and Nucleoid Occlusion (SlmA). We note that other factors, such as heterogeneous membrane composition, basic cell geometry and SlmA-independent nucleoids effects, may also contribute to the accurate placement of the division plane (Mileykovskaya & Dowhan, 2000, Mishra *et al.*, 2012, Männik *et al.*, 2012).

MinCDE System

Mutations in the *minB* operon produce a minicell phenotype, with small anucleate cells resulting from improper septum placement (Adler *et al.*, 1967, Davie *et al.*, 1984, de Boer *et al.*, 1988). Costly errors such as these suggested that minB likely encoded a factor(s) integral to the localization of the division plane. Further study found that *minB* encodes three-proteins : MinC, MinD and MinE (de Boer *et al.*, 1989).

$MinC_N$ is a FtsZ antagonist that directly binds the conserved C-terminal tail of FtsZ (Hu *et al.*, 1999, Raskin & de Boer, 1999b, Pichoff & Lutkenhaus, 2001, Shen & Lutkenhaus, 2009), and either shortens FtsZ protofilaments (Hernandez-Rocamora *et al.*, 2013) or prevents their lateral association (Dajkovic *et al.*, 2008a). MinD is a ParA-like ATPase that binds $MinC_C$ and associates with inner membrane through a conserved nucleotide-dependent amphipathic helix ($MinD_C$) (de Boer *et al.*, 1991, de Boer *et al.*, 1992b, Szeto *et al.*, 2002), thus positioning the FtsZ-antagonist near polymerization sites. $MinE_N$ binds MinD exclusively and activates MinD's ATPase activity ~10-fold, resulting in the dissociation of MinC and MinD from the membrane (Hu & Lutkenhaus, 2001, Ma *et al.*, 2003). The dynamic instability of this system directed through MinD's nucleotide cycling results in a temperature-dependent, pole-to-pole oscillation ($t_{1/2} \approx$ 10s, 30°C) of all three components (Raskin & de Boer, 1997, Raskin & de Boer, 1999a, Raskin & de Boer, 1999b, Touhami *et al.*, 2006). Other factors involved in the oscillation of MinCDE, include: 1) the cooperative oligomerization of MinD, 2) the membrane association and oligomerization of MinE, and 3) MinD's preference for anionic (Renner & Weibel, 2012).

Initial theories suggested that the effector gradient formed by MinCDE oscillation helped define the midcell plane, but recent evidence suggest that MinCDE may simply prevent polar septation (Migocki *et al.*, 2002, Rodrigues & Harry, 2012). Although a cytoskeletal helical configuration has been reported to underlie the oscillation of MinCDE (Shih *et al.*, 2003), a reaction-diffusion

mechanism involving a complex network of MinD-MinE interactions is likely employed (Howard *et al.*, 2001, Ivanov & Mizuuchi, 2010).

Nucleoid Occlusion via SlmA

slmA was identified in a synthetic lethal screen as a chromosomal deletion that required minCDE for survival (Bernhardt & de Boer, 2005). SlmA is highly conserved among Gram-negative bacteria (Tonthat *et al.*, 2013) and likely is present at 300-400 molecules cell^{-1} (Cho & Bernhardt, 2013). The N-terminus of SlmA has a TetR-like, helix-turn-helix motif that tightly associates ($K_d \approx 50$ nM) with a 12bp palindromic sequence (5'-GTgAGtaCTcAC-3') located throughout the non-Ter regions of the *E. coli* chromosome (Cho *et al.*, 2011, Tonthat *et al.*, 2011). The C-terminal domain of SlmA mediates dimerization and is responsible for interaction with FtsZ (Tonthat et al., 2011, Tonthat et al., 2013).

SlmA was initially shown to promote the polymerization of FtsZ into long, ribbon-like configurations *in vitro* (Bernhardt & de Boer, 2005). Later studies showed that in the presence of DNA, SlmA disassembles FtsZ protofilaments possibly by promoting the GTPase activity of FtsZ (Cho et al., 2011). A conflicting report suggests that only FtsZ higher-ordered structures are antagonized by SlmA (Tonthat et al., 2011) . These claims are supported by structural data illustrating that SlmA separates and orients FtsZ protofilaments in an anti-parallel fashion (Tonthat et al., 2011). Although the molecular mechanism of nucleoid occlusion by SlmA is still unclear (Cho & Bernhardt, 2013, Tonthat et

al., 2013), the cell-cycle dependent localization pattern of GFP-SlmA illustrates a general scheme (Bernhardt & de Boer, 2005).

In new born cells, the SlmA-bound oriC is positioned at midcell prior to replication, thus preventing premature septum formation. As replication progresses, the Ter MD, which is void of SlmA, is positioned at midcell, thus enabling Z-ring formation between the replicated nucleoids. In this way, SlmA can be thought of not only as a spatial regulator, but a temporal one as well.

Table 1.1 - Midcell localization screen

ASKA/KEIO	Gene	Δ morphology
JW1584	**yadQ**	n/a
JW1794	**fadD/oldD**	normal
JW0092	**ftsA**	n/a
JW0093	**ftsZ**	n/a
JW3995	**malK**	normal
JW0999	**putA/poaA**	normal
JW0727	**tolQ/fii**	chains
JW0099	**zapD (yacF)**	normal
JW0929	**zapC (ycbW)**	normal
JW2878	**zapA (ygfE)**	normal
JW2404	**zipA**	n/a

website: http://ecoli.aist-nara.ac.jp/GFP/gfp_top.jsp#

Coordinating Division

The need for cells to rapidly respond to internal and external stimuli requires that cell division be regulated in time, as well as space. If left unregulated, simple delays in DNA replication could result in the production of nonviable cells. Given the variety of cues a cell is likely to encounter (i.e. nutrient availability, quorum-sensing, etc.), a large number of regulation mechanisms likely exist, yet few have been identified in bacteria (Wang et al., 1991, Weart *et al.*, 2007).

The SOS response, described below, is the most conserved temporal regulatory mechanism, and is employed as a last ditch effort that elicits global response to harsh stimuli. More selective regulatory schemes that produce localized responses are less well understood, but likely extend to a number of stimuli and employ a variety of mechanisms, including: 1) protein mislocalization (Peters *et al.*, 2011), 2) sequestration (Modell *et al.*, 2011), 3) post-transcriptional modification (Sureka *et al.*, 2010), 4) transcriptional/translational control , and 4) active degradation (Kelly *et al.*, 1998).

Activation or inactivation via phosphorylation is a common regulatory mechanism employed throughout biology. Notably, this mechanism may affect FtsA localization (Sanchez et al., 1994) and has recently been implicated in the regulation of FtsZ polymerization. Phosphorylation of $FtsZ_{Ec}$ by a Ser/Thr Kinase from *Mycobacterium tuberculosis*, PknA, resulted in polymerization defects both *in vitro* and *in vivo* (Thakur & Chakraborti, 2006). Neither a PknA homolog, nor a parallel mechanism has been identified in *E. coli*. However, given that loss of S-

adenosylmethionine prevents recruitment of the late division proteins, FtsQLBWIN and possibly FtsK (Newman *et al.*, 1998, Wang *et al.*, 2005a), an analogous methylation mechanism may exist. This is indirectly supported by the presence of *mraW*, a S-adenosyl-methionine-dependent methyltransferase, within the *dcw* cluster and its complete conservation across bacteria (Carrion *et al.*, 1999, Vicente *et al.*, 2006). The potential target for methylation is unknown.

Transcriptional control of the E. coli *ftsQAZ* is carried out by a number of factors, including the LuxR-like SdiA quorum-sensor and the "stationary-phase" sigma factor (*rpoS*) (Sitnikov et al., 1996, Joseleau-Petit et al., 1999). Currently, however, it is unclear if *E. coli* division protein concentrations fluctuate relative to the cell-cycle (Rueda et al., 2003, Garrido et al., 1993, DeLisa *et al.*, 2001). Additionally, the impact of other factors, like ppGpp, which may upregulate factors that effectively increase FtsQAZ levels, may also be important (Wang et al., 1991, Navarro *et al.*, 1998, Vicente et al., 2006).

FtsQAZ are cotranscribed, yet present at disparate concentrations with an order of magnitude separating FtsZ from FtsA from FtsQ (effectively 100:10:1) (Barondess *et al.*, 1991, Rueda et al., 2003). This range of expression can be explained by a number of post-transcriptional events described below. mRNA processing by RNase E at a cleavage site residing within *ftsA* could potentially result in multiple mRNAs with different stabilities (Barlow *et al.*, 1998). Beyond stability, the efficiency of translation via ribosome-binding sequence favors FtsZ > FtsA > FtsQ production (Mukherjee & Donachie, 1990). Lastly, once proteins are produced their concentration is dictated by their stability or identification by

degradation machinery. FtsZ's potential direct interaction with the stabilizing factor DnaK may contribute to its high concentration (Uehara *et al.*, 2001).

SulA and the SOS Response

The transcription factor, LexA, negatively regulates the expression of a number of cell division proteins (FtsZ, FstA, FtsK, FtsQ, FtsL, FtsW, FtsI, SulA) (Vicente *et al.*, 1998, Ishino *et al.*, 1989, Dorazi & Dewar, 2000b, Lewis *et al.*, 1992, Lewis *et al.*, 1994). In response to DNA damage, activated RecA mediates the cleavage of the LexA dimer, resulting in upregulation of these proteins, as well as *sulA* (Little *et al.*, 1980, Witkin & Kogoma, 1984). The small (18.8 kDa), cytoplasmic SulA prevents Z-ring formation by sequestering FtsZ monomers 1:1, effectively reducing the concentration of active FtsZ monomers (Dajkovic *et al.*, 2008c, Chen *et al.*, 2012). Whether or not the FtsZ's GTPase activity is required for SulA inhibition remains controversial (Chen et al., 2012, Bi & Lutkenhaus, 1990, Dajkovic et al., 2008c). It is also unclear why a cell would prosper from upregulating the very division proteins it aims to inhibit.

Chapter 2

The FtsZ-Ring in Super-resolution

Introduction

The polymerization of the FtsZ into a ring-like structure at midcell initiates the assembly of the divisome (Bi & Lutkenhaus, 1991, Addinall et al., 1996, Buddelmeijer & Beckwith, 2002). In addition to functioning as a scaffold, the bending or condensation of FtsZ protofilaments within the Z-ring is thought to generate the constrictive force needed for cell division (Erickson et al., 2010, Sun & Jiang, 2011). Determining the *in vivo* structure of the Z-ring would provide significant insight to the molecular understanding of FtsZ's function. Despite this well-appreciated importance, the structure of the Z-ring remains elusive. Using conventional fluorescence light microscopy (FLM), the Z-ring predominantly appears as a closed, annular configuration (Sun & Margolin, 1998, Pogliano *et al.*, 1997). At times, however, FtsZ is apparent as a highly dynamic helical structure (Ben-Yehuda & Losick, 2002, Peters *et al.*, 2007, Thanedar & Margolin, 2004). These observations led to the hypothesis that the Z-ring itself may result from the compression of an extended helical structure (Ben-Yehuda & Losick, 2002). However, because of the limited spatial resolution of FLM (250-300 nm) (Abbe, 1873), this hypothesis has not been verified.

It is generally accepted that the Z-ring comprises a number of short (~120 nm), single-stranded (~30 subunits) FtsZ protofilaments (Stricker et al., 2002, Anderson et al., 2004, Chen & Erickson, 2005). However, the arrangement of protofilaments inside the Z-ring is unknown. EM images of bacterial cytoplasm do not show the presence of the Z-ring, possibly because the cytoplasm is too dense to offer good contrast, or because protofilaments inside the Z-ring are not

sufficiently ordered to be distinguished (Erickson, 2009, Weiss, 2004). ImmunoEM has also been unsuccessful because the antibody labeling density is too low to reveal any distinct structural features of the Z-ring (Bi & Lutkenhaus, 1991). Only one recent study using electron cryotomography (ECT) in *Caulobacter crescentus* successfully detected single filaments that were believed to be FtsZ protofilaments (Li *et al.*, 2007). This study showed that instead of a continuous ring structure, the Z-ring of *C. crescentus* is composed of two or three protofilaments scattered randomly along the membrane at midcell. However, the low number of protofilaments observed in this study is difficult to reconcile with the expected number (20-80 protofilaments) based on the FtsZ concentration and midcell localization percentage of FtsZ in *C. crescentus* (Quardokus *et al.*, 2001).

To overcome the above limitations, we took advantage of the newly developed super-resolution imaging method, photoactivated localization microscopy (PALM), to elucidate the *in vivo* structure of the *E. coli* Z-ring (Betzig *et al.*, 2006). PALM imaging combines the advantages of both conventional EM and FLM by providing spatial resolutions in the nanometer range, while maintaining unambiguous identification through specific fluorescent labeling (Betzig et al., 2006, Hell, 2009). We labeled FtsZ with the photoconvertible fluorescent protein, mEos2 (McKinney *et al.*, 2009), and were able to image the Z-ring with ~35-nm spatial resolution, an order of magnitude improvement over the spatial resolution of conventional FLM. We discovered that in addition to a ring conformation, the Z-ring of *E. coli* adopts a variety of compressed helical

conformations with tight pitches ranging from 50-300 nm. Next, we measured the width and density of the Z-rings, which describe how many protofilaments thick the ring is and how many FtsZ molecules are packed in a unit area, respectively. These structural details have not been available before and are difficult or impossible to obtain by other means. Finally, we examined the dependence of the conformation, width and density of the Z-ring on FtsZ expression level. Based on our results, we propose that the Z-ring of *E. coli* is composed of a loose bundle of FtsZ protofilaments that randomly overlap with each other in both the longitudinal and radial directions of the cell. This arrangement of protofilaments is different from the single-layered flat ribbon or random arrangement of protofilaments suggested previously (Erickson *et al.*, 1996b, Stricker et al., 2002, Margolin, 2005, Li et al., 2007).

FtsZ-mEos2 is a Reliable Label

We chose mEos2 (Figure 2.1) for PALM imaging because of its superior properties: mEos2 folds and matures well at room temperature, is minimally disruptive for tightly packed proteins and has a high contrast ratio before and after photoactivation (McKinney et al., 2009, Wiedenmann *et al.*, 2004). In addition, mEos2 emits green fluorescence before photoactivation, which allows the ensemble appearance of the Z-ring to be recorded before PALM imaging, enabling direct comparison between the conventional and super-resolution images of the Z-ring.

We fused mEos2 to the C-terminus of FtsZ (pET28 FtsZ-mEso2) and examined whether the fusion protein was able to replace endogenous $FtsZ_{wt}$. As with all other known FtsZ-FP fusions, FtsZ-mEos2 did not rescue the lethal phenotype of the conditional *ftsZ* deletion strain JKD7-2/pKD3a at nonpermissive temperature. We have screened different linker sequences between FtsZ and mEos2 and placed mEos2 at the N- or C-terminus as well as internal positions of FtsZ, but none of these fusion proteins complemented the JKD7-2/pKD3a strain (see Chapter #5-3.2.1).

Although FtsZ-mEos2 cannot function as the sole source of FtsZ, based on two previous studies we reason that the fusion of mEos2 to FtsZ imparts minimal impact on the structure of the Z-ring. In one study, a membrane-targeting sequence (mts) was placed at the C-terminus of an FtsZ-YFP fusion. The resulting fusion protein, FtsZ-YFP-mts, was able to self-assemble into ring-like structures in a reconstituted liposome system and able to contract in the

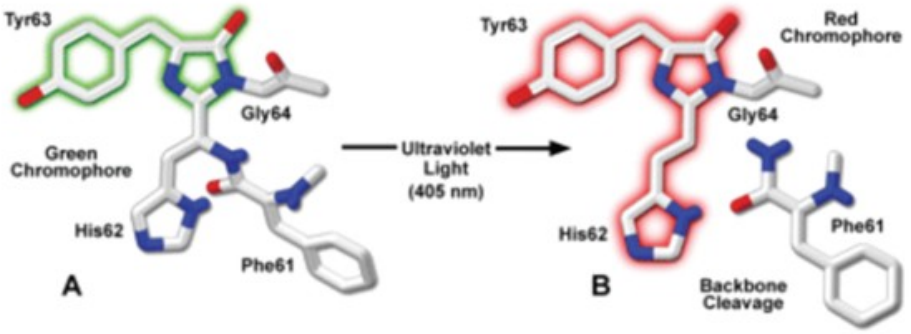

Figure 2.1 - mEos2 chromophore. The green-to-red conversion of mEos2 requires a backbone cleavage event between Phe61-His62 that results in a red-shift. The frequency of this event is enhanced by the absorption of high energy (UV) photons (modified from Rizzo *et al.* (2009)).

presence of GTP (Osawa *et al.*, 2008). This study showed that the fusion of a FP moiety to FtsZ does not disrupt the ability of FtsZ to assemble into a contractile Z-ring once a membrane anchor is provided. It also hinted that the reason FtsZ-FPs fail to support cell division is likely due to an inability to bind the membrane anchoring proteins, FtsA and ZipA, which are required for downstream processes (Aarsman et al., 2005). In a second study, EM imaging found the morphologies of single protofilaments and sheets of protofilaments comprising FtsZ and the FtsZ-YFP fusion protein indistinguishable (Osawa *et al.*, 2009). This result suggests that the fusion of an FP to the C-terminus of FtsZ does not impose detectable perturbations on the assembly of higher-order FtsZ structures. Therefore, it is reasonable to expect that the FtsZ-mEos2 fusion protein would allow for normal Z-ring assembly and could serve as a reliable label for the Z-ring.

To verify the above expectation, we first examined expression levels of FtsZ and FtsZ-mEos2 in the BL21(DE3)pLysS strain used for PALM imaging. We

found via quantitative Westerns that BL21 expresses 4000 ± 1700 FtsZ molecules cell^{-1} under the PALM imaging growth conditions (see Chapter #5-2.4). This average expression level is consistent with previous reports (3000-5000 molecules/cell) (Rueda et al., 2003, Pla *et al.*, 1991), but lower than the 10,000-15,000 molecules cell^{-1} reported by Lu et al (Lu *et al.*, 1998). We also found that our induction level resulted in FtsZ-mEos2 being expressed at ~25% of the total cellular FtsZ (wt FtsZ + FtsZ-mEos2; see Chapter #5-2.3). This ratio is within the acceptable range, as previous studies have shown a ratio of 50% or more is required for detectable growth defects (Ma *et al.*, 1996, Sun & Margolin, 1998, Thanedar & Margolin, 2004, Wang *et al.*, 2005b).

Because FtsZ-mEos2 was expressed from the strong T7 promoter of pET28, the applied induction, although brief, likely created a population with heterogeneous expression levels that cannot be accounted for by Western-blotting. Consequently, the cells selected for PALM imaging that exhibited a strong FtsZ-mEos2 signal at midcell may have represented a subset of cells over-expressing FtsZ-mEos2.

To examine this possibility, we measured the integrated green fluorescence, which reflects the expression level of FtsZ-mEos2, in individual cells of the BL21(DE3) pLysS strain on a fluorescence microscope (Chapter #5-5.3). We found that the integrated fluorescence intensity of individual cells largely followed a normal distribution (Figure 5.2A). The coefficient of variation (CV, standard deviation/mean) is 0.44. A CV value of lower than one, which is expected for an exponential distribution, is usually considered of low variability.

Most importantly, cells showing midcell Z-ring localization have a similar intensity distribution and mean intensity to that of the whole cell population. These observations suggest that the selection of cells showing midcell Z-ring localization for PALM imaging is not biased toward cells expressing extremely high FtsZ-mEos2 levels.

Having quantified the expression level of FtsZ-mEos2 and wt FtsZ, we examined whether FtsZ-mEos2 was able to localize to the midcell in the presence of wt FtsZ in a cell cycle-dependent manner. This is the standard used in the field to determine if an FtsZ-FP fusion protein retains its ability to associate with wt FtsZ and serves as an accurate label for FtsZ localization and dynamics (Sun & Margolin, 1998, Thanedar & Margolin, 2004, Stricker et al., 2002, Aarsman et al., 2005, Stricker & Erickson, 2003, Ma et al., 1996, Wang et al., 2005b). We then compared this result with that of an FtsZ-GFP fusion known to provide a reliable signal (Kitagawa et al., 2005).

To ensure a proper comparison, we replaced the *ftsZ-gfp* gene in pCA24N (Saka *et al.*, 2005) with the *ftsZ-mEos2* gene and expressed the FtsZ-mEos2 fusion protein in the same B/r A strain under the same growth conditions as the FtsZ-GFP fusion. We found that in the presence of wt FtsZ, FtsZ-mEos2 correctly localized to midcell in a cell cycle-dependent manner, similar to that of the FtsZ-GFP fusion (Figure 5.2B). In exponentially growing cultures, 80% of cells showed FtsZ-mEos2 midcell localization, which is comparable to that of FtsZ-GFP (85%). In contrast, when wt FtsZ was depleted, cells expressing FtsZ-mEos2 showed diffusive fluorescence instead of clear Z-rings at midcell, demonstrating that the

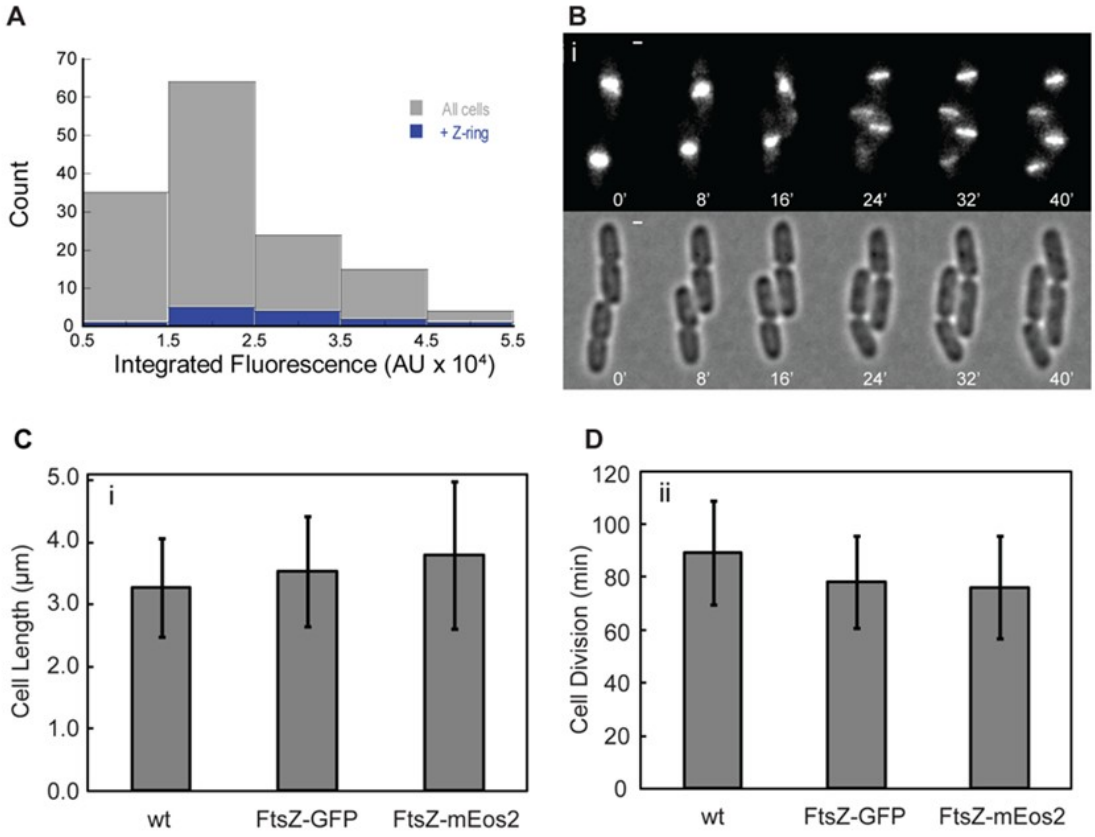

Figure 2.2 – FtsZ-mEos2 is a reliable reporter. (A) Histograms of integrated intensity levels for a B/r A population with and without FtsZ-rings, illustrate that FtsZ-mEos2 expression does not affect Z-ring assembly. (B) Time-lapse imaging of FtsZ-mEos2 in B/r A cells shows cell-cycle dependent midcell localization. (C-D) Average cell length and division time determined for B/r A cells with and without FtsZ-GFP or FtsZ-mEos2. Lengths were determined from bright-field images while division rates were determined from time-lapse movies. Mean ± standard deviation. Scale Bars, 500 nm.

midcell localization of FtsZ-mEos2 is wt FtsZ dependent. In addition, cells expressing FtsZ-mEos2 showed similar cell length and doubling time as those of cells expressing FtsZ-GFP and of parent strain cells expressing no FtsZ-FP fusion protein (Figure 5.2C-D).

The above experiments established that FtsZ-mEos2 incorporates into the Z-ring through the association with wt FtsZ, is expressed homogenously across the cell population, and does not impair cell division at the expression level used for PALM imaging. Based on these results we conclude that FtsZ-mEos2 has minimal impact on the *in vivo* structure of the Z-ring and can be used as a reliable label of the Z-ring.

The Z-ring: A Heterogeneous Structure

We first recorded the contour of the cell in the bright-field and the ensemble appearance of the Z-ring in the green fluorescence channel prior to PALM imaging (Figure 2.3Cii). We then used a near-UV laser (405 nm) simultaneously with a yellow laser (570 nm) in epi-illumination mode to continuously activate and excite single FtsZ-mEos2 molecules (Figure 2.3A). The excitation power of the 570-nm laser was adjusted high enough so that most molecules were imaged and photobleached within one frame (Figure 2.3B). Acquisition continued until 20,000 frames were acquired or until FtsZ-mEos2 activation became very infrequent. The positions of single FtsZ-mEos2 molecules in each frame of this series were then determined, calibrated and plotted together to construct a PALM image (Figure 2.3Civ, see Chapter #5-5.6). Only molecules with a localization precision (see Chapter #5-5.5) of 25 nm or better were used to construct PALM images. The average localization precision of plotted FtsZ-mEos2 molecules in images reported in this work was 14 ± 6 nm unless otherwise noted. The average spatial resolution of the resulting PALM images, determined by calculating the displacement between the fitted positions of the same molecule in two consecutive frames, was 34 ± 20 nm (see Chapter #5-5.7).

Figures 2.3C-E show the PALM images of four typical BL21(DE3)pLysS cells expressing FtsZ-mEos2. As expected for a circular structure perpendicular to the long axis of the cell, we observed a thin, sharp FtsZ-mEos2 band at the midcell. This observation is different from the diffusive cytoplasmic localization of

mEos2 by itself (Figure 2.3F), indicating that the localization pattern we observed for FtsZ-mEos2 was specific to FtsZ.

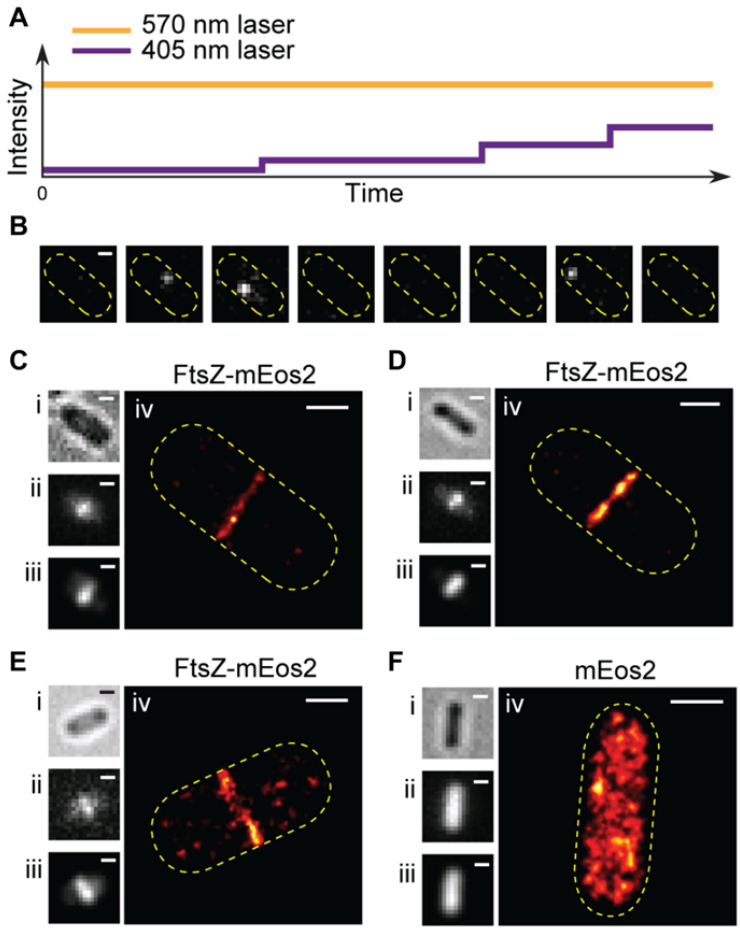

Figure 2.3 – PALM imaging of the Z-ring in *E. coli*. (A) Schematic of PALM imaging sequence using continuous illumination of the 570-nm excitation laser (yellow line) and the 405-nm activation laser (purple line) simultaneously. The illumination intensity of the 570-nm excitation laser was kept constant throughout, while that of the 405-nm activation laser was increased stepwise as the pool of inactivated FtsZ-mEos2 molecules was depleted. (B) Fluorescence images of single FtsZ-mEos2 molecules during a typical PALM imaging sequence. Usually a single FtsZ-mEos2 molecule was detected and photobleached in one single frame (frames 2, 3 and 7). (C-F) Images of cells expressing FtsZ-mEos2 and mEos2 in the order of bright-field (i), ensemble green fluorescence (ii), regenerated ensemble fluorescence image (iii) and PALM images rendered in pseudo-color (iv). Scale Bars, 500nm.

The Z-ring Is ~110 nm Wide

To gain structural insight into the arrangement of FtsZ protofilaments inside the Z-ring, we measured the width of each individual PALM band using images obtained on fixed cells (see Chapter #5-4.1). We found that the band widths were similar to each other with an average of 113 ± 25 nm (N=17). The average band width in live cells (110 ± 21 nm, N=20) was also indistinguishable from that measured with fixed cells (P=0.64).

To find out whether the similar band widths resulted from limited spatial resolution, we performed the following analyses. First, we calculated the theoretical spatial resolution based on two methods. Using the mean localization precision of 14 nm, we estimated that a single protofilament would appear to be 33 nm wide in our PALM images. Therefore, if two protofilaments are spaced 33 nm apart on a projected 2D image plane we will be able to resolve them individually. This number is the upper limit of our achievable spatial resolution. In a second method, we calculated the spatial resolution according to the Nyquist criterion, which states that to achieve a desired spatial resolution of *n* nm, the sampling frequency should be at least *n*/2 nm (Shroff *et al.*, 2008a). In other words, a 10-nm spatial resolution requires that there is one labeled molecule every 5 nm along the structure. At a low labeling percentage of 25%, we calculated that on average the Nyquist spatial resolution is 28 nm (Chapter #5-5.7). This value is comparable to that determined from the average localization precision, indicating that the theoretical spatial resolution is not limited by the labeling percentage of the Z-ring. Next, we determined the actual measurement

error by isolating molecules that lasted more than one frame in the PALM imaging sequence and measured the molecules' displacements between subsequent frames (Chapter #5-5.7, Figure 5.6). The histogram of displacements fit well to a normal distribution with a main peak at 34 nm, in agreement with the upper limit of spatial resolution calculated based on the localization precision. Therefore, we estimate that the actual spatial resolution in our PALM images is ~35 nm, which is still significantly smaller than the measured band width at 110 nm.

Because the average band width was ~110 nm, much wider than the apparent width of a single protofilament in PALM images, the Z-ring must contain more than one protofilament laterally. This observation is consistent with previous estimations based on the average number of FtsZ monomers inside the cell (Stricker et al., 2002, Erickson, 2009). We are currently unable to deduce how many protofilaments are required to laterally associate/align to generate the ~110-nm Z-ring.

Z-ring Is Multi-layered

Knowing how tightly FtsZ molecules are packed inside the Z-ring will lend insight into the spatial arrangement of FtsZ protofilaments. For a flat ribbon configuration in which FtsZ protofilaments tightly align with each other in a single layer (Figure 2.10A), we calculated that the packing density would be maximally 5 FtsZ monomers per PALM pixel (15 x 15 nm^2). By comparing the number of individual FtsZ-mEos2 molecules detected per pixel in the PALM bands to the theoretical number estimated from the flat ribbon configuration, we can assess if such a configuration is possible. However, because an epi-PALM image is the 2D projection of a 3D structure, FtsZ packing densities are inaccurately estimated.

To circumvent this problem, we performed total internal reflection (TIR) PALM imaging. By adjusting the incident angle of the activation and excitation lasers, TIR allowed detection of FtsZ-mEos2 molecules in a thin layer (~200 nm) at the cell-glass interface. In this way, only FtsZ-mEos2 molecules located on the bottom membrane of the cell can be selectively excited and imaged. Figure 2.4C shows a typical TIR PALM image of one cell with a single band at midcell. The intensity of the band in the middle was higher than that on the two edges (Figure 2.4C); this is the opposite of what we observed via epi-PALM, and is expected of a ring-like structure under TIR illumination.

We counted the number of FtsZ-mEos2 molecules per pixel in the TIR PALM images and found that approximately 40% of the pixels in the midcell band have a density ranging from 2-8 FtsZ-mEos2 molecules $pixel^{-1}$ (Figure 2.4D).

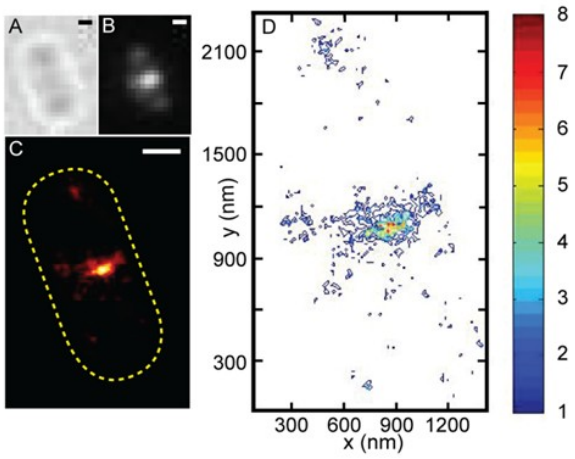

Figure 2.4 – Z-ring density determined by TIR-PALM. mage of a fixed cell expressing FtsZ-mEos2 in the order of bright-field (A), TIR ensemble fluorescence image (B), TIR-PALM image (C), and contour plot of FtsZ packing density in units of number of FtsZ-mEos2 molecules per PALM pixel (15x15 nm^2). Bars, 500nm.

Similar results were found in other TIR PALM images of different cells. We note that the density distribution of the midcell band is not uniform, which may indicate that FtsZ protofilaments inside the Z-ring are not uniformly distributed. However, it is also possible that the non-uniform density distribution is due to the stochastic activation of FtsZ-mEos2 molecules. Considering that the expected maximal density for a single-layered FtsZ protofilament arrangement is ~ 5 FtsZ molecules/ PALM pixel, that not all FtsZ molecules inside the Z-ring were labeled with mEos2, and that not all FtsZ-mEos2 molecules are fluorescent due to the slow maturation of mEos2 (McKinney et al., 2009), the observation of large regions with high densities suggests that some regions of the Z-ring contain multiple layers of FtsZ protofilaments that overlap along the radial direction of the cell.

FtsZ Adopts a Helical Conformation

Previous studies have shown that the Z-ring is highly dynamic (Anderson et al., 2004, Chen & Erickson, 2005, Stricker et al., 2002), and extended FtsZ helical structures have been observed to constantly collapse or emanate from the midcell Z-ring (Ben-Yehuda & Losick, 2002, Peters et al., 2007, Thanedar & Margolin, 2004). Consequently, in order to obtain a clear snapshot of the Z-ring, we fixed BL21(DE3)pLysS expressing FtsZ-mEos2 from pET28 and performed PALM imaging on cells of normal length that showed a single green fluorescent band at midcell.

In cells displaying a single ensemble green channel fluorescent band, we typically observed a single, sharp PALM band. However, in some cells these structures resolved into two or more, closely-spaced PALM bands (Figure 2.5). Interestingly, these thin PALM bands adopted a variety of conformations with different lengths, tilting angles and separation distances ranging from 50-400 nm (see Chapter #5-5.10).

Since PALM images are 2-dimensional (2D) projections of 3-dimensional (3D) structures, we hypothesized that the observed patterns of multiple bands resulted from 3D helical structures along the inner membrane surfaces. To test this hypothesis, we modeled a helix along the inner cylindrical surface of a typical *E. coli* cell using a set of measured parameters including the length, tilting angles and positions of the thin bands from the PALM images, the size of an FtsZ monomer and the number of total FtsZ molecules inside the cell (Figure 2.5iv). We then projected this helix onto a 2D plane and produced a simulated PALM

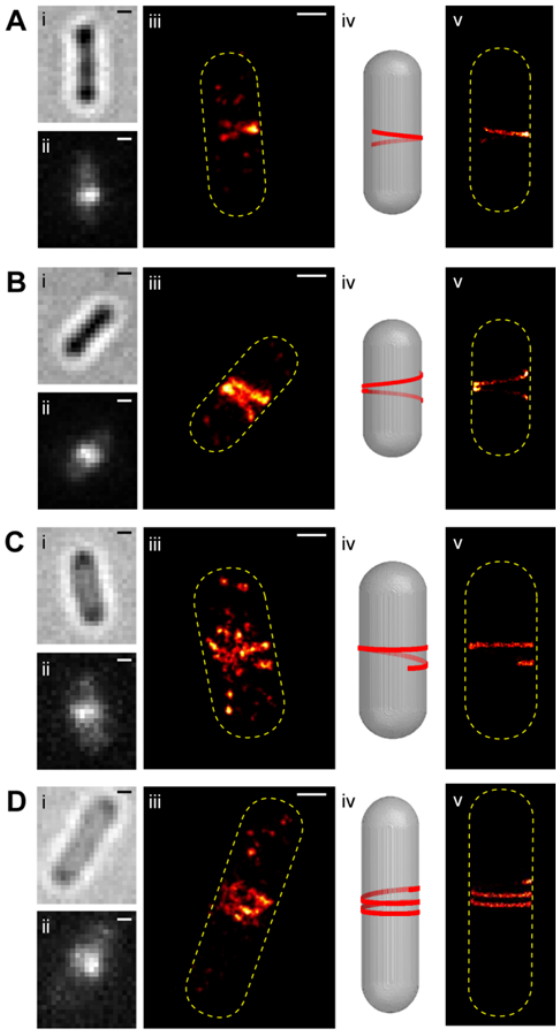

Figure 2.5 – Modeling fixed-cell PALM images of the Z-ring as helices. Representative images of fixed BL21(DE3)pLysS cells expressing FtsZ-mEos2 from pET28 displayed in the order to bright-field (i), ensemble green fluorescence (ii) and PALM image (iii). A 3-dimensional helix with variable pitch and length (iv) was simulated. Comparison of the 2-dimensional projection of the helical model rendered as a PALM image (v) with the actual PALM image (iii) illustrates the potential helicity of the Z-ring. Scale Bars, 500 nm.

image (Figure 2.5v, see Chapter #5-5.8.2) by taking into account multiple factors that would influence the final PALM image such as the defocusing effect, stochastic activation of FtsZ-mEos2 molecules and single molecule photon fluctuations.

We found that the best way to produce a simulated PALM image that matched the measured tilting angles of bands and the separation distances between bands in the real PALM images was by modeling a helix with variable pitches along the helical path. If a helix with a constant pitch is modeled and

projected onto a 2D plane, the distance between the simulated PALM bands (*l'*), is significantly different from the measured distance between the real PALM bands (*l*). Therefore, we allowed the pitch along the helical path to vary and successfully simulated PALM images that matched well with the real PALM images (Figure 2.5iii). In addition, the lengths of these helices varied from cell to cell, further establishing the large variability of these helical conformations.

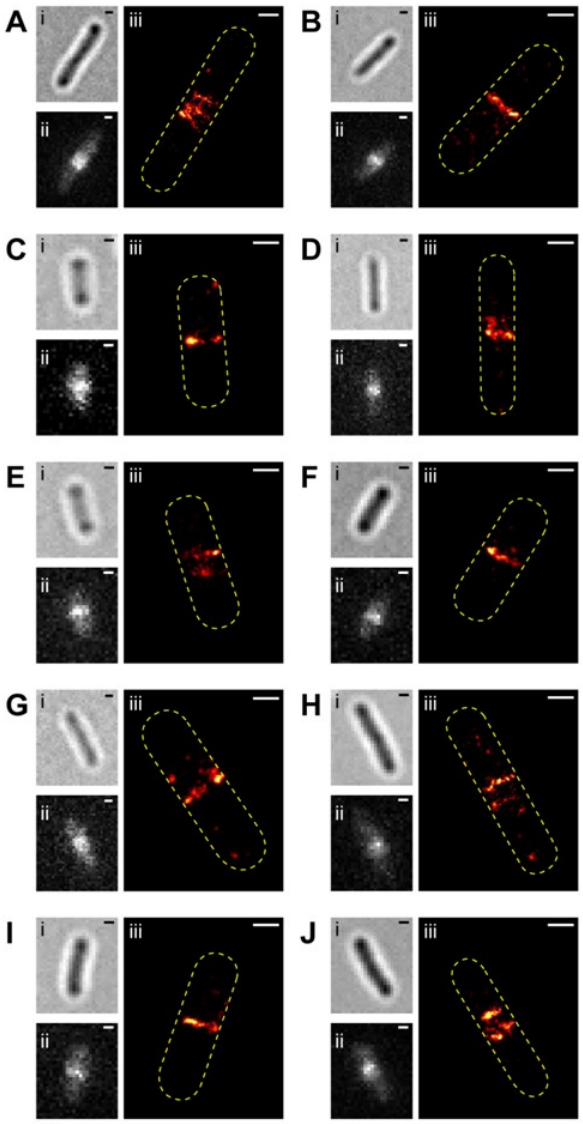

Figure 2.6 – Live-cell PALM imaging of the Z-ring in *E. coli*. (A-J) Representative images of live cells expressing FtsZ-mEos2 from pET28 displayed in the order to bright-field (i), ensemble green fluorescence (ii) and PALM image (iii). The acquisition time of ~20s was sufficient to temporally freeze the dynamic structure. Scale Bars, 500 nm.

Helical Structures Are Not Artifacts of Fixation

Chemical fixation may distort cellular structures at the nanometer scale, especially when the structure of interest is attached to the membrane (Bozzola & Dee Russell, 1999). To avoid chemical fixation artifacts or any other possible structural alterations during sample preparation, it is best to image the Z-ring in live cells. PALM imaging, however, requires the acquisition of thousands of frames, typically sampled over several minutes. Based on fluorescence recovery after photobleaching (FRAP) experiments we believe the Z-ring is a highly dynamic structure, turning over on a time scale of 10-30 s (Anderson et al., 2004, Stricker et al., 2002). Therefore, in order to obtain a clear PALM image of the Z-ring in live cells, it is critical to speed up the PALM acquisition time.

To image the Z-ring in live *E. coli* cells with a high spatial resolution, we developed a fast PALM imaging protocol. In this protocol we sped up the imaging time by using a high excitation intensity (1.8-2.5 kW cm^{-2}), short exposure time (7 ms) and small illumination area (50 x 50 pixels). We were able to acquire a live-cell PALM image of the Z-ring within 20 s with a similar localization precision to the fixed cells images (23 ± 7 nm). This 20-30 s imaging time is fast enough to "freeze" the Z-ring in action. As with the fixed cells, some live cells showed a single PALM band at midcell and some cells showed two or three thin PALM bands reminiscent of the compressed helical structure (Figure 2.6). This result strongly suggests that the helical conformation of the Z-ring we observed for fixed cells is not an artifact caused by fixation, but rather a genuine structural feature of the Z-ring.

Concentration Dependence of Z-ring Conformation

It is known that the assembly of FtsZ superstructures *in vitro* is concentration-dependent (RayChaudhuri & Park, 1992, de Boer et al., 1992a), and that overexpression of FtsZ *in vivo* often leads to multiple Z-rings and spiral structures (Ma et al., 1996). However, because of limited spatial resolution in conventional FLM, it is difficult to assess in detail how the structure of the Z-ring responds to different FtsZ expression levels. Here we examine the effect of cellular FtsZ levels on the conformation of the Z-ring using PALM imaging.

We first established a standard curve so that the total cellular FtsZ level of an individual cell can be easily inferred from its integrated green fluorescence of FtsZ-mEos2 instead of relying on a population-averaged expression level measured by immunoblotting (Figure 2.7A). To obtain a wide range of total cellular FtsZ levels, employed a "serial dilution by division" strategy by pulse-inducing $P_{T5\text{-}Lac}$::*ftsZ-meos2* from pJB004. We harvested cells after different induction times, and quantified both the average expression level of FtsZ-mEos2 using immunoblotting and the corresponding average integrated fluorescence of a population of single cells using fluorescence microscopy. Assuming a constant expression level of wt FtsZ from its chromosomal locus, we plotted total cellular FtsZ level (in units of wt FtsZ level, WTU) against the average integrated green fluorescence of the cell (Figure 2.7A). This standard curve allowed us to analyze the conformational properties of the Z-ring in accordance with the total cellular FtsZ level in individual cells. We note here that in order to use fluorescence as an expression marker we varied the total cellular FtsZ level by changing the levels of

FtsZ-mEos2 instead of wt FtsZ. Therefore, the conformational changes we observed could be due to mEos2 tag, and not FtsZ. Although this remains a formal possibility, previously it was shown that overexpression of FtsZ or FtsZ-FPs resulted in similar spiral Z-ring conformations (Ma et al., 1996, Sun & Margolin, 1998), suggesting that the structure of the Z-ring is mainly influenced by FtsZ, not the FP tag.

To qualitatively analyze the dependence of Z-ring conformation on FtsZ expression level we arranged PALM images of representative cells according to their integrated green fluorescence intensity (Figure 2.7B). As with the BL21(DE3)pLysS strain, we observed two types of cells exhibiting either single or double bands at the midcell in the B/r A strain (Figure 2.7B). In the intensity range of 25,000-70,000, which corresponds to a total cellular FtsZ level of 1-2 WTU, all cells (N=29) exhibited a single band, presumably a ring-like conformation at midcell. In the intensity range of 70,000-200,000, which corresponds to a total cellular FtsZ level of 2-5 WTU, a few cells (4 out of 26) showed more than one PALM band at the midcell, reminiscent of the compressed helical structures observed in the BL21(DE3)pLysS strain. The ensemble green fluorescence images of the cells exhibiting multiple PALM bands still showed one single band. When the fluorescence intensity was above 300,000 (total cellular FtsZ level > 8 WTU, N=3), we found that both the ensemble green fluorescence images and PALM images of cells showed multiple, widely-spaced bands at the midcell.

Our observations suggest that the Z-ring has an increased tendency to form helical, or multi-band structures at elevated expression levels of FtsZ (Figure 2.7C). This observation has been made previously (Ward & Lutkenhaus, 1985, Ma et al., 1996), but concluded that these aberrant structures were non-functional. We conclude that although severe overexpression does result in aberrant, non-functional structures,

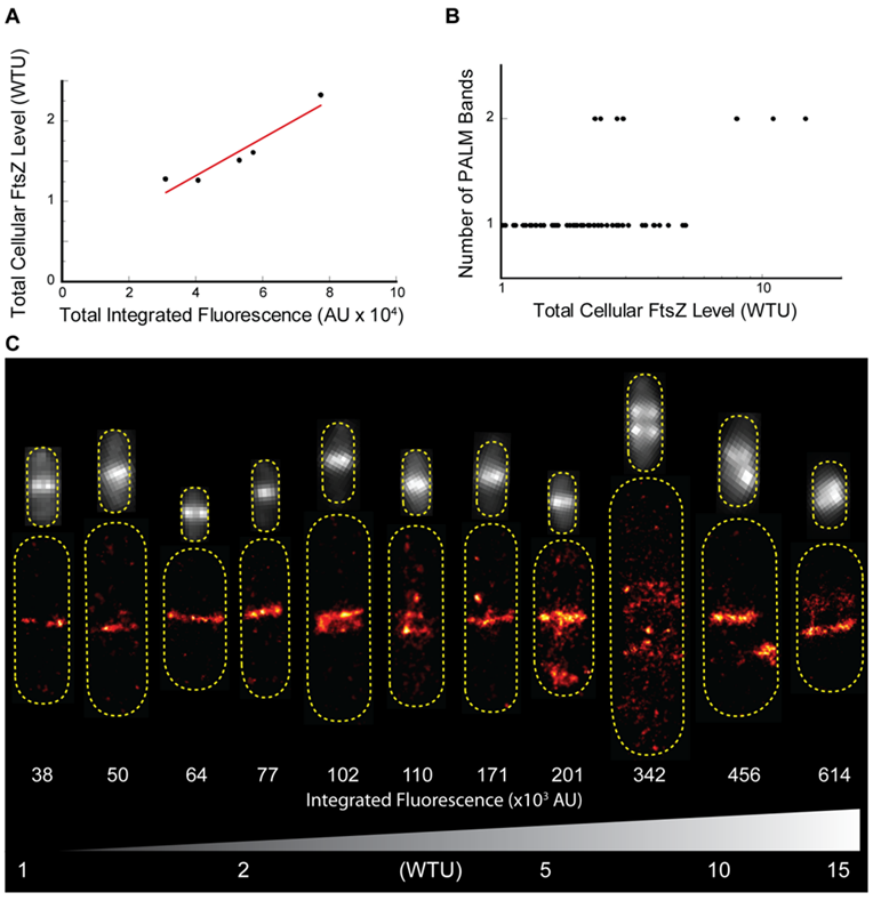

Figure 2.7 – Dependence of Z-ring conformation on FtsZ expression level. (A) Correlation plot showing the linear relationship between the total FtsZ expression level ($FtsZ_{wt}$ + FtsZ-mEos2) of determined by immunoblotting and the corresponding average integrated fluorescence intensity. A linear fit was applied and this conversion is used to estimate the total cellular FtsZ expression level from the integrated ensemble fluorescence (y=0.4+2.32e-5x, R^2=0.898). (B) Plot of Z-ring conformations observed in the PALM images, represented as number of bands versus total cellular FtsZ level in WTU (log-scale). (C) Representative PALM plots (red-hot, bottom) and ensemble fluorescence images (bw, top) are labeled with and arranged according to increasing total integrated fluorescence (AU x 10^3) to illustrate the dependence of ring conformation on FtsZ expression level. A gradient corresponding to the increase in total FtsZ expression level (WTU) is displayed at the bottom.

intermediate expression levels (2-5 WTU) promote the formation of a previously unidentified compressed helical conformation. This helical structure is also apparent at low frequencies in cells expressing near-native FtsZ levels, suggesting that this conformation may be physiologically relevant.

Given the dynamic nature of FtsZ and its ability to maintain function while undergoing significant structural transitions—the midcell band splits in two and appears helical despite limited spatial resolution (Figure 2.8)—an attractive hypothesis is that FtsZ exists in an equilibrium between closed ring and open helix. Clearly, further experiments examining the dynamics of the helix-ring transition with super-resolution imaging will provide important insight into the structural organization of the Z-ring.

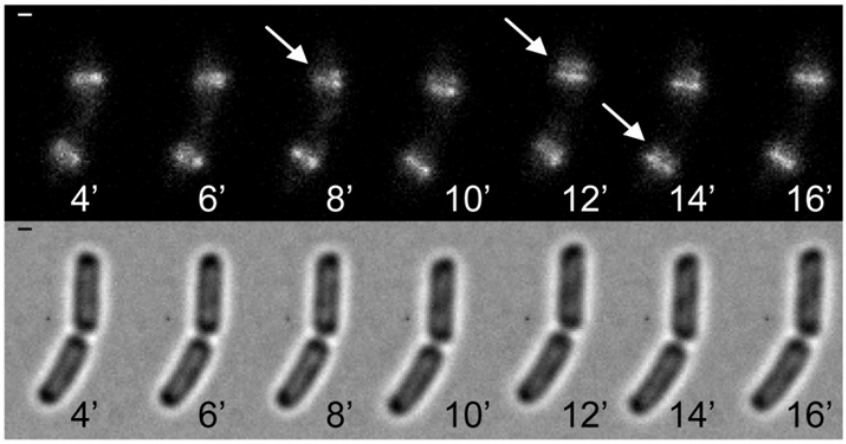

Figure 2.8 – Time-lapse imaging of FtsZ helix-ring transitions. A representative montage of two cell B/r A cells expressing FtsZ-mEos2 constitutively from pJB004. Cells e imaged in the absence of inducer and individual frames were acquired every 30 s.

Concentration Dependence of Z-ring Width and Density

Next, we analyzed how the width of the Z-ring responds to elevated FtsZ levels. The average Z-ring width for B/r A cells (108 ± 25 nm, N=29) was similar to what was measured for BL21(DE3)pLysS cells (p= 0.48). We plotted the measured PALM band width against the FtsZ expression level for each cell (Figure 2.9A). In contrast to the conformation of the Z-ring, we found that Z-ring width is independent of concentration. The constant width of the Z-ring over a wide range of FtsZ expression levels suggests that either the Z-ring is a fixed structure that does not incorporate additional molecules, or the Z-ring is a loose structure that does incorporate additional molecules without dimensional perturbation. If the former, increases in FtsZ expression level should result in a larger pool of FtsZ molecules outside of the Z-ring. If the latter, increases in FtsZ expression level should result in increased occupancy of the Z-ring, whereby additional molecules essentially fill-in or add-to the existing structure.

To examine the first possibility, we calculated the percentage of FtsZ-mEos2 localized to the midcell by dividing the number of FtsZ-mEos2 molecules detected in the Z-ring by the total number of FtsZ-mEos2 molecules detected in the cell. Midcell percentage did not scale with expression level (Figure 2.9Aii), suggesting that more FtsZ-mEos2 molecules localize to the midcell at elevated concentrations. We note that the average percentage of FtsZ-mEos2 at midcell (47 ± 12%) agrees with previous measurements based on conventional FLM (~30-40%) (Anderson et al., 2004, Geissler *et al.*, 2007).

To examine the second possibility, we measured both the occupancy and density of the Z-ring and plotted each against the integrated fluorescence signal. To measure these parameters, we first recorded the ensemble green fluorescence of each cell using epi-illumination mode and then switched to TIR illumination to record the corresponding PALM image. As expected, the width of the Z-ring measured by TIR-PALM was similar to the measurement made via epi-PALM measurements (108 ± 17 nm , N=7) and were similarly independent of FtsZ expression level. To measure the occupied area of the Z-ring, we selected a region encompassing the Z-ring and determined the percent of pixels within this region that contained at least one molecule. When plotted against FtsZ expression level (Figure 2.9B), the occupied area of the Z-ring scaled linearly. Interestingly, neither the average number of molecules per occupied pixel, nor the maximal density per Z-ring varied considerably (Figure 2.9C). These results suggest that Z-ring is a loose structure and that incorporation of additional molecules occurs by filling-in empty spaces.

Discussion and Conclusions

Arrangement of protofilaments inside the Z-ring

Although we could not resolve individual protofilaments inside the Z-ring, our measurements provide insight into the arrangement of protofilaments. Based on the average number of FtsZ molecules per cell determined by immunoblotting (4000 molecules/cell) and the percentage of FtsZ localized to the midcell (47%), we estimated that the wt midcell Z-ring of the *E. coli* BL21 and B/r A strains would contain ~ 1900 FtsZ molecules. If all these FtsZ molecules are connected head-to-tail, they would form a filament about 8 μm long (each FtsZ monomer is 4.3 nm (Erickson et al., 1996b)). This filament would be long enough to encircle the waist of a typical *E. coli* cells 2.5 times. Therefore, the Z-ring is ~ 2-3 protofilament thick (Stricker et al., 2002). If these protofilaments were arranged side-by-side in a flat ribbon configuration (Figure 2.10A) with a 9-nm spacing between each protofilaments (Li et al., 2007), the width of the Z-ring would be ~ 20-30 nm. This number is in contrast to what we measured using PALM imaging (~110 nm). It is more likely that these protofilaments are not aligned tightly but loosely arranged inside the Z-ring as illustrated in Figure 2.10B. Because of the short length of FtsZ protofilaments (~120 nm on average (Stricker et al., 2002, Anderson et al., 2004, Chen & Erickson, 2005)) relative to the curvature of the cell membrane, it is also possible that FtsZ protofilaments are orientated in all directions at midcell, not just circumferentially. This random arrangement of protofilaments would also increase the apparent width of the Z-ring. Interestingly, although the width measurements indicate that the Z-ring is most

likely is a loose structure, our TIRF PALM imaging showed that in some areas of the Z-ring, FtsZ protofilaments have higher packing density than what is expected for a single-layered configuration. This observation indicates that the Z-ring may not be a homogenous structure but in some areas FtsZ protofilaments overlap with each other in space. In addition, the concentration-dependent PALM imaging experiment showed that when additional FtsZ protofilaments are added to the Z-ring, they do not increase the apparent width of the Z-ring but fill-in empty spaces, further supporting the hypothesis that the Z-ring is a loose structure.

Considering the above measurements and observations, we propose that the most likely arrangement of protofilaments inside the Z-ring is a 3D bundle in which randomly oriented FtsZ protofilaments loosely associate and overlap with each other in space (Figure 2.10B). The bundle allows FtsZ protofilaments to overlap with each other so that when the structure is projected onto a 2D plane the FtsZ packing density is higher than a single-layered ribbon configuration. The bundle is also loose so that its projected width (110 nm) is larger than that of a structure in which the same number of protofilaments are aligned side-by-side as illustrated in Figure 2.10A. The ribbon model also predicts that at increased expression levels of FtsZ we would observe increased width but not density of the Z-ring since additional FtsZ protofilaments can only be added to the two edges of the ribbon. This prediction is the opposite of what we observed.

A previous model proposed that the Z-ring is comprised of short protofilaments randomly scattered in a narrow band around midcell (Figure

2.10C) (Li et al., 2007, Osawa et al., 2008). In this model there are large spaces between FtsZ protofilaments along the membrane and hence there are no lateral associations (Osawa et al., 2008). The loose bundle model we propose is similar to this model in that we believe the Z-ring is also a loose structure with randomly oriented FtsZ protofilaments. However, our model is different in that we speculate that short FtsZ protofilaments are staggered not only along the circumference of the cell, but also along the radial direction of the cell (Figure 2.10B). This model brings forth an interesting prediction—lateral interactions among protofilaments are required to organize a 3D bundle, since radially overlapping protofilaments may not be anchored to the membrane.

Currently the presence of lateral interactions between FtsZ protofilaments inside the Z-ring remains controversial. Lateral surfaces of FtsZ are different from those of its homolog tubulin, which exhibits strong lateral interactions (Nogales *et al.*, 1998) and the lateral bond energy of FtsZ was estimated at only about 1/50 of that of the longitudinal bond (Chen *et al.*, 2005, Chen & Erickson, 2005, Lan *et al.*, 2008). However, a few results argue strongly for the presence of lateral interactions between FtsZ protofilaments. First, an FtsZ mutant that is defective in making lateral contacts *in vitro* does not support cell division (Monahan *et al.*, 2009). Second, the MinC protein, a known cell division inhibitor, was found to prevent lateral interactions between FtsZ filaments *in vitro* (Dajkovic et al., 2008a). Finally, four newly discovered cytoplasmic proteins (ZapA, ZapB, ZapC, ZapD) are found to interact with FtsZ and promote Z-ring assembly *in vivo* (Ebersbach et al., 2008, Small et al., 2007, Gueiros-Filho & Losick, 2002,

Mohammadi et al., 2009, Low et al., 2004). These proteins may serve as the "glue" that mediates the lateral associations of FtsZ protofilaments.

If there are indeed lateral associations between FtsZ protofilaments, we reason that they are likely weak and not uniformly distributed along the longitudinal directions of protofilaments. The weak lateral associations between FtsZ protofilaments are necessary for a loose bundle and may facilitate the dynamic structural remodeling of the Z-ring between the helical and ring conformations.

In summary, our PALM images of the Z-ring point to a loose 3D bundle model in which FtsZ protofilaments weakly associate with each other via non-uniform lateral interactions or mediator proteins. The looseness of the bundle may also help to explain why the Z-ring of *E. coli* is invisible using EM or ECT, which usually detects densely- or regularly-packed cellular structures. To validate this model, further experiments investigating the influence of lateral interactions or mediator proteins on the structural organization of the Z-ring are required.

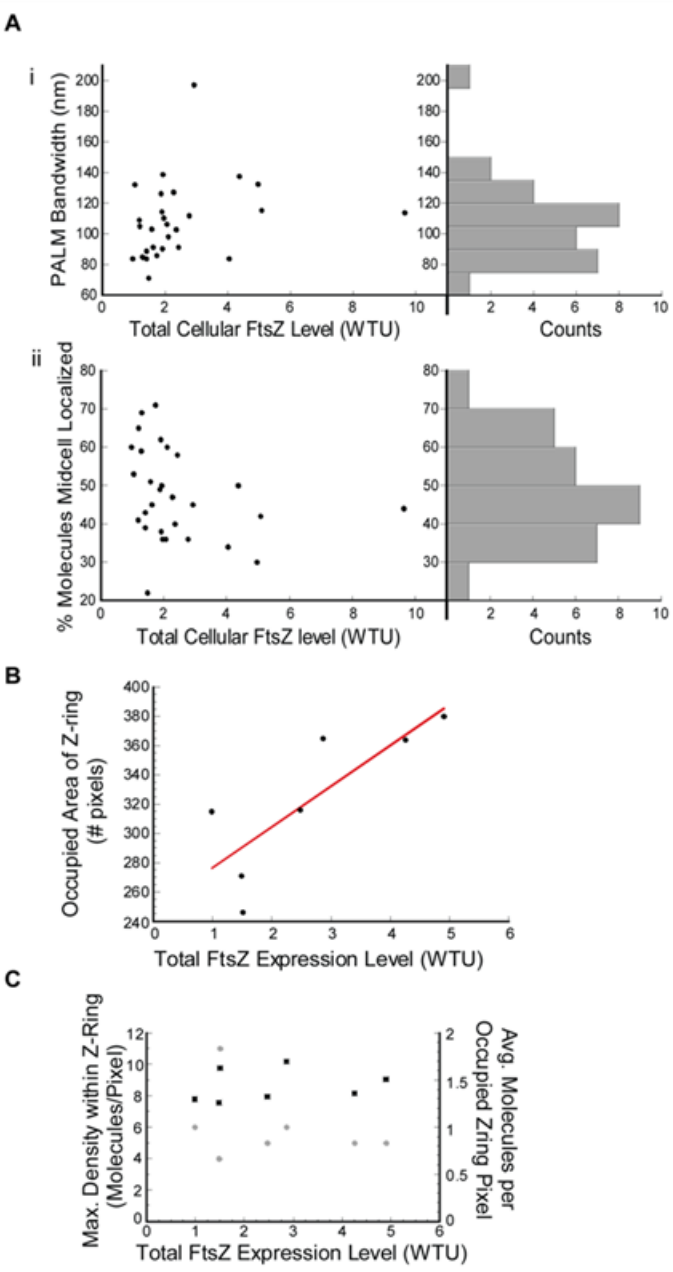

Figure 2.9 – Dependence of Z-ring properties on FtsZ expression level. (A) PALM bandwidth (i) and the percent of molecules detected during PALM imaging that were localized to the Z-ring (ii) are plotted against the total cellular FtsZ expression level in WTU, indicating that higher expression of FtsZ leads to an increased number of FtsZ molecules in the Z-ring, but not to a wider Z-ring. Each plot is conjoined on the right with a representative distribution of PALM bandwidths (i) or percent of molecules localized to the Z-ring (ii). (B) Correlation plot showing the linear relationship between the total pixel area of the Z-ring, calculated from the PALM image as the number of pixels containing molecules within the user-defined region, and the total FtsZ expression level, indicating that additional FtsZ molecules preferentially fill in empty spaces in the Z-ring. (C) Maximum (black squares) and average Z-ring density (grey circles) are plotted against total FtsZ expression level. Maximum Z-ring density refers to the highest number of molecules assigned to a single pixel within the user-defined Z-ring boundary. Average Z-ring density only takes into account the occupied pixels.

The helical and ring-like conformations of the Z-ring

The midcell Z-ring has long been viewed as a closed circle. Here, using PALM, we imaged the Z-ring of *E. coli* with ~35-nm spatial resolution. We discovered that in addition to the ring-like conformation, FtsZ also adopts a variety of compressed helical conformations with variable pitch and length. These compressed helical structures are indistinguishable from ring-like conformations under conventional fluorescence, and are therefore in contrast to the non-functional, extended helical structures that result from FtsZ overexpression (Ma et al., 1996). Since these structures are observed under non-perturbing FtsZ concentrations in dividing-cells, the functional structure of FtsZ is now ambiguous—ring, helix, helix-ring equilibrium? Further complicating the issue is the fact that all of the compressed helical structures observed by PALM lacked the continuity expected of an unbroken polymer. Although this observation could be an artifact of PALM's stochastic detection coupled with our incomplete labeling density, it is also possible that the helical structure we observed was a fractured Z-ring.

We are interested in understanding what factors may promote or regulate FtsZ assembly into compressed helical conformations. One possibility is that the FtsZ helix may arise from an underlying structural determinant such as heterogeneous membrane composition, which has recently been shown to exist in *B. subtilis* (Barak *et al.*, 2008). Another possibility is that the FtsZ helix is the natural result of a polymer growing on the cylindrical surface of a rod-shaped cell. The shape of this helix would be governed by the polymer's intrinsic mechanical

properties and its interaction with the surrounding environment (Andrews & Arkin, 2007). The latter model is supported by the polymorphic nature of FtsZ structures that exhibit substantial environmental sensitivity. Furthermore, a number of proteins (MinC, SulA, FtsA, ZipA, SlmA, ZapA and ZapB) are also known to interact with FtsZ *in vivo*, likely modulating its polymerization (Bernhardt & de Boer, 2005, Ebersbach et al., 2008, Harry *et al.*, 2006, Michie *et al.*, 2006, Small et al., 2007). These interactions may occur at various stages during the cell cycle or at various positions along the polymer, leading to an FtsZ structure with variable length and pitch. Lastly, if these helices are not continuous and represent fractured Z-rings, then perhaps the Z-ring itself is not contiguous but an alignment of smaller constituents. Clearly more work is needed to understand the assembly pathway and purpose of the FtsZ helix.

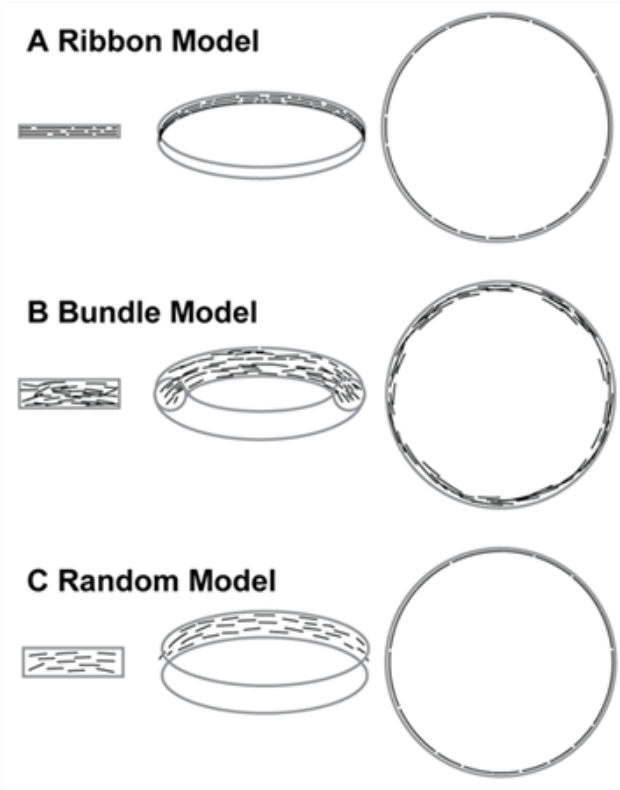

Figure 2.10 – Schematic drawings of Z-ring protofilament arrangements. (A) Flat-ribbon model. (B) Loose bundle model. (C) Random model. In each model, the 3D view of the arrangement of FtsZ protofilaments is shown in the middle. The 2D projection of a section of the ring along the long axis of the cell is shown on the left. The cross section of the ring along the short axis of the cell is shown on the right. FtsZ protofilaments are shown as black short arcs and the overall boundary of the Z-ring is outlined in gray. In the flat-ribbon model, FtsZ protofilaments are side-by-side in a single layer. They may or may not be connected head-to-tail to make longer filaments. In the bundle model, FtsZ protofilaments loosely associate with each other via non-uniform lateral interactions mediated by the intrinsic affinity between protofilaments and/or bundle-promoting proteins such as ZipA, ZapA and ZapB (not pictured). Individual FtsZ protofilaments are not necessarily aligned with each other and they may have different curvatures. In the random model, FtsZ protofilaments randomly scatter in a narrow band at the midcell and there are large spaces separating individual protofilaments, which do not engage in lateral interactions. Note that the sizes of the cell, the Z-ring and FtsZ protofilaments are not drawn to scale in order to enlarge details in the arrangement of FtsZ protofilaments.

Chapter 3

FtsZ-Ring Organization by ZapA and ZapB

Introduction

While the *in vitro* polymerization properties of FtsZ have been extensively characterized (Erickson et al., 1996b, Mukherjee & Lutkenhaus, 1999, Caplan & Erickson, 2003, Oliva et al., 2004, Chen et al., 2005, Esue *et al.*, 2005), attempts to determine the *in vivo* structure of the Z-ring have been difficult. Recently a series of studies using advanced high-resolution microscopy methods have begun to shed light on the *in vivo* structure of the Z-ring. In *Caulobacter crescentus*, electron cryotomography has shown that the Z-ring consists of a few short, single FtsZ protofilaments scattered around the division site (Li et al., 2007). In *E. coli*, we used a single-molecule based fluorescence method, Photoactivated Localization Microscopy (PALM) (Betzig et al., 2006), to image the Z-ring. We found that the apparent width of the Z-ring is ~110 nm and in some regions the molecule density of the Z-ring is higher than a single layer of protofilaments (Fu *et al.*, 2010). These results suggested that the Z-ring consists of loosely-associated protofilaments randomly overlapping in both the longitudinal and radial directions. A later three-dimensional super-resolution study found that the Z-ring in *C. crescentus* has a width (60-110 nm) and radial thickness that support our finding of a loose, overlapping structure (Biteen *et al.*, 2012). Finally, in *Bacillus subtilis* and *Staphylococcus aureus,* stimulated emission depletion microscopy (STED) and structured illumination microscopy (SIM) illustrated the highly irregular and discontinuous nature of the Z-ring, whereby regions of high and low densities were interspaced along the midcell plane (Jennings *et al.*, 2011, Strauss *et al.*, 2012).

One observation common to all of these *in vivo* studies is that FtsZ protofilaments appear to adopt a loose, heterogeneous arrangement within the Z-ring. This observation is in contrast to the largely ordered and aligned arrangements of protofilaments observed *in vitro*, where protofilaments associate with each other through intrinsic lateral interactions (Erickson et al., 1996b, Milam *et al.*, 2012). Hence, it is likely that factors other than the intrinsic lateral interactions are responsible for organizing the loose, heterogeneous arrangement of FtsZ protofilaments *in vivo*.

Recently, a group of FtsZ-associated proteins (ZapA, ZapB, ZapC and ZapD) have been identified and found to promote Z-ring assembly *in vivo* (Gueiros-Filho & Losick, 2002, Small et al., 2007, Ebersbach et al., 2008, Durand-Heredia et al., 2011, Hale et al., 2011, Durand-Heredia et al., 2012). Deletion of a single *zap* gene is not lethal, but often leads to abnormal Z-ring morphology visible to conventional fluorescence microscopy (Gueiros-Filho & Losick, 2002, Ebersbach et al., 2008, Dajkovic et al., 2010). Deletion of multiple *zap* genes results in severe cell division defects, suggesting that these Zap proteins have overlapping, but important functions in cell division (Durand-Heredia et al., 2011, Hale et al., 2011, Small et al., 2007, Durand-Heredia et al., 2012). To gain a deeper understanding of the *in vivo* contribution of Zap proteins to Z-ring structure and function, in this study we provide a quantitative characterization of the Z-ring in the absence of ZapA and ZapB.

ZapA is a small cytoplasmic protein (~12 kDa) that forms a dimer, which further associates into a tetramer upon increased concentration (Low et al., 2004,

Pacheco-Gómez et al., 2013). ZapA binds FtsZ directly with high-affinity (Galli & Gerdes, 2012) and promotes bundling of FtsZ protofilaments *in vitro* (Small et al., 2007, Gueiros-Filho & Losick, 2002, Mohammadi et al., 2009, Monahan et al., 2009, Dajkovic et al., 2010, Coltharp et al., 2012). ZapB is also a small cytoplasmic protein (~10 kDa) that can self-associate; its α-helical nature enables extensive coiled-coil interactions, resulting in the formation of long ZapB filaments and bundles *in vitro* (Ebersbach et al., 2008, Galli & Gerdes, 2012). ZapB does not bind FtsZ directly (Galli & Gerdes, 2012) but is associated with the Z-ring through its direct interaction with ZapA (Galli & Gerdes, 2010). Deletion of *zapA* or *zapB* results in cells that, while viable, display similar abnormal FtsZ structures, such as arcs, spirals and broad, diffusive bands (Ebersbach et al., 2008, Dajkovic et al., 2010). The similarity in deletion phenotype and ability to associate directly with each other suggests that these two proteins may function as a complex or in the same pathway to promote the assembly of the Z-ring. Due to the limited spatial resolution and qualitative nature of conventional fluorescence microscopy, the structural details of abnormal Z-rings formed in the absence of *zapA or zapB* are difficult to discern. Understanding the structure and dynamics of the Z-ring in the absence of *zapA* or *zapB* will help elucidate the cell division defect imposed by these mutants.

ΔzapA and ΔzapB display abnormal septa

We first characterized the effect of *zapA* or *zapB* deletion on cell length and division rates. We grew Δ*zapA* and Δ*zapB* cells (Baba *et al.*, 2006) in liquid $M9^+$ media and found that cells doubled with rates ($t_{1/2} \approx 160$) similar to the wild-type parental strain BW25113 (Datsenko & Wanner, 2000). However, when observed under a microscope, Δ*zapA* and Δ*zapB* cells exhibited significant increases in cell length (4.3 ± 1.1 μm, 4.2 ± 1.2 μm and 3.5 ± 0.6 μm for Δ*zapA,* Δ*zapB* and wt respectively). These findings are consistent with previous reports (Ebersbach et al., 2008, Dajkovic et al., 2010, Durand-Heredia et al., 2011).

We then used scanning electron microscopy (SEM) to examine septum morphology. We found that Δ*zapA* and Δ*zapB* cells often displayed abnormal septa that were oriented non-perpendicular to the cell's long axis, or not placed precisely at the midcell (Figure 3.1). In addition, ~ 20% of Δ*zapA* (n = 132) and Δ*zapB* cells (n = 197) contained more than one septum (Figure 3.1). In contrast, all constricting wt cells possessed a single furrow, oriented perpendicular to the long axis and aligned at or near midcell. This multi-septa phenotype is qualitatively different from the highly twisted septa caused by FtsZ GTPase variants FtsZ2 and FtsZ26 (Addinall *et al.*, 1997b, Bi & Lutkenhaus, 1992), or the mini-cell septa produced by FtsZ over-expression (Ward & Lutkenhaus, 1985). Because it was shown that septal geometry is determined by the geometry of underlying FtsZ structures (Addinall & Lutkenhaus, 1996b), the abnormal morphology and positioning of septa observed for Δ*zapA* and Δ*zapB* cells

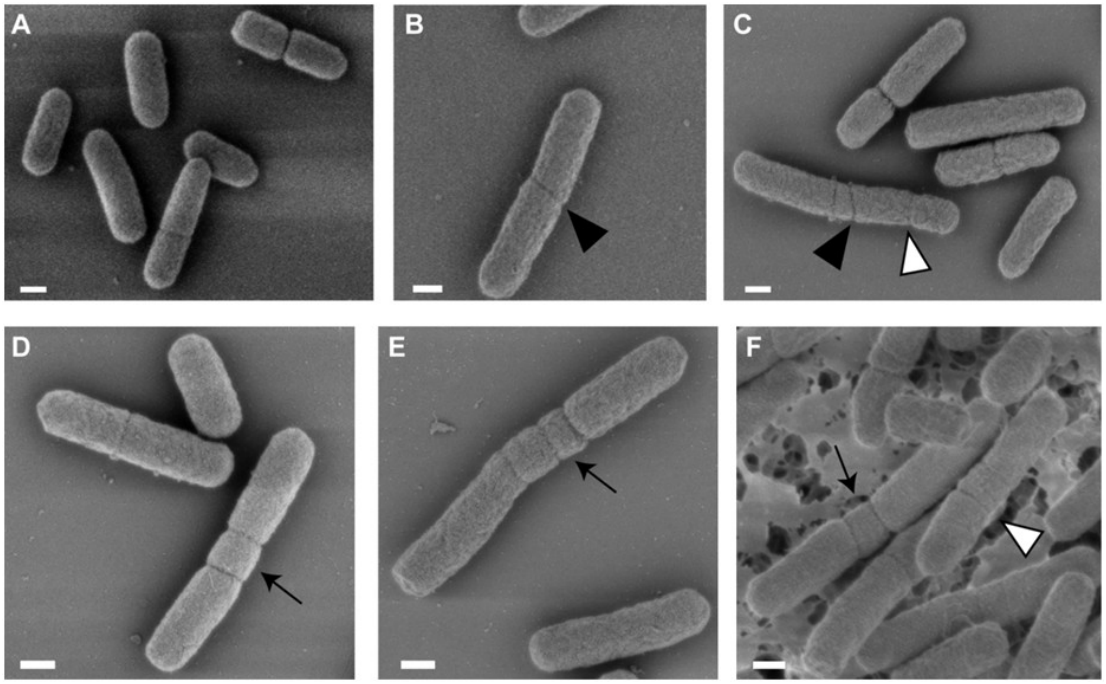

Figure 3.1 – Scanning electron micrographs of dividing *E. coli* cells. (A) BW25113 cells show single, midcell septa oriented perpendicular to the cells' long axes. In Δ*zapA* (B,C) and Δ*zapB* (D,E,F) cells, slanted (▲), non-midcell (Δ) and multiple (↑) septa are observed. Cells were imaged on PLL-treated coverslips (A-E) or on 0.2 μm filters in the absence of PLL (F). Scale Bars, 500 nm.

suggest that the morphology and positioning of FtsZ structures in the absence of ZapA and ZapB are also abnormal.

FtsZ structures are highly dynamic in ΔzapA or ΔzapB cells

To investigate the effect of ZapA and ZapB on the morphology and positioning of FtsZ structures, we ectopically expressed a partially functional FtsZ-GFP fusion protein (Kitagawa et al., 2005, Fu et al., 2010) in the Δ*zapA* or Δ*zapB* strains. We monitored the green fluorescence of FtsZ-GFP during cell division using conventional fluorescence light microscopy. Due to the leaky expression of the T5-lac promoter, FtsZ-GFP fluorescence was clearly visible in uninduced cells and was found to localize to midcell in ~75% of the wt population (Figure 3.2Ai). Although more than 60% of the Δ*zapA* and Δ*zapB* cells also showed distinct FtsZ midcell localization, a significant fraction (>35%) of these structures were qualitatively different from the sharp band typically observed in wt cells; instead, these structures appeared to be broad and diffusive, or contained multiple bands (Figure 3.2Aii-iii). Similar observations have been reported previously (Ebersbach et al., 2008, Dajkovic et al., 2010).

To monitor the dynamics of FtsZ structures during cell division in the absence of ZapA or ZapB, we observed exponentially growing Δ*zapA* and Δ*zapB* cells harboring the FtsZ-GFP plasmid without induction on a microscope stage for multiple generations. In contrast to the relatively stationary localization of FtsZ-GFP in wt cells (Figure 3.2Bi), we observed highly dynamic FtsZ-GFP structures transitioning back and forth between multiple sites in Δ*zapA* and Δ*zapB* cells (Figure 3.2Bii and 3.2Biii). These dynamic FtsZ-GFP structures often led to visible cell wall indentations, likely corresponding to the multiple septa observed by SEM (Figure 3.1). At late stages of the cell cycle these FtsZ-GFP

structures appeared to consolidate to a single site, where the cell completed septation (Figure 3.2Bii 175' and 3.2Biii 50'). Once division completed, FtsZ-GFP quickly localized to the midcell region of both daughter cells. Interestingly, in cases where FtsZ-GFP localized to a site in a newborn daughter cell that already possessed a clear indentation, presumably due to previous occupation by FtsZ, cell division ensued more than two-fold faster than those with no visible indentation (Figure 3.2Bii-iii and 3.2C). Consequently, the distributions of cell generation times for actively dividing Δ*zapA* and Δ*zapB* cells are shifted to shorter times relative to the wt population (Figure 3.2C). We note that the difference in relative division rates observed by time-lapse microscopy (Figure 3.2C) versus liquid media growth can be explained by the increased death rate caused by *zapA* (and presumably *zapB*) deletion (Dajkovic et al., 2010). The death rate contributes to the bulk doubling time measured in liquid media, but not to the division time measured from our time-lapse imaging analysis, which only included cells that divided successfully. Thus, the higher death rate of Δ*zapA* and Δ*zapB* cells may be compensated by faster division times to result in bulk doubling times that are similar to wt cells.

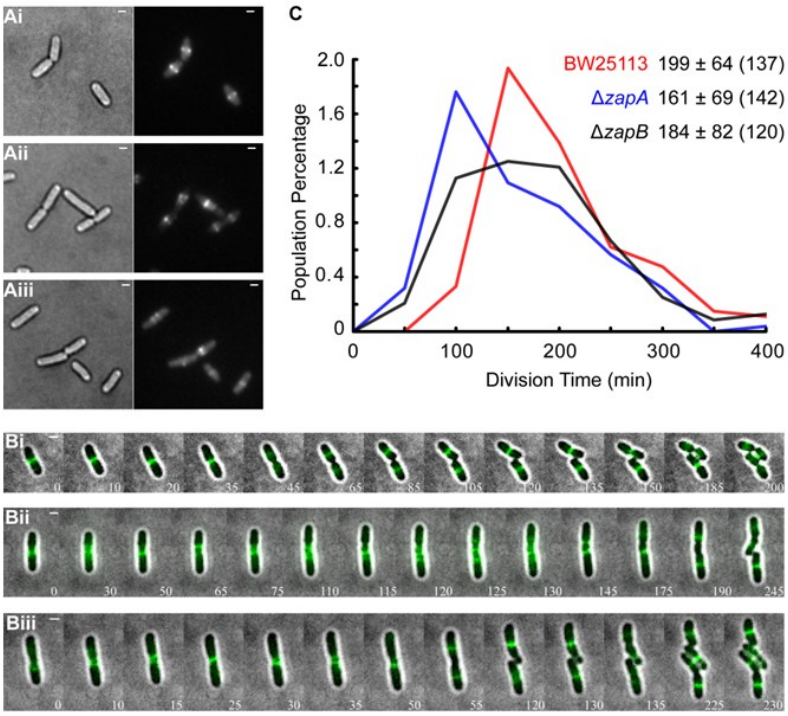

Figure 3. 2 – Localization and dynamics of FtsZ-GFP in wt, Δ*zapA* and Δ*zapB* cells. (A) Snapshots of BW25113 (Ai), Δ*zapA* (Aii) and Δ*zapB* (Aiii) cells expressing FtsZ-GFP. Bright-field images and corresponding fluorescence images are displayed side by side. (B) Montages from time-lapse movies of BW25113 (Bi), Δ*zapA* (Bii) and Δ*zapB* (Biii) cells expressing FtsZ-GFP during cell division. At each time point, the fluorescence image (green) was overlaid with the corresponding bright-field image (gray) with the time (min) indicated in the bottom corner. (C) Distributions of cell division times for BW25113 (red) Δ*zapA* (blue) or Δ*zapB* (black) cells determined from time-lapse movies. The average division time of wt cells is significantly different from that of Δ*zapA* and Δ*zapB* (ks-test, $P < 0.01$). Subpopulations of Δ*zapA* and Δ*zapB* cells in which FtsZ relocalized to visibly constricted sites in newborn daughter cells (ex. Bii 145', 190', and 245' top cells; Biii 135', 225' and 230' middle cells) divided significantly faster than the general population with division times of 83 ± 11 min (n = 15) and 77 ± 13 min (n = 6), respectively. Mean ± standard deviation (# of division events). Scale Bars, 1 μm.

Ring-like FtsZ structures in ΔzapA and ΔzapB cells resemble wild-type Z-rings

We showed in Figure 3.2A that in the absence of ZapA and ZapB, FtsZ forms broad and diffusive, or extended, multi-band structures in addition to the single-band structure characteristic of the Z-ring. However, details of these FtsZ structures are not discernible under conventional fluorescence light microscopy due to diffraction-limited resolution. We employed the single-molecule based super-resolution imaging method PALM (Betzig et al., 2006), which enables quantitative structural measurements (Coltharp et al., 2012, Renz *et al.*, 2012, Sengupta *et al.*, 2011, Annibale *et al.*, 2011, Lando *et al.*, 2012, Ulbrich & Isacoff, 2007), to investigate these FtsZ structures. Comparing FtsZ structures formed in a wt background to those assembled in the absence of ZapA or ZapB should provide insight into how ZapA and ZapB help promote Z-ring assembly.

We performed PALM imaging using an FtsZ-mEos2 construct described previously (Fu et al., 2010, Coltharp et al., 2012). We imaged live cells where FtsZ-mEos2 was ectopically expressed at ~30% of the total cellular FtsZ level in BW25113, Δ*zapA* and Δ*zapB* (Figure 3.3). Since only slowly moving molecules could be detected at our imaging frame rate, live-cell PALM images comprise molecules that are either membrane-associated or incorporated into large superstructures. We found that of cells displaying distinct FtsZ structures, 36% of Δ*zapA* (n = 99) and 35% of Δ*zapB* (n = 103) cells showed a single, sharp band at midcell, reminiscent of the typical Z-ring observed in wt cells (Figure 3.4). These Z-rings contained 69% of the total detected FtsZ-mEos2 molecules present

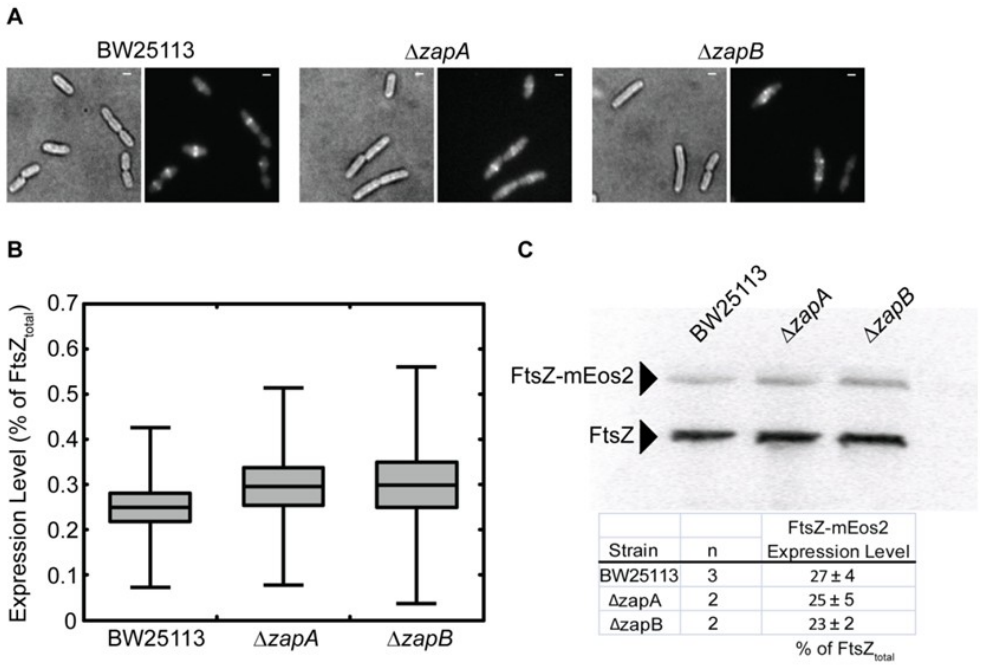

Figure 3.3 – Expression level of FtsZ-mEos2. (A) Induced populations of BW25113, Δ*zapA*, and Δ*zapB* cells expressing FtsZ-mEos2 from pJB042. (B) The integrated green fluorescence signal of mEos2 was used to calculate FtsZ-mEos2 expression as a percent of $FtsZ_{total}$ ($FtsZ_{wt}$ + FtsZ-mEos2) for the BW25113, Δ*zapA*, and Δ*zapB* cells. Distributions are presented as the mean boxed by the 95% confidence interval, bounded by the standard deviation. (C) A representative immunoblot of BW25113, Δ*zapA*, and Δ*zapB* cells grown under PALM growth conditions and stained with α-FtsZ illustrates FtsZ-mEos2 relative to $FtsZ_{wt}$ was ~1:3. Both the measurements suggest that FtsZ-mEos2 is present at about 30% of $FtsZ_{total}$ (~1,500 molecules per cell). Scale Bars, 1 μm.

within cells. In contrast, 50% of wt cells (n = 117) displayed ring-like structures at midcell and 76% of the detected cellular FtsZ-mEos2 molecules localized to these structures (Table 3.1). Despite these differences, we found that the ring-like structures in all three strains had similar widths (~110 nm, $P > 0.05$) and diameters (~1μm, $P > 0.05$), suggesting that the structural organization of the ring-like FtsZ structure formed in the absence of ZapA or ZapB is similar to that

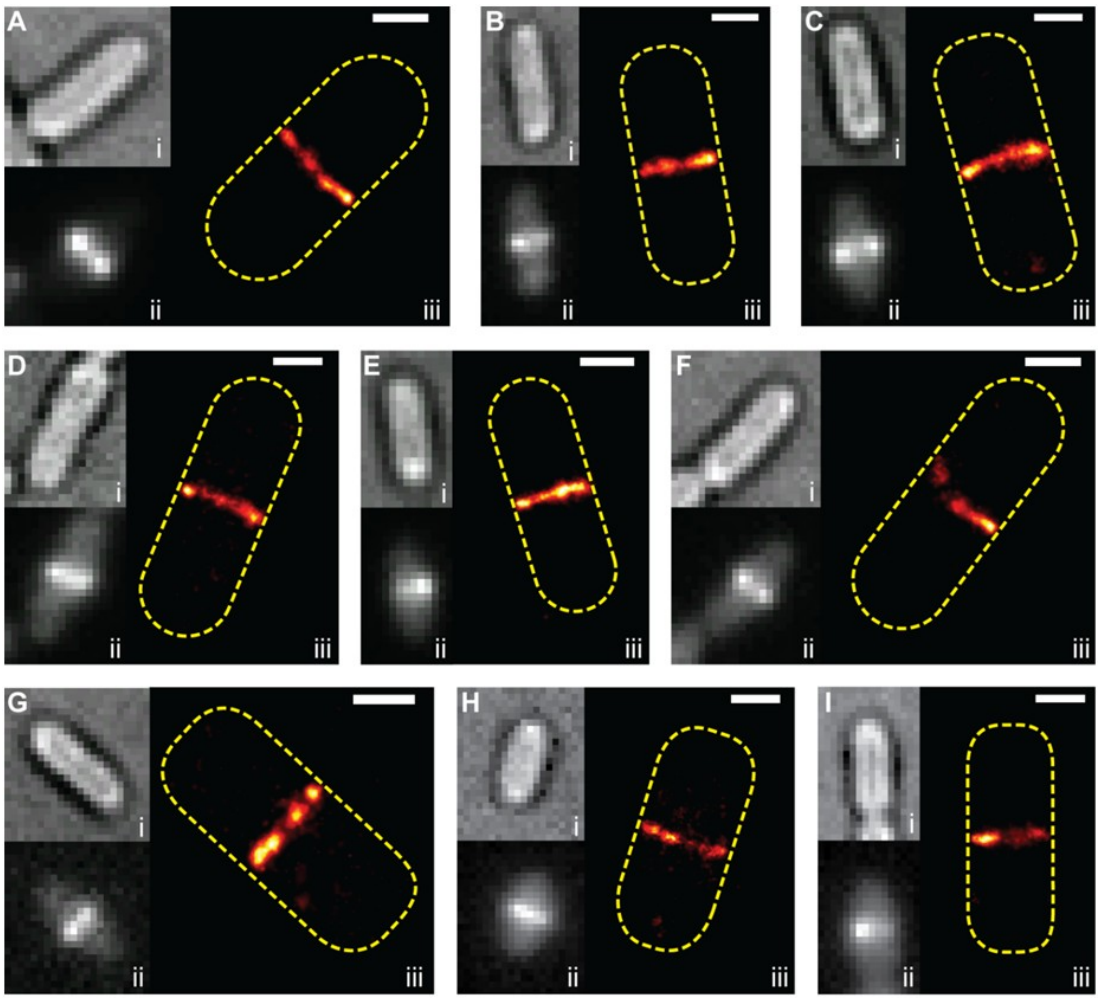

Figure 3.4 – Live-cell PALM imaging of ring-like FtsZ structures. Images of live BW25113 (A-C), Δ*zapA* (D-F) and Δ*zapB* (G-I) cells expressing FtsZ-mEos2 from pJB042 are shown in the order of bright-field (i), ensemble green fluorescence image (ii), and PALM image (iii). The dotted yellow line is a general indicator of the cell outline. All cells show a single band at midcell, indicative of a normal Z-ring. Scale Bars, 500 nm.

in wt cells. We note that with a working resolution of ~50 nm under live-cell imaging conditions (see Chapter 5-5.4.4), we cannot exclude differences at the molecular level.

Table 3.1 – Dimensional analysis of ring-like FtsZ structures.

	#. of cells	Ring[a] Width (nm)	Ring[b] Diam. (nm)	% Molecules in Midcell Structure
BW25113	58	113 ± 3	960 ± 15	76 ± 2
ΔzapA	36	117 ± 5	1000 ± 20	69 ± 3
ΔzapB	36	104 ± 4	960 ± 20	69 ± 3

a. Full width half maximum.

b. Non-constricting cells (BW25113 n=37, ΔzapA n=20, ΔzapB n=22). Mean ± Standard Error.

Non-ring FtsZ structures in ΔzapA and ΔzapB cells are composed of dispersed clusters

In PALM images of Δ*zapA* and Δ*zapB* cells, 65% and 64% of cells showed a variety of non-ring structures, respectively (Figure 3.5D-O). While these non-ring FtsZ-mEos2 structures appeared to adopt broad, diffusive or extended, multi-band structures in conventional fluorescence images, the corresponding PALM images all revealed a widely dispersed, clustered appearance (Figure 3.5D-O). Since only FtsZ-mEos2 molecules that moved slowly, presumably tethered to the membrane or confined in large superstructures, were detectable by live-cell PALM, we suspect that the clusters in the PALM images are composed of membrane-tethered FtsZ molecules and/or polymers.

In 50% of wt cells we also observed non-ring FtsZ structures that had clustered appearances (Figure 3.5A-C). However, these non-ring FtsZ structures appeared qualitatively different from those observed in Δ*zapA* and Δ*zapB* cells (Figure 3.5D-O); in general, FtsZ-mEos2 clusters in wt cells were either a single focus at midcell, a pair of foci at the periphery of the midcell plane, or multiple foci tightly distributed around midcell, reminiscent of the compact helical structure observed previously (Fu et al., 2010). Furthermore, the corresponding ensemble images of these wt non-ring structures resembled the single-band or peripheral dot structures typically attributed to normal Z-rings (Den Blaauwen *et al.*, 1999, Erickson et al., 2010, Dajkovic et al., 2010), and are in stark contrast to the broad

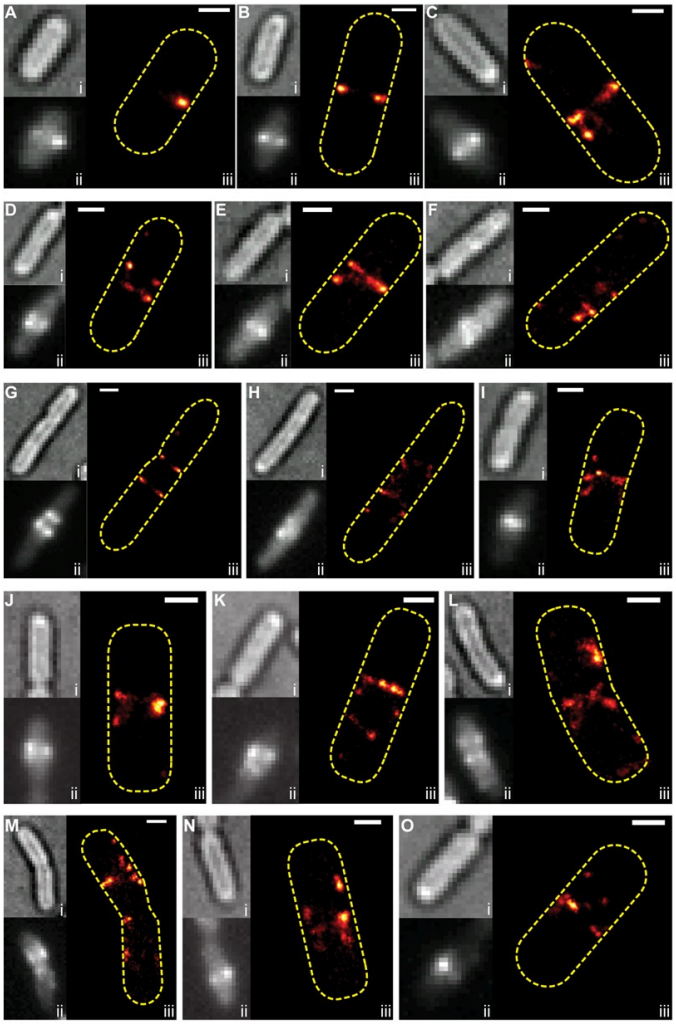

Figure 3.5 – Live-cell PALM imaging of non-ring FtsZ structures. Images of live BW25113 (A-C), Δ*zapA* (D-I) and Δ*zapB* (J-O) cells expressing FtsZ-mEos2 from pJB042 are displayed in the order of bright-field (i), ensemble green fluorescence image (ii), and PALM image (iii). Although the ring-like band conformations shown in Figure 3.3 are the predominant structures formed in wt cells, PALM imaging reveals that some wt cells possess punctate structures, characterized by a single focus (A), two foci (B) or multiple foci reminiscent of a compact helix (C). For Δ*zapA* and Δ*zapB* cells, while the ensemble green fluorescence images show broad, diffusive, or extended multi-band structures, the corresponding PALM images all resolve into various discontinuous arrangements of clusters. Scale Bars, 500 nm.

or extended ensemble images observed in the deletion strains. These observations suggest that these FtsZ clusters may be inherent to the assembly of the Z-ring, and that ZapA or ZapB may affect the composition and spatial distribution of these clusters.

To ascertain whether the clustered appearance of FtsZ-mEos2 in Δ*zapA* and Δ*zapB* cells was caused by differences in FtsZ expression levels relative to wt cells, we performed quantitative immunoblotting. We found that both the endogenous FtsZ and the FtsZ-mEos2 expression levels were similar in all three strains (Figure 3.3 and 5.3). We also found that when ZapA or ZapB was expressed *in trans* in Δ*zapA* or Δ*zapB*, wt Z-ring morphology was restored (Figure 3.6). These observations suggest that FtsZ-mEos2 clusters were not produced as a result of FtsZ or FtsZ-mEos2 overexpression, and were specific to the deletion of *zapA* and *zapB*.

Next, we examined whether the observed FtsZ-mEos2 clusters in Δ*zapA* and Δ*zapB* cells were an artifact of the self-aggregation of the mEos2 protein (Landgraf *et al.*, 2012, Swulius & Jensen, 2012). We replaced mEos2 with two other photoactivatable fluorescent proteins, Dronpa (Ando *et al.*, 2004) and mEos3 (Zhang *et al.*, 2012), which have been shown to be truly monomeric. We observed similarly dispersed clusters in Δ*zapA* and Δ*zapB* cells with both fluorescent proteins (Figures 3.7-8). Additionally, we performed super-resolution immunofluorescence imaging on *ΔzapA* and *ΔzapB* cells expressing native, untagged FtsZ using stochastic optical reconstruction microscopy (STORM) (Rust *et al.*, 2006). Again we observed dispersed FtsZ clusters similar to what

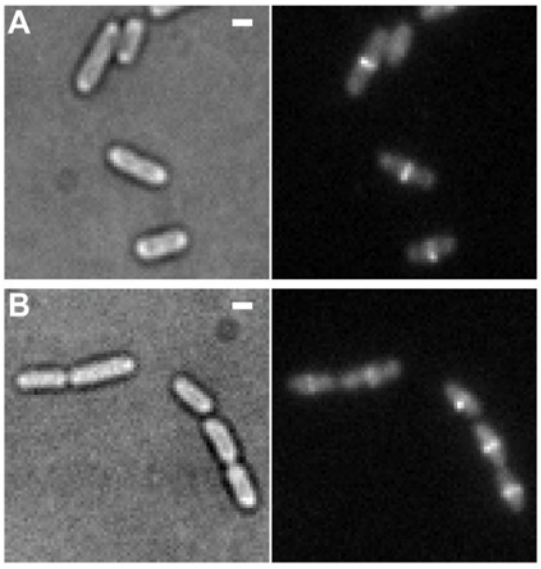

Figure 3.6 – Dispersed FtsZ clusters are specific to the absence of ZapA and ZapB. Bright-field and ensemble fluorescence images of Δ*zapA* (A) and Δ*zapB* (B) cells expressing FtsZ-mEos2 from pJB004, supplemented with ZapA or ZapB from pJB056 or pJB065, respectively. ZapA and ZapB expression was induced with 0.2% arabinose for 1 hr followed by a wash and a 3 hr outgrowth. Scale Bars, 1 μm.

were observed in FtsZ-mEos2 PALM imaging (Figure 3.9). These observations demonstrate that the FtsZ-mEos2 clusters in *ΔzapA* and *ΔzapB* cells are not fluorescent-protein specific but reflect the intrinsic property of native FtsZ in the absence of ZapA or ZapB.

To test whether the FtsZ-mEos2 clusters were dependent on FtsZ polymerization, we examined the effect of SulA, a negative regulator of FtsZ polymerization that sequesters FtsZ monomers (Dajkovic *et al.*, 2008b, Chen et al., 2012). In cells overexpressing SulA, we observed a homogenous, diffusive fluorescence signal for FtsZ-mEos2 by conventional fluorescence and detected very few FtsZ-mEos2 molecules via PALM (Figure 3.10B). This observation is consistent with the notion that SulA-sequestered FtsZ monomers are largely cytoplasmic, and thus undetectable by live-cell PALM. Finally, when wt cells were treated with cinnamaldehyde, a known inhibitor of Z-ring assembly (Domadia *et al.*, 2007), we found that FtsZ-mEos2 assembled into large, cohesive clusters at

the cell poles (Figure 3.10C), in contrast to the dispersed FtsZ-mEos2 clusters observed in the Δ*zapA* and Δ*zapB* strains (Figure 3.5D-O). These results suggest that the widely dispersed FtsZ-mEos2 clusters are likely composed of polymerized FtsZ molecules.

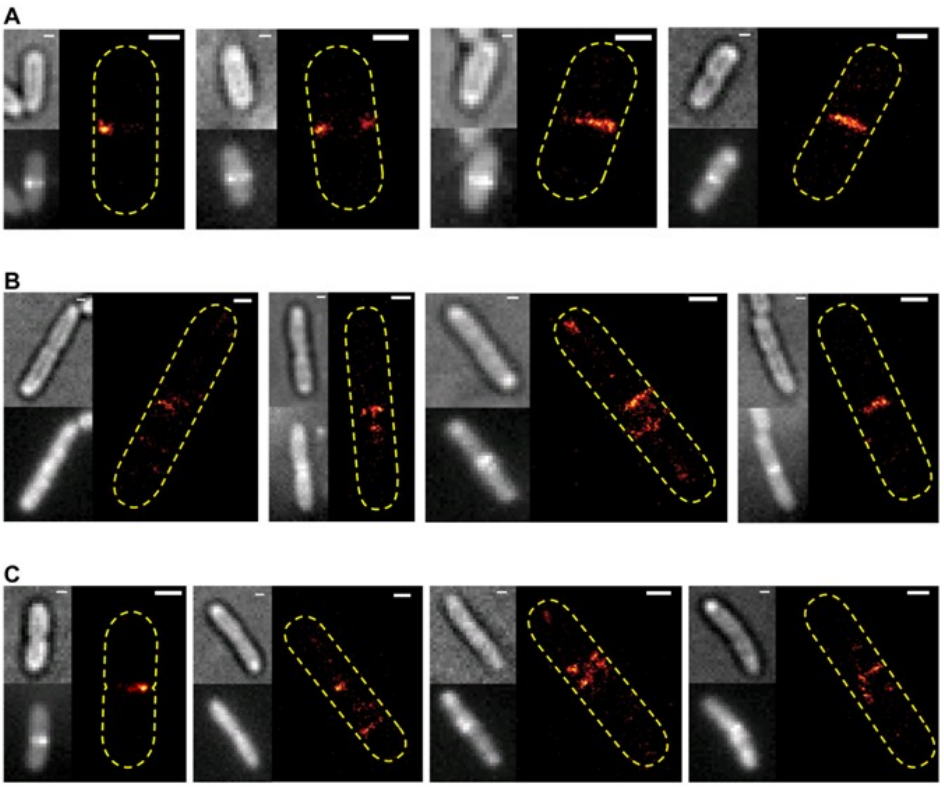

Figure 3.7 – PALM imaging of FtsZ-Dronpa. BW25113 (A), Δ*zapA* (B), and Δ*zapB* (C) cells expressing FtsZ-Dronpa were imaged by PALM. Four cells are shown for each strain. Each cell is displayed as a bright-field image atop a constructed ensemble image adjacent to a PALM image. Dronpa is a photoswitchable protein that cycles between on and off green states, consequently the PALM acquisition scheme was slightly altered. Instead of a single 3,000 frame acquisition with 561-nm excitation, two sets of 1,500 frames were acquired using 488-nm excitation (350 W cm^{-2}). Continuous 405-nm activation was only applied to the second set of frames. Since only a small subset of Dronpa molecules are fluorescent at the start of an experiment, ensemble fluorescence images of Dronpa are not reliable. The constructed ensemble images shown approximate an ensemble fluorescence image using Z-projections of all acquired PALM frames. Qualitatively, FtsZ-Dronpa results in the same morphologies observed for FtsZ-mEos2, including the dispersed cluster arrangement. Scale Bars, 500nm.

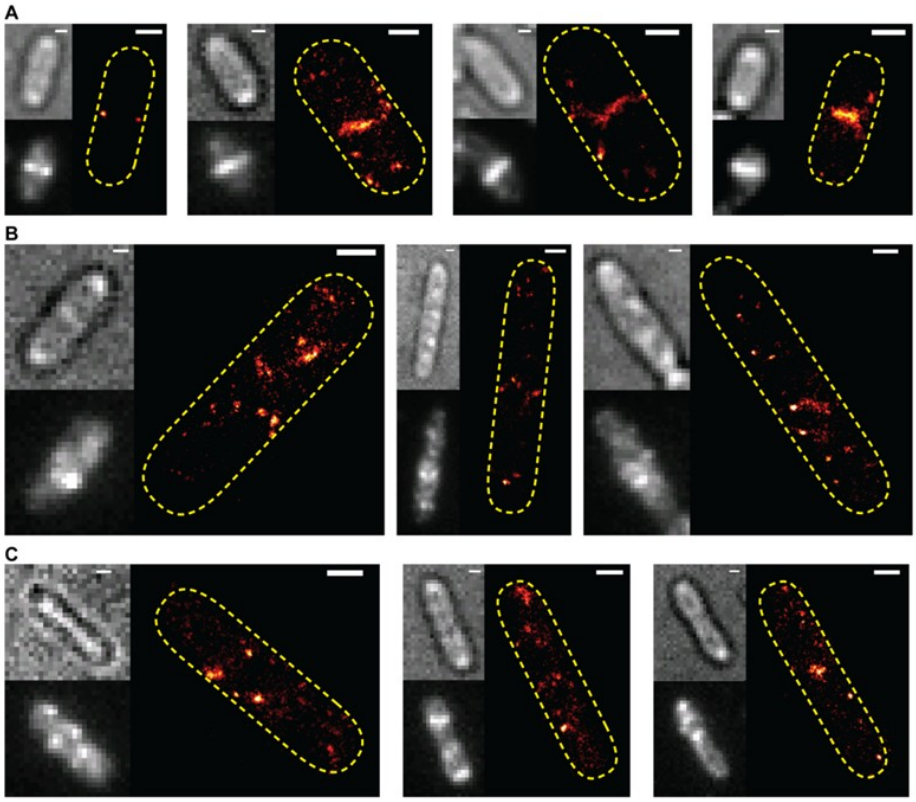

Figure 3.8 – PALM imaging of FtsZ-mEos3. BW25113 (A), Δ*zapA* (B), and Δ*zapB* (C) cells expressing FtsZ-mEos3 were imaged by PALM. Four cells are shown for each strain. Each cell is displayed as a bright-field image atop an ensemble fluorescence image adjacent to a PALM image. All images were acquired using the same imaging scheme as applied for FtsZ-mEos2. Qualitatively, FtsZ-mEos3 results in the same morphologies observed as for FtsZ-mEos2, including the dispersed cluster arrangement. Scale Bars, 500nm.

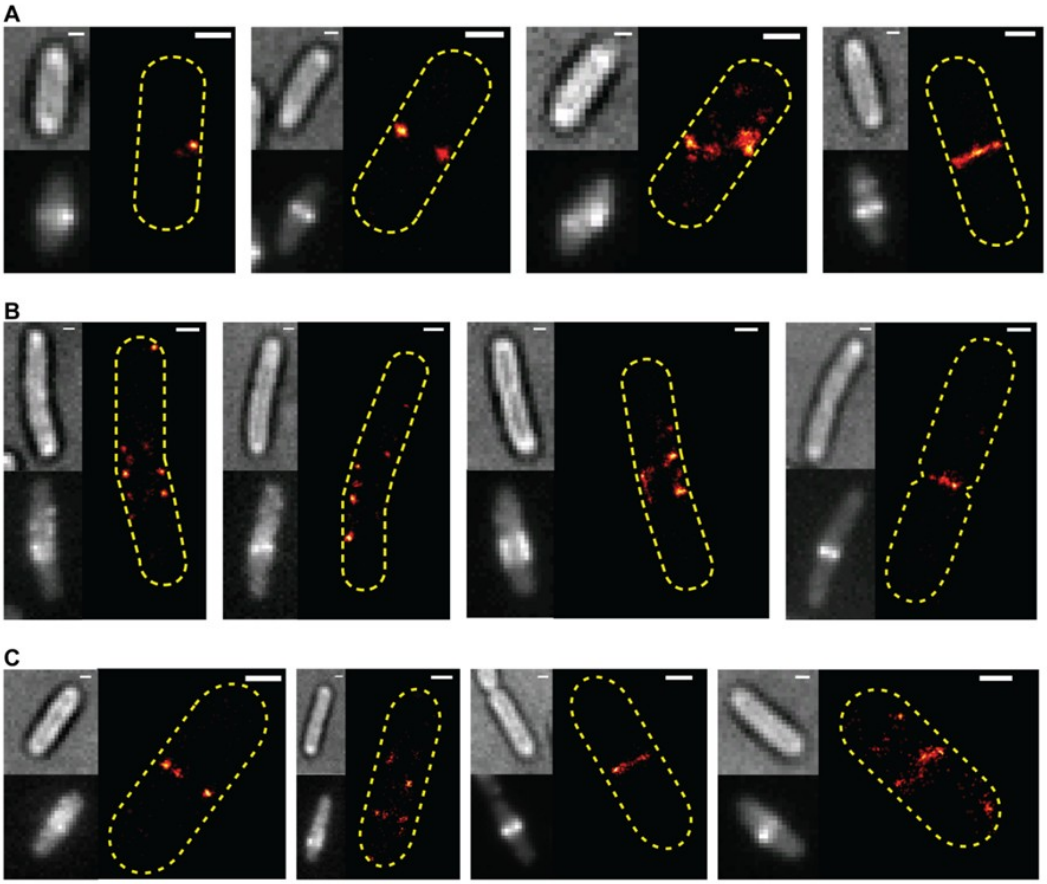

Figure 3.9 – STORM imaging of FtsZ in immunolabeled *E. coli*. BW25113 (A), Δ*zapA* (B), and Δ*zapB* (C) cells labeled with α-FtsZ and Alexa-568 were imaged by STORM. Each cell is displayed as a bright-field image atop an "ensemble" fluorescence image adjacent to a STORM image. The abnormal septa of elongated Δ*zapA* and Δ*zapB* cells resolved into dispersed cluster arrangements that are in contrast to the band-like, midcell structures characteristic of wt cells. Due to the blinking properties of Alexa-568, the contrast of the STORM images was adjusted to enhance morphology identification. Scale Bars, 500nm.

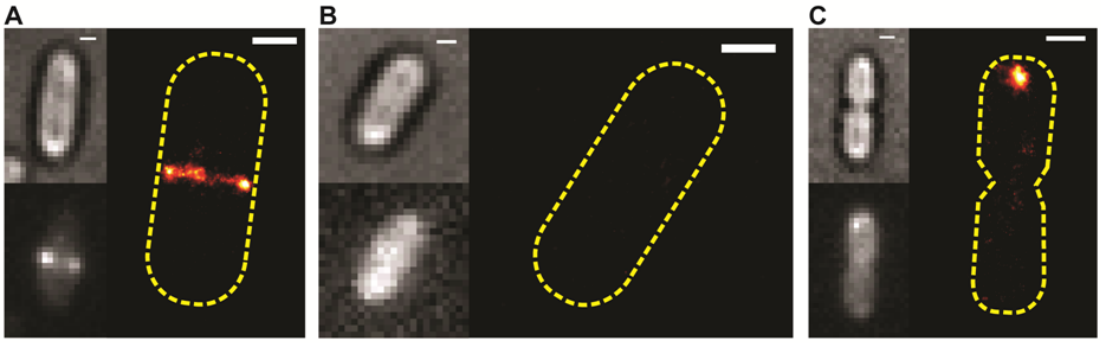

Figure 3.10 – Dispersed FtsZ clusters are dependent on the polymerization of FtsZ. (A-C) BW25113 cells containing pJB042 ($P_{T5\text{-}Lac}$::FtsZ-mEos2) and pJB095 (P_{BAD}::SulA) were grown under normal PALM growth conditions. During the outgrowth period, the culture was split into three fractions. A representative cell from each fraction is shown as a bright-field image atop an ensemble fluorescence image, adjacent to a PALM image. All PALM images are displayed with the same contrast to illustrate the effect of various methods of depolymerization on FtsZ-mEos2 localization. Fraction #1 (A) illustrates the normal midcell localization of FtsZ-mEos2. Fraction #2 (B) was induced for SulA expression with 0.2% arabinose 30 min prior to imaging. Fraction #3 (C) was treated with 10 mM Cinnamaldehyde 30-60 min prior to imaging. Scale Bars, 500 nm.

FtsZ clusters in ΔzapA and ΔzapB cells are quantitatively different from those in wt cells

We have previously shown that quantitative measurements of dimensions and molecule density of the Z-ring can be obtained from PALM images, as PALM is a single-molecule based super-resolution method (Fu et al., 2010, Coltharp et al., 2012). To reduce the measurement uncertainty associated with two-dimensional projections of three-dimensional cellular structures in wide-field illumination, we performed total internal reflection (TIR) PALM imaging on the three strains. TIR-PALM confines activation and excitation of FtsZ-mEos2 molecules to a thin layer (~200 nm) at the interface of the coverslip and cell, hence only FtsZ-mEos2 molecules at the bottom membrane of the cell are selectively imaged, avoiding contributions of FtsZ-mEos2 molecules from the cytoplasm and top membrane (Fu et al., 2010).

Using TIR-PALM, we observed similar ring and non-ring structures for FtsZ-mEos2 (Figure 3.11) as in wide-field PALM (Figure 3.4-5). We then applied the same thresholding algorithm to all three strains to isolate individual clusters (Chapter #5-5.5.3). Since ring structures were also heterogeneous and slightly punctate, we included both ring and non-ring structures in the analysis to avoid bias. For all three strains, we found that 80% of FtsZ-mEos2 localizations were contained within 23-33% of the identified clusters (Chapter #5-5.5.3), suggesting that most detected FtsZ-mEos2 molecules were confined in a few large clusters and were not evenly distributed. We selected these large clusters and determined the following four parameters for each cluster: number of detected

FtsZ-mEos2 molecules, area occupied, molecule density (number of molecules per unit area), and displacement from the midcell plane (Figure 3.11A).

We found that on average FtsZ-mEos2 clusters of Δ*zapA* and Δ*zapB* cells contained fewer molecules (<50% wt), occupied less area (<60% wt), were less dense (~80% wt), and were displaced three-fold farther away from the midcell plane than wt clusters (Figure 3.11B-E, Table 3.2). All differences were statistically significant ($P < 1e\text{-}5$). We also observed small, but significant differences ($P < 0.01$) in all measurements between Δ*zapA* and Δ*zapB,* except for the molecule density measurement ($P = 0.06$). Interestingly, all measurements of Δ*zapB* were closer to wt than those of Δ*zapA* were to wt. None of the four measurements showed a strong correlation with cell length (Figure 3.12), suggesting that a cell cycle-dependent progression of cluster formation is unlikely. Next, we analyzed the shapes of these clusters by comparing the lengths and orientations of the major and minor axes of individual clusters among the three strains (Figure 3.11, 3.13 and Table 3.2). In wt cells, a ring-like FtsZ-mEos2 structure would have a major axis length proportional to the ring diameter, a minor axis length proportional to the width of the Z-ring, and an orientation parallel to the cell's short axis. We found that on average the major axis lengths of Δ*zapA* and Δ*zapB* clusters were ~50% the length of wt clusters, whereas the minor axis lengths of Δ*zapA* and Δ*zapB* clusters were only reduced by ~20%. Interestingly, the major axis length distributions for all three strains exhibited a 2-fold larger variation ($\sigma/\bar{x}$) than the minor axis length distribution, suggesting that clusters predominantly differ from each other in length rather

than width (Figure 3.11F-G). Furthermore, we found the ratio of major:minor axis length was significantly larger than one for all strains (Figure 3.11H), indicating that clusters preferentially adopt elongated shapes. Finally, in contrast to wt clusters where the major axis is largely parallel to the short axis of the cell (within ±15°), that of Δ*zapA* and Δ*zapB* clusters were tilted farther away (±30°) from the short axis of the cell (Figure 3.11I).

Figure 3.11 - Cluster analysis of FtsZ-mEos2 TIR-PALM images. (Ai-iii) Images of a BW25113 cell expressing FtsZ-mEos2 are shown in the order of bright-field (i), ensemble green fluorescence image (ii) and TIR-PALM image (iii). A threshold was applied to the TIR-PALM image to generate a binary image (iv) where the white region indicates an identified cluster. Using the cluster coordinates we determined the number of molecules localized within each identified region and the overall size of the region. (v) Expanded view of the boxed area in iv illustrates additional cluster measurements: major axis length (a), minor axis length (b), displacement of centroid (c) from midcell plane and orientation of major axis relative to midcell plane (d). FtsZ-mEos2 clusters observed in BW25113 (red), Δ*zapA* (blue) and Δ*zapB* (black) cells were compared for molecule counts (B), size (C), density (D), location (E), shape (F-G), and orientation (I). Histograms for each measurement were plotted using the same bin size (max/10) and normalized by the total number of counts. These measurements are summarized in Table 3.2. All the measured properties of clusters in Δ*zapA* and Δ*zapB* showed significant differences ($P < 1e\text{-}5$) from wt, with Δ*zapB* clusters closer to wt values. This observation was true independent of threshold value. Scale Bars, 500 nm.

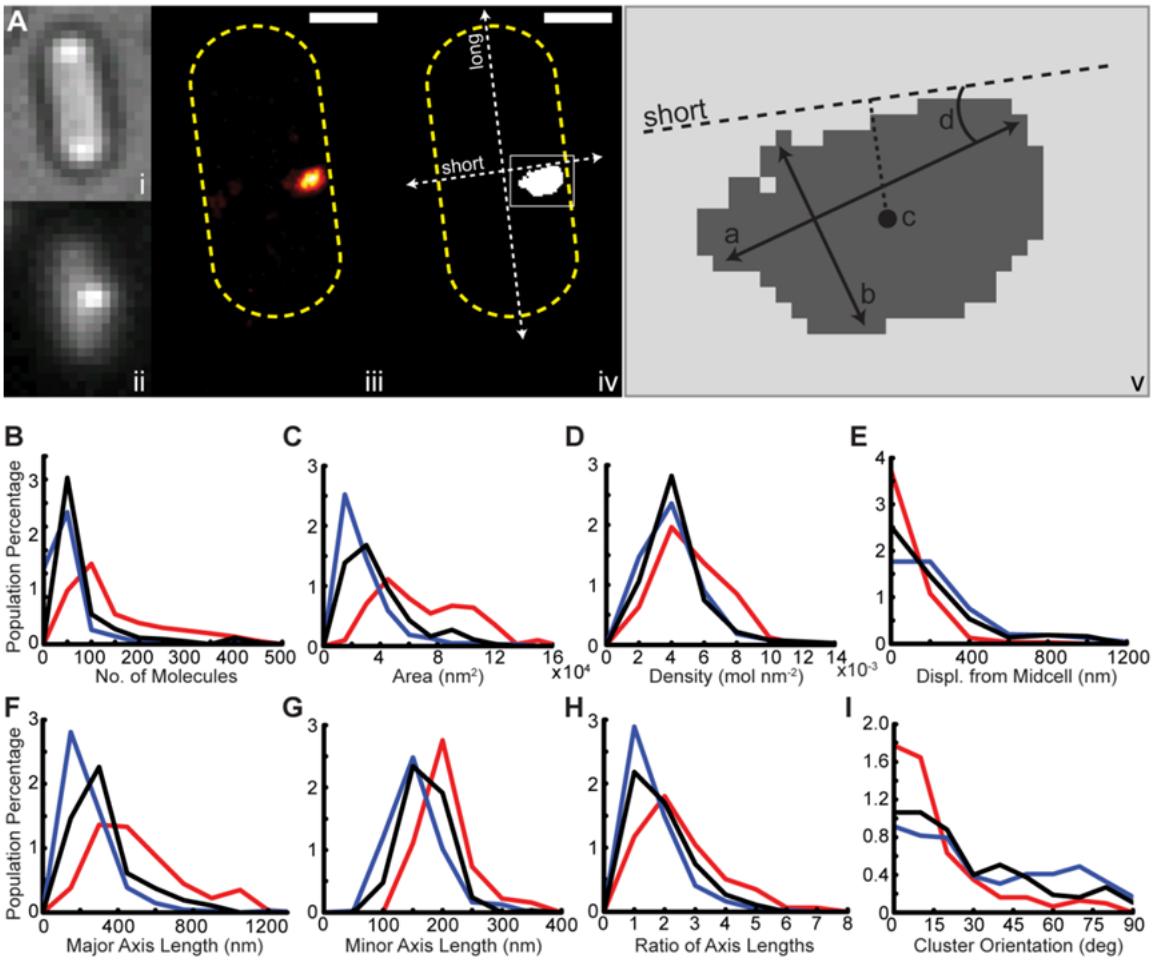

Figure 3.11 - Cluster analysis of FtsZ-mEos2 TIR-PALM images.

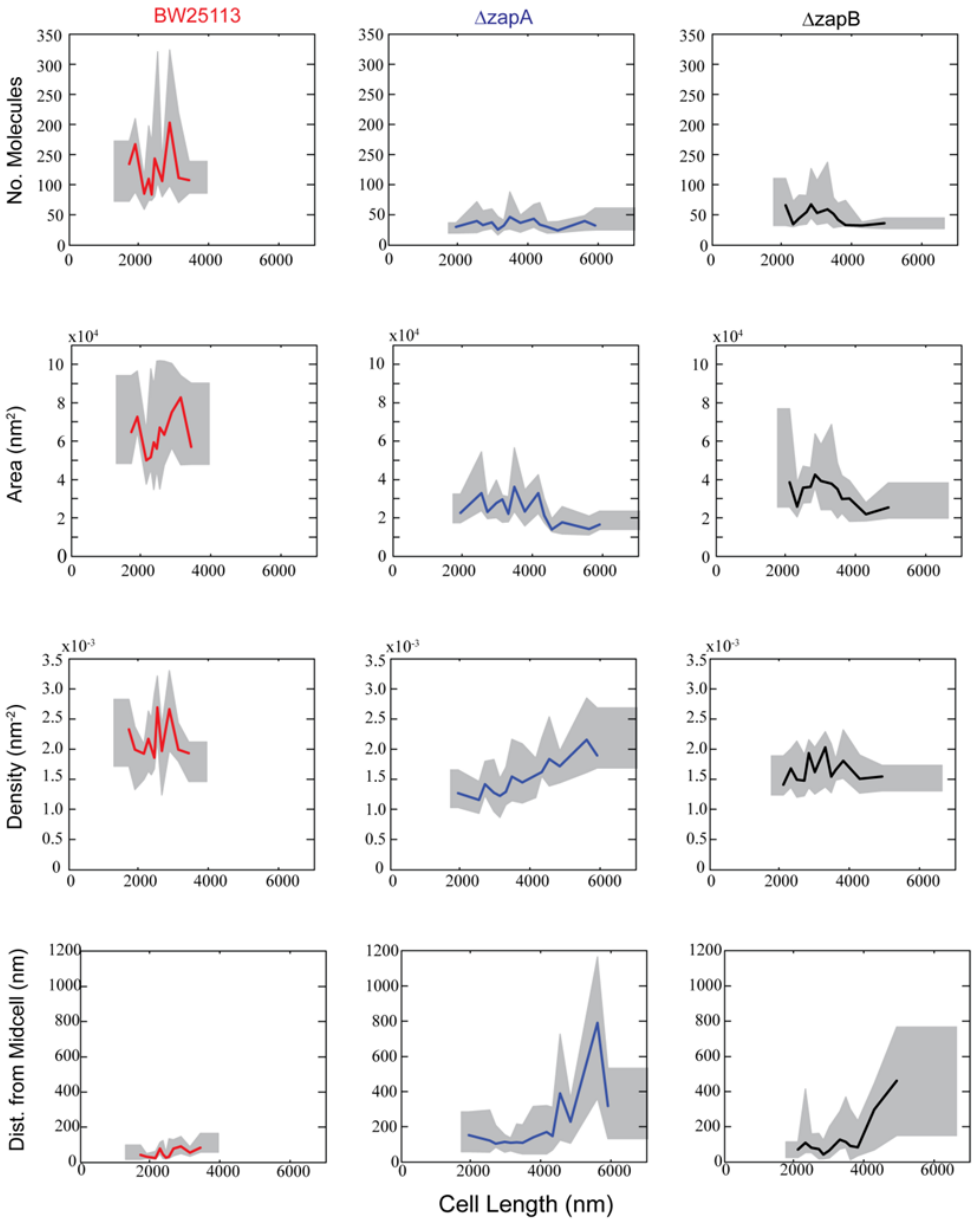

Figure 3.12 – Cell-cycle dependence of cluster composition and dimension. Cluster attributes identified in BW25113 (red), Δ*zapA* (blue), or Δ*zapB* (black) are plotted against the corresponding cell length in order to gain insight into how cluster attributes change over time. Cluster data are binned according to cell length and the median of each bin are connected by a bold line. The grey region indicates the binned inter-quartile range.

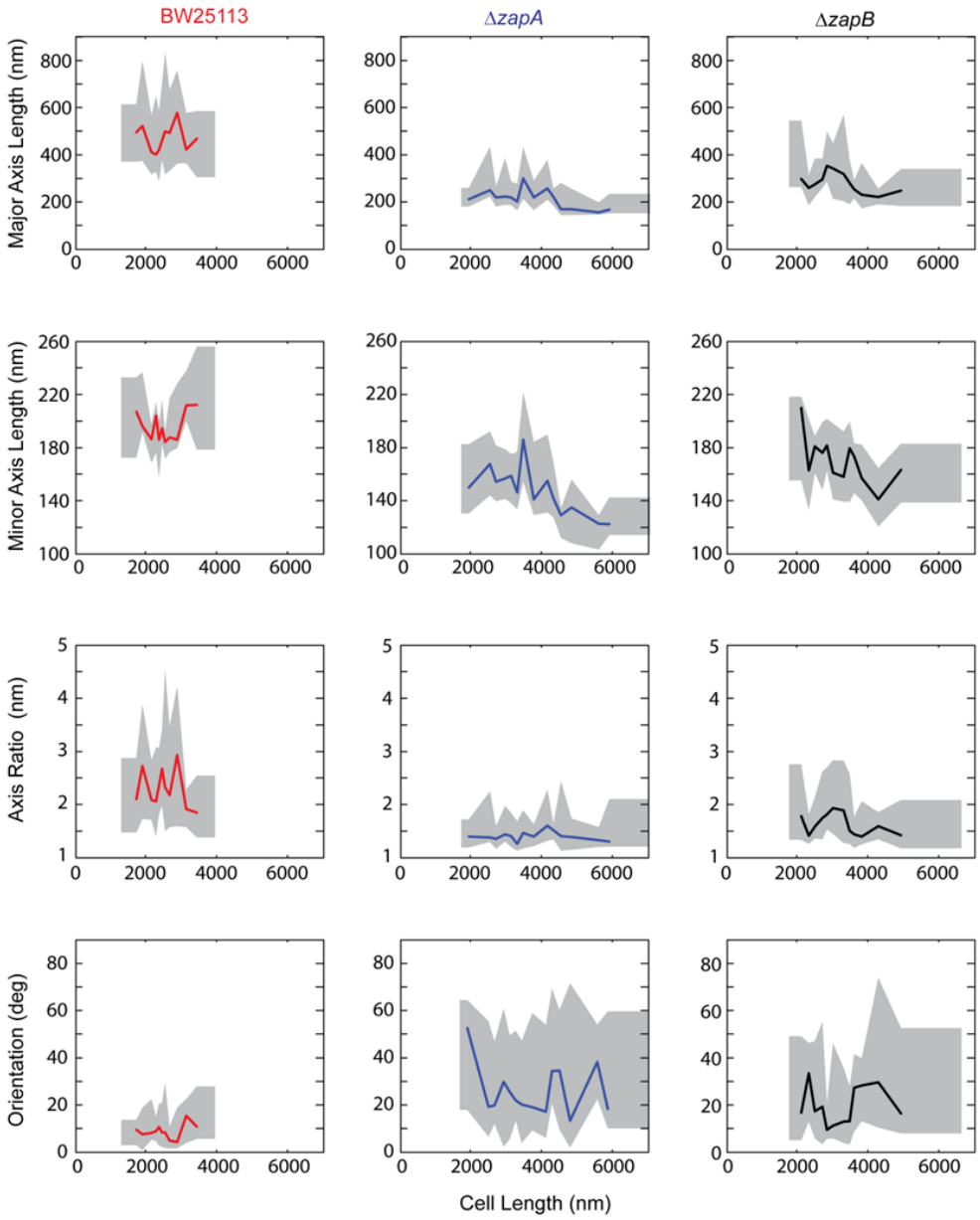

Figure 3.13 – Cell-cycle dependence of cluster shape. Cluster attributes identified in BW25113 (red), Δ*zapA* (blue), or Δ*zapB* (black) are plotted against the corresponding cell length in order to gain insight into how clusters attributes change over time. Cluster data are binned according to cell length and the median of each bin are connected by a bold line. The grey region indicates the binned inter-quartile range.

FtsZ-mEos2 molecules in clusters are stationary

We have shown that FtsZ clusters formed in the absence of ZapA or ZapB, while smaller than those in wt cells, still contain large numbers of FtsZ molecules (~50-70 molecules per cluster). To further investigate the polymerization state of FtsZ within these clusters, we measured and compared the mobility of individual FtsZ-mEos2 molecules in the wt and deletion strains using single molecule tracking. We reasoned that if these FtsZ molecules are in polymerized forms, their mobility would be significantly restricted relative to individual, membrane-tethered FtsZ monomers. We used very low activation power to turn on one FtsZ-mEos2 molecule at a time and tracked its movement every 200 ms with an exposure time of 50 ms. Figure 3.14A shows two typical tracking trajectories of FtsZ-mEos2 molecules in Δ*zapA* cells. We then used trajectories that lasted for at least ten frames (2 s in total) to compute the mean squared displacement (MSD) at different time lags (Figure 3.14B, n = 136, 431, and 211 for wt, Δ*zapA*, Δ*zapB*, respectively). The MSD plots of all three strains can be well described by a simple random Brownian diffusion model on the time scale from 0.2 to 2 s: the MSD scales linearly with the time lags; the slope is proportional to the apparent 2D diffusion coefficient and the y-intercept is determined by the experimental spatial resolution. The observed apparent 2D diffusion coefficients for FtsZ-mEos2 in wt, Δ*zapA* and Δ*zapB* cells were 0.0004 ± 0.00003, 0.0005 ± 0.00001, and 0.0006 ± 0.00003 $\mu m^2 s^{-1}$, respectively. While there is a slight increase in the mobility of FtsZ-mEos2 molecules in the absence of ZapA or ZapB, these diffusion coefficients are orders of magnitude smaller

than that expected for a typical freely-diffusing inner membrane protein (0.01 to 0.1 $\mu m^2 s^{-1}$) (Deich *et al.*, 2004, Kim *et al.*, 2006, Mullineaux *et al.*, 2006, Leake *et al.*, 2006). The slow, essentially immobile FtsZ-mEos2 molecules in the clusters are also consistent with the stationary FtsZ-Dendra2 population reported previously (Niu & Yu, 2008), suggesting that these clusters are likely composed of membrane-tethered FtsZ polymers. Consistent with this notion, the single-step displacement (200 ms) histogram was dominated by a single population centered around 75 nm (Figure 3.14C), suggesting that a significant population of mobile FtsZ-mEos2 does not exist in the absence of ZapA or ZapB.

Table 3.2 – Summary of PALM cluster analysis.

Strain	No. of clusters	No. of molecules	Area (nm^2)	Density (mol nm^{-2})	Displ. from midcell (nm)	Major Axis Length (nm)	Minor Axis Length (nm)	Orientation (deg)
BW25113	158	154 ± 8	69,000 ± 2,400	0.0022 ± 0.0001	81 ± 8	508 ± 18	206 ± 4	15 ± 1
Δ*zapA*	246	48 ± 3	28,000 ± 1,200	0.0017 ± 0.0001	280 ± 23	255 ± 9	154 ± 3	34 ± 2
Δ*zapB*	188	77 ± 6	39,000 ± 1,600	0.0018 ± 0.0001	194 ± 18	327 ± 12	170 ± 3	27 ± 2

Mean ± Standard Error. Standard errors were determined by bootstrapping with 1000 simulations.

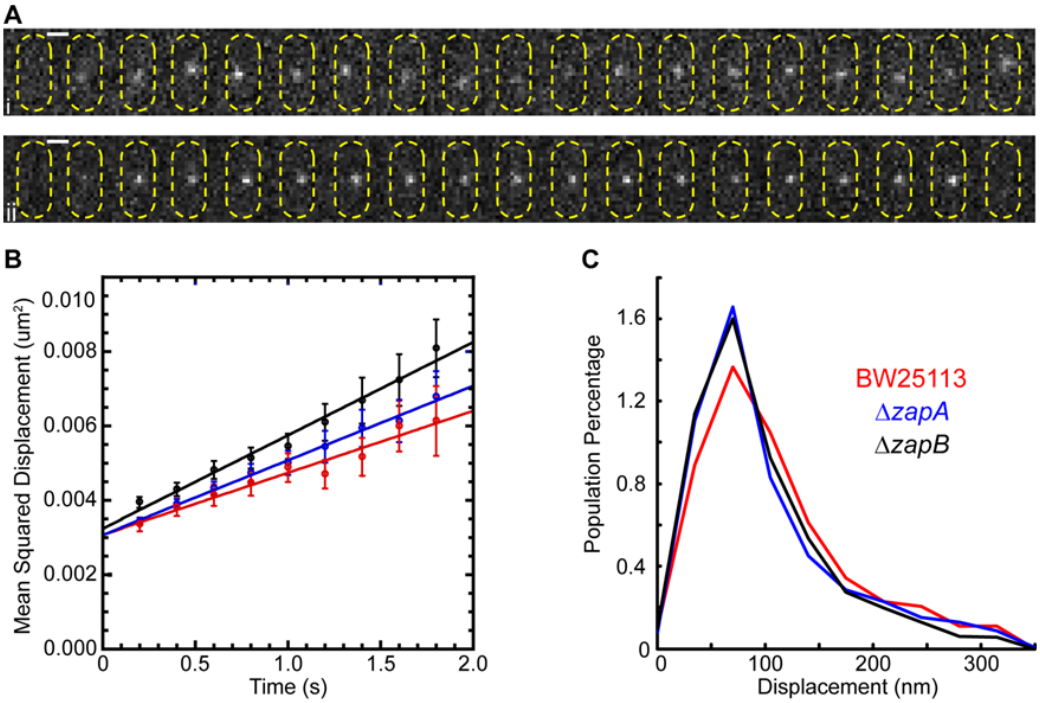

Figure 3.14 – Single molecule tracking of FtsZ-mEos2. (A) Representative single-molecule trajectories of consecutive frames for a mobile (Ai) and immobile (Aii) FtsZ-mEos2 molecule in Δ*zapA*. Fluorescence images were acquired every 200 ms. (B) Mean squared displacements (closed circles) are plotted at different time lags for BW25113 (red), Δ*zapA* (blue) and Δ*zapB* (black) cells. Error bars indicate Standard Error. The data were fit to a linear equation (y=4Dx+A). The diffusion coefficients for BW25113, Δ*zapA* and Δ*zapB* strains determined from the fits are 0.0004 ± 0.00003, 0.0005 ± 0.00001, 0.0006 ± 0.00003 $\mu m^2 s^{-1}$, respectively. (C) Histograms of single-step (200 ms) displacements of the three strains show predominate immobile populations centered around 75 nm. Scale Bars, 1 μm.

Abnormal Z-ring localization observed in ΔmatP only under fast growth condition

It was recently reported that MatP, a DNA-binding protein that condenses the Ter macrodomain (MD), directly interacts with ZapB (Mercier et al., 2008, Espeli et al., 2012). Since deletion of ZapA or ZapB results in early segregation of the Ter MD through the loss of the ZapB-MatP interaction (Espeli et al., 2012), it is possible that the dispersed FtsZ clusters we observed in Δ*zapA* and Δ*zapB* cells did not result directly from the loss of ZapA or ZapB, but were instead caused by the loss of ZapB-MatP interaction. In this scenario, the loss of ZapB-MatP interaction would lead to an abnormally positioned nucleoid, resulting in aberrant distribution pattern of the nucleoid occlusion protein, SlmA, and consequently mislocalized FtsZ structures (Bernhardt & de Boer, 2005, Tonthat et al., 2011, Cho & Bernhardt, 2013).

To examine this possibility, we first investigated the localization of FtsZ-GFP in a Δ*matP* strain. We found that under our slow growth condition ($M9^+$ at RT, $\tau \approx 160$ min), FtsZ-GFP localization in Δ*matP* cells was indistinguishable from that in wt cells (Figure 3.15A). PALM imaging of FtsZ-mEos2 under the same growth condition confirmed this observation (Figure 3.16A-D). These results are consistent with previous reports that the deletion of *matP* does not result in any distinguishable phenotype under slow growth conditions (Mercier et al., 2008) and suggest that the dispersed FtsZ clusters we observed in Δ*zapA* and Δ*zapB* cells are not caused by the loss of ZapB-MatP interaction.

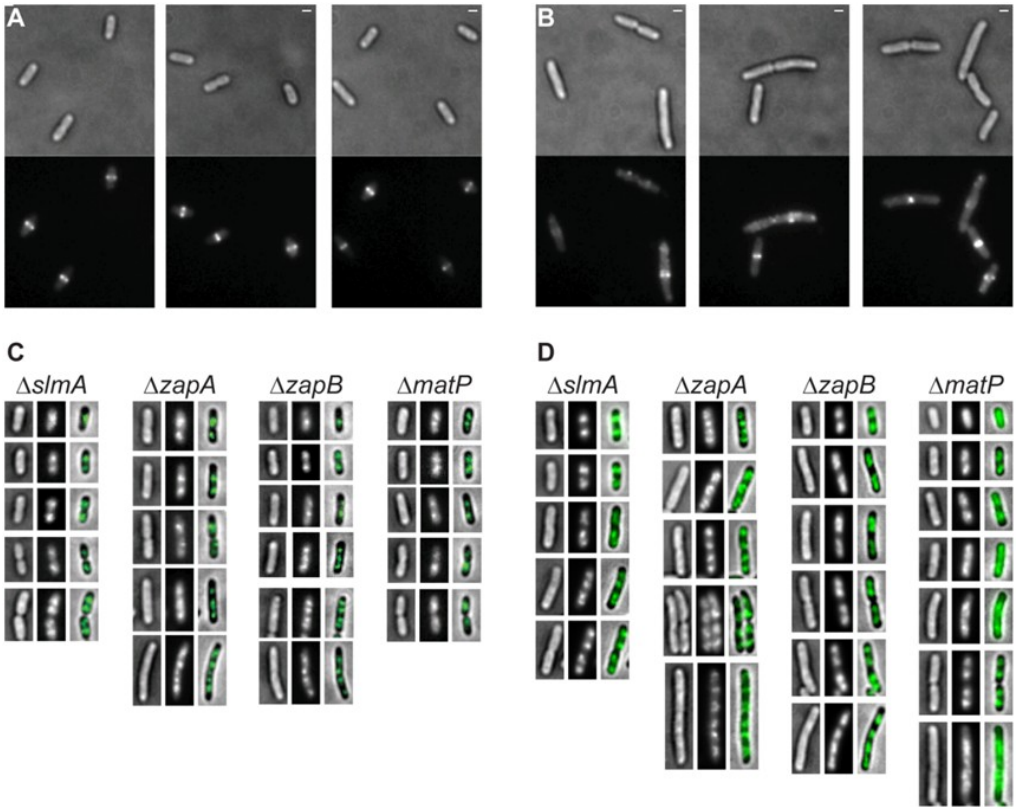

Figure 3.15 – Growth-dependent localization of FtsZ and SlmA in Δ*matP*. (A-B) Representative images of live Δ*matP* cells expressing FtsZ-GFP under slow (A) or fast (B) growth conditions. A bright-field image is displayed atop an ensemble fluorescence image. (C-D) Individual Δ*slmA*, Δ*zapA*, Δ*zapB* and Δ*matP* cells expressing mEos2-SlmA in the absence of inducer under the slow growth condition (C) and GFP-SlmA under the fast growth condition (D). Each bright-field image is displayed next to the corresponding ensemble fluorescence image (full dynamic range), which is adjacent to an overlaid, intensity-adjusted image. Scale Bars, 1 μm.

Previous reports have shown that under fast growth conditions, deletion of *matP* results in severe chromosome segregation and cell division defects (Mercier et al., 2008). Therefore, we next investigated the localization of FtsZ-GFP in *ΔmatP, ΔzapA*

and ΔzapB cells under a fast growth condition (rich defined media at 37°C, τ ≈ 45 min). We found that in addition to a slight increase in cell length (Figure 3.16E), 17% (n = 69) of Δ*matP* cells also displayed abnormal FtsZ-GFP localizations (Figure 3.15B). In contrast, we did not observe a significant increase in the percentage of cells displaying abnormal FtsZ structures in Δ*zapA* (44%, n = 52) or Δ*zapB* (35%, n = 161) cells compared to that under the slow growth condition. We were unable to resolve these abnormal FtsZ structures via PALM imaging due to the maturation defects of mEos2 at 37°C (McKinney et al., 2009).

To further investigate whether the abnormal localizations of FtsZ in Δ*matP* cells observed under the fast growth condition were caused by the altered spatial distribution of SlmA, we constructed an mEos2-SlmA fusion protein. When this fusion protein is expressed in a Δ*slmA* strain, we found that it formed a punctate, nucleoid-dependent localization pattern (Figure 3.15C), similar to what was observed previously for a fully-functional GFP-SlmA construct (Bernhardt & de Boer, 2005). We then used this construct to determine the SlmA distribution pattern in Δ*matP*, Δ*zapA* and Δ*zapB* cells under both growth conditions. We found that under our normal slow growth condition, the localization patterns observed for mEos2-SlmA in Δ*matP* cells were indistinguishable from Δ*slmA* (Figure 3.15C). In Δ*zapA* and Δ*zapB* cells, we found that although there were often multiple fluorescent puncta per cell, the segregated, nucleoid-dependent localization pattern of SlmA was conserved (Figure 3.15C). The observation of multiple puncta in Δ*zapA* and Δ*zapB* cells is consistent with a cytokinetically

defective mutant possessing multiple chromosomes. PALM imaging confirmed that under the slow growth condition, the localization pattern of SlmA was generally similar across the four strains (Figure 3.17A-D). Lastly, when we imaged FtsZ-mEos2 in two double deletion strains, Δ*slmA*Δ*zapA* and Δ*slmA*Δ*zapB*, under the same slow growth condition, we found that the percentage of cells (>30%) displaying abnormal FtsZ structures and the appearance of dispersed FtsZ clusters under PALM imaging remained similar to that in the single deletion strains, Δ*zapA* and Δ*zapB* (Figure 3.18A-C). These observations further suggest that under slow growth, SlmA does not mislocalize and does not contribute significantly to the FtsZ phenotype in Δ*zapA* and Δ*zapB* cells.

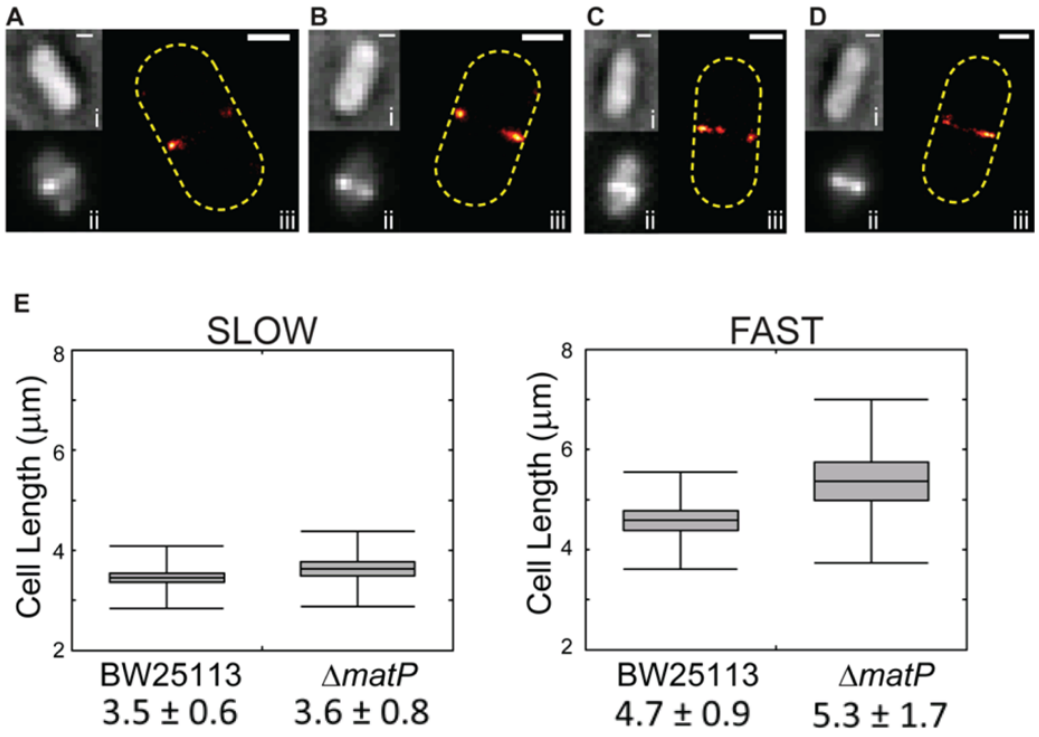

Figure 3.16 – Live-cell PALM imaging of FtsZ structures in Δ*matP*. (A-D) Images of live Δ*matP* cells expressing FtsZ-mEos2 from pJB042 under the slow growth condition are displayed in the order of bright-field image (i), ensemble green fluorescence image (ii) and PALM image (iii). (E) Box plots comparing the cell length distributions for wt and Δ*matP* cells under slow and fast growth. Distributions are displayed by notBoxPlot (MATLAB) as the mean boxed by 95% confidence intervals and bounded by the standard deviation. A significant ($P < 0.01$) difference relative to wt cell length was only observed under fast growth. Scale Bars, 500 nm.

Under a fast growth condition, however, we found that ~30% of Δ*matP* (n = 122) cells displayed a significantly more diffusive SlmA localization pattern (Figure 3.15D). In particular, elongated cells of Δ*matP* typically displayed a more homogenous, non-segregated SlmA distribution, likely resulting from non-segregated or disorganized nucleoids. This is in contrast to what was observed in elongated Δ*zapA* and Δ*zapB* cells grown under the same fast growth condition—SlmA still forms segregated puncta (Figure 3.15D). These results suggest that the mislocalization of FtsZ in Δ*matP* cells under the fast growth condition is likely due to abnormal distributions of SlmA on incorrectly segregated or organized nucleoids.

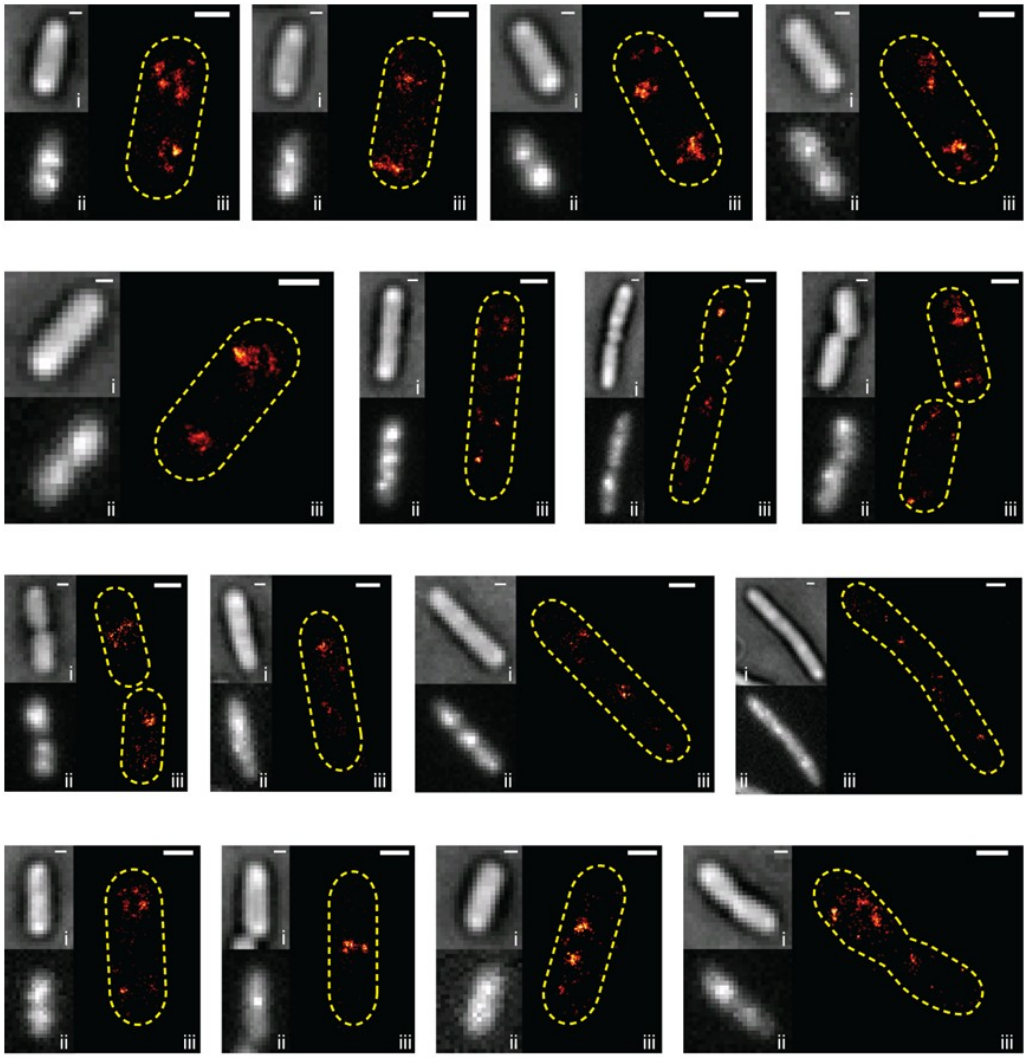

Figure 3.17 – Live-cell PALM imaging of mEos2-SlmA. Images of live Δ*slmA* (A), Δ*zapA* (B), Δ*zapB* (C), and Δ*matP* (D) cells expressing mEos2-SlmA from pJB139 under slow growth are displayed in the order of bright-field image (i), ensemble green fluorescence image (ii) and PALM image (iii). Scale Bars, 500 nm.

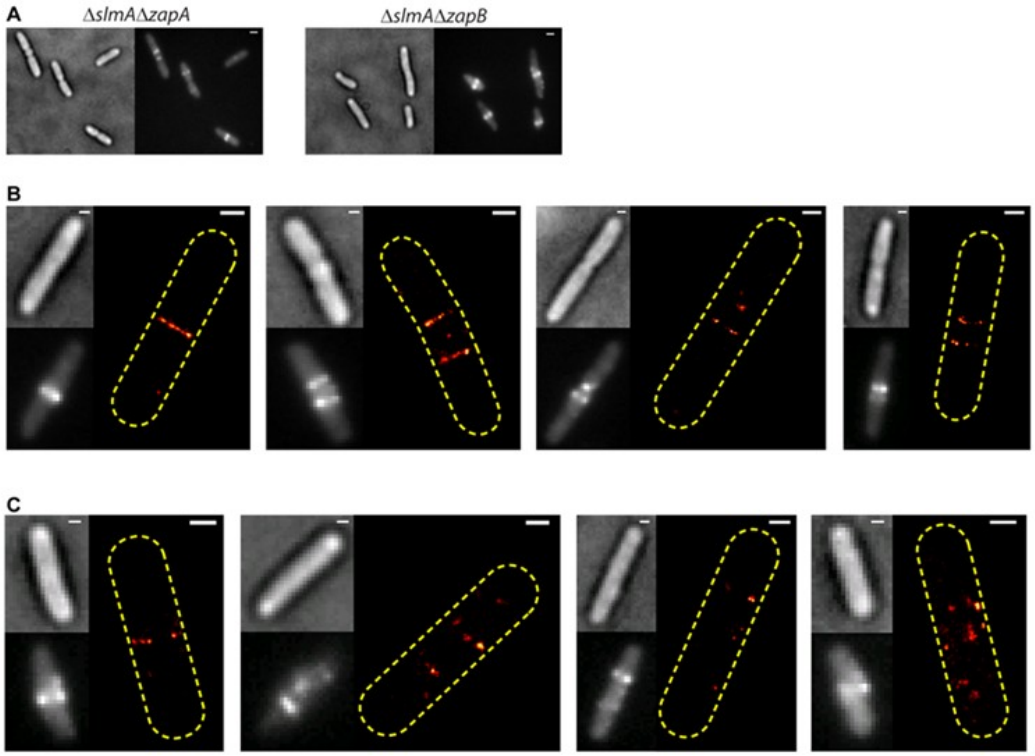

Figure 3.18 – Abnormal FtsZ structures persist in the absence of SlmA. (A) Representative ensemble fluorescence images of FtsZ-GFP in Δ*slmA*Δ*zapA* (n = 61) and Δ*slmA*Δ*zapB* (n = 82) under slow growth. Images are displayed as a bright-field image adjacent to a fluorescence image. PALM images of FtsZ-mEos2 expressed in Δ*slmA*Δ*zapA* (B) and Δ*slmA*Δ*zapB* (C) under slow growth. Images are displayed in the order of bright-field (i), ensemble green fluorescence image (ii) and PALM image (iii). Scale Bars, 1 μm (A), 500 nm (B-C).

ΔzapA or ΔzapB does not affect the arrival time of downstream division proteins

Previous studies have shown that ZapA and ZapB localize to the midcell in a FtsZ-dependent manner early in cell division (Gueiros-Filho & Losick, 2002, Ebersbach et al., 2008, Aarsman et al., 2005, Goehring *et al.*, 2005) and that ZapA directly interacts with a number of other essential division proteins, including FtsA, FtsI and FtsN (Di Lallo et al., 2003, Alexeeva et al., 2010, Maggi et al., 2008). As the assembly of the divisome in *E. coli* follows a largely linear order, in which the arrival of most division proteins is dependent on that of an earlier one (Errington *et al.*, 2003, Aarsman et al., 2005, Gamba *et al.*, 2009), we investigated whether the arrival times of the essential division proteins are altered in the absence of ZapA or ZapB. Furthermore, since Δ*zapA* and Δ*zapB* cells display a more dynamic FtsZ structure and more dispersed FtsZ clusters, we were interested to find out whether the formation of these abnormal structures affected downstream protein recruitment.

To examine the arrival time of division proteins in the absence of ZapA and ZapB, we used a previously developed assay (Aarsman et al., 2005), in which we scored and compared the percentages of cells showing midcell localization of each division protein in a steady-state population undergoing exponential growth. Proteins that arrive to the divisome early will be localized to the midcell in a larger percentage of cells than those that arrive late. We fused a fast-maturing yellow fluorescent protein, Venus (V) (Nagai *et al.*, 2002), to the N- or C- terminus of ten essential division proteins, to generate FtsZ-V, V-FtsA, V-

ZipA, V-FtsK, V-FtsQ, FtsL-V, V-FtsB, FtsW-V, V-FtsI and V-FtsN. We expressed these fusion proteins at extremely low levels from the *lac* promoter on a miniF plasmid without an inducer. All fusion proteins localized correctly to

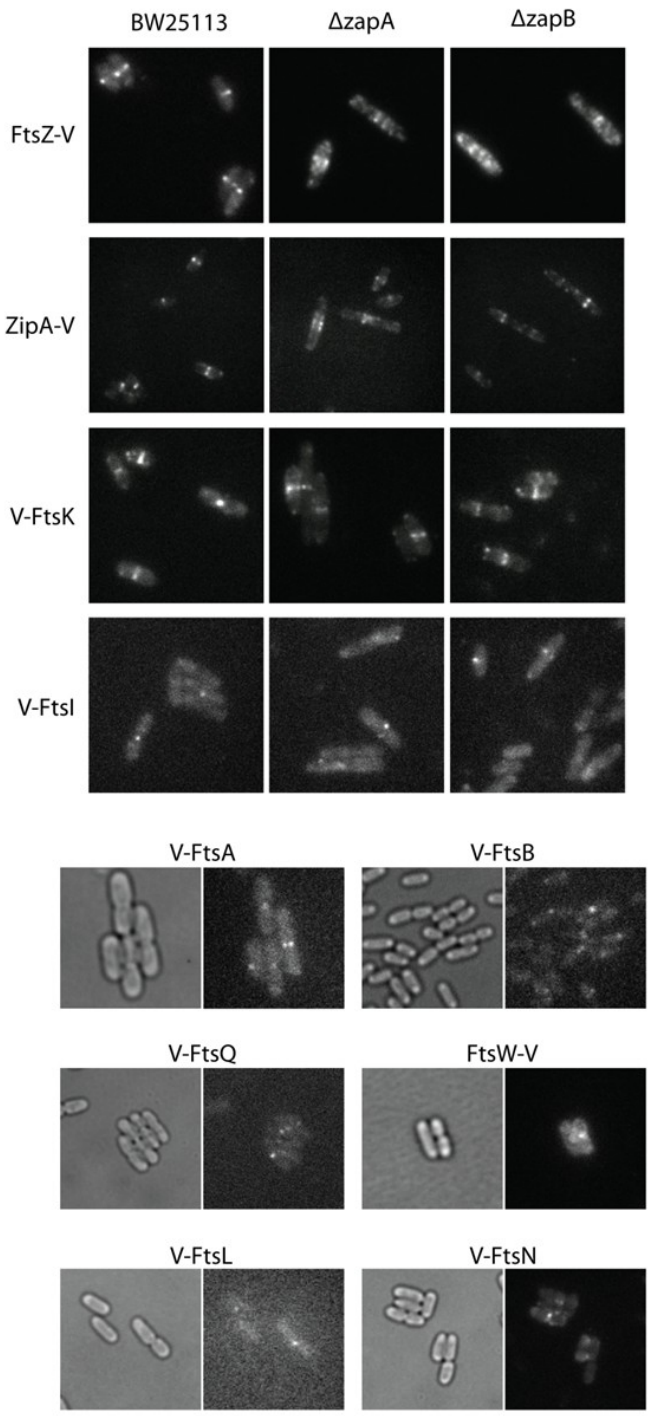

Figure 3.19 – Midcell localization of Venus fusions.(A) Fluorescence images for FtsZ-V, ZipA-V, V-FtsK, V-FtsN in wt, Δ*zapA*, and Δ*zapB* cells are shown. In wt, all fusions can be seen to localize precisely to midcell, indicating their ability to associate with the divisome. In the absence of ZapA and ZapB, the apparent localization of these division proteins is clearly affected. (B) Tandem bright-field and fluorescence images are shown for V-FtsA, V-FtsQ, V-FtsL, V-FtsB, FtsW-V, and V-FtsI in B/r A wild-type cells, again illustrating the partial functionality of these fusion. The decreased signal displayed by the latter group compounded with the delocalization caused by Δ*zapA* or Δ*zapB* prevented further analysis of these fusion proteins. Images are of different scale.

the midcell in a wt background (Figure 3.19). In addition, V-FtsA, V-FtsK, V-FtsQ, FtsW-V, V-FtsI and V-FtsN complemented their respective deletion or depletion strains (Figure 5.4)

We transformed each of the ten plasmids carrying fusion proteins into BW25113, Δ*zapA* and Δ*zapB* strains and imaged these cells on a microscope stage. We found that in Δ*zapA* and Δ*zapB* cells, the localization patterns of several division proteins became difficult to score, likely due to the altered localization pattern of FtsZ in the deletion strains, and extremely low expression levels of these fusion proteins without induction. Therefore, we only scored the midcell localization for FtsZ-V, ZipA-V, V-FtsK and V-FtsI. We used the fraction of cells displaying midcell localization to calculate the arrival time of each division protein relative to the cell cycle of each strain (Figure 3.20). We found that the localization pattern of the early division protein, ZipA, also formed broad or diffusive bands at the midcell, whereas the late division proteins FtsK and FtsI largely formed single, sharp bands at the midcell. Nevertheless, the arrival time of the four division proteins did not vary significantly between the three strains ($P > 0.25$). Therefore, we conclude that under our experimental conditions, the arrival times of these essential division proteins do not appear to depend on ZapA or ZapB and that the recruitment of these proteins does not appear to depend on the formation of a coherent Z-ring.

A

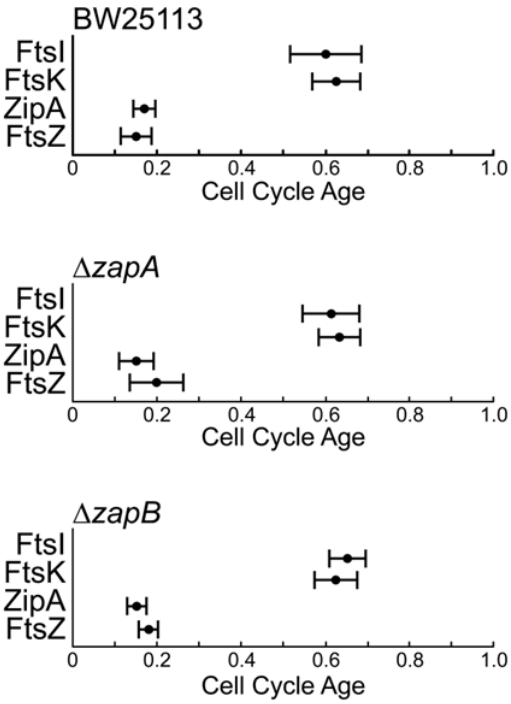

B

	Midcell Recruitment (% of Cell Age)			
	FtsZ	ZipA	FtsK	FtsI
BW25113	15 ± 3	17 ± 2	63 ± 5	60 ± 8
ΔzapA	20 ± 6	15 ± 4	63 ± 5	61 ± 7
ΔzapB	18 ± 2	15 ± 2	62 ± 5	65 ± 4

Figure 3.20 – Arrival time of essential division proteins. Snapshots of BW25113 (top), Δ*zapA* (middle) and Δ*zapB* (bottom) cells expressing FtsZ-Venus, ZipA-Venus, Venus-FtsK or Venus-FtsI were analyzed to determine the fraction of the population that displayed a midcell fluorescence signal. (A) The distribution of calculated arrival times for each of the four fusion proteins are illustrated relative to the cell cycle of each strain (mean ± standard deviation). These results are summarized in B. The mean arrival time ± standard deviation for three independent measurements, each of more than 100 cells, are shown. In all cases, FtsZ and ZipA arrived significantly ($P < .002$) earlier than FtsK and FtsI.

Discussion and Conclusions

We previously showed that in *E. coli* the Z-ring is likely composed of a loose bundle of FtsZ protofilaments that randomly overlap with each other in space (Fu et al., 2010). We proposed that lateral interactions between FtsZ protofilaments, either mediated by the intrinsic lateral affinity of protofilaments or by other protein factors that bind FtsZ, are required to organize such a loose bundle. In this work, we investigated the role of ZapA and ZapB in promoting the assembly of the Z-ring.

Deletion of zapA or zapB affects septum morphology and FtsZ dynamics

In cells deleted of *zapA* or *zapB*, we observed a minor cell division defect similar to what was reported previously: on average Δ*zapA* and Δ*zapB* cells are about 20% longer than wt cells and grow with a similar rate as wt cells in liquid media (Gueiros-Filho & Losick, 2002, Ebersbach et al., 2008). However, when observed under SEM, we found that many Δ*zapA* or Δ*zapB* cells showed abnormal septa that were not precisely aligned at the midcell or parallel to the cell's short axis (Figure 3.1). Additionally about 20% of cells showed more than one septum around the midcell region. These observations argue that ZapA and ZapB may facilitate the correct positioning of cell division plane, possibly by organizing the structure and localization of the Z-ring (see below).

When investigated using time-lapse fluorescence imaging, we observed dynamic FtsZ structures moving back and forth between multiple sites in Δ*zapA* and Δ*zapB* cells, often resulting in visible cell wall indentations at these sites (Figure 3.2B). These multiple constriction sites likely correspond to the multi-

septa observed in Δ*zapA* and Δ*zapB* cells by SEM. At later stages of cell division FtsZ structures coalesced to a single site to achieve complete septation. As a result, the corresponding daughter cells contained visible constriction sites that were previously occupied by FtsZ in their parent cell. Interestingly, in a subpopulation of these daughter cells FtsZ relocalized to the partially constricted sites and completed cell division at a significantly faster rate than the average population (Figure 3.2C).

The ability of FtsZ to relocalize to aborted constriction sites in Δ*zapA* and Δ*zapB* cells conflicts with a previous study performed with a temperature-sensitive FtsZ GTPase mutant, *ftsZ84* (Addinall et al., 1997b). Addinall *et al*. showed that FtsZ84 does not return to aborted division sites that had initiated constriction, and proposed that the localization signal for FtsZ is lost once cell wall constriction begins (Addinall et al., 1997b). Since the localization of FtsZ to midcell is likely a result of the combined mechanisms of nucleoid occlusion, MinCDE antagonism and membrane properties, a specific localization signal may not be involved (Bernhardt & de Boer, 2005, Lutkenhaus, 2007, Mileykovskaya & Dowhan, 2005). Therefore, we suspect that the conflicting observations may be due to the inefficient polymerization of the FtsZ84 mutant (Bramhill & Thompson, 1994).

The question of why reinitiated constriction sites complete septation faster than the general population is intriguing. One possible explanation is that some division proteins, such as peptidoglycan modification enzymes, are not completely disassembled upon the departure of FtsZ from these sites, hence

when FtsZ returns, the reassembly of the divisome and reinitiation of cell wall constriction occurs more rapidly. While many genetic studies have shown that the midcell recruitment of all other division proteins are dependent on the presence of FtsZ (Addinall et al., 1997b, Buddelmeijer & Beckwith, 2002, Errington et al., 2003), it has not been systematically shown that all the division proteins leave immediately upon the disassembly of the Z-ring. In fact, a few studies observed that at the end of septation, FtsK and FtsN persist at the midcell even after FtsZ leaves (Wang et al., 2005b, Möll *et al.*, 2010). However, it is not known how long these late division proteins persist after the departure of FtsZ. If they persist at aborted septa in Δ*zapA* and Δ*zapB* cells until the beginning of the next cell cycle, we would expect their calculated arrival times to be shorter in the deletion strains than in wt cells. In our own study (Figure 3.20), we did not observe significant changes in the arrival time of the division proteins we investigated (ZipA, FtsK and FtsI), possibly due to our limited temporal resolution.

Enhanced global dynamics of FtsZ in ΔzapA and ΔzapB cells are likely due to weakened structural stability

We observed more dynamic, global movement of FtsZ structures in the absence of ZapA and ZapB than in wt cells (Figure 3.2). However, we showed through single molecule tracking experiments that this apparent increase in global movement is not due to the enhanced mobility of individual FtsZ molecules. FtsZ molecules are known to turn over rapidly inside the Z-ring on the time scale of tens of seconds (Stricker et al., 2002), resulting in a constant flux of

molecules dissociating from and reassociating into the ring. This turnover process may drive the global movement of FtsZ structures and is consistent with the observed density fluctuations within the Z-ring recently reported for wt *Bacillus subtilis* cells (Strauss et al., 2012). As FRAP experiments have shown that the turnover rate of FtsZ molecules in *Bacillus subtilis* is not affected by the absence of ZapA (Anderson et al., 2004), we reason that the global dynamics of FtsZ may only appear to be enhanced in Δ*zapA* and Δ*zapB* cells because of the increased ability of FtsZ molecules to reassociate at positions farther away from midcell. This could be caused by the removal of some structural constraints imposed by ZapA and ZapB (see below). Consistent with this suggestion we observed using PALM imaging that FtsZ clusters in Δ*zapA* and Δ*zapB* cells were more widely dispersed than in wt cells (Figure 3.5,7-8).

ZapA and ZapB likely function together in organizing Z-ring structure

In vitro biochemical studies have shown that ZapA is capable of promoting FtsZ bundling by itself (Gueiros-Filho & Losick, 2002, Small et al., 2007, Mohammadi et al., 2009, Galli & Gerdes, 2012, Dajkovic et al., 2010). Other studies on ZapB have shown that its ability to promote Z-ring assembly is entirely dependent on ZapA, as it directly binds to ZapA but not FtsZ (Ebersbach et al., 2008, Galli & Gerdes, 2012). Therefore, we expected that *in vivo* ZapA may be able to function alone in the absence of ZapB and that deletion of *zapB* would have a milder effect than deletion of *zapA*. Although statistically different, our results show that deletion of *zapB* results in a similar adverse phenotype as

the deletion of *zapA*. Both deletion strains displayed increased cell length, abnormal septum morphology, heterogeneous cell cycle time, highly dynamic and abortive Z-ring assembly, and significantly smaller FtsZ clusters compared to wt. These results suggest that ZapA and ZapB's function in promoting Z-ring assembly *in vivo* may be dependent on each other. Interestingly, although the phenotypes of Δ*zapA* and Δ*zapB* were more similar to each other than to wt, we did notice that the effect of Δ*zapB* on FtsZ clusters was milder than Δ*zapA*: FtsZ clusters in Δ*zapB* were bigger, less dispersed and contained more molecules than those in Δ*zapA*. These observations are consistent with the expectation that ZapA does retain some ability to promote FtsZ assembly in the absence of ZapB, but the presence of ZapB greatly enhances this ability.

Influence of MatP on FtsZ structure

ZapB was initially identified as a plasmid-partitioning factor (Ebersbach et al., 2008) and has recently been implicated in chromosome segregation through its interaction with MatP (Espeli et al., 2012). The loss of ZapB-MatP interaction in Δ*zapA* and Δ*zapB* cells could impact the segregation of nucleoid, and hence the localization of the nucleoid occlusion factor, SlmA. We investigated FtsZ and SlmA localization in Δ*matP,* Δ*zapA* and Δ*zapB* cells. We found that FtsZ and SlmA localizations are only perturbed in Δ*matP* cells under a fast growth condition. In contrast, FtsZ and SlmA localization in Δ*zapA* and Δ*zapB* cells are similar both in fast and slow growth conditions.

Our results suggest that the abnormal FtsZ localization in Δ*matP* cells under the fast growth is likely caused by a nucleoid segregation defect that alters the SlmA distribution, whereas the dispersed FtsZ clusters we observed in Δ*zapA* and Δ*zapB* cells are not due to nucleoid segregation defects. These observations are also consistent with previous studies that deletion of ZapB has no effect on nucleoid segregation (Ebersbach et al., 2008) or the mobility of the chromosome outside of the Ter region (Thiel et al.). Note that the loss of ZapB-MatP interaction in Δ*zapA* or Δ*zapB* cells is not equivalent to the loss of MatP function in Δ*matP* cells. The severely affected FtsZ localization in Δ*matP* under fast growth condition but essentially the same FtsZ localization in Δ*zapA* and Δ*zapB* under both growth conditions supports a minimal role of ZapB-MatP interaction in organizing the Z-ring, but a significant role of MatP in organizing the nucleoid.

It is known that under fast growth conditions where cell doubling time is close to or shorter than that required for a complete round of chromosome replication (~ 40 min), bacterial cells usually initiate multiple rounds of chromosome replication before the previous round is finished. As a result, multiple, partially replicated chromosomes present a significant topological challenge for correct and efficient nucleoid segregation. Therefore, it is reasonable to expect that under this condition the coordination between cytokinesis, initiated by the Z-ring assembly at the midcell, and nucleoid segregation, in which MatP has a significant role, is more tightly coupled to

ensure proper cell division. Hence, it is not surprising that the loss of MatP function in Δ*matP* cells leads to significantly altered FtsZ localization.

FtsZ clusters formed in the absence of ZapA or ZapB contain higher-ordered FtsZ polymers

As described above, we found that FtsZ formed small, widely dispersed clusters around the midcell in the absence of ZapA or ZapB. We showed that these FtsZ clusters are not due to aggregation of the fluorescent proteins, but are specific to the deletion of *zapA* or *zapB* and the polymerization of FtsZ.

To gain further molecular insight, we compared these clusters' composition to that expected for a single FtsZ protofilament, the presumed basic structural unit of the Z-ring (Erickson *et al.*, 1996a, Chen & Erickson, 2005, Li et al., 2007). The average numbers of FtsZ-mEos2 molecules in Δ*zapA* and Δ*zapB* clusters were ~50 and ~80, respectively, while that in the wt clusters was ~150 (Table 3.2). Using individual cellular fluorescence and population-based immunoblotting measurements we showed that on average FtsZ-mEos2 was expressed at ~30% of total cellular FtsZ levels (Figure 3.3). Therefore, FtsZ clusters in Δ*zapA,* Δ*zapB,* and wt cells would contain ~160, ~250, and ~500 FtsZ molecules, respectively. We note that since not all FtsZ-mEos2 molecules were detected within the limited imaging time, these estimates represent lower bounds. These underestimates are still significantly larger than the estimated ~30 monomers that comprise single FtsZ protofilaments (Romberg et al., 2001,

Huecas *et al.*, 2008, Chen et al., 2005). This calculation suggests that FtsZ clusters in all three strains are much larger than a typical single FtsZ protofilament observed *in vitro.*

Consistent with this suggestion, we found that the measured areas of these clusters were also much larger than that expected for a single protofilament. Given our spatial resolution of imaging (~50 nm), a single FtsZ protofilament based on *in vitro* EM measurement (120 nm x 5 nm) (Erickson et al., 1996b) would occupy an area of 6,500 nm^2 (130 nm x 50 nm). In contrast, the average measured area of FtsZ-mEos2 clusters in Δ*zapA* or Δ*zapB* cells was ~30,000 nm^2, and in wt cells was ~70,000 nm^2. These values are more than five-fold the expected value of a single protofilament. The dimensions of these clusters (~300 nm x 150 nm) were also significantly larger than the respective dimensions of a single protofilament, consistent with the previous observation that these clusters contain more molecules than a single protofilament. Based on the dimensions observed, it is unlikely that FtsZ molecules in these clusters are arranged into a single, long FtsZ filament, as such a long filamentous configuration would give rise to a much larger cluster length (major axis length) and a much smaller cluster width (minor axis length). It is also unlikely that FtsZ protofilaments in these clusters adopt a tightly aligned ribbon configuration, as the cluster width would be significantly smaller than what we observed. Based on these estimations, we suggest that FtsZ clusters formed in wt cells and in the absence of ZapA and ZapB are loosely-associated FtsZ polymers that likely consist of multiple FtsZ protofilaments. More work is needed to determine what

other factors are required to maintain these loose associations of higher-ordered FtsZ polymers.

ZapA and ZapB mainly function at the level of organizing higher-ordered FtsZ polymers

We observed that the ring-like FtsZ structures formed in the Δ*zapA* and Δ*zapB* cells are dimensionally indistinguishable from those observed in wt cells (Figure 3.4). This observation is consistent with the fact that a number of other factors, besides ZapA and ZapB, have been shown to promote Z-ring assembly. FtsZ by itself has been shown to form ring-like structures on liposomes *in vitro* or in a non-native cellular environment (Osawa et al., 2008, Srinivasan *et al.*, 2008), suggesting that intrinsic lateral interactions between protofilaments alone can mediate the formation of large FtsZ assemblies. Additionally, at least two other Zap proteins, ZapC and ZapD, have been identified that display functions similar to ZapA and ZapB in promoting the association of FtsZ protofilaments *in vitro* and Z-ring assembly *in vivo* (Durand-Heredia et al., 2011, Hale et al., 2011, Durand-Heredia et al., 2012).

Given our observation of higher-ordered FtsZ polymers in Δ*zapA* and Δ*zapB* cells, it is plausible that ZapA and ZapB do not function at the level of promoting the association of single protofilaments. However, given the redundant mechanisms described above we cannot formally exclude this possibility. Nevertheless, the most significant defect that we observed on Z-ring assembly in Δ*zapA* and Δ*zapB* cells is that FtsZ forms clusters that are smaller, less dense, and more dispersed away from the midcell region. This suggests that although

ZapA and ZapB may promote the association of single protofilaments as postulated in previous *in vitro* studies (Dajkovic et al., 2010), their major contribution *in vivo* is to facilitate the assembly of these higher-ordered FtsZ polymers into the Z-ring.

To understand how ZapA and ZapB might facilitate the assembly of FtsZ clusters into the Z-ring, we further analyzed the shape and orientation of FtsZ clusters. In all strains we found that FtsZ clusters were elongated and generally oriented along the short axis of the cell (Table 3.2). The length (major axis) of FtsZ clusters in Δ*zapA* and Δ*zapB* cells was ~50% shorter than wt clusters, whereas their width (minor axis) was only reduced by ~20%. Considering the preferential alignment of FtsZ clusters, the larger differences in cluster lengths between strains suggests that ZapA and ZapB may have a greater affect on the growth of FtsZ polymers along the short axis of the cell.

Previously, we and other groups have reported that the width of the Z-ring (~110 nm) is largely invariant between different bacterial species and FtsZ expression levels (Fu et al., 2010, Biteen et al., 2012, Jennings et al., 2011). Consistent with these reports, we observed tight, largely symmetric width distributions for clusters in all three strains (Figure 3.11G).These observations suggest that the polymerization of FtsZ along the long axis of the cell is tightly regulated by factors other than ZapA and ZapB. Whether this regulation is mediated by negative factors such as SlmA and MinC, which impose physical constraints on FtsZ polymerization, or by positive factors that regulate the lateral associations of FtsZ remains to be seen.

ZapA and ZapB promote Z-ring assembly by aligning FtsZ clusters

Assembly of the Z-ring has been proposed to consist of multiple steps (Adams & Errington, 2009, Margolin, 2005). In the first step, FtsZ monomers polymerize to form single-stranded protofilaments. Next, these single-stranded protofilaments can further grow in length and also associate with others laterally to assemble the Z-ring. In this study, we observed that in the absence of ZapA and ZapB, FtsZ formed small, widely-dispersed clusters. These clusters have larger sizes and more molecule counts than what would be expected from a single FtsZ protofilament, suggesting that they are higher-ordered structures composed of multiple FtsZ protofilaments.

Based on these observations, we propose that these clusters, or multi-stranded FtsZ polymers, represent a distinct polymeric species of FtsZ that is inherent to the assembly pathway of the Z-ring (Figure 3.21). Furthermore, we propose that the main function of ZapA and ZapB *in vivo* is to bring these dynamic FtsZ clusters into close proximity at midcell and this coherent alignment of FtsZ clusters enables proper Z-ring assembly (Figure 3.21). In the absence of ZapA or ZapB, FtsZ clusters easily break off from each other, leading to dispersed localizations and consequently abnormal septa. This model is consistent with our observation of larger clusters in wt cells, as well as a recent study that used three-dimensional structured illumination to show that the Z-ring in *Bacillus subtilis* adopts a non-uniform, bead-like configuration (Strauss et al., 2012). It is likely that these beads are analogous to the FtsZ clusters we observed and the *in vivo* function of ZapA and ZapB is to corral these clusters at

midcell. Future characterization of the mechanisms by which these FtsZ clusters are organized will be pivotal to our understanding of Z-ring assembly and function.

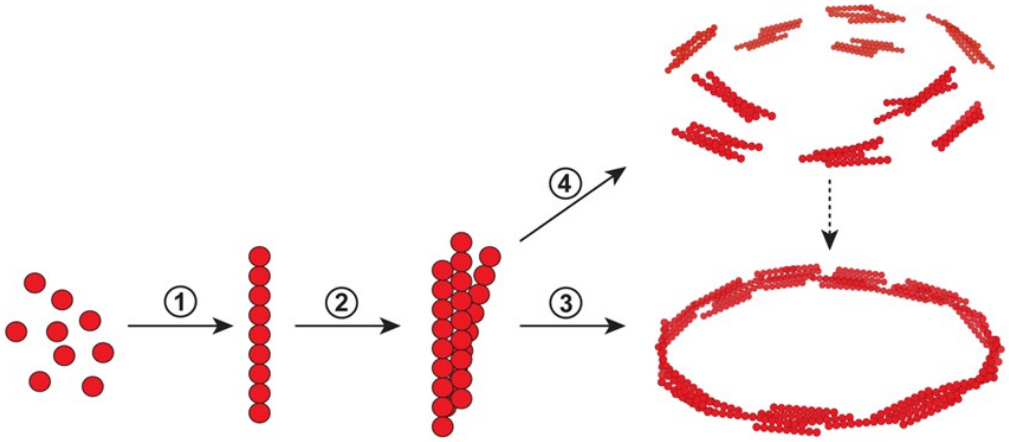

Figure 3.21 – Model of how ZapA and ZapB promote Z-ring assembly. 1. FtsZ monomers associate longitudinally into FtsZ protofilaments. 2. FtsZ protofilaments laterally associate to form FtsZ clusters, or higher-ordered polymers consisting of multiple FtsZ protofilaments. This process may be mediated by the intrinsic properties of FtsZ and/or other protein factors. ZapA and ZapB may participate but are not required for this step. 3. FtsZ clusters are corralled at midcell through the combined function of ZapA and ZapB, resulting in larger continuous structures. 4. In the absence of ZapA and ZapB, FtsZ clusters scatter throughout the midcell region and some unknown mechanism (dashed arrow) is responsible for proper Z-ring assembly.

Chapter 4

Structure and Dynamics of ZapA and ZapB

Introduction

Bacterial cell division is a complex process that involves the coordinated assembly of a macromolecular complex (divisome) at midcell (Aarsman et al., 2005, Goehring et al., 2006, Di Lallo et al., 2003). This process is initiated by the polymerization of FtsZ into a ring-like structure, termed the Z-ring (Bi & Lutkenhaus, 1991, Sun & Margolin, 1998). In the absence of the Z-ring, no other cell division proteins localize to midcell, implicating this structure as a cytoskeleton-like scaffold that supports the assembly of the divisome (Addinall et al., 1996, Buddelmeijer & Beckwith, 2002, Stricker et al., 2002). The Z-ring, however, may also serve as a force-generating structure, as FtsZ protofilaments alone can deform liposomes *in vitro* (Osawa et al., 2009, Li *et al.*, 2013). Regardless of whether FtsZ generates the force required for cytokinesis or simply functions to recruit the force-generating elements, it is clear that the spatial and structural regulation of the Z-ring is essential for efficient proliferation.

Recently a number of Z-ring associating proteins (ZapA, ZapB, ZapC, ZapD) have been identified that positively regulate Z-ring structure (Gueiros-Filho & Losick, 2002, Ebersbach et al., 2008, Hale et al., 2011, Durand-Heredia et al., 2011, Durand-Heredia et al., 2012). In the absence of any Zap, the Z-ring has an increased propensity to adopt extended, non-ring conformations, suggesting Zap's function as Z-ring stabilizers (Ebersbach et al., 2008, Dajkovic et al., 2010, Durand-Heredia et al., 2011, Durand-Heredia et al., 2012). Furthermore, *in vitro* Zap's tend to promote the association of single-stranded FtsZ protofilaments into higher-ordered bundles (Gueiros-Filho & Losick, 2002, Dajkovic et al., 2010).

Taken together it would seem that Zap's directly modulate the polymerization state of FtsZ, and the polymer form they promote lends stability to the Z-ring.

ZapA and ZapB represent a distinct subset of the Zap family and appear to work together in promoting the Z-ring structure *in vivo*. ZapA is a small cytoplasmic protein that exists in a dimer:tetramer equilibrium and has been suggested to cross-link FtsZ filaments *in vitro* (Low et al., 2004, Dajkovic et al., 2010, Small et al., 2007). A follow-up study found that the ZapA tetramer is required for the *in vitro* bundling of FtsZ protofilaments (Pacheco-Gómez et al., 2013). It is unclear if ZapA's cross-linking function is dependent on tetramerization. It is also unclear to what extent ZapA bundles FtsZ *in vivo*. In fact, it remains possible that ZapA does not function to bundle FtsZ *in vivo*, but to bridge FtsZ with ZapB (Galli & Gerdes, 2010).

ZapB is an α-helical protein that was crystallized as an antiparallel, coiled-coil dimer about ~12 nm in length (Ebersbach et al., 2008). Like FtsZ, ZapB assembles into single-stranded protofilaments that further associate into long, thick cables in the presence of divalent cations and/or ZapA (Ebersbach et al., 2008, Galli & Gerdes, 2012). A recent study conducted by Galli & Gerdes (2010) showed that ZapB may form a concentric ring internal to the Z-ring. This observation offers the attractive possibility that ZapB may provide an additional layer of structural organization to the Z-ring.

In our previous work using the super-resolution microscopy method, photoactivated localization microscopy (PALM), we found that in the absence of

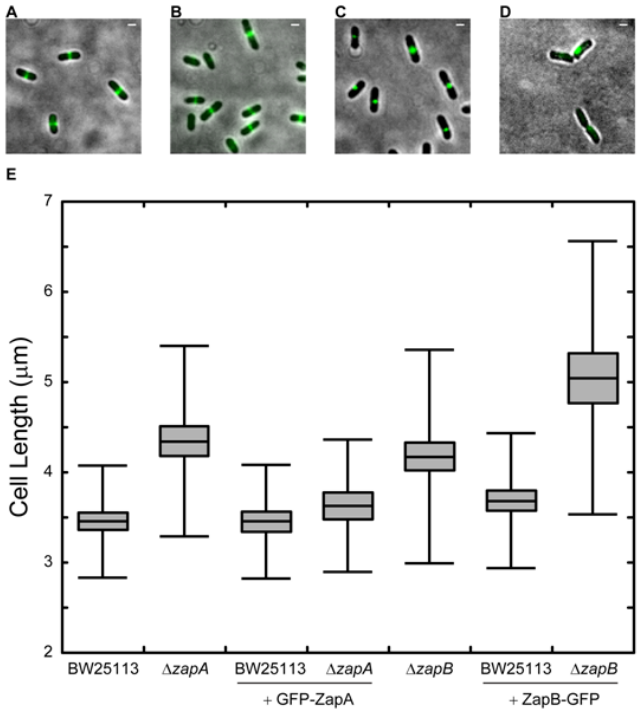

Figure 4.1 – Characterizing GFP-ZapA and ZapB-GFP constructs. (A,C) Bright-field and fluorescence images of BW25113 cells expressing GFP-ZapA (A) or ZapB-GFP (C). (B,D) Bright-field and fluorescence images of GFP-ZapA (B) and ZapB-GFP (D) expressed in their respective deletion strains. (E) Cell length distributions of BW25113, Δ*zapA* and Δ*zapB* cells in the absence or presence of GFP-ZapA or ZapB-GFP are illustrated in a box plot. Distributions were plotted by notBoxPlot (MATLAB) as the mean boxed by the 95% confidence interval and bounded by the standard deviation. Scale Bars, 1 μm.

ZapA or ZapB, FtsZ adopted a dispersed cluster morphology, whereby multi-stranded groupings of FtsZ were displaced away from the midcell region (Buss et al., 2013a). Thus, we proposed that ZapA and ZapB may promote Z-ring assembly by corralling FtsZ clusters at midcell.

In this study we were interested in understanding how ZapA and ZapB might corral FtsZ clusters at midcell. From previous work one would presume that the structures formed by ZapA and ZapB are similar to those formed by FtsZ, both in terms of morphology and dimension (Gueiros-Filho & Losick, 2002, Ebersbach et al., 2008). However, this presumption has recently been contested (Galli & Gerdes, 2010). Here we investigate the structure and dynamics of ZapA and ZapB through a variety of high-resolution fluorescence microscopy methods to gain insight to the relative arrangement of the FtsZ-ZapA-ZapB complex.

Global dynamics of ZapA but not ZapB mimics that of FtsZ

The FtsZ structure is highly dynamic, undergoing rapid turnover and significant structural rearrangements on the timescale of tens of seconds (Stricker et al., 2002, Strauss et al., 2012). To better understand how ZapA and ZapB interact with FtsZ, we first set out to understand their global dynamics. We performed time-lapse imaging of GFP-ZapA (pXY018) or ZapB-GFP (ASKA) expressed constitutively from a leaky T5-lac promoter in the wild-type (wt) strain, BW25113. Both fusion proteins localized to midcell in ~80% of the population (Figure 4.1A-B), and cells expressing these fusion proteins retained normal cell length (Figure 4.1C). We found GFP-ZapA was capable of complementing the Δ*zapA* strain; it rescued the mild filamentous phenotype and was recruited to midcell in a similar fashion as in wt cells (Figure 4.1D). ZapB-GFP did not rescue the filamentous phenotype of Δ*zapB* and failed to localize to midcell in the absence of endogenous ZapB. Given earlier reports of a fully functional ZapB-GFP construct (Ebersbach et al., 2008, Galli & Gerdes, 2010), we tested different linker sequences but were unable to achieve complete complementation of the Δ*zapB* strain with any C-terminal fusion. However, since the ZapB-GFP construct localized correctly in wt cells as previously reported (Ebersbach et al., 2008), we reason that this partially functional construct, when expressed ectopically in the presence of $ZapB_{wt}$, can provide a reliable readout on ZapB dynamics.

Qualitatively, GFP-ZapA displayed the same dynamics documented previously for FtsZ (Sun & Margolin, 1998, Den Blaauwen et al., 1999, Buss et al., 2013a); namely, upon septation, ZapA signal dispersed throughout the

cytoplasm, localized as dynamic foci in newborn cells and eventually coalesced to form a band-like structure at midcell (Figure 4.2A). ZapB-GFP, however, was less dynamic, as it failed to disperse throughout the cytoplasm following septation. Instead, it remained largely stationary at the new pole (Figure 4.2B) and eventually migrated to the midcell as a cohesive unit.

Recently it was reported that ZapB interacts with MatP (Espeli et al., 2012), a DNA-binding protein involved in Ter MD condensation (Mercier et al., 2008). Therefore, we hypothesized that ZapB may be less dynamic upon septation because it remains anchored to the Ter MD through MatP. To test this hypothesis, we characterized the movement of ZapB-GFP in Δ*matP* (Figure 4.2C). We found that in the absence of MatP, ZapB-GFP redistributed throughout the cytoplasm upon septation in a similar fashion as observed previously for FtsZ and ZapA (Figure 4.2C). These results support a role for MatP in orchestrating ZapB-GFP movement and confirm that ZapB-GFP (ASKA) can exhibit dynamic movements. Although these observations suggest that ZapB-GFP can accurately report on ZapB dynamics, a more thorough characterization with a functional fusion would help confirm these results.

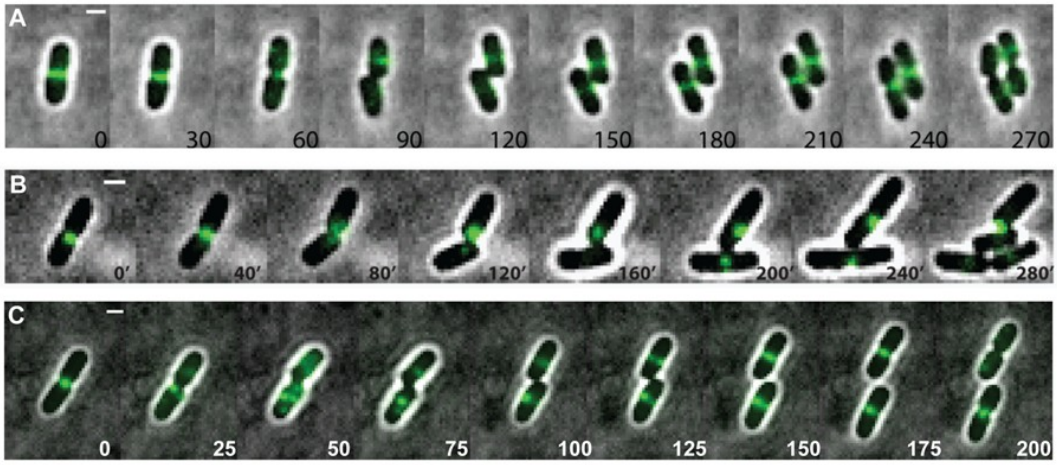

Figure 4.2 – Time-lapse ensemble imaging of ZapA and ZapB. Montages of time-lapse fluorescence images overlaid with bright-field images. (A) GFP-ZapA expressed in wt cells. (B-C) ZapB-GFP expressed in wt (B) and Δ*matP* (C) cells. Numbers indicate time (min). Scale Bars, 1 μm.

Dimensional analysis of ZapA and ZapB superstructures

Previously we and others have shown that the deletion of *zapA* or *zapB* imposes structural instability on the assembly of the Z-ring (Dajkovic et al., 2010, Buss et al., 2013a). Although the way in which ZapA and ZapB provide structural stability to the Z-ring remains unknown, their arrangement relative to FtsZ is likely reflective of their function. Initial work along these lines by the Gerdes group showed that ZapB may exist as a concentric ring internal to the FtsZ and ZapA rings (Galli & Gerdes, 2010). However, given the resolution of conventional fluorescence imaging (~250 nm), the degree of structural displacement could not be determined. In this study we use the improved resolution of PALM to characterize the relative arrangement of FtsZ, ZapA and ZapB with subdiffraction-limited resolution.

We fused mEos2 (McKinney et al., 2009), a highly characterized green-to-red photoconvertible fluorophore, to the N- or C-termini of ZapA and ZapB, respectively. The functionality of mEos2-ZapA (pJB051) and ZapB-mEos2 (pJB045) were similar to the GFP-ZapA and ZapB-GFP constructs described previously (Figure 4.3). We expressed mEos2-ZapA and ZapB-mEos2 in wt cells under optimized conditions to provide homogenous labeling densities, while preventing artifacts caused by overexpression. Given the reported endogenous concentrations of 5,000 and 13,000 molecules $cell^{-1}$ (Small et al., 2007, Ebersbach et al., 2008) and our ability to convert the integrated green fluorescence signal of mEos2 to total number of mEos2 per cell (Fu et al., 2010),

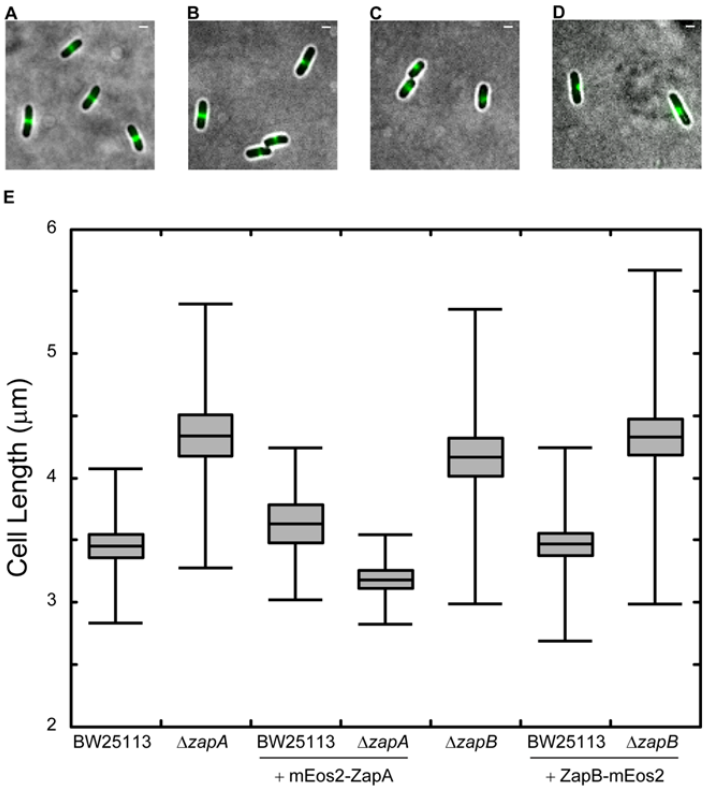

Figure 4.3 – Characterizing mEos2-ZapA and ZapB-mEos2 constructs. (A,C) Bright-field and fluorescence images of BW25113 cells expressing mEos2-ZapA (A) or ZapB- mEos2 (C). (B,D) Bright-field and fluorescence images of mEos2-ZapA (B) and ZapB- mEos2 (D) expressed in their respective deletion strains. (E) Cell length distributions of BW25113, Δ*zapA* and Δ*zapB* cells in the absence or presence of mEos2-ZapA or ZapB- mEos2 are illustrated in a box plot. Distributions were plotted by notBoxPlot (MATLAB) as the mean boxed by the 95% confidence interval and bounded by the standard deviation. Scale Bars, 1 μm.

we estimate that mEos2-ZapA and ZapB-mEos2 constitute ~40% and 5% of total cellular ZapA and ZapB levels, respectively.

The structures we observed for mEos2-ZapA in BW25113 cells (Figure 4.4A-F) were qualitatively similar to those observed previously for FtsZ-mEos2 (Fu et al., 2010, Buss et al., 2013a). All cells expressing mEos2-ZapA with appreciable

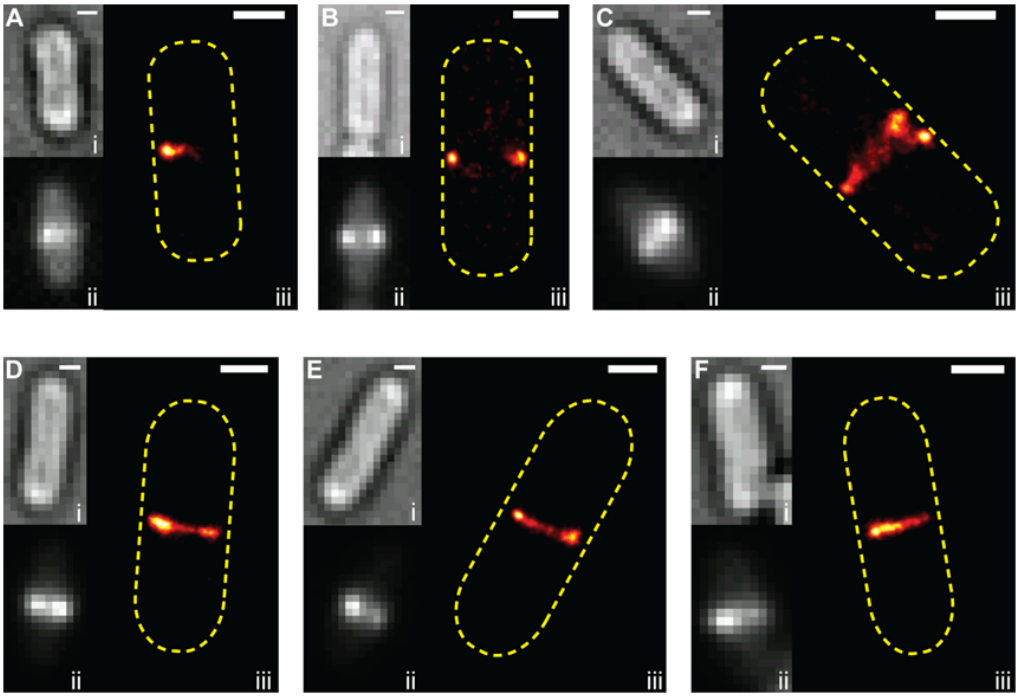

Figure 4.4 – PALM imaging of mEos2-ZapA in live *E. coli* cells. (A-F) Wt cells expressing mEos2-ZapA were imaged by PALM. Each cell is displayed as a bright-field image (i) atop an ensemble fluorescence image (ii) adjacent to a PALM image (iii) colored in pseudo-red. ZapA adopted four predominant morphologies: peripheral focus (A), peripheral foci (B), nonplanar foci (C) and ring-like band structure (D-F). Scale Bars, 500 nm.

midcell fluorescence were described by four morphological patterns: 1) a single focus, 2) a pair of peripheral foci, 3) multiple foci on different planes suggestive of a compact helix, and 4) a ring-like band structure. The band morphology was the most prevalent structure, apparent in 41% of cells (n = 229). The width of the mEos2-ZapA ring was 106 ± 3 nm (n = 94) and comprised 79 ± 2% of the localized molecules (Table 4.1). This dimension and composition is similar to what was observed previously for FtsZ (P ≈ 0.1) (Buss *et al.*, 2013). The diameter of the mEos2-ZapA ring in non-constricting cells was 923 ± 12 nm (n = 104); similar to the dimensions found for FtsZ (935 nm ± 9 nm; P > 0.4). Analysis

of mEos2-ZapA in Δ*zapA* produced similar morphological and dimensional results (data not shown).

ZapB-mEos2 also adopted the same four morphological patterns observed for FtsZ and ZapA (Figure 4.5A-F). The ZapB-mEos2 ring-like structure was present in 59% of all cells (n = 137), a higher percentage than either FtsZ or ZapA. Dimensional analysis revealed that the ZapB-mEos2 ring was 142 ± 9 nm wide and comprised 83 ± 2% of all localized molecules (Table 4.1). ZapB ring width was significantly larger than FtsZ and ZapA ($P < 0.002$). The diameter of the ZapB-mEos2 ring was 849 ± 17 nm (Table 4.1), significantly less than both FtsZ and ZapA ($P < 5e\text{-}4$).

Table 4.1 – Dimensional analysis of ZapA and ZapB structures

	Ring[a] Width. (nm)	Ring[b] Diam. (nm)
FtsZ	113 ± 3	935 ± 9
ZapA	106 ± 3	923 ± 12
ZapB	142 ± 9	849 ± 17

a. Only applied to band morphologies (FtsZ n=58, ZapA n=94, ZapB n=54)

b. Only non-constricting cells, all morphologies included (FtsZ n=93, ZapA n=104, ZapB n=67)

Mean ± Standard Error.

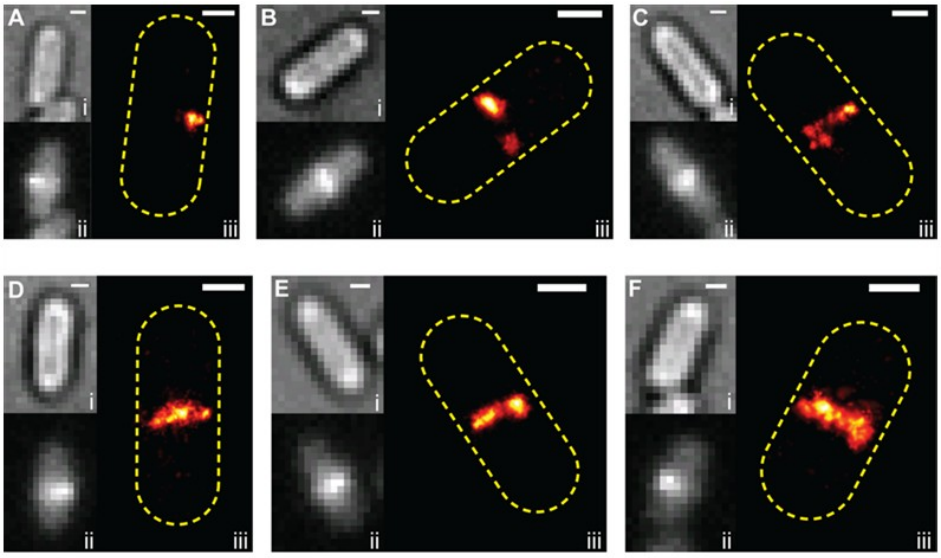

Figure 4.5 – PALM imaging of ZapB-mEos2 in live *E. coli* cells. BW25113 cells expressing ZapB-mEos2 were imaged by PALM. Each cell is displayed as a bright-field image (i) atop an ensemble fluorescence image (ii) adjacent to a PALM image (iii) colored in pseudo-red. ZapB adopted four predominant morphologies: peripheral focus (A), peripheral foci (B), nonplanar foci (C) and ring-like band structure (D-F). Scale Bars, 500 nm.

High-resolution immunofluorescence supports wider ZapB structure

We further investigated ZapB superstructure using the immunofluorescence-based super-resolution imaging method, stochastic optical reconstruction (STORM). Since this method is only dependent on the endogenous ZapB population, it overcomes potential artifacts associated with the introduction of a non-functional pool of ZapB-mEos2. STORM imaging of ZapB produced similar morphological patterns as PALM imaging (Figure 4.6). This observation suggests that the functionality and expression of ZapB-mEos2 was sufficient for accurate structure determination. The average ring width of ZapB STORM images (146 ± 9, n = 45) was significantly wider than FtsZ and ZapA structures rendered by PALM ($P < 5e-4$), but similar to ZapB PALM structures ($P > 0.7$)

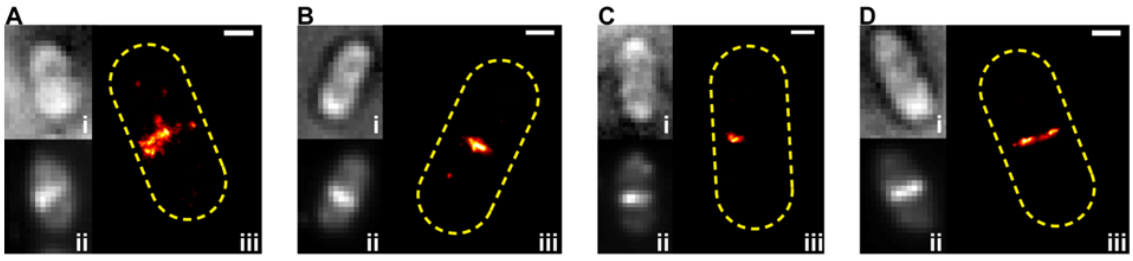

Figure 4.6 – Immuno-STORM imaging of ZapB. BW25113 cells were fixed, labeled with α-ZapB (gift from K. Gerdes), stained with goat anti-rabbit Alexa-568, and imaged by Immuno-STORM. Each cell is displayed as a bright-field image (i) atop an ensemble fluorescence image (ii) adjacent to a STORM image (iii) colored in pseudo-red. Scale Bars, 500 nm.

Concentration effects on ZapA and ZapB ring dimensions and density

Over-expression of ZapA (7- to 12-fold) affects the localization of itself, as well as ZapB and FtsZ (Galli & Gerdes, 2012). To determine how the mEos2-ZapA structure is affected by variable ZapA concentration we used the green fluorescence signal of mEos2 to provide a direct readout on mEos2-ZapA expression. By plotting the mEos2-ZapA ring width against the corresponding green fluorescence intensity (Figure 4.7A), we found that ZapA concentration has little effect on band width. A similar analysis of ring occupancy (Figure 4.7B), which describes the relative density of the structure by measuring the percent of midcell pixels that contain mEos2-ZapA molecules, showed that increases in mEos2-ZapA concentration lead to increases in the midcell occupancy. This result suggests that additional ZapA can be incorporated into the midcell structure without increasing its overall structural dimensions and is consistent with our previous findings (Fu et al., 2010) that the divisome is a loose, flexible structure. Interestingly, the incorporation of extra mEos2-ZapA appeared to saturate at sufficiently high concentrations that we estimate to be in the range of 4-fold the endogenous expression level.

The effect of ZapB overexpression on ZapB structure is poorly understood, likely owing to its propensity to aggregate at elevated concentration. Nevertheless, using the same approach described above, we were able to observe how the ZapB structure changed in response to a range of 1-1.5-fold overexpression. Similar to FtsZ and ZapA, we found that ZapB ring width remained largely constant over the range of expression levels tested (Figure

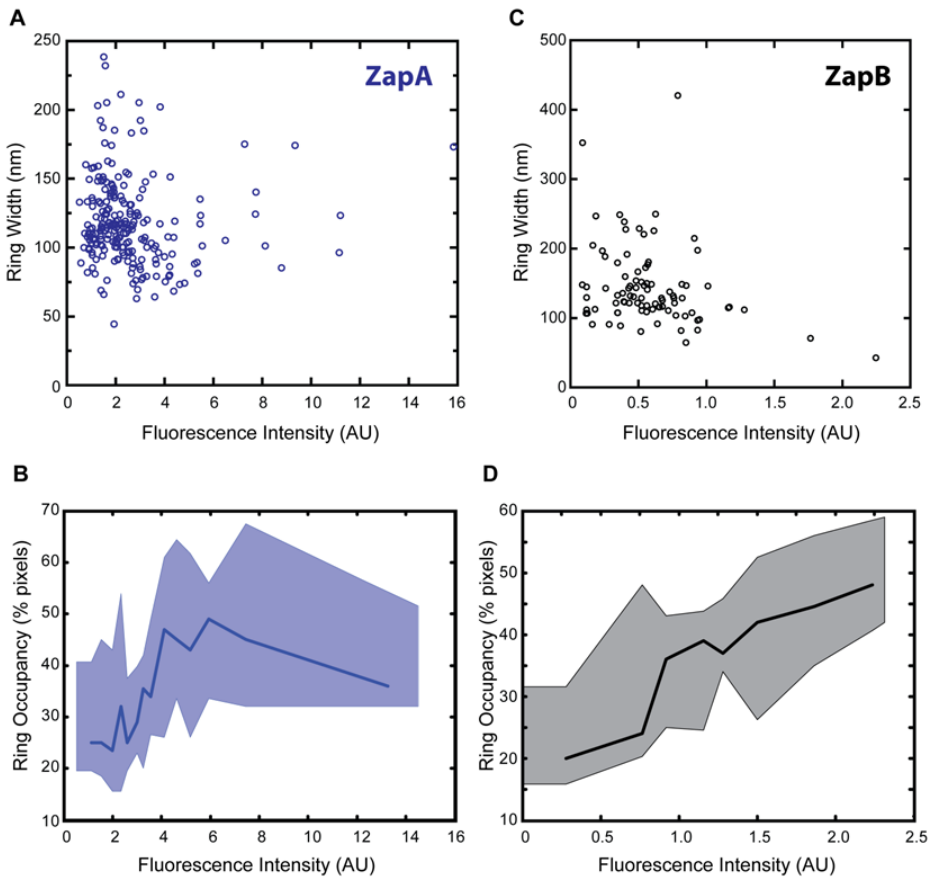

Figure 4.7 – Concentration dependence of ZapA and ZapB. (A,C) For each cell displaying a ring-like ZapA (A) or ZapB (C) structure, the ring width and integrated fluorescence intensity were determined and displayed as a scatter plot. Fluorescence intensity, which provides a direct readout on the concentration of mEos2-ZapA or ZapB-mEos2, displays no correlation with ring width. Ring occupancy, or the percent of pixels within the midcell area containing molecules of ZapA (B) or ZapB (D), is plotted against fluorescence intensity and illustrated as a binned scatter plot (MATLAB) with the bold line indicating the median values and the outline indicating the inter-quartile range. Ring occupancy appears to scale linearly with fluorescence intensity, suggesting a loose, flexible structure.

4.7C). Also similar to FtsZ and ZapA, ZapB ring occupancy scaled linearly with increased concentration, providing further support to a midcell structure capable of incorporating additional material.

ZapA clusters are similar to FtsZ, ZapB clusters differ

Previously we and others showed that FtsZ clusters are likely inherent to the formation of the Z-ring (Strauss *et al.* 2012) and that deletion of ZapA or ZapB results in smaller clusters dispersed farther away from midcell (Buss et al., 2013a). To understand how ZapA and ZapB organize FtsZ clusters into a coherent Z-ring, we imaged mEos2-ZapA and ZapB-mEos2 in wt cells by total internal reflection PALM (TIR-PALM). This imaging method selectively detects molecules associated with the cell membrane proximal to the coverslip, thus removing projection artifacts and enabling more precise counting. TIR-PALM resulted in similar morphological appearance for ZapA and ZapB as in epi-PALM (Figure 4.8). We employed the same clustering algorithm previously applied to FtsZ-mEos2 TIR-PALM images (Buss et al., 2013a) and found that while ZapA and ZapB clusters were almost identical to FtsZ clusters in area (Table 4.2), they contained almost 50% more molecules per cluster. Consequently, the resulting density of ZapA and ZapB clusters was significantly higher (ks-test, $P < 1e\text{-}5$). We note that even though ZapB density was significantly higher than ZapA ($P \approx 0.01$), if the relative labeling densities of FtsZ/ZapA (~30%) and ZapB (~5%) were taken into account, it is likely that ZapB greatly outnumbered FtsZ/ZapA at midcell.

Table 4.2 – Summary of ZapA and ZapB cluster analysis.

Strain	No. of clusters	No. of molecules	Area (nm^2)	Density (mol nm^{-2})	Midcell Displ. (nm)	Major Axis Length (nm)	Minor Axis Length (nm)	Major:Minor	Orientation (deg)
FtsZ	158	154 ± 8	69,000 ± 2,400	0.0022 ± 0.0001	81 ± 8	508 ± 18	206 ± 4	2.5 ± 0.1	15 ± 1
ZapA	97	226 ± 11	74,000 ± 2,900	0.0031 ± 0.0001	84 ± 11	522 ± 23	212 ± 5	2.6 ± 0.1	16 ± 2
ZapB	71	252 ± 15	71,000 ± 3,300	0.0045 ± 0.0005	92 ± 21	411 ± 19	241 ± 6	1.7 ± 0.1	27 ± 3

Mean ± Standard Error. Standard errors were determined by bootstrapping with 1000 simulations.

We next compared the shapes and positions of FtsZ, ZapA and ZapB clusters. We found that the similarly sized clusters of FtsZ and ZapA also adopted similar shapes ($P > 0.8$) and orientations ($P > 0.2$). ZapB clusters, however, were significantly different from FtsZ and ZapA clusters. ZapB clusters were both wider (larger minor axis lengths, $p < 5e\text{-}7$) and shorter (smaller major axis lengths, $P < 0.01$), adopting a significantly more circular shape ($P < 2e\text{-}4$). While FtsZ and ZapA were significantly different from ZapB in shape and density, the relative displacement of all clusters from midcell was similar ($P > 0.3$), with all clusters localizing within ~5% of the calculated midcell position.

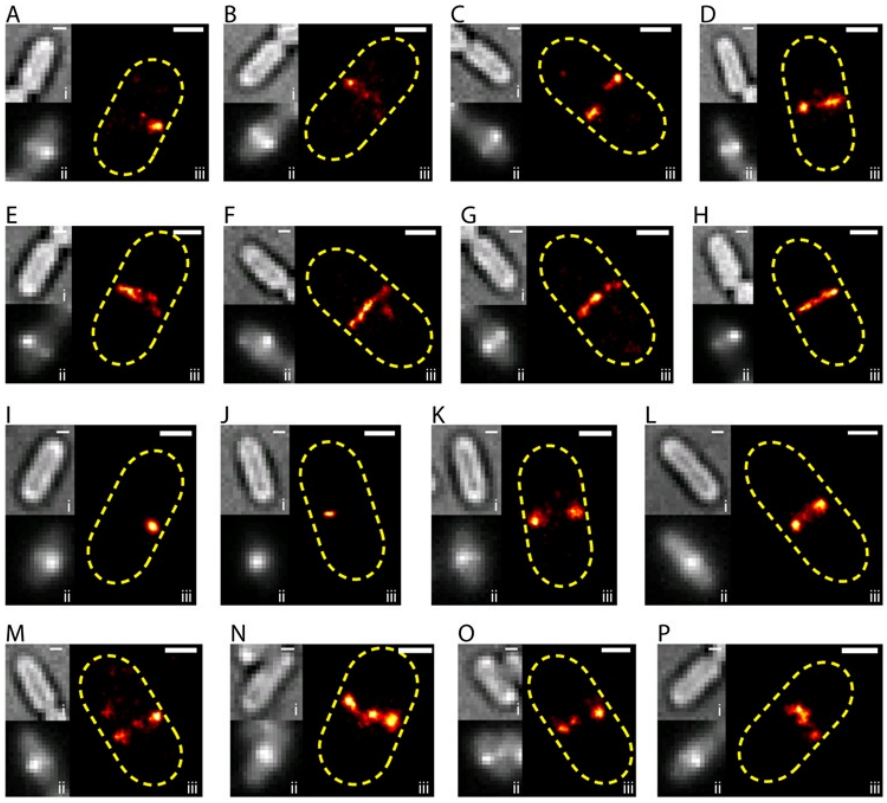

Figure 4.8 – TIR-PALM imaging of ZapA and ZapB. Wt cells expressing mEos2-ZapA (A-H) or ZapB-mEos2 (I-P) were imaged by total internal reflection PALM. Each cell is displayed as a bright-field image (i) atop an ensemble fluorescence image (ii) adjacent to a PALM image (iii) colored in pseudo-red. The dotted yellow line provides a general indicator of the cell outline. The ZapA and ZapB structures revealed by TIR-PALM were described by the same four morphologies discussed previously. These images were used for Cluster Analysis. Scale Bars, 500 nm.

Molecular mobility of ZapB is enhanced relative to FtsZ and ZapA

Although the Z-ring undergoes rapid turnover and significant global rearrangements on the timescale of tens of seconds, most membrane-associated FtsZ molecules are virtually immobile on the timescale of 0.2 – 2.0 s (Buss et al., 2013a, Niu & Yu, 2008). Since the recruitment of ZapA and ZapB to midcell is dependent on FtsZ, it is likely that their intracellular dynamics are intimately linked to that of FtsZ.

To further investigate the dynamics of individual protein molecules in these structures, we performed single-molecule tracking on wt cells ectopically expressing mEos2-ZapA or ZapB-mEos2. Both constructs were grown in the absence of inducer and were imaged with a 50 ms exposure time at an interval of 200 ms for up to 5 min. Detection of overlapping emitters was prevented by application of a very low 405-nm activation laser. The computed mean-squared displacement at different time lags is plotted in Figure 4.9. The mean squared displacement (MSD) for ZapA and ZapB on the timescale of 0.2 - 2.0 s can be described by a simple Brownian diffusion model, whereby the apparent 2D diffusion coefficient is proportional to the slope of the fitted line. The apparent 2D diffusion coefficients for ZapA and ZapB were 0.0004 ± 0.00004 $\mu m^2 s^{-1}$ and 0.0009 ± 0.00003 $\mu m^2 s^{-1}$, respectively, similar to that of FtsZ (0.0004 ± 0.00003 $\mu m^2 s^{-1}$) (Buss et al., 2013). These diffusion coefficients are an order of magnitude slower than that expected for a freely diffusing membrane protein (~0.2 to 0.02 $\mu m^2 s^{-1}$) (Deich et al., 2004, Kim et al., 2006, Leake et al., 2006,

Mullineaux et al., 2006). From these studies it is apparent that FtsZ, ZapA, and ZapB are effectively immobilized upon association with the division complex.

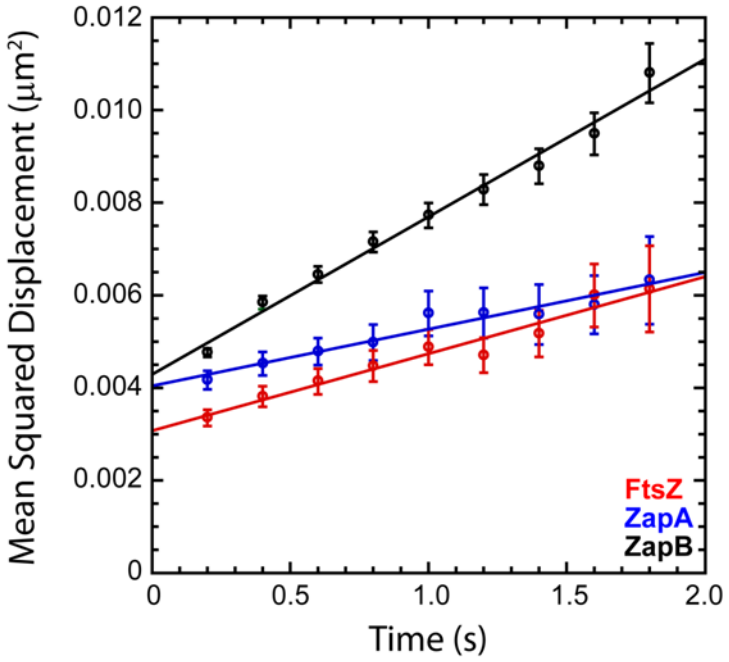

Figure 4.9 – Single-molecule tracking of ZapA and ZapB. Mean squared displacements (closed circles) are plotted at different time lags for wt cells expressing mEos2-ZapA (blue) or ZapB-mEos2 (black). Similar data for FtsZ-mEos2 (red) is also included for comparison (Buss et al., 2013). The bold lines illustrate the linear fit (y = 4Dx + A) used to calculate the apparent two-dimensional diffusion coefficients: ZapA, 0.0004 ± 0.0004 $\mu m^2 s^{-1}$; ZapB, 0.0009 ± 0.0003 $\mu m^2 s^{-1}$. Error bars indicate standard error.

ZapA movement deviates from FtsZ in non-divisional cells

Previous work showed that ZapA colocalizes with FtsZ throughout the cell cycle (Gueiros-Filho & Losick, 2002, Galli & Gerdes, 2010). Here, we have shown that ZapA exhibits similar global dynamics, structural dimensions and cluster attributes to FtsZ. Therefore, it is likely that ZapA structure directly mimics that of FtsZ. Nevertheless, it has also been shown that ZapA likely interacts with a number of division proteins other than FtsZ (Maggi et al., 2008), suggesting that structural deviations may exist.

We directly investigated the relative arrangements between ZapA and FtsZ by performing fast, time-lapse imaging on a dual-labeled sample ectopically

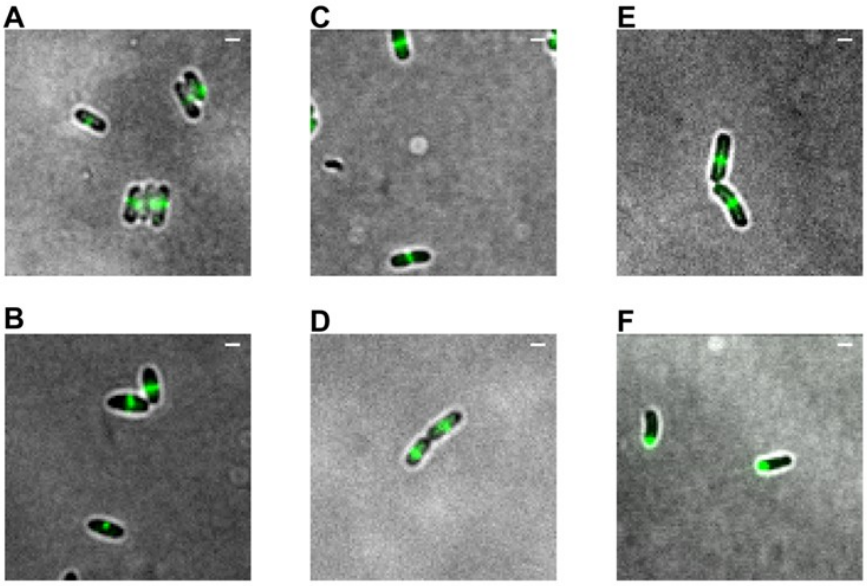

Figure 4.10 –Characterization of two-color PALM constructs. Representative snapshots displayed as an ensemble fluorescence image overlaid with a bright-field image. mCherry-ZapA in wt cells (A), FtsZ-PAmCherry1 in wt cells (B), Dronpa-ZapA in wt (C) and Δ*zapA* cells (D), and ZapB-Dronpa in wt (E) and Δ*zapB* cells (F). Scale Bars, 1 μm.

expressing mCherry-ZapA (pJB077, Figure 4.10A) and FtsZ-GFP from P_{BAD} and $P_{T5\text{-}lac}$ promoters, respectively. We induced mCherry-ZapA expression for 30 min with 0.2% arabinose, washed away inducer and continued growth for 2-3 hr to dilute induced protein. The leaky expression of $P_{T5\text{-}lac}$ was sufficient for FtsZ-GFP localization. Fluorescence images of both fusion proteins were acquired simultaneously in wt cells every 20 s (Figure 4.11A). Consistent with previous reports, the ZapA and FtsZ signals predominantly adopted ring-like structures that overlapped at midcell. However, at various time points we observed structural deviations between the ZapA and FtsZ structures, suggesting that although ZapA is dependent on FtsZ for its recruitment to midcell, ZapA does not replicate the dynamics of FtsZ, and hence the two may exist as separate structures.

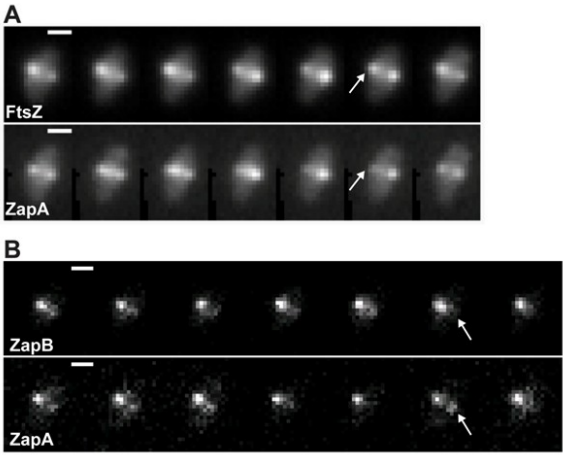

Figure 4.11 –Two-color time-lapse imaging of FtsZ, ZapA and ZapB. (A) FtsZ-GFP and mCherry-ZapA or (B) ZapB-GFP and mCherry-ZapA were expressed in wt cells and imaged simultaneously every 20 s for 2 min. Both structures predominantly overlap and adopt similar morphological features at the same time. Arrows point to instances where morphological differences were observed. Scale Bars, 1 μm.

ZapB movement deviates from ZapA in non-divisional cells

In *E. coli*, the midcell localization of ZapB is dependent on FtsZ and ZapA (Ebersbach et al., 2008). To examine whether the dynamics and structure of ZapB are dependent on ZapA, we similarly performed fast, time-lapse imaging on wt cells expressing P_{BAD}::mCherry-ZapA (pJB077) and $P_{T5\text{-}lac}$::ZapB-GFP. Samples were induced and imaged as described above. Consistent with previous reports (Galli & Gerdes, 2010), the ZapA and ZapB signals were present at midcell in the same general area in all cells (Figure 4.11B). However, as with ZapA and FtsZ, we observed slight deviations between the ZapA and ZapB morphologies.

ZapA and ZapB appear to bridge FtsZ structures

To directly compare the *in vivo* structures of FtsZ, ZapA and ZapB with high-resolution, we performed two-color PALM (2C-PALM) on live wt cells ectopically expressing FtsZ-PAmCherry1 (pJB066) and Dronpa-ZapA (pJB057) or ZapB-Dronpa (pJB073). Dronpa-ZapA appeared functional as it was recruited to the midcell of Δ*zapA* cells (Figure 4.10C-D). FtsZ-PAmCherry1 and ZapB-Dronpa were unable to localize to midcell in their respective depletion or deletion strains, but did produce characteristic signals in wt cells (Figure 4.10B,E-F). To achieve similar ratios of two different constructs in the same cell while maintaining relatively low expression levels, we constructed a bigenic operon under $P_{T5\text{-}Lac}$ containing two different ribosome-binding sites of similar low strength (Salis, 2011).

Expression from $P_{T5\text{-}lac}$ in wt cells was induced with 20 μm IPTG for 2 hr followed by a 2 hr outgrowth. Most cells (80%, n = 93) displayed similar structures for ZapA and FtsZ, both in terms of shape and position, suggesting that both proteins were largely overlapping and adopted similar morphologies at the same time (Figure 4.12A). In the remaining 20% of cells, ZapA and FtsZ adopted different morphologies and appeared structurally distinct from each other (Figure 4.12B). Furthermore, in ~25% of these cells, a ZapA cluster was positioned in between two FtsZ clusters (Figure 4.12Bii-iii) and appeared to bridge FtsZ clusters.

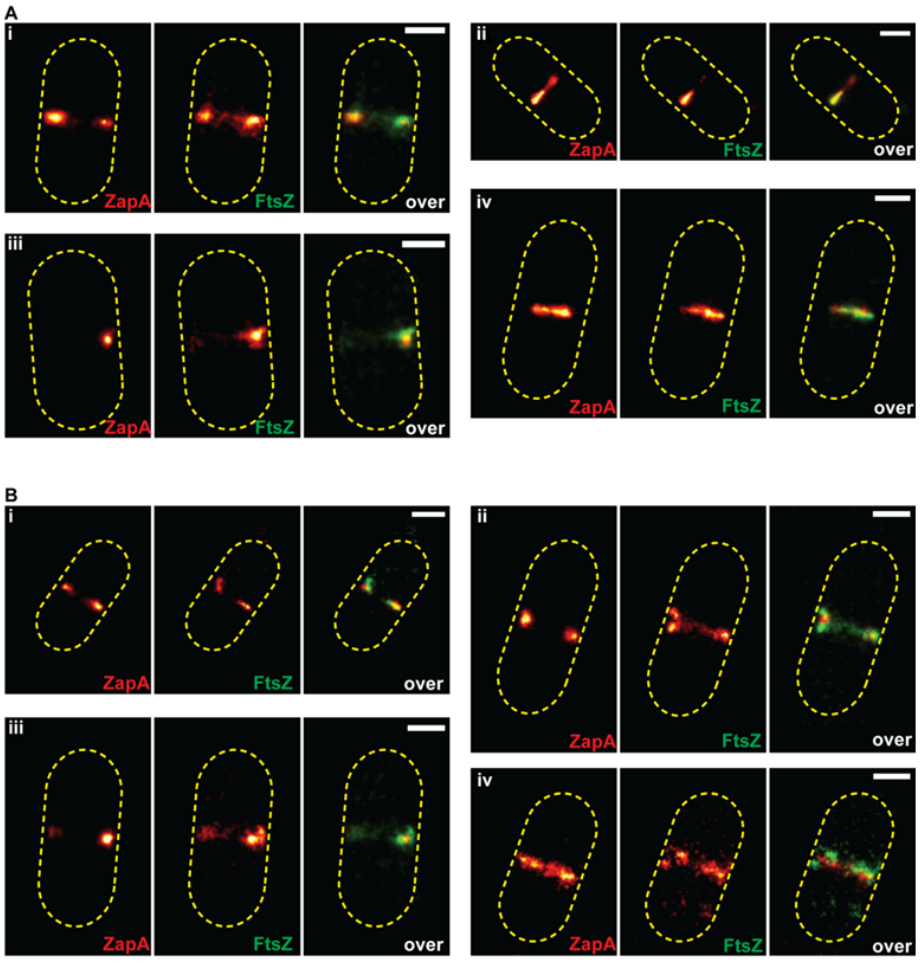

Figure 4.12 – Two-Color PALM imaging of ZapA and FtsZ. Representative PALM images of cells expressing Dronpa-ZapA (red) and FtsZ-PAmCherry1 (green) are displayed. (Ai-iv) The majority of cells (80%) illustrated the overlapping nature of ZapA and FtsZ, whereby both structures adopt the same shape and size. (Bi-iv) A subpopulation of cells display structural deviation between ZapA and FtsZ. (Bii) In some instances ZapA appears to bridge FtsZ clusters. Scale Bars, 500 nm.

A similar comparison of the ZapB and FtsZ structures was complicated by the expression of ZapB-Dronpa. We were unable to apply the same bigenic approach described above, because the required induction of FtsZ-PAmCherry1 caused ZapB-Dronpa to aggregate. Instead we engineered a construct (pJB073) that expressed ZapB-Dronpa at a basal level that was high enough to perform

PALM imaging, but low enough to avoid aggregation. We used this construct in conjunction with a compatible low-copy plasmid expressing FtsZ-PAmCherry1 from P_{BAD}. A 1 hr induction of P_{BAD} with 0.2% arabinose followed by a 3 hr outgrowth was sufficient for visualization of FtsZ-PAmCherry1. The ZapB-Dronpa signal was internal to the FtsZ-PAmCherry1 signal in 72% of cells (n = 88, Figure 4.13A-D). Since the 28% of cells not displaying an internal ZapB signal were all non-constricting, we reason that our inability to measure ZapB internal to FtsZ via conventional PALM (Table 4.1) was due to population averaging. Unexpectedly, we also observed different structural morphologies for ZapB and FtsZ in 45% of all cells (Figure 4.13E-H), with ZapB typically present as a band-like structure in contrast to the focal FtsZ.

We note that although the Dronpa and PAmCherry1 signals were acquired simultaneously over a ~30 s period, their different photoproperties resulted in somewhat sequential activation of Dronpa and PAmCherry1. To verify if the structural displacements we observed above were caused by the largely sequential imaging of Dronpa and PAmCherry1, we performed a control experiment in which we imaged PAmCherry1-ZapA and Dronpa-ZapA from pJB090 under the exact the same conditions (pJB090). We found that in all cells except one (n = 22), Dronpa-ZapA and PAmCherry1-ZapA adopted the exact same morphology and appeared to overlap completely (Figure 4.14A). These results suggest that the structural displacements we observed are unlikely due to the temporal artifacts resulting from the differential activation and imaging of PAmCherry1 and Dronpa. Furthermore, when we performed the same 2-color

imaging on TetraSpec fluorescent beads that are visible simultaneously in both channels, we observed no structural deviation at all. This control demonstrates that the structural displacement we observed are unlikely caused by errors in image registration and calibration.

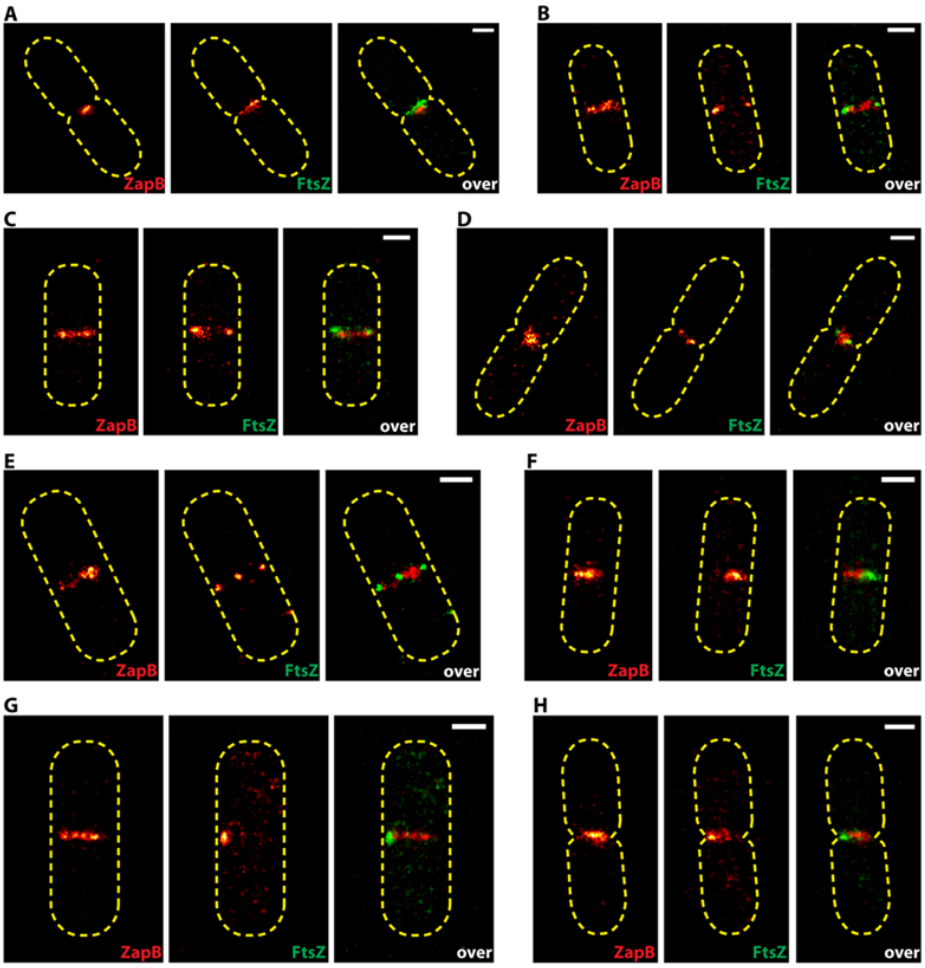

Figure 4.13 – Two-color PALM imaging of ZapB and FtsZ. Representative PALM images of cells expressing ZapB-Dronpa (red) and FtsZ-PAmCherry1 (green) are displayed. (A-D) The degree of overlap for ZapB and FtsZ structures is less than that previously observed for ZapA and FtsZ (Figure 4.11). In most cells (70%), ZapB adopts a different morphology than FtsZ, often appearing as a more contiguous structure internal to the focal FtsZ. (E-H) In a smaller fraction of cells (30%), ZapB and FtsZ display very little overlap. Scale Bars, 500 nm.

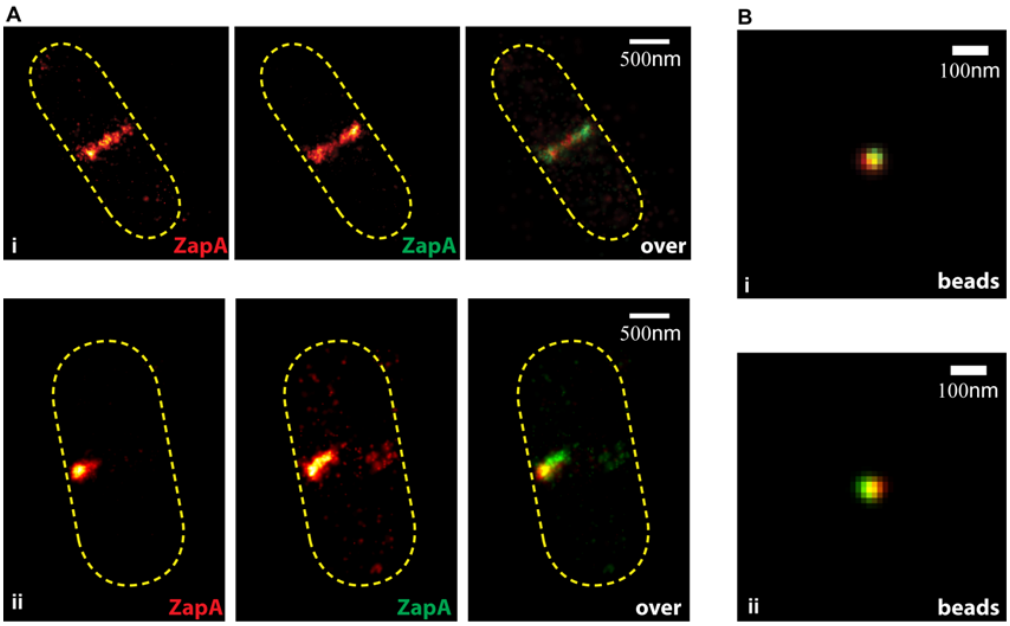

Figure 4.14 –Two-color PALM imaging of ZapA-ZapA and Beads. Representative PALM images of 100nm TetraSpec beads or cells expressing Dronpa-ZapA (red) and PAmCherry1-ZapA (green). (Ai-ii) The ZapA morphologies were similar in 95% of cells, illustrating the ability of 2C-PALM to resolve the position of two different photoactivatable fluorescence constructs in the same cell at the same time. (Bi-ii) Fluorescence beads that provide a constant signal in both channels were used to determine the accuracy of our image translation. Our translational accuracy was determined to be ~25 nm, indicating that the structural deviations observed in the overlaid images was not an artifact of our imaging method.

ZapB exists internal to FtsZ and ZapA

Direct comparison of the ZapB and FtsZ structures via 2C-PALM supports previous findings that ZapB may exist as a concentric ring internal to FtsZ (Galli & Gerdes, 2010). However, because PALM images are two-dimensional projections of 3-dimensional objects, we were unable to determine the degree of displacement separating ZapB from FtsZ accurately. Therefore, we applied interferometric PALM (iPALM) imaging (Shtengel *et al.*, 2009, Kanchanawong *et al.*, 2010). iPALM employs the same general principles of conventional PALM imaging to identify a molecule's X- and Y-positions beyond the diffraction limit, while utilizing the interference of emitted light to determine the molecule's Z-position. Compared to other fluorescence super-resolution approaches, iPALM currently offers the best Z-resolution.

iPALM imaging was performed on fixed wt cells expressing FtsZ-mEos2, mEos2-ZapA or ZapB-mEos2. Alexa Fluor® 568 and fixed cells were sequentially adhered to a gold-embedded coverslip via poly-l-lysine and then enclosed in a PBS-buffered (pH 7.4) environment. Regions of high cell density were selected and imaged continuously for 30,000-100,000 frames. We used total internal reflection to resolve a thin layer (~250 nm) proximal to the membrane. The embedded gold beads were used to calibrate for sample drift. The Alexa Fluor® 568 layer produced a narrow, normally-distributed fluorescence signal at the glass surface. The Z-positions of each sample were determined relative to the Alexa Fluor® 568 signal, thus providing

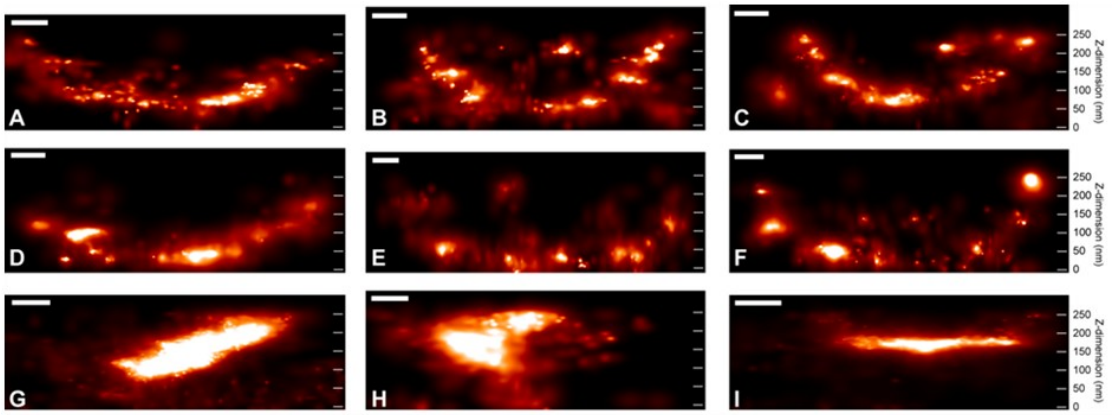

Figure 4.15 – Three-dimensional imaging of FtsZ, ZapA, and ZapB. Representative iPALM images of fixed wt cells expressing FtsZ-mEos2 (A-C), mEos2-ZapA (D-F), or ZapB-mEos2 (G-I) are illustrated along the cellular circumference. Images were acquired with TIRF excitation so as to limit detection to a thin layer (~250 nm) proximal to the coverslip. All images are in scale along the Z-axis. Relative Z-dimensions are included at the right of each row. Images are not in scale along the X-axis.

a basis of comparison for all samples tested. Using this setup we achieved a Z-resolution of ~20 nm and an X- and Y-resolution of ~25 nm.

When iPALM images of FtsZ, ZapA and ZapB structures were viewed along the circumferential plane of the cell, we observed significant morphological differences. FtsZ and ZapA both adopted arch-like, heterogeneous arrangements characterized by varying density, depth and thickness (Figure 4.15A-F). The arch-like shapes likely illustrate the direct or indirect association of FtsZ and ZapA with membrane proteins. ZapB, on the other hand, formed seemingly homogenous, dense structures that were noticeably independent of membrane curvature (Figure 4.15F-I). ZapB rarely adopted the punctate structures common to ZapA or FtsZ, suggesting that the observed punctate structures of FtsZ and ZapA are unlikely caused by the mEos2 label or the stochastic activation of

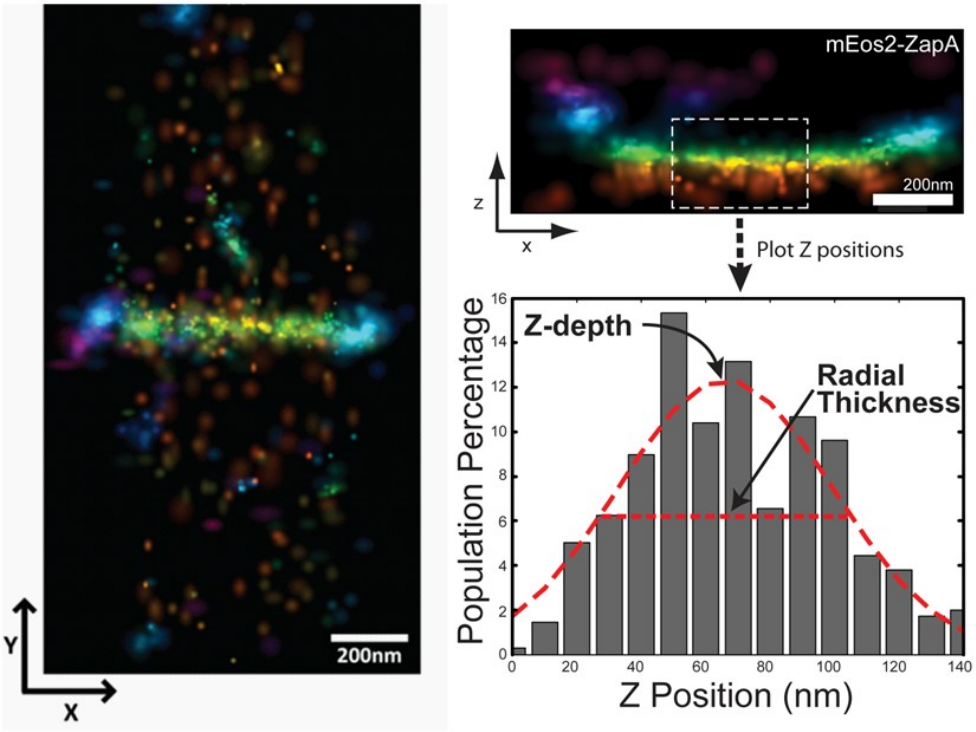

Figure 4.16 – An explanation of iPALM measurements. A wt *E. coli* cell expressing mEos2-ZapA is illustrated (left) along the X-Y axes and colored according to Z-Position. The midcell region of the same cell has been cropped-out and illustrated along the X-Z axes (right, top). The membrane-proximal region of the ZapA structure was selected (white outline, dotted) and the distribution of Z-positions for all the molecules within this region were plotted (right, bottom). The distribution was fit to a Gaussian function. The mean and the standard deviation approximate the average Z-Position and radial thickness of the ZapA structure, respectively.

PALM imaging. The striking contrast between ZapB and FtsZ-ZapA, further supports a model for FtsZ-ZapA-ZapB in which ZapB is structurally distinct.

We next measured the average Z-position for each structure in non-constricting cells by selecting regions proximal to the coverslip and extracting a mean Z-position for each structure in each cell (Figure 4.16, Table 4.3). Since the Z-position is measured relative to the Alexa Fluor® 568 signal (i.e. the coverslip),

a small Z-position indicates proximity to the inner membrane, while a large Z-position indicates separation from the inner membrane. We found that the mean Z-position of FtsZ and ZapA was 75 ± 2 nm (n = 125) and 65 ± 2 nm (n = 178), respectively. These values, although significantly different, are within our spatial resolution (~20 nm). The Z-position of ZapB, however, was 120 ± 2 nm (n = 226), significantly more removed from the membrane than FtsZ and ZapA ($P < 0.001$). It is important to note that although the average Z-positions were significantly different, the distributions of Z-positions for all three proteins displayed considerable overlap (Figure 4.17).

To provide a general reference for how far FtsZ, ZapA and ZapB are displaced from the inner membrane we next imaged mEos2 fused N-terminally to the peripheral membrane-targeting sequence (MTS) of MinD from *Bacillus subtilis* (pXY029). We found the average Z-position for mEos2-MTS was 54 ± 15 nm (n = 321, Table 4.3). These results suggest that under our conditions the average position of FtsZ and ZapA was ~15-20 nm away from the cytoplasmic face of the inner membrane.

Table 4.3 – Summary of iPALM measurements

Sample	n	Z-Depth (nm)	Radial Thickness (nm)
FtsZ	125	75 ± 2	22 ± 1
ZapA	178	65 ± 2	28 ± 1
ZapB	226	120 ± 2	30 ± 1
MTS	321	54 ± 1	23 ± 1

Mean ± standard error

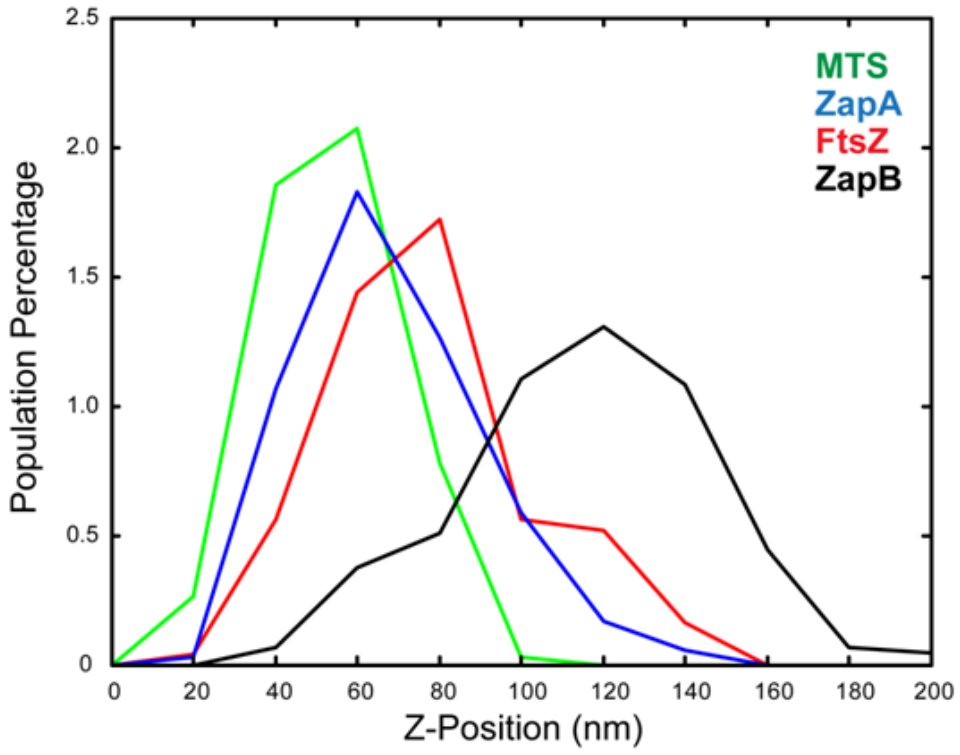

Figure 4.17 – Determining the Z-position of FtsZ, ZapA and ZapB. The distribution of mean Z-positions for each wt cell expressing mEos2-MTS (green), mEos2-ZapA (blue), FtsZ-mEos2 (red) and ZapB-mEos2 (black) is illustrated as a histogram with 20 nm bins. The results are indicated in Table 4.3. The distribution widths do not reflect the width of the underlying structure, but rather the heterogeneity in the sample mean.

Discussion and Conclusions

Dynamic association between FtsZ and ZapA

We used a variety of imaging methods and quantitative measurements to investigate the structure of ZapA and its relation to that of FtsZ. We found that ZapA largely mimics FtsZ — it dynamically redistributed upon septation, adopted a loose ring-like structure of similar width (~110 nm), formed clusters of the same size and shape, possessed similar molecular mobility, and was significantly external to ZapB. The only direct comparisons between ZapA and FtsZ, however, showed that ZapA structures do not always replicate FtsZ dynamics or structure: ZapA morphology occasionally deviated from FtsZ and ZapA appeared to bridge FtsZ clusters.

Earlier studies have shown that ZapA is recruited to midcell by its interaction with FtsZ (Gueiros-Filho & Losick, 2002) and the two proteins remain colocalized throughout the cell cycle (Galli & Gerdes, 2010). Additionally, ZapA also associates with the polymeric ZapB structure at midcell (Galli & Gerdes, 2010) and potentially numerous other division proteins (Maggi et al., 2008). While the similar dimensions and dynamics of ZapA and FtsZ likely reflect the high degree of structural overlap they share, the structural deviations illustrate the dynamic nature of this association.

ZapB is spatially and structurally distinct from FtsZ and ZapA

In all the ways that ZapA was similar to FtsZ, ZapB was different — it remained as a polar mass upon septation, adopted a wider (~140 nm) ring-like structure with a smaller diameter, formed clusters of different shape and density, and was significantly displaced from the membrane. Furthermore, instead of appearing as an arched, punctate structure along the radial plane, ZapB adopted a dense, homogenous structure that did not conform to the membrane curvature. The lack of curvature could be due to the fact that ZapB does not directly associate with membrane proteins, but may also reflect the intrinsic polymerization properties of ZapB (Ebersbach et al., 2008, Galli & Gerdes, 2012). The large numbers of molecules (~250) detected per cluster in spite of the low labeling density (~5%), are also consistent with a highly polymerized ZapB structure. In summary, the vast morphological differences apparent between ZapB and FtsZ, suggest that ZapB assembles into a distinct structure internal to FtsZ that possibly has a structural role in maintaining the stability of the Z-ring.

FtsZ and ZapA are 15-20nm from the inner membrane

FtsZ is tethered to the membrane through its association with the membrane proteins, ZipA and FtsA, via a short, highly conserved peptide at the end of its C-terminus. Between the C-terminal peptide and the globular domain of FtsZ is a long, intrinsically disordered linker that displays considerable sequence variability (Gardner et al., 2013). Proper FtsZ function is dependent on the length

of this linker sequence in both *E. coli* and *B. subtilis* (Buske and Levin, 2012; Gardner et al., 2013). A current hypothesis proposes that this linker may function as an entropic spring that enables force generation by coupling FtsZ protofilament bending to membrane deformation. Therefore, measuring the actual distance that FtsZ is away from the inner membrane may provide insight into possible mechanisms of force generation of the Z-ring.

Using iPALM, we measured the Z-position of mEos2 tagged to four different cytoplasmic proteins: MTS, FtsZ, ZapA and ZapB. Using a previous ultrastructure study (Matias *et al.*, 2003), we estimated that the cytoplasmic face of the inner membrane should be separated from the cellular exterior by ~40 nm. In agreement with this estimate, the average Z-position of mEos2-MTS, which served as a reference for the inner membrane position, was displaced ~55 nm from the coverslip (Figure 4.18). FtsZ-mEos2 and mEos2-ZapA had an additional displacement of ~10-20 nm from MTS-mEos2, and ZapB-mEos2 was an extra ~40-50 nm away from FtsZ and ZapA. The 10-20 nm distance separating FtsZ from MTS supports with the 11-14 nm displacement recently estimated by Gardner *et al*. (2013) for the membrane association of FtsZ by FtsA. It is important to note that this 10-20 nm separation does not take into account the thickness of the FtsZ structure along the radial direction. Consequently the distance we measured is likely an over-estimation of the actual separation.

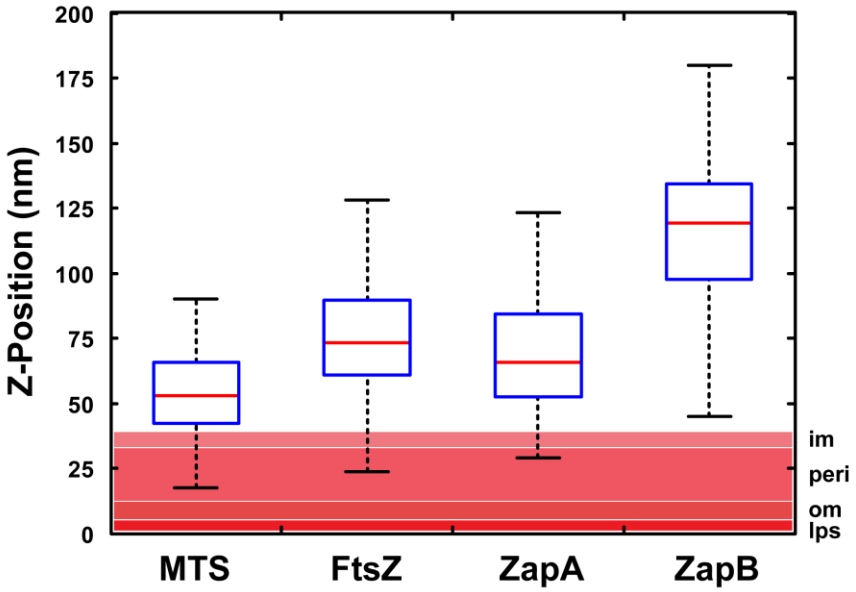

Figure 4.18 – FtsZ-ZapA-ZapB in the context of cellular ultrastructures. The full distribution of mean Z-positions for wt cells expressing mEos2-MTS, FtsZ-mEos2, mEos2-ZapA and ZapB-mEos2 are illustrated as box plots (MATLAB) with the median (red) boxed by the inter-quartile range (blue) bounded by the min/max (dotted). The relative position of the lipopolysaccharide layer (lps, 4 nm), the outer membrane (om, 7 nm), the periplasm (peri, 21 nm) and the inner membrane (im, 6 nm), as determined by Matias *et al.* (2003), are overlaid in shades of red so as to provide cellular context to the determined Z-positions. The proximity of the MTS distribution to the estimated position of the inner leaflet of the inner membrane illustrates the accuracy of our method.

ZapB may serve as a cytoplasmic raft to anchor FtsZ clusters

ZapA and FtsZ both displayed an arch-like, punctate structure of similar width and thickness that was close to the membrane. In contrast, ZapB displayed a wide, amorphous structure internal to ZapA and FtsZ. The structural similarity of FtsZ and ZapA, and structurally dissimilarity of FtsZ-ZapA to ZapB, suggest that ZapB does indeed form a distinct structure internal to the FtsZ -ring. Given

our previous results as well as initial work from the Gerdes group (Galli & Gerdes, 2010), we propose that ZapA tethers FtsZ to ZapB, and the large, internal structure of ZapB provides structural stability to the Z-ring (Figure 4.19).

How might ZapB provide structural stability to the FtsZ-ring? The FtsZ-ring is known to be a dynamic structure, and the basis for this dynamics reportedly comes from the GTPase activity of FtsZ. Since ZapB is not governed by nucleotide-dependent changes, this structure is likely more stable. We reason that this large, internal structure of ZapB could serve as a cytoplasmic anchor for FtsZ clusters proximal to the midcell region and that the delayed response of ZapB dynamics to FtsZ depolymerization may help maintain the division site selection by not immediately diffusing away upon GTPase-driven depolymerization. Since FtsZ clusters appear to be capable of supporting constriction without ZapA and ZapB (Buss et al., 2013a), the corralling of FtsZ clusters at midcell by ZapA and ZapB, would only serve to enhance the efficiency of division. Interestingly, when clusters are efficiently aligned, this alignment is characterized by a specific width (~110 nm) that is not affected by the deletion of ZapA or ZapB. This observation suggests that other regulatory mechanisms must be at play. Further investigations regarding the redundant mechanisms of ZapC and ZapD are needed to determine the degree of functional overlap.

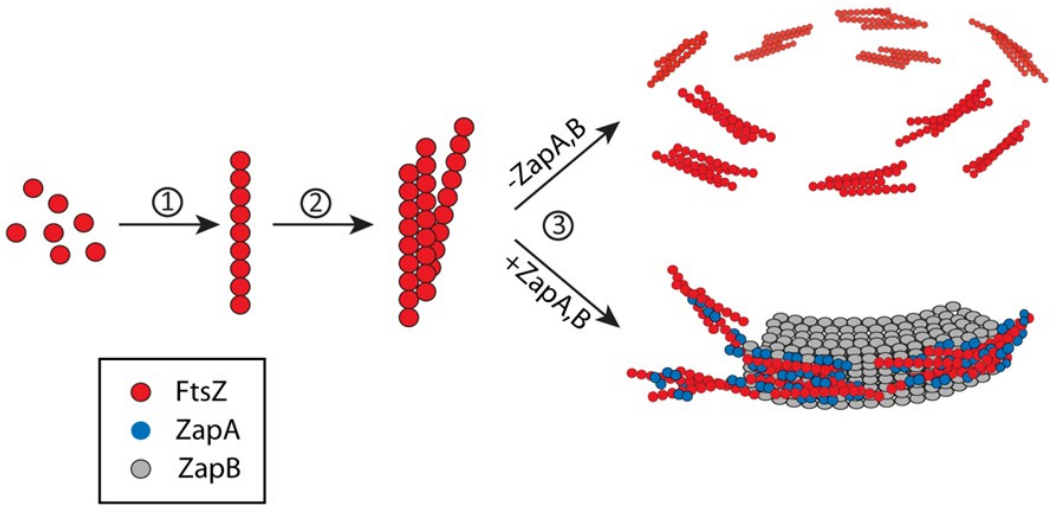

Figure 4.19 – Model of FtsZ-ring organization by ZapA and ZapB. 1. FtsZ monomers associate longitudinally into FtsZ protofilaments. 2. FtsZ protofilaments laterally associate to form FtsZ clusters, or higher-ordered polymers consisting of multiple FtsZ protofilaments. 3. FtsZ clusters are corralled at midcell by ZapA and ZapB to form the FtsZ-ring. Central to this hypothesis is the ZapA-mediated tethering of dynamic FtsZ clusters to the large, internal ZapB structure. In this model, ZapB essentially serves as a stable, cytoplasmic raft that effectively increases the local FtsZ concentration by forcing performed clusters into close proximity that enables further polymerization. In the absence of ZapA and ZapB, FtsZ clusters scatter throughout the midcell region. Given the viability of *zapA* and *zapB* null mutants, redundant mechanisms must exist that promote cluster alignment.

Chapter 5

Materials & Methods

1. Molecular Cloning

1.1. Bacterial Growth

Bacterial strains and plasmids are indicated in Appendix 1.1-2. For all experiments, cells were typically streaked from a frozen stock onto an LB plate and grown overnight at 37°C. The next day, single colonies were used to inoculate 3mL of LB media and grown overnight at 37°C with shaking (~220 rpm). Plates were stored at 4°C for up to one month. Saturated LB cultures were then used to inoculate (~1:500) 3mL of M9 minimal media [0.4% Glucose, supplemented with MEM Vitamins and MEM Amino Acids] ($M9^{+}$), and the cultures were grown at room temperature (RT) prior to fixation or imaging. When appropriate, 150 μg ml^{-1} chloramphenicol, 50 μg ml^{-1} kanamycin or 50 μg ml^{-1} carbenicillin was added. For fast growth conditions, we applied EZ Rich Defined Media (Teknova) supplemented with 0.4% Glucose and incubated at 37°C. PfuUltra II polymerase (Agilent) was used for PCR amplification.

1.2. DNA purification

1.2.1. Plasmid DNA was purified using the ubiquitous spin column technology.

1.2.2. Genomic DNA was purified by a standard alkaline lysis procedure described previously (Sambrook & Russell, 2001).

1.3. Restriction Enzyme Digest

All restriction enzymes were purchased from New England Biolabs and used according to the manufacture's specifications.

Typically 2-3 µg of plasmid DNA was restricted in 50 µl reaction for 3 hrs.

1.4. Polymerase Chain Reaction (PCR)

1.4.1. Molecular Cloning PCR was performed with PfuUltra II Fusion HS Polymerase from Agilent Technologies. This polymerase quickly (15s kb^{-1}) provided high fidelity (10^{-6} errors bp^{-1}) products. A single 50 µl reaction was typically produced sufficient DNA (~3 µg)for downstream processes.

1.4.2. Colony PCR was performed with One *Taq*® DNA Polymerase from NEB. A portion of a single colony was resuspended in 100 µl of dH_2O (OD600 << 0.1) and 1 µl was used as a template in 20 µl reaction. The reaction was assembled and incubated as suggested by the One *Taq*® protocol, except the initial denaturing step was performed at 94°C for 5 min.

1.5. Gel-purifying DNA Fragments

Restricted DNA fragments (> 2 µg) were run on a 1% Agarose gel in TAE buffer, stained in TAE containing 0.01 % Ethidium Bromide (v/v) for 30-60 min and imaged briefly. The banding pattern was checked against the 1 kB DNA ladder (NEB) to confirm proper length and the appropriate bands were extracted and treated according to the GeneJet Gel Extraction Kit (Thermo).

1.6. Dephosphorylating DNA Fragments

The 5' phosphate of problematic vector backbones was removed to prevent false positives during ligation. This was accomplished by treating gel-purified fragments with Antarctic Phosphatase from NEB prior to ligation. Incubations typically lasted 30 min, as prolonged incubation was found to be deleterious.

1.7. Ligating DNA fragments

The Quick Ligation™ Kit from NEB was used as suggested. A 6:1 ratio of insert to backbone was applied when possible and 2 µl was used to transform chemically competent cells, as this method is incompatible with electrotransformation.

1.8. LR Recombination - Construction of Gateway Vectors

The attR1-cat-ccdB-attR2 region was amplified from pMK2017, restricted with NotI or AscI and ligated with similarly digested pUC19 vector containing the fast-maturing yellow fluorescent protein, Venus (Nagai et al., 2002), under the lac promoter. This resulted in the production of P_{Lac}::attR1-cat-ccdb-attR2-Venus and P_{Lac}::Venus-attR1-cat-ccdb-attR2, respectively. The pUC19 pBR322 origins were replaced with the oriS, repE and ParABC elements from pETcoco™-2, generating the low copy destination vectors pVS133 (C-terminal fusion) and pVS155 (N-terminal fusion). Two pairs of primers were designed for each division protein, corresponding to the N- or C-terminal fusion (primers 32-67, Appendix 1.3). Amplified products were purified and inserted into the attL-containing pENTR™ vector via the

Gateway® Cloning System. Correct transformants were confirmed via sequencing and then recombined with attR- and Venus-containing pVS133 (C-terminal fusion) or pVS155 (N-terminal fusion) destination vectors. The resulting linker for the C-terminal fusion was KGGRADPAFLYKVVDHLVILRLRGGL. The N-terminal fusion was linked via INKFVQKSRLRGRPLHQM.

1.9. FLP/FRT Recombination (λ Red)

The double deletion strains, Δ*slmA*Δ*zapA* and *ΔslmA*Δ*zapB*, were constructed from JW5641 (Δ*slmA*::kan) using lambda red technology (Datsenko & Wanner, 2000). First, JW5641 cells were made electro-competent (see Chapter 5-1.10), transformed with pCP20 and incubated at 30°C for ~36 hrs on LB agar containing carbenicillin. Resulting colonies were streaked on to LB agar and grown at 42°C overnight. Sensitivity to kanamycin and carbenicillin confirmed *slmA*::*frt*. Next, the kanamycin cassette of pKD4 was amplified with the primer sequences complimentary to the termini of *zapA* or *zapB* (Baba et al., 2006). Electro-competent *slmA*::*frt* cells containing pKD46 (induced with 0.2% Arabinose for 3hrs at 30C; competency > 10^9) were transformed with the appropriate gel-purified fragments and grown at 30C. Transformants were selected and regrown at 42C to cure pKD46. Sequencing and sensitivity to carbenicillin confirmed insertion and pKD46 removal, respectively.

1.10. Chemical Competent Cell Preparation

Chemically competent cells were prepared according to the Modified Calcium Chloride Method (Swords, 2003). Briefly, the desired cell line was grown in LB at 37°C to an $OD_{600} \approx 0.4\text{-}0.7$, put on ice for 10 min, pelleted at 4,100 rpm for 10 min at 4C, resuspended in 1/10-volume ice-cold TFB (10 mM MES (6.3), 45 mM $MnCl_2$, 10mM $CaCl_2$, 100 mM RbCl, 3 mM hexamine cobalt chloride) for 10 min on ice, pelleted, resuspended in 1/25-volume TFB and snap-frozen in 50 µl aliquots (~$10^{6\text{-}8}$ cfu per µg). When in-house preparations were not used, Subcloning Efficiency™ DH5α™ Competent Cells (Invitrogen, ~10^6 cfu per µg) was the preferred choice.

1.11. Electro-competent Cell Preparation

Electro-competent cells were prepared similar to chemically competent cells. Briefly, cells were grown in LB at 37°C to an $OD_{600} \approx 0.4\text{-}0.7$, put on ice for 15 min, pelleted at 4,100 rpm for 10 min at 4C, resuspended in equal volume ice-cold dH2O, pelleted, resuspended in 1/2-volume 10% glycerol (v/v), pelleted, resuspended in 1/50-volume 10% glycerol, pelleted, resuspended in 1/100-volume GYT (10% (v/v) glycerol, 0.125% (w/v) yeast extract, 0.25% (w/v) tryptone), and snap-frozen in 50 µl aliquots (~$10^{8\text{-}10}$ cfu per µg).

1.12. E. coli Transformation

All transformations were performed in 50 µl reactions and utilized 1 - 10 ng of DNA. Chemically competent cells were subjected to heat shock (42°C for 20-45 s), put on ice for 2 min, and then recovered at 37°C for 1-2 hr in 1 mL SOC media (2% (w/v) tryptone, 0.5% (w/v) yeast extract, 0.05% (w/v)

NaCl, 2.5 mM KCl, 10 mM $MgCl_2$, 20 mM glucose). Electrocompetent cells were electroporated in 2mm cuvettes (25 μF, 25 kV, 200 Ω) and recovered for 1 hr in SOC.

2. Protein Expression, Purification & Quantification

2.1. Purification of FtsZ and FtsZ-mEos2

pJB041 (P_{T7}::6xHis-Myc-TEV-FtsZ) and pJB040 (P_{T7}::6xHis-Myc-TEV-FtsZ-mEos2) were transformed into BL21(DE3)pLysS cells, grown in 50 mL LB at 37°C to OD_{600} ≈ 1.0, induced for 2 hr with 0.5 mM IPTG and collected by centrifugation at 4,100 rpm for 15 min at 4°C. Cells were then processed according to the ProBond™ native protocol (Invitrogen), which included a sonication step. After elution, the pooled sample was dialyzed in 1x ProBond Native Buffer and simultaneously incubated with 300ug of TEV Protease (a gift from D. Leahy). Cleavage of the 6xHis-Myc-TEV tag (Geisbrecht *et al.*, 2006) was confirmed via SDS-PAGE electrophoresis and the sample was reapplied to native ProBond to remove the His-tagged TEV Protease (Figure 5.1). Pooled samples were dialyzed against FtsZ Storage Buffer (20mM Tris-HCl, 250mM KCl, 1mM EDTA, 10% Glycerol) and stored at -80°C. Purified FtsZ was determined to be ~95% pure via Coomassie staining. A BCA assay was used to determine the concentration of purified FtsZ and FtsZ-mEos2.

2.2. BCA Protein Assay

FtsZ lacks most aromatic residues required for the standard A280 quantification methods. Consequently, indirect colorimetric tests, like the BCA assay, offer more consistent results (Lu & Erickson, 1998). We used the Pierce® BCA Protein Assay Kit (Thermo) as suggested for the 'Standard Test

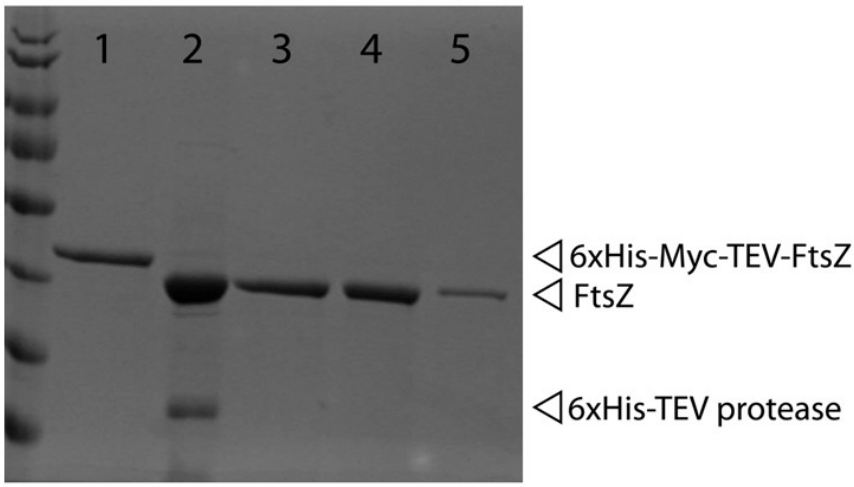

Figure 5.1 – Purification of FtsZ. Protein gel (4%) of FtsZ aliquots at different stages of purification: 1. 6xHis-Myc-TEV-FtsZ is purified from the His-column and dialyzed to remove Immidazole. 2. 6xHis-TEV protease is added and cleaves the N-terminal tag resulting in FtsZ with one amino acid scar. 3-5. FtsZ + 6xHis-TEV is reapplied to the His-column and purified FtsZ is found in the unbound fraction.

Tube Protocol'. Measurements were made in duplicate and the final protein concentration was determined given the FtsZ/BSA color ratio of 0.75.

2.3. *Determining the Relative Concentration of FtsZ and FtsZ-mEos2*

To assess the expression level of FtsZ-mEos2 under our PALM imaging condition, we determined the ratio of expressed FtsZ-mEos2 to total cellular FtsZ level (wt FtsZ + FtsZ-mEos2) for BL21(DE3)pLysS cells harboring the pET28-FtsZ-mEos2 plasmid. Cells were cultured in LB overnight at RT, and reinoculated in $M9^{+}$ the next morning. When the culture's OD_{600} reached ~0.4, 50 μM IPTG was added for 30 min. After

induction, cell culture was harvested by centrifugation and snap frozen. Thawed samples were boiled in 300µl of Western Sample Buffer (1ml 1x Laemmli Buffer, 700µl 3x Laemmli loading dye, 300µl 20% (w/v) SDS, 70 µl 1M DTT), separated on 10% SDS-PAGE gels (Bio-Rad), semi-dry transferred to Trans-blot nitrocellulose membranes (Bio-Rad) and blocked overnight in (5% Non-fat Milk, TBS (8.0), 0.1% (v/v) Tween-20) at RT. Primary incubation was with a affinity purified anti-FtsZ rabbit antibody (gift from H Erickson) diluted 1:1500 in TBS + Tween + 1% BSA for 120 min. Secondary incubation was with Goat anti-Rabbit HRP Conjugate (Bio-Rad) diluted 1:45,000 in TTBS for 60 min. Blots were treated with the Immun-Star WesternC^{TM} Chemiluminescence Kit (Bio-Rad) and signal was detected either by autoradiography film or a Typhoon 9410 variable mode imager. Autoradiography films were subsequently scanned using a Canon Scanner (CanoScan LiDE 30). Image analysis was performed using ImageJ (NIH). Blots were performed in duplicate. We found that on average (six repeats) FtsZ-mEos2 was expressed at 25 ± 7 % of total cellular FtsZ (Figure 5.2).

2.4. Determining the endogenous FtsZ concentration in E. coli cells

M9^{+} cultures of BW25113, Δ*zapA* and Δ*zapB* cells were grown at room temperature to mid-log phase ($0D_{600}$ ≈ 0.4), counted with a Petroff-Hausser counting chamber and then applied to SDS-PAGE. A 20-250 ng of purified FtsZ were included for comparison. After semi-dry transfer (25 V, 2 hr, 4°C) and blocking (5% (w/v) non-fat milk in TBS (8.0)), primary incubation was

performed for 1 hr at RT with an affinity purified anti-FtsZ rabbit antibody (gift from H. Erickson) diluted 1:3000 in TBS containing 0.05% Tween-20 and 1% BSA. Blots were washed. Secondary incubation was with Goat anti-rabbit HRP (Bio-Rad) diluted 1:45,000 in TBS + Tween-20 for 1 hr at RT. After washing 3 times with TBS+Tween for 10 min each, blots were developed using Immun-Star™ WesternC™ (Bio-Rad; 1-2 ml $blot^{-1}$, 5 min at RT) and imaged on a Typhoon Scanner (GE LifeSciences). Band intensities were determined using ImageJ and found to be similar at ~5,000 FtsZ molecules $cell^{-1}$ (Figure 5.3). A similar analysis was performed on BL21(DE3)pLysS and B/r A cells, and a similar concentration was measured (4100 ± 1700 FtsZ molecules $cell^{-1}$).

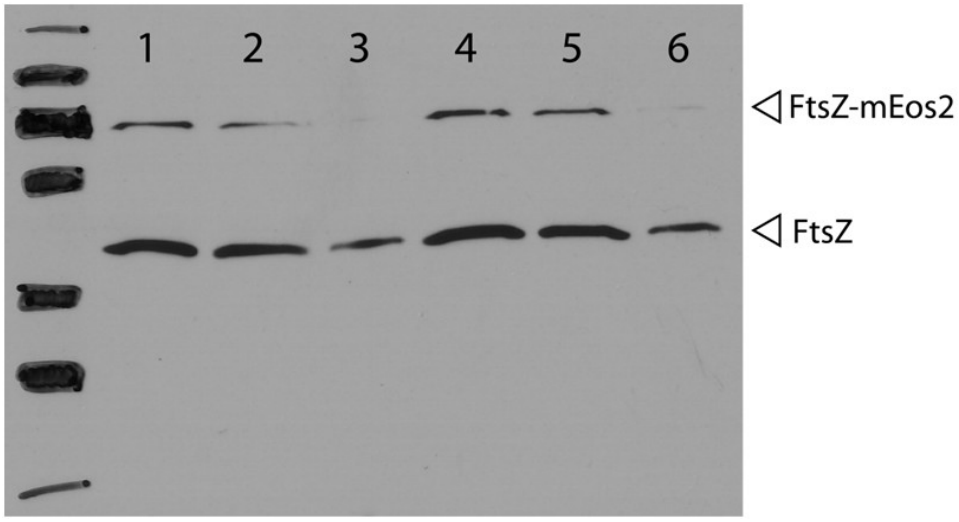

Figure 5.2 – Relative expression of FtsZ-mEos2:FtsZ$_{total}$. A scanned film displaying FtsZ and FtsZ-mEos2 bands for three separate cell densities (1,4; 2,5; 3,6) of BL21(DE3)pLysS cells harboring pET28-FtsZ-mEos2 in the absence (1-3) or presence (4-6) of 50 μM IPTG for 30 min. The protein ladder at the left (130, 100, 70, 55, 35, 25, 15 kDa) approximates the PageRuler™ Plus Prestained bands that were apparent on the corresponding blot. Under the induced condition, FtsZ-mEos2 was found to express at ~25% FtsZ$_{total}$ (FtsZ$_{wt}$ + FtsZ-mEos2).

3. Cell-based Assays

3.1. Growth Rate Determination

Growth rates were measured optically at 600 nm (OD_{600}) predominantly using a NanoDrop ND-1000 Spectrophotometer. Optical density measurements between 0.1-0.8 were fitted by an exponential in KaleidaGraph.

3.2. Complementation Assays

3.2.1. Complementation of JKD7/pKDA by FtsZ-mEos2

The chromosomal copy of *ftsZ* in JKD7 is disrupted by the insertion of a kanamycin cassette. Cell survival requires FtsZ expression from pKD3, a plasmid with a temperature-sensitive replication defect (Dai & Lutkenhaus, 1991). To examine if FtsZ-mEos2 was capable of complementing the depletion of $FtsZ_{wt}$, pJB004 was transformed into JKD7-2/pKD3 and a plate complementation assay was performed. Cells were grown to mid-log phase in LB containing 0-1.0 mM IPTG. Serial dilutions of the cultures were then plated on corresponding IPTG plates in duplicate and grown at permissive (30°C) and nonpermissive (42°C) temperatures. Numbers of colonies grown at 42°C and 30°C at each IPTG concentration were then compared. No growth was detected at 42°C, indicating that FtsZ-mEos2 was incapable of supporting growth. To date, all FtsZ-mEos2 constructs that we have tested have failed to compliment the depletion strain.

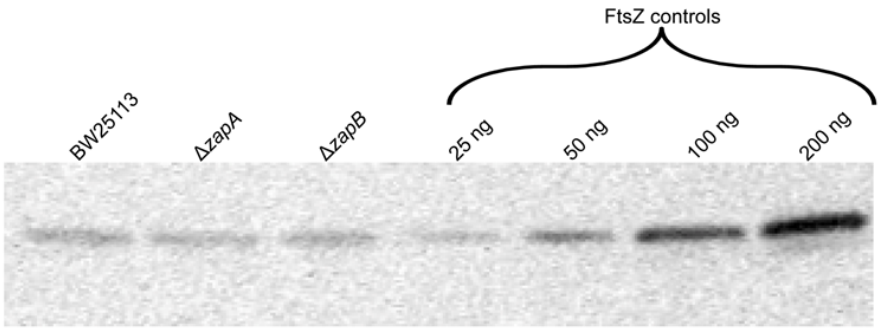

Strain	# FtsZ cell^{-1}
BW25113	5000 ± 1800
Δ*zapA*	5400 ± 1300
Δ*zapB*	4600 ± 1600

Figure 5.3 – FtsZ$_{wt}$ concentration of BW25113, Δ*zapA* and Δ*zapB* cells. A representative immunoblot of BW25113, Δ*zapA*, and Δ*zapB* cells stained with α-FtsZ. A series of purified FtsZ standards was included to quantitatively determine the number of FtsZ molecules in each cell. The corresponding table indicates the average expression level ± standard deviation of at least three independent experiments. The endogenous expression of FtsZ was determined to be similar ($p >> 0.05$) between the three strains (~5,000 FtsZ molecules per cell).

3.2.2. Determining the functionality of Venus constructs.

The midcell localization of the Venus constructs was assayed by fluorescence imaging. All pVS133 and pVS155 vectors were transformed into the wild-type *E. coli* strain B/r A (ATCC 12407), grown at room temperature in M9^{+} and imaged live in the absence of inducer. pVS133-FtsZ, pVS155-FtsA, pVS133-ZipA, pVS155-FtsQ, pVS155-FtsI, pVS155-FtsK, pVS155-FtsL, pVS155-FtsB, pVS133-FtsW, and pVS155-FtsN all to localized to midcell (Figure 3.19).

To further test for functionality, all pVS133 and pVS155 constructs were transformed into their respective temperature-sensitive or conditional-depletion (Dai et al., 1993, Pichoff & Lutkenhaus, 2002, Chen & Beckwith, 2001, Robichon *et al.*, 2008, Gonzalez et al., 2010, Mercer & Weiss, 2002, Buddelmeijer & Beckwith, 2004). All temperature-sensitive strains were grown in LB at 30°C overnight. The following day $M9^+$ was inoculated at 1:500 from the LB cultures and growth was continued at 30°C. Once mid-log phase was achieved, the cultures were diluted to an OD_{600} of 0.1, then further diluted to OD_{600} of 10^{-3} and 10^{-5}. The dilutions were plated on duplicate $M9^+$ plates, which were then grown at either 30°C or 42°C overnight. pVS155-FtsA, pVS155-FtsI, pVS133-FtsQ and pVS155-FtsQ were found to support growth at the non-permissive temperature (42°C, Figure 5.4A). No FtsZ or ZipA fusions were found to be capable of supporting division. Since pVS133-FtsQ failed to localize to midcell but was capable of supporting division, we speculate that Venus is either cleaved or fails to mature in the periplasm, consequently it was omitted from future experiments.

All conditional-depletion strains were grown in LB at 37°C overnight in the presence of 0.2% arabinose. The following day cultures were diluted 1:1,000 in LB+ arabinose. Once mid-log phase was achieved, 2 µl of a 1:100 and 1:10,000 dilution were plated on LB agar containing either 0.2% arabinose or 0.4% glucose. Both the pVS155 and pVS133 versions of FtsN, FtsW and FtsK, as well as pVS133-FtsL were found to support

growth under non-permissive conditions (0.4% glucose, Figure 5.4B). since pVS155-FtsW and pVS133-FtsK failed to localize distinctly to midcell, these fusions were discarded. Based on western analysis (data not shown), pVS155-FtsN was selected over the partially degraded pVS133-FtsN. The FtsB conditional mutants, which failed to be selected by growth on plates, were further assayed via growth in liquid culture (Figure 5.4C). From this analysis the pVS133-FtsB was determined to be functional.

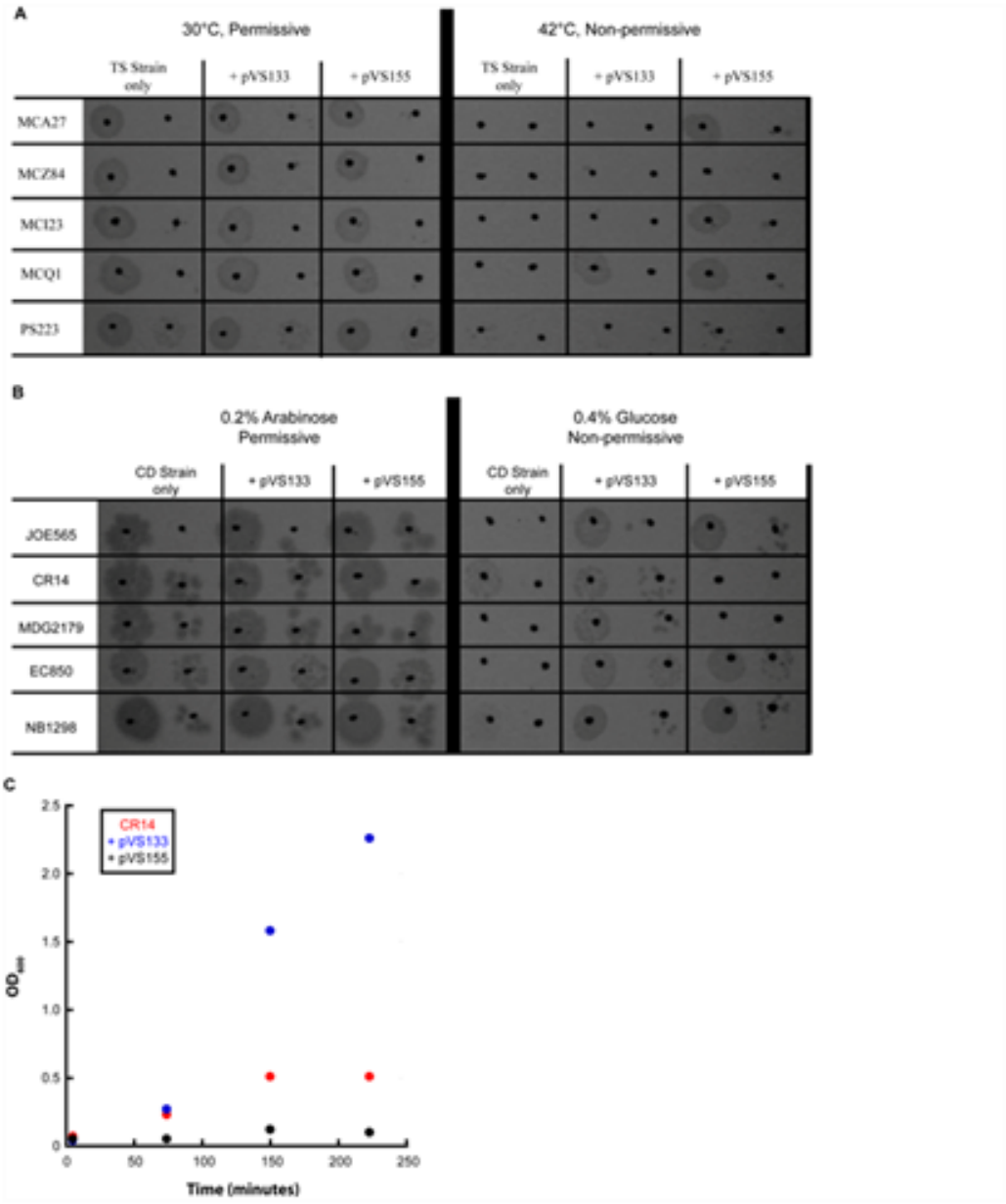

Figure 5.4 – Complementation assays of Venus fusions. N- (pVS155) or C-terminal (pVS133) Venus fusions were assayed for their ability to rescue the conditionally lethal phenotype of corresponding temperature-sensitive (A) or conditional-depletion (B) strains. The presence of growth under non-permissive conditions (42° or 0.4% glucose) indicates a fusion's ability to support growth in the absence of the wt protein. (C) The lethal phenotype of the FtsB depletion strain (CR14) failed to be detected on plates, however a clear distinction was observed by following the non-permissive growth of liquid cultures.

4. Microscopy

4.1. Cell Fixation of PALM and iPALM imaging

Cells were grown in $M9^{+}$ at RT and typically induced at $OD_{600} \approx 0.2$. Following the indicated induction times and outgrowth periods, cells ($OD_{600} \approx 0.4$) were applied 1:1 to a fixative solution with a final concentration of 1xPBS (7.4) and 4% (v/v) Formaldehyde (16% Paraformaldehyde, EM Grade, EMS). Fixation was carried out at RT for 45' and then washed 3 times with PBS (7.4). Final resuspensions were concentrated and stored in PBS at 4°C in the dark.

Formaldehyde was our preferred fixative because it penetrates the cytoplasm quickly. Another crosslinking agent, glutaraldehyde, is often used, but its penetration is slower and it often reacts to form cyclic compounds that increase the fluorescence background. At times a mixture of two (2.6% Formaldehyde, 0.005-0.05% Glutaraldehyde) was used, but no discernible change in dimension or morphology was observed.

4.2. Conventional Fluorescence Imaging

Prior to imaging, samples were washed with M9 minimal media [0.4% Glucose, supplemented with MEM Amino Acids] ($M9^{-}$), and sandwiched between a 3% agarose gel pad situated in a Bioptechs FCS2 chamber and a #1 glass coverslip (VWR). The assembled chamber was locked into a complimentary stage adaptor atop an inverted microscope (IX-81, Olympus) equipped with a 100x oil-immersion objective lens (Olympus) and a motorized

stage. Images were captured with one of two cooled EMCCD cameras (Andor Ixon DU888 or DU897E). Excitation was provided by a 488-nm Sapphire™ Laser (Coherent), an Innova Ion I-308 laser (Coherent), or a 561-nm Sapphire™ Laser (Coherent). Applied power densities typically ranged from of 0.5-1 kW cm^{-2}. MetaMorph software was used to interface between the various devices. A schematic depicting our general microscope setup is shown in Figure 5.5.

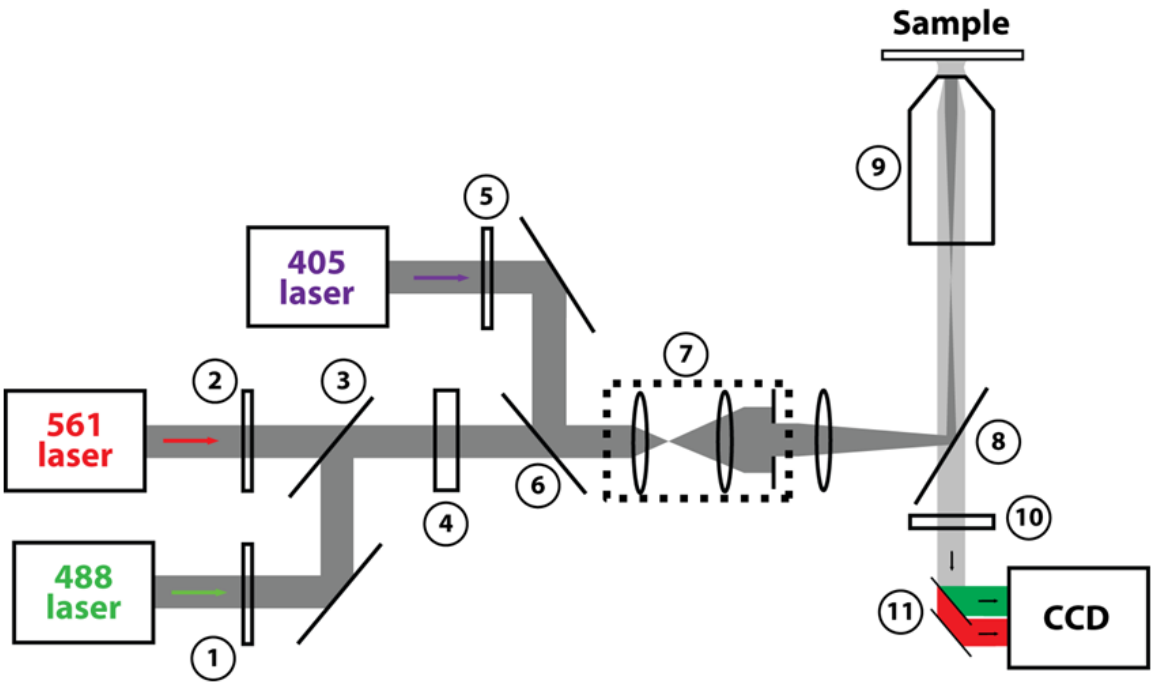

Figure 5.5 – Microscope setup. 1. Excitation Filter (488/25). 2. Excitation Filter (488/25). 3. Dichroic Filter. 4. Mechanical Shutter. 5. Neutral Density Filter (optional). 6. Dichroic Filter. 7. Adjustable Platform. 8. Dual-band Dichroic Filter. 9. Objective. 10. Dual-band Emission Filter. 11. Beam splitter (optional).

4.3. Time-lapse imaging

Time-lapse imaging was performed as described previously for conventional fluorescence imaging (Chapter 5-4.2) with the following exceptions. Lower excitation power densities (~10 W $cm^{-}2$) were applied to reduce photobleaching effects. Multiple frames of the same region were captured with a defined frequency. For long time-lapse movies (> 1 hr), frames were acquired every 5 min. These movies required an automated centralizing and focusing code prior to each acquisition to combat sample drift. Given the extended timeframe between acquisitions, multiple cells were imaged during a single experiment by iterating through 7-10 different positions.

4.4. Two-color Conventional Fluorescence Imaging

Two-color imaging was performed in the same way as described for conventional fluorescence imaging (Chapter 5-4.2) with the only difference being the integration of the Optosplit II (Andor) at position #11 in Figure 5.5. This device split the different excitation signals and projected them onto separate halves of the same CCD chip enabling simultaneous determination of two different fluorophores. Image overlay required a transformation step that was achieved by using the multi-colored emission spectrum of 100nm TetraSpeck™ beads. Fluorescence images of a single TetraSpeck bead, which was apparent in both channels, were acquired at various positions throughout the imaging region to generate a large dataset of control points.

Transformation of two-color data was calculated by the cp2tform function in MATLAB (The MathWorks, Inc., Natick, MA) using these control points. This type of global transformations resulted in ~10-nm registration error in our microscope setup.

Time-lapse imaging of two-color samples were performed as described above. Movie lengths were limited to short intervals because automated centralization and focusing were complicated by the split images.

4.5. Single Molecule Tracking (SMT)

Sample preparation is identical to the methods described above. All SMT imaging employed a 50 ms integration time and ~350 W cm^{-2} 561-nm excitation power density. A frame rate of 5 s^{-1} was achieved through the insertion of 150-ms dark intervals via an acousto-optic modulator. The applied 405-nm activation power was ~50 mW cm^{-2}. Imaging of individual regions never exceeded 5 min. Single molecules were detected via the ImageJ plugin Octane (Niu & Yu, 2008). All traces were inspected by eye and any trace suspected of containing multiple overlapping emitters was discarded. Mean squared displacements were calculated in MATLAB and only determined for traces lasting 10 frames or longer.

4.6. Immunofluorescence Imaging

Cells were fixed, permeabilized and labeled as described elsewhere (Potluri *et al.*, 2010) with the following exceptions. After growth in $M9^{+}$ at room temperature to OD_{600} ≈ 0.4 phase, cells were fixed in 2.6% Formaldehyde

and 0.05% Glutaraldehyde in PBS (7.4) at room temperature for 15 min. Cells were then washed twice in GTE (50mM Glucose, 20mM Tris-HCl (pH 7.5), 10mM EDTA) and resuspended in PBS. After permeabilization (0.1% Triton in PBS; 45' at RT) and partial lysis (100ug/mL + 5mM EDTA in PBS; 45' at RT) cells were blocked with PBS containing 10% Goat Serum (Sigma) at 37°C for 30 min. Affinity-purified FtsZ antibody (a gift from H. Erickson) and Goat anti-Rabbit IgG-FITC (Invitrogen) were applied at 1:250 and 1:500 in Blocking Buffer, respectively. After incubation with both antibodies, cells were washed 3-5 times with PBS containing 0.05% Tween-20. Cells were imaged as for conventional fluorescence on agarose gel pads. All centrifugations were at 4,500g for 5 min and cells were rotated continuously during incubations.

4.7. PALM Imaging

For all PALM studies, the expression of the construct was optimized to produce the highest labeling density while preventing overexpression artifacts, like protein aggregation of ZapB and multiple band morphology of FtsZ. FtsZ-mEos2 from pJB042 and mEos2-ZapA from pJB051 were induced with 20 μM IPTG for 2 hrs followed by a washing step and an additional 2-3 hr outgrowth at RT. ZapB-mEos2 from pJB045 was induced with 5 μM IPTG for 1 hr followed by a washing step and an additional 2-3 hr outgrowth. mEos2-MTS from pXY029 was induced with 15 μM IPTG for 2 hrs followed by 2 hr outgrowth.

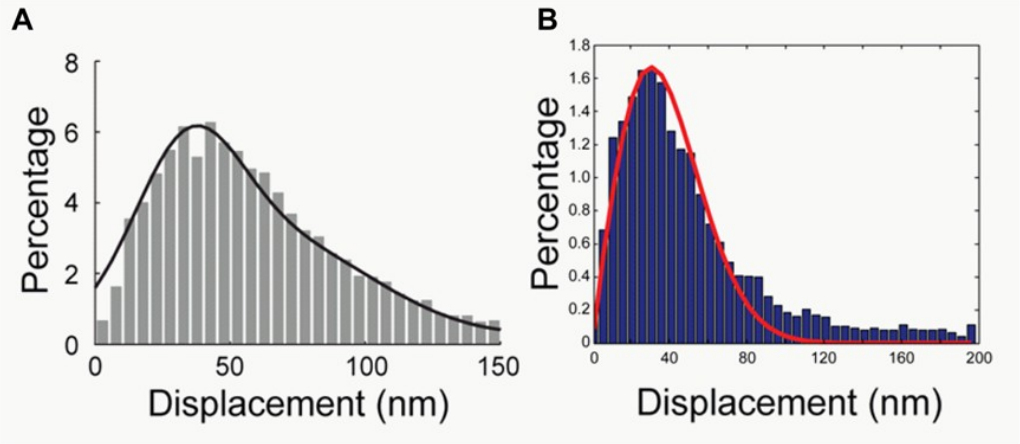

Figure 5.6 – PALM spatial resolution. The experimental spatial resolution can be obtained from the histogram of pair-wise displacement between repeat localizations of the same molecule. A fixed sample of wt cells expressing FtsZ-mEos2 from pET28-FtsZ-mEos2 or mEos2 from pJB044 were imaged under fixed cell PALM conditions (A) or live cell PALM conditions (B). The distribution in A is fitted (black line) to a polynomial with the peak identified at ~34 nm. The distribution in B is fitted (red line) to the following equation:

$$p(r) = \left(\frac{r}{2\sigma^2} e^{\frac{-r^2}{4\sigma^2}}\right)$$

where *p(r)* is probability of observing displacement, *r*, in two dimensions and *σ* is the mean standard deviation in localized spot positions (Coltharp *et al.*, 2012). The achieved spatial resolution is calculated as the full width half maximum (FWHM) calculated from the fitted *σ* (FWHM = *2.35σ*). The fitted spatial resolution of this sample under live-cell PALM conditions is 52 ± 2 nm (*σ* = 22 ± 1 nm).

Live-cell PALM imaging was achieved over the course of 30 s using a frame rate of 100 s^{-1}, a 561-nm excitation of ~1 kW cm^{-2} and continuous 405-nm activation at ~5 W cm^{-2}. A resolution of ~50 nm (Figure 5.6) was achieved. Fiducial markers were not used for live-cell PALM imaging, as sample drift during the 30 s of acquisition was undetectable.

Fixed-cell PALM imaging typically required the acquisition of ~20,000 frames at rate of 33 s^{-1}. Since diffusive, cytoplasmic molecules that were not apparent in live cells are detected in fixed-cell imaging, the 405-nm activation power was reduced. Excitation power remained similar. Gold beads (50nm, Microspheres-Nanospheres) were used as fiducial markers to calibrate for the sample drift resulting from the extended acquisition time.

Total internal reflection PALM (TIR-PALM) on fixed or live cells was performed in the same manner as the corresponding epi-PALM described above. The only difference was that the incident angle was adjusted by translation of the adjustable platform (Figure 5.5 #7) perpendicular to the light path. See Buss et al., 2013b for a more thorough explanation .

4.8. Two-color PALM (2C-PALM) Imaging

2C-PALM was performed in the same general manner as the corresponding epi-PALM methods described above. The major difference being the integration of the OptoSplit II (Andor). Dronpa-PAmCherry1 is the only two-color fluorophore set that has been successful in our hands, but we have not exhaustively tested the other combinations. We found Dronpa sensitive to the 405-nm activation power required for PAmCherry1 detection. To image both fluorophores in the same cell, 1,500 frames at a rate of 100 s-1 were acquired with 405-nm activation at ~500 mW cm^{-2} followed by a second acquisition at ~5 W cm^{-2}. Although both fluorophores are detected in both acquisitions, Dronpa is predominantly present in the first, while

PAmCherry1 the second. To generate the two-color PALM images (Figure 4.12-14), images were first constructed as described below (Chapter 5-5.5) and then transformed as described above (Chapter 5-4.4).

4.9. STORM Imaging

STORM imaging employs the same immunofluorescence protocol described above (Chapter 5-4.6) with the following exceptions. After primary incubation and washing, Alexa Fluor® 568 Goat Anti-Rabbit IgG (Invitrogen) was applied at 1:1,000 for 30-60 min at RT in the dark. Cells were washed extensively (5-10 times) with PBS (7.4) containing 0.05% Tween-20 and then resuspended in a 'GLOX and thiol' imaging buffer (50 mM Tris (pH 8.0), 10 mM NaCl, 0.5 mg ml^{-1} glucose oxidase (Sigma-Aldrich), 40 µg ml^{-1} catalase (Roche), 10% (w/v) glucose and 10 mM MEA (Fluka)) (Dempsey *et al.*, 2011). Gold beads (50 nm, Microspheres-Nanospheres) were included (1:10 dilution) to calibrate for sample drift and the solution was applied to an agarose gel pad. Immediately prior to imaging additional imaging buffer was perfused into the assembled imaging chamber. Activation and excitation of Alexa Fluor® 568 was achieved solely through exposure to a 561-nm Sapphire™ laser at a power density of ~1 kW cm^{-2}. Following an initial bleaching step, a total of 9,000 frames were acquired at a frame rate of 50 s^{-1}. Spot identification, drift calibration and image construction were performed as described below (Chapter 5-5.4-5). The STORM 'ensemble' image illustrates the fluorescence signal prior to bleaching.

4.10. iPALM

Wt cells expressing FtsZ-mEos2 (pJB042), mEos2-ZapA (pJB051), ZapB-mEos2 (pJB045) and mEos2-MTS (pXY029) were grown and induced as described above (Chapter 5-4.7). A the end of the outgrowth period, cells were fixed in 4% formaldehyde in PBS (7.4) for 45' at room temperature, washed two times with equal volume PBS and resuspended in 500 µL PBS to an OD_{600} ≈ 2.0. Fixed samples were stored in the dark at 4°C for no more than 5 days prior to imaging.

iPALM sample preparation was performed as described before (Shtengel et al., 2009, Kanchanawong et al., 2010) with the following exceptions. Gold-embedded coverslips were coated with 0.2% Poly-L-Lysine (Ted Pella) for 20 min, washed with PBS, and gently dried with purified air. Alexa Fluor® 568 was diluted (~2e-9) in PBS and applied to the coverslip for 15 min, followed by similar washing and drying. Samples were subsequently applied in a similar fashion. Each image is the product of 45,000-100,000 frames. The average spatial resolution obtained for the x-, y- and z-axes was 21 nm, 23 nm, and 17 nm respectively.

Three replicate samples were performed for each fusion protein on different days (Figure 5.7). The average standard deviation in Z-position for each protein across the different days was ~10 nm. Given the low degree of variability across the samples, the datasets were collated and the reported errors are representative of the total sample. Data were processed via the

custom PeakSelector v9.3 software. Extracted coordinates and fitting errors were further analyzed in MATLAB.

4.11. Scanning Electron Microscopy

BW25113, Δ*zapA*, and Δ*zapB* cells were grown up to mid-log phase in $M9^+$ at RT, concentrated by centrifugation, washed with $M9^+$ and then applied either directly to Poly-L-lysine(PLL)-treated 18 mm coverslips (0.01% PLL for 10 min, 5 min dH_20 wash) or passed through 13mm 0.2 µm Polypropylene Membrane Filters (Sterlitech). Coverslips and filters were then submerged in fixative (2% Formaldehyde, 2% Glutaraldehyde, 0.08 M Sorenson's Phosphate Buffer (SPB), 3mM $MgCl_2$, pH = 7.2) for at least 1 hr at RT and then washed with PBS (7.4). Samples were then post-fixed in 0.8% potassium ferrocyanide reduced 1% OsO4 in 0.0 8M SPB and 3 mM MgCl2 for 1 hr on ice in the dark. Following a rinse in 0.08 M Maleate Buffer (3 x 5 min), samples were placed in 2% Uranyl Acetate in Maleate for 1 hr at RT in the dark. En-bloc staining was followed by dehydration through a graded series of ethanol to 100% ethanol, then passed through a 1:1 solution of 100% ethanol and hexamethyldisiloxane (HMDS), and finally pure HMDS. Coverslips were then placed in a desiccator overnight to dry. The next day, coverslips were attached to aluminum stubs via carbon sticky tabs (Ted Pella), and coated with 20 nm AuPd via a Denton Vacuum Desk II sputter coater. Stubs were viewed and digital images captured on a Leo 1540 FESEM operating at 1 kV.

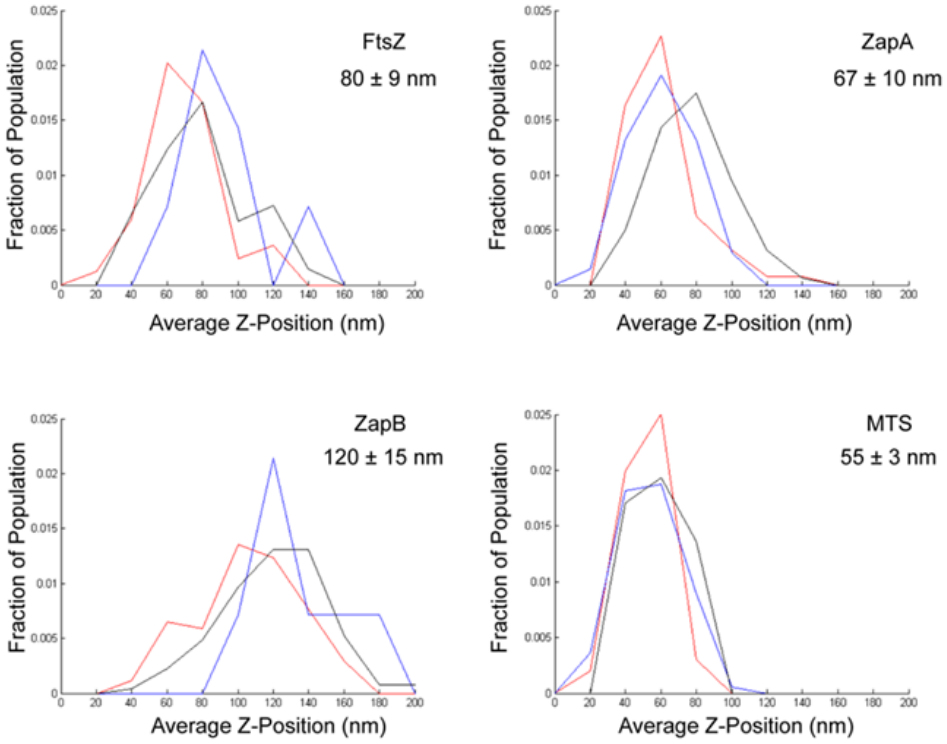

Figure 5.7 – Comparison of iPALM Z-position measurements. The average Z-position distribution for three replicate samples (red, blue, black) are shown for FtsZ-mEos2 (top, left), mEos2-ZapA (top, right), ZapB-mEos2 (bottom, left) and mEos2-MTS (bottom, right). Mean ± standard deviation (n = 3).

5. Quantitative Image Analyses

5.1. Cell length and Growth Analysis

Cell length measurements (ex. Figure 3.16E) were made on bright-field images by custom coding in MATLAB that identified the cell outline through contrast differences. The regionprops function (MATLAB) was used to identify the major axis length which provided an approximation of the cell length that could be used as a relative comparison between populations.

Division times (ex. Figure 3.2) were determined empirically by visual inspection of cell morphology and midcell fluorescence signal in time-lapse movies. Only actively dividing cells were assayed, as division times were determined by the amount of time separating two constriction events.

5.2. Arrival Time Determination

The fraction of population, F(x), displaying midcell fluorescence was determined by eye and used to calculate the arrival time (t_{arr}) relative to the cell cycle of each strain (Den Blaauwen et al., 1999), using:

$$t_{arr} = 1 - \frac{\ln[F(x) + 1}{\ln 2}$$

The arrival times presented in Figure 3.20 were generated from three independent experiments, each including more than 100 cells.

5.3. Integrated Intensity Determination

Similar to cell length measurements, integrated intensity determination required identification of the cell outline. Once identified, the pixel values within the outlined regions were summed.

For correlating the integrated intensity of mEos2 to FtsZ-mEos2 expression level, B/r A cells containing pJB004 were grown in M9 at 25°C. The overnight culture was diluted 1:500 in 50 mL of $M9^+$ at 25°C and grown to an $OD_{600} \approx 0.2$, at which time the culture was induced with 15 μM IPTG for 2 hrs. Cells were then collected via centrifugation and resuspended in $M9^+$. This process was repeated once more to remove the inducer. Cells were then returned to growth at RT and processed at 30 min intervals for a total of 4hrs. The culture was diluted as needed to maintain steady-state growth. Each time point was then processed for live-cell fluorescence imaging and immunoblotting.

Western samples were processed as described above (Chapter 5-2.3). The concentration of FtsZ-mEos2 was determined relative to that of $FtsZ_{wt}$. A large sample size of live cells (N > 100) were analyzed at each time point via ensemble (green channel) epi-fluorescence. Assuming the endogenous wt FtsZ expression level is independent of the expressed FtsZ-mEos2 level, the relative expression level of FtsZ-mEos2 over $FtsZ_{wt}$ level determined by immunoblotting could then be converted to the total cellular FtsZ level (FtsZ-mEos2 + FtsZ) and correlated with the average fluorescence intensity level of the same cell population at each time point (Figure 2.7A). Establishing such a correlation between the average total FtsZ expression level and the

corresponding average fluorescence intensity level, we then used the integrated fluorescence intensity of individual cells as an indicator for the expression level of total cellular FtsZ level in that particular cell (WTU).

5.4. Single Molecule Identification

Our molecular localization program was written in MATLAB. Individual FtsZ-mEo2 molecules in the 561-nm channel were identified by subtracting an empirically determined intensity threshold that is calculated from the running average (window = 150 frames) of maximum intensity values across the PALM image stack. All regions that had more than 3 adjacent pixels greater than the applied threshold were considered to be FtsZ-mEos2 molecules and were fit using a nonlinear least squares algorithm (MATLAB function lsqcurvefit) to a two-dimensional Gaussian function, which is an approximation of the point spread function (PSF):

$$PSF(x,y) = B + A \times \exp\{-[(x-x_0)^2 + (y-y_0)^2]/2 \times s^2\}$$

where (x_0, y_0) is the coordinate of the centroid position of the molecule, A is the fluorescence intensity at the centroid position, B is the background intensity, and s is the standard deviation of the Gaussian function (Thompson *et al.*, 2002). The fitted parameters A, B, x_0, y_0 and s were recorded for single FtsZ-mEos2 molecules.

Drift calibration for fixed cell PALM required the single molecule detection of gold beads in each PALM image. Spot identification of gold

beads was performed exactly as described above and the displacement between centroid positions relative to frame #1 was determined. This displacement was then applied to each identified molecule.

5.5. *Localization Precision.*

The theoretical localization precision is given by:

$$\sigma_{x,y}^2 = \frac{s^2 + a^2/12}{N} + \frac{8\pi s^4 b^2}{a^2 N^2}$$

where *s* is the standard deviation of the PSF, *α* is the pixel size in the image, *N* is the total number of photons measured from the molecule, and *b* is the background noise (McKinney et al., 2009). The number of photons a molecule emitted was converted from the EMCCD detector's counts according to manufacturer's specifications and camera settings. The pixel size of the camera is 16 μm, corresponding to an effective pixel size of 167 nm with a 96x magnification (60x from the objective and 1.6x from the microscope slider). We measured the average photon number emitted from a single FtsZ-mEos2 molecule is 910 ± 690 photons (Figure 5.8A). Based on this formula, we calculated that our localization precision for all plotted FtsZ-mEos2 molecules was 14 ± 6 nm. These numbers agree well with published values of mEos2 (McKinney et al., 2009).

5.6. *Image Construction*

PALM images were rendered by custom coding in MATLAB with pixel size set at 15 nm. The position of each single FtsZ-mEos2 molecule in each

image frame of the PALM sequence was determined using the algorithm described above (Chapter 5-5.4). For fixed cells, if two molecules in successive frames were located less than three PALM pixels (45 nm) apart, we considered them to be the same molecule and the position of the molecule was recorded only once and the rest discarded. Only molecules with localization precisions smaller than 25nm (fixed cell, Figure 5.8B) or 40nm (live cell) were plotted in the final PALM images. For standard PALM images, each molecule was plotted as a unit-area Gaussian function with *s* equal to the localization precision (Betzig et al., 2006). All Gaussian profiles were then superimposed together to generate the corresponding PALM image. For Density PALM images, each molecule is plotted without the Gaussian profile such that each molecule is assigned to a single pixel corresponding to its centroid position. In this way, the intensity of each pixel represents the total number of molecules detected in that pixel. ImageJ software (NIH) was used to apply pseudocolor using the 'red-hot' lookup table.

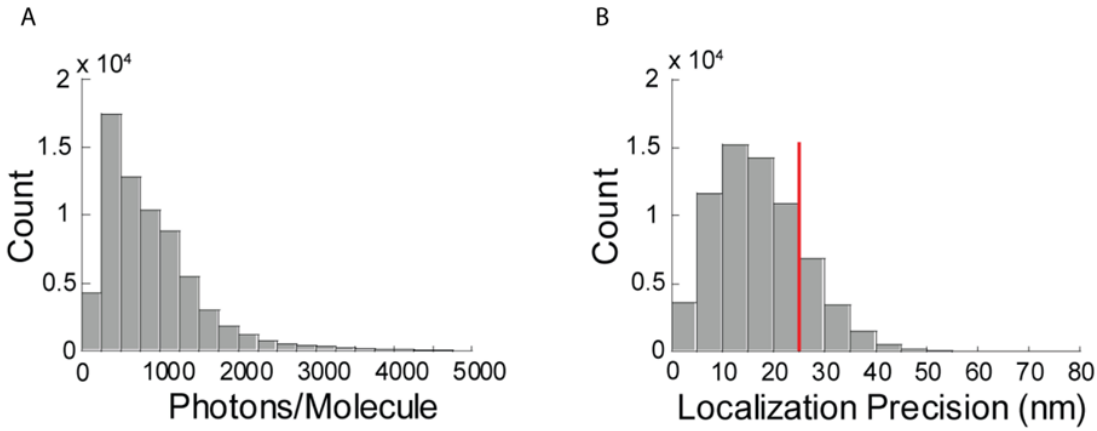

Figure 5.8 – Localization precision of fixed cell PALM. A. Histogram of total number of photons detected for all the FtsZ-mEos2 molecules detected in fixed B/r A and BL21 samples (mean = 910 photons). B. Histogram of all the localization precisions for all the molecules detected from both the B/r A and BL21(DE3)pLysS fixed samples (mean = 17 nm), As indicated by the red line, only molecules possessing a localization precision of 25nm or better were used to construct fixed PALM images.

5.7. *Spatial resolution of FtsZ-mEos2 in fixed-cell PALM*

Spatial resolution determines how far away two objects need to be in order to be spatially resolved from each other. We computed the theoretical spatial resolution in our PALM imaging using the following two methods. First, for single molecules that are localized to a precision of *n* nanometers, the theoretical spatial resolution is equal to the full width at half maximum (FWHM) of the replotted PSF, which is calculated by the formula FWHM=2.35*n*. Therefore, given the average localization precision determined for FtsZ-mEos2 in fixed-cell PALM was 14 nm, the minimal distance between two single FtsZ-mEos2 molecules needed to be 33 nm for them to be resolved. Second, for protofilaments that consist of a mixture of wild-type

FtsZ and FtsZ-mEos2 molecules, the Nyquist criterion states that the ability to distinguish two such protofilaments on a 2D PALM image is directly related to the labeling density of the protofilaments such that

$$d \geq \frac{2}{\sqrt{\rho}}$$

where d is the desired spatial resolution in nm and ρ is the density of FtsZ-mEos2 molecules that can be resolved to d or better in molecules nm^{-2} (Betzig et al., 2006, Shannon, 1949, Greenfield *et al.*, 2009, Shroff *et al.*, 2008b) We measured the average labeling density for each cell by dividing the total number of detected FtsZ-mEos2 molecules by the corresponding occupied area in the PALM image (ranged from 0.003 to 0.015 molecules nm^{-2}), and calculated an average spatial resolution to be 28 ± 7 nm. The average spatial resolution defined by Nyquist criterion is indistinguishable from the one calculated from the localization precision of single FtsZ-mEos2 molecules, indicating that here the spatial resolution was not limited by the labeling density of the Z-ring.

The above value is the upper bound of achievable spatial resolution. We calculated the actual spatial resolution by determining the displacement distribution of single FtsZ-mEos2 molecules that lasted more than one frame in PALM imaging sequences. If the displacement between the fitted positions of two molecules in two consecutive frames was less than 167 nm, we treated these two molecules as the same molecule. Therefore, the positions generated by the same molecule in consecutive frames reflected the error in the position determination of single molecules, i.e., the actual spatial

resolution of PALM imaging. We plotted the distribution of the displacement of all these molecules and found the distribution peaked at ~35 nm for fixed cell PALM (Figure 5.6A) and ~50nm for live-cell PALM (Figure 5.6B).

5.8. *PALM Image Analysis*

5.8.1. *Ring Width, Diameter, and Density*

Band width and diameter were measured from Gaussian-plotted PALM images. Each image was rotated by eye (Figure 5.9A), the midcell region was cropped out, and a cumulative intensity profile was generated along the cell's long axis (Figure 5.9B) and short axis (Figure 5.9C). The profile along the long axis was fit to a Gaussian distribution and the full width half maximum (FWHM) of the fitted distribution was recorded as the ring width (Figure 5.9B). The full length of the intensity profile along the short axis (Figure 5.9C, Table 3. 1) or the length of the region bounded by 5% of the maximum intensity value (Table 4.1) were defined as the ring diameter.

Density measurements like ring occupancy were determined on Density PALM images, where the intensity of each pixel is equal to the number of molecules localized to that pixel. The midcell structure was cropped out manually by drawing a polygon. The number of pixels, number of molecules, number of pixels containing molecules and maximum number of molecules per pixel was determined within this user-defined area.

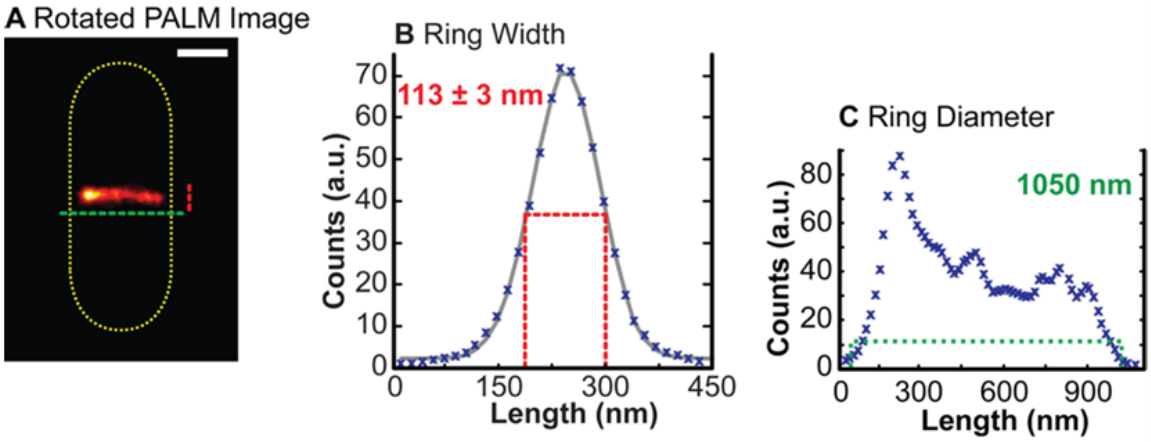

Figure 5.9 – PALM measurements. (A) A PALM image showing schematic representations of Z-ring width (red) and Z-ring diameter (green). (B) Ring width is calculated by fitting the projected intensity profile (blue X's) along the long axis of the cell with a Gaussian function (gray line) and then determining the FWHM (red dotted line). Here, the ring width was determined to be 113nm. (C) Ring diameter is determined by first projecting the intensity profile along the short axis of the cell and then calculating the full length (green dotted line) of the intensity profile above zero. The diameter of the Z-ring was determined to be 1050 nm.

5.8.2. *Simulation of Helices with Variable Length and Pitch*

Prior to this work, earlier studies observed FtsZ (Peters, 2007, Thanedar & Margolin, 2004) and several other proteins (Shih et al., 2003, Vats *et al.*, 2009) adopt helical structures. Consequently, the nonplanar structures illustrated in our PALM images were initially interpreted as contiguous helical structures whose apparent discontinuity resulted from a combination of PALM's stochastic activation and our low labeling density. The methods we used to model helices of variable length and pitch and render them as 2D projections is described below.

Figure 5.10A depicts a helix with radius, *R,* and constant pitch, *l,* wrapping around the cylindrical surface of a typical *E. coli* cell 1.5 turns. Based on our single cell measurements, *R* typically equals 0.5 μm. When projected onto a 2D imaging plane along the long axis of the cell (Figure 5.10B), this 3D helix results in two parallel lines (red solid lines) that are separated by a distance equal to the pitch (*l)* and are tilted at an angle (*α)* with respect to the short axis of the cell. *α* is directly related to *l* in that $\tan(\alpha) = l/4R$. The larger the tilting angle, the larger the helical pitch, and hence the wider the separation between the two parallel bands. Therefore, by measuring *α* from the 2D PALM image we can calculate what the pitch of the helix should be (*l'*). We then compare this calculated pitch (*l'*) with the measured separation between the two parallel bands (*l)* to check if the two bands indeed result from the projection of a helix with constant pitch (*l)*.

To find out if a helix with variable pitch could give rise to the observed pattern of parallel bands for cells shown in Figure 2.5D and 2.6HE, we modeled such a helix inside the cell and simulated the resulting 2D PALM images using custom code in MATLAB. A helix with a constant pitch along the cell's inner surface would turn into a straight line if the cell is unrolled along its long axis (Figure 5.10C). This straight line can be described by the equation $y' = (l / 2\pi R) \cdot x'$. The angle of the line with respect to the short axis (*θ)* of the cell is related to the pitch in the form of $\tan(\theta) = l / 2\pi R$. If *θ* is equal to zero, the line will be perpendicular to the

cell's long axis, leading to a ring if the cell is rolled up. If θ is greater than zero and varies along the length, the resulting helix will have variable pitch, leading to a curve instead of a straight line on the flattened cell surface. Therefore, we used a curve that consists of short straight lines connected by short smooth arcs to model the helix. The length and pitch of each segment and the length and diameter of the cell were measured from the corresponding PALM image.

After generating such a helix model inside the cell, we simulated the resulting PALM image of such a structure. To simplify the simulation, we assumed that the helix was a single layer flat ribbon that was seven FtsZ protofilaments thick (Stricker et al., 2002) [Note that here we focus on the conformation of the Z-ring so the arrangement of protofilaments inside the Z-ring is of less importance]. The spacing between each neighboring filaments was 9 nm and each FtsZ monomer in the filament was spaced 5 nm from the next one in the longitudinal direction (Li et al., 2007). We then simulated the PALM imaging process by randomly "activating" FtsZ molecules inside the helix one at a time and projected its image along the long axis of the cell onto a 2D plane. Specifically, an FtsZ molecule with a coordinate of (x, y, z) inside the helix was randomly selected and its projected position (x', y') on the 2D plane was determined. Next, we simulated the fluorescence image of this molecule on the 2D plane using a Gaussian PSF function. This PSF function was then modified by taking into account the following factors: (1) the number of photons described by

this PSF followed a normal distribution; (2) the width of the PSF (defocusing effect) was calculated using the distance of the FtsZ molecule away from the focal plane of the objective lens (van Oijen *et al.*, 1998); and (3) background noise, including photon shot noise estimated based on real imaging conditions, was added to the PSF. We then fit the simulated fluorescence image of the molecule on the 2D plane using the molecular localization algorithm, generating the corresponding centroid position (x", y") and the associated standard deviation σ_{xy} of the molecule. Using the σ_{xy} and simulated photon numbers we calculated the localization precision of this molecule and plotted its image as a unit-Gaussian PSF with its standard deviation equal to the localization precision. This process was then repeated thousands of times until ~25% of FtsZ molecules inside the helical structure were selected and localized. The final resulting image, the simulated PALM image, was then compared with the original image to verify if the separation and tilting angle of the parallel bands matched those measured from the original image. If not, θ was varied and the above process repeated until the resulting simulated PALM matched reasonably well with the original PALM image. Using this procedure we simulated PALM images for cells shown in Figure 2.5A-D. The corresponding helices on a flattened cell surfaces for these cells were shown in Figure 5.10Di-iv.

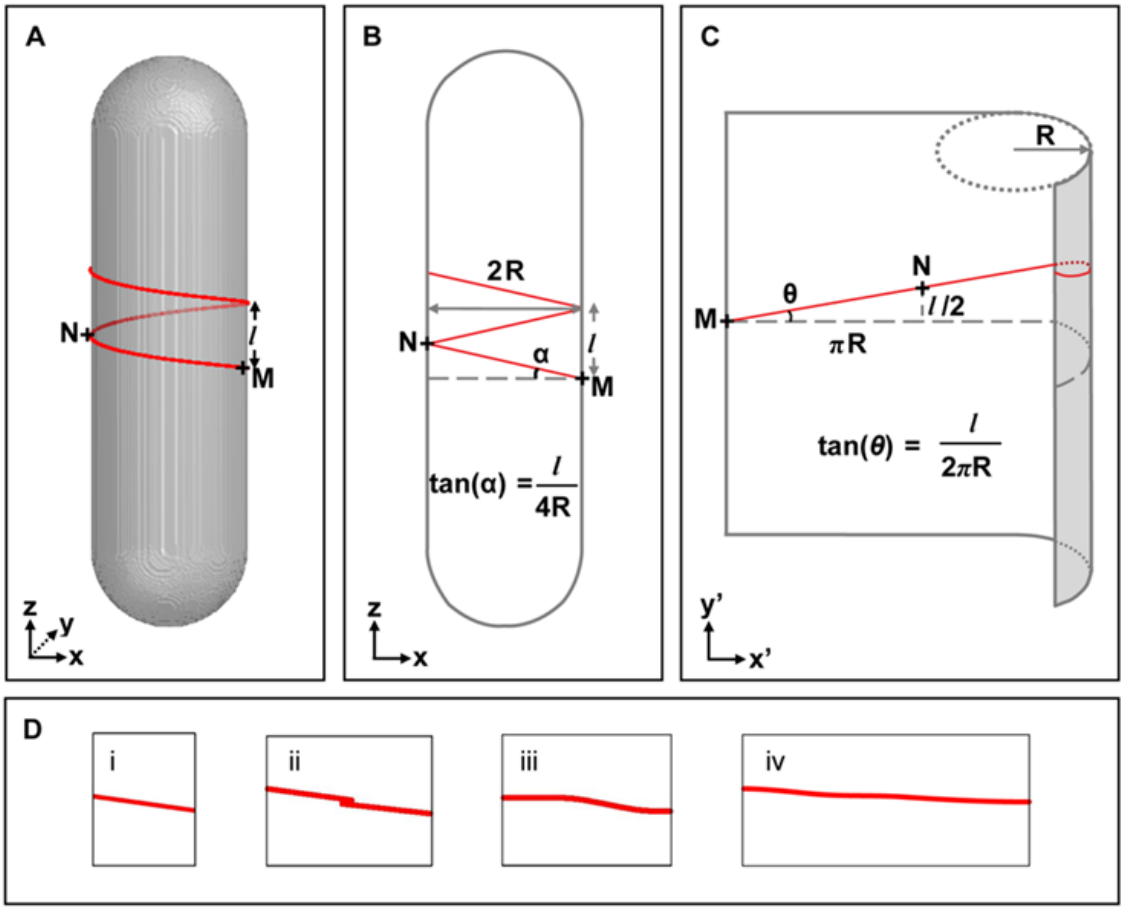

Figure 5.10 – Modeling the FtsZ-ring as a helix. A. A helix (red) is modeled along the surface of a 3D cell. B. The helix in A is projected onto a 2D plane. C. The helix in A becomes a straight line with an angle of θ when the cell is unrolled along its long axis. R is the radius of the cell, l is the pitch of the helix, and α is the tilting angle between line MN and the short axis of the cell, which can be measured from the projected image of the helix in A. D. Helices with variable pitches and lengths on flattened cell surfaces used to generate the helix models shown in Figure 2.5. for cells A-D, respectively.

5.8.3. *Cluster Determination and Analysis*

Analysis of TIR-PALM images was performed using custom MATLAB software. Spot identification and plotting was carried out as described above. For all cells, a single empirically determined threshold

(0.00045) was applied as a percentage of the total integrated signal of the Gaussian-plotted PALM image (Figure 5.11). Groups of more than 5 adjacent pixels above the threshold were identified as clusters. The coordinates of the cluster were used to identify the localizations within those regions. Number of molecules per cluster was calculated from the number of localizations using the conversion factor determined in Figure 5.12. The regionprops function of MATLAB® was used to identify area, centroid position, major axis length, minor axis length and orientation of each cluster (Figure 3.11A). The cellular pole positions were determined by eye and used to calculate cell length, cellular axes and midcell plane. Cluster orientations are reported as absolute values relative to the midcell plane, where 0° indicates a parallel alignment. The significant deviation away from 0° observed for wt structures is likely due to the error associated with cell pole selection as well as the irregularity in cluster shape. Midcell position, cellular orientation and cluster centroid position were used to calculate the displacement of clusters away from the midcell plane.

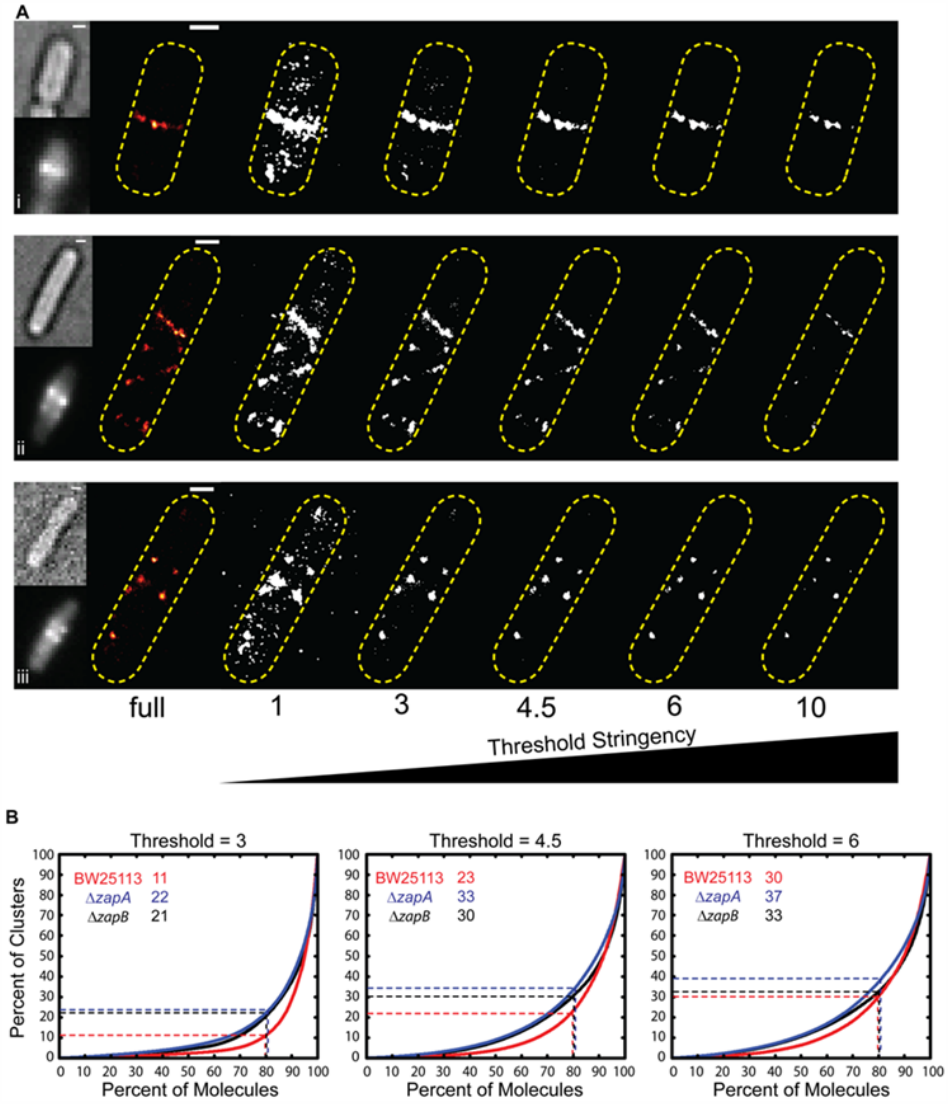

Figure 5.11 – Determining cluster threshold. (A) A series of thresholds (1-10x10^{-4} AU) were applied to the constructed TIR-PALM images of BW25113 (i), Δ*zapA* (ii) and Δ*zapB* (iii) cells. The images in Ai-iii are presented as a brightfield image atop an ensemble fluorescence image, adjacent to a PALM image followed by a series of thresholded PALM images displayed in binary. (B) To compare cluster compositions, the cumulative sum distributions for the number of molecules per cluster were plotted for thresholds 3, 4.5 and 6. The dotted lines indicate the percent of clusters that contain 80% of the detected molecules. All thresholds suggest that a small fraction (< 37%) of clusters contain a large fraction (80%) of the detected molecules. Scale Bars, 500 nm.

5.8.4. *Z-Depth and Radial Thickness*

For each iPALM image of a non-constricting cell the region most proximal to the coverslip was selected. This region was small so as to not introduce significant curvature which would affect our measurements along the Z-axis. The Z-positions of every molecule localized within the selected region were plotted as a histogram and fit to a Gaussian function. The extracted mean value was identified as the average Z-position of the structure and the FWHM of the Gaussian distribution was identified as the structure's radial thickness (Figure 4.16).

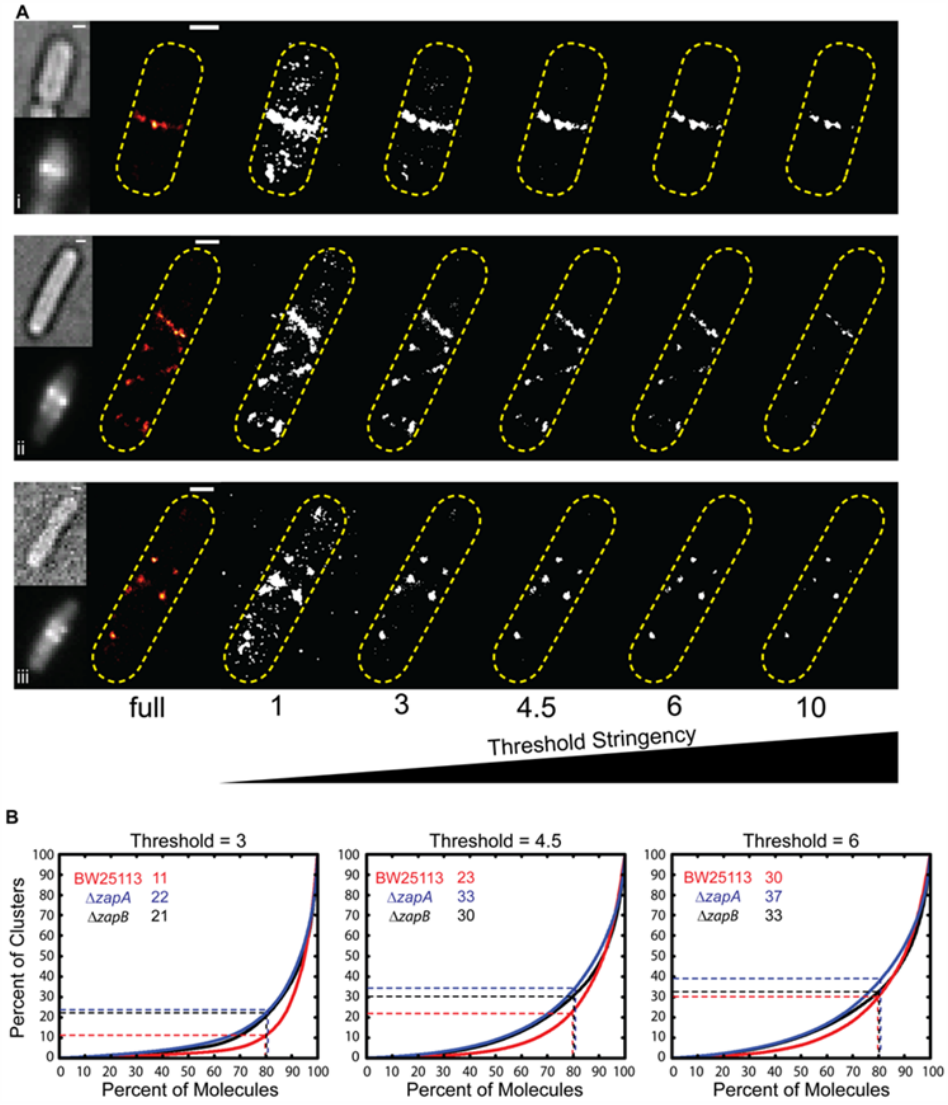

Figure 5.11 – Determining cluster threshold. (A) A series of thresholds (1-10x10^{-4} AU) were applied to the constructed TIR-PALM images of BW25113 (i), Δ*zapA* (ii) and Δ*zapB* (iii) cells. The images in Ai-iii are presented as a brightfield image atop an ensemble fluorescence image, adjacent to a PALM image followed by a series of thresholded PALM images displayed in binary. (B) To compare cluster compositions, the cumulative sum distributions for the number of molecules per cluster were plotted for thresholds 3, 4.5 and 6. The dotted lines indicate the percent of clusters that contain 80% of the detected molecules. All thresholds suggest that a small fraction (< 37%) of clusters contain a large fraction (80%) of the detected molecules. Scale Bars, 500 nm.

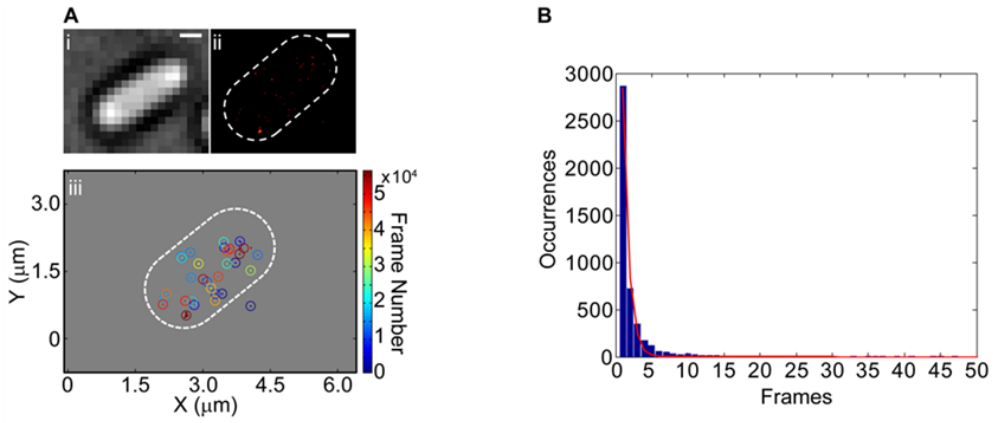

Figure 5.12 – Characterization of localizations per molecule. (A) Representative images of a fixed *E. coli* BW25113 cell expressing mEos2 from pJB044. Brightfield (i) and PALM (ii) images are shown for comparison. The cell outline is represented by the white, dotted line. Localizations from the 47 detected mEos2 molecules are shown in (iii) as small, filled circles, which are colored by detection time. Localizations from the same molecule are enclosed in a larger, open circle, which is colored by the mean detection time of all enclosed localizations. Uninduced cells were harvested during exponential growth from an $M9^{+}$ culture, which was prepared and fixed with 2.6% Formaldehyde and 0.006% Glutaraldehyde in PBS (7.4). Localization data were acquired under the same conditions and frame rate used to acquire live-cell PALM images, but using much lower activation power (<< 50 mW cm^{-2}) so activation events within a cell were separated by several seconds. (B) Histogram of localizations per molecule from 4552 molecules (blue bars) and corresponding fit to an exponential distribution (red line; fitted mean = 0.81 ± 0.02). Calculation of the ensemble mean localizations per molecule (2.4 ± 4.8) includes only observed molecules that lasted at least one frame, and is consequently larger than the fitted mean, which includes contributions from values less than one frame. This ensemble mean value was used in all molecule number calculations. Scale Bars, 500 nm.

REFERENCES

Aarsman, M.E., A. Piette, C. Fraipont, T.M. Vinkenvleugel, M. Nguyen-Disteche & T. den Blaauwen, (2005) Maturation of the Escherichia coli divisome occurs in two steps. *Molecular microbiology* 55: 1631-1645.

Abbe, E., (1873) Beiträge zur Theorie des Mikroskops und der mikroskopischen Wahrnehmung. *Arch. Mikr. Anat.* 9: 413-468.

Adams, D.W. & J. Errington, (2009) Bacterial cell division: assembly, maintenance and disassembly of the Z ring. *Nat Rev Microbiol* 7: 642-653.

Addinall, S.G., E. Bi & J. Lutkenhaus, (1996) FtsZ ring formation in fts mutants. *J Bacteriol* 178: 3877-3884.

Addinall, S.G., C. Cao & J. Lutkenhaus, (1997a) FtsN, a late recruit to the septum in Escherichia coli. *Molecular microbiology* 25: 303-309.

Addinall, S.G., C. Cao & J. Lutkenhaus, (1997b) Temperature shift experiments with an ftsZ84(Ts) strain reveal rapid dynamics of FtsZ localization and indicate that the Z ring is required throughout septation and cannot reoccupy division sites once constriction has initiated. *J Bacteriol* 179: 4277-4284.

Addinall, S.G. & J. Lutkenhaus, (1996a) FtsA is localized to the septum in an FtsZ-dependent manner. *J Bacteriol* 178: 7167-7172.

Addinall, S.G. & J. Lutkenhaus, (1996b) FtsZ-spirals and -arcs determine the shape of the invaginating septa in some mutants of Escherichia coli. *Molecular microbiology* 22: 231-237.

Adler, H.I., W.D. Fisher, A. Cohen & A.A. Hardigree, (1967) MINIATURE escherichia coli CELLS DEFICIENT IN DNA. *Proceedings of the National Academy of Sciences of the United States of America* 57: 321-326.

Alexeeva, S., T.W.J. Gadella, J. Verheul, G.S. Verhoeven & T. Den Blaauwen, (2010) Direct interactions of early and late assembling division proteins in Escherichia coli cells resolved by FRET. *Molecular microbiology* 77: 384-398.

Anderson, D.E., F.J. Gueiros-Filho & H.P. Erickson, (2004) Assembly dynamics of FtsZ rings in Bacillus subtilis and Escherichia coli and effects of FtsZ-regulating proteins. *J Bacteriol* 186: 5775-5781.

Ando, R., H. Mizuno & A. Miyawaki, (2004) Regulated fast nucleocytoplasmic shuttling observed by reversible protein highlighting. *Science* 306: 1370-1373.

Andrews, S.S. & A.P. Arkin, (2007) A mechanical explanation for cytoskeletal rings and helices in bacteria. *Biophysical journal* 93: 1872-1884.

Angelini, S., S. Deitermann & H.-G. Koch, (2005) FtsY, the bacterial signal-recognition particle receptor, interacts functionally and physically with the SecYEG translocon. *EMBO Rep* 6: 476-481.

Annibale, P., S. Vanni, M. Scarselli, U. Rothlisberger & A. Radenovic, (2011) Identification of clustering artifacts in photoactivated localization microscopy. *Nat Meth* 8: 527-528.

Arifuzzaman, M., M. Maeda, A. Itoh, K. Nishikata, C. Takita, R. Saito, T. Ara, K. Nakahigashi, H.C. Huang, A. Hirai, K. Tsuzuki, S. Nakamura, M. Altaf-Ul-

Amin, T. Oshima, T. Baba, N. Yamamoto, T. Kawamura, T. Ioka-Nakamichi, M. Kitagawa, M. Tomita, S. Kanaya, C. Wada & H. Mori, (2006) Large-scale identification of protein-protein interaction of Escherichia coli K-12. *Genome research* 16: 686-691.

Aussel, L., F.X. Barre, M. Aroyo, A. Stasiak, A.Z. Stasiak & D. Sherratt, (2002) FtsK Is a DNA motor protein that activates chromosome dimer resolution by switching the catalytic state of the XerC and XerD recombinases. *Cell* 108: 195-205.

Baba, T., T. Ara, M. Hasegawa, Y. Takai, Y. Okumura, M. Baba, K.A. Datsenko, M. Tomita, B.L. Wanner & H. Mori, (2006) Construction of Escherichia coli K-12 in-frame, single-gene knockout mutants: the Keio collection. *Mol Syst Biol* 2: 2006 0008.

Barak, I., K. Muchova, A.J. Wilkinson, P.J. O'Toole & N. Pavlendova, (2008) Lipid spirals in Bacillus subtilis and their role in cell division. *Molecular microbiology* 68: 1315-1327.

Barlow, T., M. Berkmen, D. Georgellis, L. Bayr, S. Arvidson & A. von Gabain, (1998) RNase E, the major player in mRNA degradation, is down-regulated in Escherichia coli during a transient growth retardation (diauxic lag). *Biological chemistry* 379: 33-38.

Barondess, J.J., M. Carson, L.M. Guzman Verduzco & J. Beckwith, (1991) Alkaline phosphatase fusions in the study of cell division genes. *Res Microbiol* 142: 295-299.

Beech, P.L. & P.R. Gilson, (2000) FtsZ and organelle division in Protists. *Protist* 151: 11-16.

Begg, K.J., S.J. Dewar & W.D. Donachie, (1995) A new Escherichia coli cell division gene, ftsK. *J Bacteriol* 177: 6211-6222.

Ben-Yehuda, S. & R. Losick, (2002) Asymmetric cell division in B. subtilis involves a spiral-like intermediate of the cytokinetic protein FtsZ. *Cell* 109: 257-266.

Bernhardt, T.G. & P.A. de Boer, (2003) The Escherichia coli amidase AmiC is a periplasmic septal ring component exported via the twin-arginine transport pathway. *Molecular microbiology* 48: 1171-1182.

Bernhardt, T.G. & P.A. de Boer, (2005) SlmA, a nucleoid-associated, FtsZ binding protein required for blocking septal ring assembly over Chromosomes in E. coli. *Mol Cell* 18: 555-564.

Betzig, E., G.H. Patterson, R. Sougrat, O.W. Lindwasser, S. Olenych, J.S. Bonifacino, M.W. Davidson, J. Lippincott-Schwartz & H.F. Hess, (2006) Imaging intracellular fluorescent proteins at nanometer resolution. *Science* 313: 1642-1645.

Bi, E. & J. Lutkenhaus, (1990) Analysis of ftsZ mutations that confer resistance to the cell division inhibitor SulA (SfiA). *J Bacteriol* 172: 5602-5609.

Bi, E. & J. Lutkenhaus, (1992) Isolation and characterization of ftsZ alleles that affect septal morphology. *J Bacteriol* 174: 5414-5423.

Bi, E.F. & J. Lutkenhaus, (1991) FtsZ ring structure associated with division in Escherichia coli. *Nature* 354: 161-164.

Bigot, S., J. Corre, J.M. Louarn, F. Cornet & F.X. Barre, (2004) FtsK activities in Xer recombination, DNA mobilization and cell division involve overlapping and separate domains of the protein. *Molecular microbiology* 54: 876-886.

Bigot, S., O.A. Saleh, C. Lesterlin, C. Pages, M. El Karoui, C. Dennis, M. Grigoriev, J.F. Allemand, F.X. Barre & F. Cornet, (2005) KOPS: DNA motifs that control E. coli chromosome segregation by orienting the FtsK translocase. *Embo J* 24: 3770-3780.

Biteen, J.S., E.D. Goley, L. Shapiro & W.E. Moerner, (2012) Three-Dimensional Super-Resolution Imaging of the Midplane Protein FtsZ in Live Caulobacter crescentus Cells Using Astigmatism. *ChemPhysChem* 13: 1007-1012.

Bork, P., C. Sander & A. Valencia, (1992) An ATPase domain common to prokaryotic cell cycle proteins, sugar kinases, actin, and hsp70 heat shock proteins. *Proceedings of the National Academy of Sciences of the United States of America* 89: 7290-7294.

Botta, G.A. & J.T. Park, (1981) Evidence for involvement of penicillin-binding protein 3 in murein synthesis during septation but not during cell elongation. *J Bacteriol* 145: 333-340.

Bowler, L.D. & B.G. Spratt, (1989) Membrane topology of penicillin-binding protein 3 of Escherichia coli. *Molecular microbiology* 3: 1277-1286.

Boyle, D.S., M.M. Khattar, S.G. Addinall, J. Lutkenhaus & W.D. Donachie, (1997) ftsW is an essential cell-division gene in Escherichia coli. *Molecular microbiology* 24: 1263-1273.

Bozzola, J. & L. Dee Russell, (1999) *Electron microscopy: principles and techniques for biologists*. Joans and Bartlett Publishers, Sudbury, MA.

Bramhill, D. & C.M. Thompson, (1994) GTP-dependent polymerization of Escherichia coli FtsZ protein to form tubules. *Proc Natl Acad Sci* 91: 5813-5817.

Buddelmeijer, N. & J. Beckwith, (2002) Assembly of cell division proteins at the *E. coli* cell center. *Curr Opin Microbiol* 5: 553-557.

Buddelmeijer, N. & J. Beckwith, (2004) A complex of the Escherichia coli cell division proteins FtsL, FtsB and FtsQ forms independently of its localization to the septal region. *Molecular microbiology* 52: 1315-1327.

Busiek, K.K., J.M. Eraso, Y. Wang & W. Margolin, (2012) The early divisome protein FtsA interacts directly through its 1c subdomain with the cytoplasmic domain of the late divisome protein FtsN. *J Bacteriol* 194: 1989-2000.

Buss, J., C. Coltharp, T. Huang, C. Pohlmeyer, S.C. Wang, C. Hatem & J. Xiao, (2013a) In vivo organization of the FtsZ-ring by ZapA and ZapB revealed by quantitative super-resolution microscopy. *Molecular microbiology*.

Buss, J., C. Coltharp & J. Xiao, (2013b) Super-resolution Imaging of the Bacterial Division Machinery. *J Vis Exp*: e50048.

Butland, G., J.M. Peregrin-Alvarez, J. Li, W. Yang, X. Yang, V. Canadien, A. Starostine, D. Richards, B. Beattie, N. Krogan, M. Davey, J. Parkinson, J. Greenblatt & A. Emili, (2005) Interaction network containing conserved and essential protein complexes in Escherichia coli. *Nature* 433: 531-537.

Caldas, T., E. Binet, P. Bouloc, A. Costa, J. Desgres & G. Richarme, (2000) The FtsJ/RrmJ heat shock protein of Escherichia coli is a 23 S ribosomal RNA methyltransferase. *J Biol Chem* 275: 16414-16419.

Camberg, J.L., J.R. Hoskins & S. Wickner, (2009) ClpXP protease degrades the cytoskeletal protein, FtsZ, and modulates FtsZ polymer dynamics. *Proceedings of the National Academy of Sciences of the United States of America* 106: 10614-10619.

Caplan, M.R. & H.P. Erickson, (2003) Apparent cooperative assembly of the bacterial cell division protein FtsZ demonstrated by isothermal titration calorimetry. *The Journal of biological chemistry* 278: 13784-13788.

Carrion, M., M.J. Gomez, R. Merchante-Schubert, S. Dongarra & J.A. Ayala, (1999) mraW, an essential gene at the dcw cluster of Escherichia coli codes for a cytoplasmic protein with methyltransferase activity. *Biochimie* 81: 879-888.

Carson, M.J., J. Barondess & J. Beckwith, (1991) The FtsQ protein of Escherichia coli: membrane topology, abundance, and cell division phenotypes due to overproduction and insertion mutations. *J Bacteriol* 173: 2187-2195.

Chen, J.C. & J. Beckwith, (2001) FtsQ, FtsL and FtsI require FtsK, but not FtsN, for co-localization with FtsZ during Escherichia coli cell division. *Molecular microbiology* 42: 395-413.

Chen, J.C., M. Minev & J. Beckwith, (2002) Analysis of ftsQ mutant alleles in Escherichia coli: complementation, septal localization, and recruitment of downstream cell division proteins. *J Bacteriol* 184: 695-705.

Chen, Y., K. Bjornson, S.D. Redick & H.P. Erickson, (2005) A rapid fluorescence assay for FtsZ assembly indicates cooperative assembly with a dimer nucleus. *Biophysical journal* 88: 505-514.

Chen, Y. & H.P. Erickson, (2005) Rapid in vitro assembly dynamics and subunit turnover of FtsZ demonstrated by fluorescence resonance energy transfer. *The Journal of biological chemistry* 280: 22549-22554.

Chen, Y., S.L. Milam & H.P. Erickson, (2012) SulA Inhibits Assembly of FtsZ by a Simple Sequestration Mechanism. *Biochemistry* 51: 3100-3109.

Cherepanov, P.P. & W. Wackernagel, (1995) Gene disruption in Escherichia coli: TcR and KmR cassettes with the option of Flp-catalyzed excision of the antibiotic-resistance determinant. *Gene* 158: 9-14.

Cho, H. & T.G. Bernhardt, (2013) Identification of the SlmA Active Site Responsible for Blocking Bacterial Cytokinetic Ring Assembly over the Chromosome. *PLoS Genet* 9: e1003304.

Cho, H., H.R. McManus, S.L. Dove & T.G. Bernhardt, (2011) Nucleoid occlusion factor SlmA is a DNA-activated FtsZ polymerization antagonist. *Proceedings of the National Academy of Sciences* 108: 3773-3778.

Coltharp, C., R.P. Kessler & J. Xiao, (2012) Accurate Construction of Photoactivated Localization Microscopy (PALM) Images for Quantitative Measurements. *PLoS ONE* 7: e51725.

Cordell, S.C., E.J. Robinson & J. Lowe, (2003) Crystal structure of the SOS cell division inhibitor SulA and in complex with FtsZ. *Proceedings of the*

National Academy of Sciences of the United States of America 100: 7889-7894.

D'Ulisse, V., M. Fagioli, P. Ghelardini & L. Paolozzi, (2007) Three functional subdomains of the Escherichia coli FtsQ protein are involved in its interaction with the other division proteins. *Microbiology* 153: 124-138.

Dai, K. & J. Lutkenhaus, (1991) ftsZ is an essential cell division gene in Escherichia coli. *J Bacteriol* 173: 3500-3506.

Dai, K. & J. Lutkenhaus, (1992) The proper ratio of FtsZ to FtsA is required for cell division to occur in Escherichia coli. *J Bacteriol* 174: 6145-6151.

Dai, K., Y. Xu & J. Lutkenhaus, (1993) Cloning and characterization of ftsN, an essential cell division gene in Escherichia coli isolated as a multicopy suppressor of ftsA12(Ts). *J Bacteriol* 175: 3790-3797.

Dai, K., Y. Xu & J. Lutkenhaus, (1996) Topological characterization of the essential Escherichia coli cell division protein FtsN. *J Bacteriol* 178: 1328-1334.

Dajkovic, A., G. Lan, S.X. Sun, D. Wirtz & J. Lutkenhaus, (2008a) MinC Spatially Controls Bacterial Cytokinesis by Antagonizing the Scaffolding Function of FtsZ. *Current biology : CB* 18: 235-244.

Dajkovic, A., A. Mukherjee & J. Lutkenhaus, (2008b) Investigation of regulation of FtsZ assembly by SulA and development of a model for FtsZ polymerization. *J Bacteriol* 190: 2513-2526.

Dajkovic, A., A. Mukherjee & J. Lutkenhaus, (2008c) Investigation of the Regulation of FtsZ assembly by SulA and Development of a Model for FtsZ Polymerization. *J Bacteriol*.

Dajkovic, A., S. Pichoff, J. Lutkenhaus & D. Wirtz, (2010) Cross-linking FtsZ polymers into coherent Z rings. *Molecular microbiology* 78: 651-668.

Datsenko, K.A. & B.L. Wanner, (2000) One-step inactivation of chromosomal genes in Escherichia coli K-12 using PCR products. *Proc Natl Acad Sci* 97: 6640-6645.

Davie, E., K. Sydnor & L.I. Rothfield, (1984) Genetic basis of minicell formation in Escherichia coli K-12. *J Bacteriol* 158: 1202-1203.

de Boer, P., R. Crossley & L. Rothfield, (1992a) The essential bacterial cell-division protein FtsZ is a GTPase. *Nature* 359: 254-256.

de Boer, P.A., R.E. Crossley, A.R. Hand & L.I. Rothfield, (1991) The MinD protein is a membrane ATPase required for the correct placement of the Escherichia coli division site. *Embo J* 10: 4371-4380.

de Boer, P.A., R.E. Crossley & L.I. Rothfield, (1988) Isolation and properties of minB, a complex genetic locus involved in correct placement of the division site in Escherichia coli. *J Bacteriol* 170: 2106-2112.

de Boer, P.A., R.E. Crossley & L.I. Rothfield, (1989) A division inhibitor and a topological specificity factor coded for by the minicell locus determine proper placement of the division septum in E. coli. *Cell* 56: 641-649.

de Boer, P.A., R.E. Crossley & L.I. Rothfield, (1992b) Roles of MinC and MinD in the site-specific septation block mediated by the MinCDE system of Escherichia coli. *J Bacteriol* 174: 63-70.

de la Fuente, A., P. Palacios & M. Vicente, (2001) Transcription of the Escherichia coli dcw cluster: evidence for distal upstream transcripts being involved in the expression of the downstream ftsZ gene. *Biochimie* 83: 109-115.

de Leeuw, E., B. Graham, G.J. Phillips, C.M. ten Hagen-Jongman, B. Oudega & J. Luirink, (1999) Molecular characterization of Escherichia coli FtsE and FtsX. *Mol Microbiol* 31: 983-993.

Deich, J., E.M. Judd, H.H. McAdams & W.E. Moerner, (2004) Visualization of the movement of single histidine kinase molecules in live Caulobacter cells. *Proc Natl Acad Sci* 101: 15921-15926.

DeLisa, M.P., C.F. Wu, L. Wang, J.J. Valdes & W.E. Bentley, (2001) DNA microarray-based identification of genes controlled by autoinducer 2-stimulated quorum sensing in Escherichia coli. *J Bacteriol* 183: 5239-5247.

Dempsey, G.T., J.C. Vaughan, K.H. Chen, M. Bates & X. Zhuang, (2011) Evaluation of fluorophores for optimal performance in localization-based super-resolution imaging. *Nat Meth* 8: 1027-1036.

Den Blaauwen, T., N. Buddelmeijer, M.E. Aarsman, C.M. Hameete & N. Nanninga, (1999) Timing of FtsZ assembly in Escherichia coli. *J Bacteriol* 181: 5167-5175.

Derouaux, A., B. Wolf, C. Fraipont, E. Breukink, M. Nguyen-Distèche & M. Terrak, (2008) The Monofunctional Glycosyltransferase of Escherichia coli Localizes to the Cell Division Site and Interacts with Penicillin-Binding Protein 3, FtsW, and FtsN. *Journal of Bacteriology* 190: 1831-1834.

Dewar, S.J., K.J. Begg & W.D. Donachie, (1992) Inhibition of cell division initiation by an imbalance in the ratio of FtsA to FtsZ. *J Bacteriol* 174: 6314-6316.

Di Lallo, G., M. Fagioli, D. Barionovi, P. Ghelardini & L. Paolozzi, (2003) Use of a two-hybrid assay to study the assembly of a complex multicomponent protein machinery: bacterial septosome differentiation. *Microbiol* 149: 3353-3359.

Domadia, P., S. Swarup, A. Bhunia, J. Sivaraman & D. Dasgupta, (2007) Inhibition of bacterial cell division protein FtsZ by cinnamaldehyde. *Biochem Pharmacol* 74: 831-840.

Dorazi, R. & S.J. Dewar, (2000a) Membrane topology of the N-terminus of the Escherichia coli FtsK division protein. *FEBS Lett* 478: 13-18.

Dorazi, R. & S.J. Dewar, (2000b) The SOS promoter dinH is essential for ftsK transcription during cell division. *Microbiology* 146 (Pt 11): 2891-2899.

Draper, G.C., N. McLennan, K. Begg, M. Masters & W.D. Donachie, (1998) Only the N-terminal domain of FtsK functions in cell division. *J Bacteriol* 180: 4621-4627.

Dubarry, N., C. Possoz & F.X. Barre, (2010) Multiple regions along the Escherichia coli FtsK protein are implicated in cell division. *Molecular microbiology* 78: 1088-1100.

Durand-Heredia, J., E. Rivkin, G. Fan, J. Morales & A. Janakiraman, (2012) Identification of ZapD as a Cell Division Factor That Promotes the Assembly of FtsZ in Escherichia coli. *J Bacteriol* 194: 3189-3198.

Durand-Heredia, J.M., H.H. Yu, S. De Carlo, C.F. Lesser & A. Janakiraman, (2011) Identification and Characterization of ZapC, a Stabilizer of the FtsZ Ring in Escherichia coli. *J Bacteriol* 193: 1405-1413.

Ebersbach, G., E. Galli, J. Moller-Jensen, J. Lowe & K. Gerdes, (2008) Novel coiled-coil cell division factor ZapB stimulates Z ring assembly and cell division. *Molecular microbiology* 68: 720-735.

Egan, A.J. & W. Vollmer, (2013) The physiology of bacterial cell division. *Ann N Y Acad Sci* 1277: 8-28.

Erickson, H.P., (1995) FtsZ, a prokaryotic homolog of tubulin? *Cell* 80: 367-370.

Erickson, H.P., (2009) Modeling the physics of FtsZ assembly and force generation. *Proceedings of the National Academy of Sciences of the United States of America* 106: 9238-9243.

Erickson, H.P., D.E. Anderson & M. Osawa, (2010) FtsZ in Bacterial Cytokinesis: Cytoskeleton and Force Generator All in One. *Microbiol Mol Biol Rev* 74: 504-528.

Erickson, H.P. & D. Stoffler, (1996) Protofilaments and rings, two conformations of the tubulin family conserved from bacterial FtsZ to alpha/beta and gamma tubulin. *J Cell Biol* 135: 5-8.

Erickson, H.P., D.W. Taylor, K.A. Taylor & D. Bramhill, (1996a) Bacterial cell division protein FtsZ assembles into protofilament sheets and minirings, structural homologs of tubulin polymers. *Proc Natl Acad Sci* 93: 519-523.

Erickson, H.P., D.W. Taylor, K.A. Taylor & D. Bramhill, (1996b) Bacterial cell division protein FtsZ assembles into protofilament sheets and minirings, structural homologs of tubulin polymers. *Proc Natl Acad Sci U S A* 93: 519-523.

Errington, J., (2013) L-form bacteria, cell walls and the origins of life. *Open Biology* 3.

Errington, J., R.A. Daniel & D.J. Scheffers, (2003) Cytokinesis in bacteria. *Microbiol Mol Biol Rev* 67: 52-65.

Espeli, O., R. Borne, P. Dupaigne, A. Thiel, E. Gigant, R. Mercier & F. Boccard, (2012) A MatP-divisome interaction coordinates chromosome segregation with cell division in E. coli. *EMBO J* 31: 3198-3211.

Esue, O., M. Cordero, D. Wirtz & Y. Tseng, (2005) The assembly of MreB, a prokaryotic homolog of actin. *The Journal of biological chemistry* 280: 2628-2635.

Flardh, K., P. Palacios & M. Vicente, (1998) Cell division genes ftsQAZ in Escherichia coli require distant cis-acting signals upstream of ddlB for full expression. *Molecular microbiology* 30: 305-315.

Fraipont, C., S. Alexeeva, B. Wolf, R. van der Ploeg, M. Schloesser, T. den Blaauwen & M. Nguyen-Distèche, (2011) The integral membrane FtsW protein and peptidoglycan synthase PBP3 form a subcomplex in Escherichia coli. *Microbiology* 157: 251-259.

Fu, G., T. Huang, J. Buss, C. Coltharp, Z. Hensel & J. Xiao, (2010) *In Vivo* Structure of the *E. coli* FtsZ-ring Revealed by Photoactivated Localization Microscopy (PALM). *PLoS ONE* 5: e12680.

Galli, E. & K. Gerdes, (2010) Spatial resolution of two bacterial cell division proteins: ZapA recruits ZapB to the inner face of the Z-ring. *Molecular microbiology* 76: 1514-1526.

Galli, E. & K. Gerdes, (2012) FtsZ-ZapA-ZapB Interactome of Escherichia coli. *J Bacteriol* 194: 292-302.

Gamba, P., J.W. Veening, N.J. Saunders, L.W. Hamoen & R.A. Daniel, (2009) Two-step assembly dynamics of the Bacillus subtilis divisome. *J Bacteriol* 191: 4186-4194.

Gardner, K.A., D.A. Moore & H.P. Erickson, (2013) The C-terminal linker of Escherichia coli FtsZ functions as an intrinsically disordered peptide. *Molecular microbiology* 89: 264-275.

Garrido, T., M. Sanchez, P. Palacios, M. Aldea & M. Vicente, (1993) Transcription of ftsZ oscillates during the cell cycle of Escherichia coli. *Embo J* 12: 3957-3965.

Geisbrecht, B.V., S. Bouyain & M. Pop, (2006) An optimized system for expression and purification of secreted bacterial proteins. *Protein Expr Purif* 46: 23-32.

Geisbrecht, B.V., B.Y. Hamaoka, B. Perman, A. Zemla & D.J. Leahy, (2005) The Crystal Structures of EAP Domains from Staphylococcus aureus Reveal an Unexpected Homology to Bacterial Superantigens. *Journal of Biological Chemistry* 280: 17243-17250.

Geissler, B. & W. Margolin, (2005) Evidence for functional overlap among multiple bacterial cell division proteins: compensating for the loss of FtsK. *Molecular microbiology* 58: 596-612.

Geissler, B., D. Shiomi & W. Margolin, (2007) The ftsA* gain-of-function allele of Escherichia coli and its effects on the stability and dynamics of the Z ring. *Microbiology* 153: 814-825.

Gerding, M.A., B. Liu, F.O. Bendezu, C.A. Hale, T.G. Bernhardt & P.A. de Boer, (2009) Self-enhanced accumulation of FtsN at Division Sites and Roles for Other Proteins with a SPOR domain (DamX, DedD, and RlpA) in Escherichia coli cell constriction. *J Bacteriol* 191: 7383-7401.

Gerding, M.A., Y. Ogata, N.D. Pecora, H. Niki & P.A. de Boer, (2007) The trans-envelope Tol-Pal complex is part of the cell division machinery and required for proper outer-membrane invagination during cell constriction in E. coli. *Molecular microbiology* 63: 1008-1025.

Gervais, F.G., P. Phoenix & G.R. Drapeau, (1992) The rcsB gene, a positive regulator of colanic acid biosynthesis in Escherichia coli, is also an activator of ftsZ expression. *J Bacteriol* 174: 3964-3971.

Ghigo, J.M., D.S. Weiss, J.C. Chen, J.C. Yarrow & J. Beckwith, (1999) Localization of FtsL to the Escherichia coli septal ring. *Molecular microbiology* 31: 725-737.

Gilson, P.R., X.C. Yu, D. Hereld, C. Barth, A. Savage, B.R. Kiefel, S. Lay, P.R. Fisher, W. Margolin & P.L. Beech, (2003) Two Dictyostelium orthologs of

the prokaryotic cell division protein FtsZ localize to mitochondria and are required for the maintenance of normal mitochondrial morphology. *Eukaryot Cell* 2: 1315-1326.

Goehring, N.W., M.D. Gonzalez & J. Beckwith, (2006) Premature targeting of cell division proteins to midcell reveals hierarchies of protein interactions involved in divisome assembly. *Molecular microbiology* 61: 33-45.

Goehring, N.W., F. Gueiros-Filho & J. Beckwith, (2005) Premature targeting of a cell division protein to midcell allows dissection of divisome assembly in Escherichia coli. *Genes & development* 19: 127-137.

Goehring, N.W., C. Robichon & J. Beckwith, (2007) Role for the nonessential N terminus of FtsN in divisome assembly. *J Bacteriol* 189: 646-649.

Gonzalez, M.D., E.A. Akbay, D. Boyd & J. Beckwith, (2010) Multiple Interaction Domains in FtsL, a Protein Component of the Widely Conserved Bacterial FtsLBQ Cell Division Complex. *Journal of Bacteriology* 192: 2757-2768.

Gonzalez, M.D. & J. Beckwith, (2009) Divisome under Construction: Distinct Domains of the Small Membrane Protein FtsB Are Necessary for Interaction with Multiple Cell Division Proteins. *Journal of Bacteriology* 191: 2815-2825.

Graham, J.E., D.J. Sherratt & M.D. Szczelkun, (2010) Sequence-specific assembly of FtsK hexamers establishes directional translocation on DNA. *Proceedings of the National Academy of Sciences of the United States of America* 107: 20263-20268.

Greenfield, D., A.L. McEvoy, H. Shroff, G.E. Crooks, N.S. Wingreen, E. Betzig & J. Liphardt, (2009) Self-organization of the Escherichia coli chemotaxis network imaged with super-resolution light microscopy. *PLoS Biol* 7: e1000137.

Gueiros-Filho, F.J. & R. Losick, (2002) A widely conserved bacterial cell division protein that promotes assembly of the tubulin-like protein FtsZ. *Genes & development* 16: 2544-2556.

Guzman, L.M., J.J. Barondess & J. Beckwith, (1992) FtsL, an essential cytoplasmic membrane protein involved in cell division in Escherichia coli. *J Bacteriol* 174: 7716-7728.

Guzman, L.M., D.S. Weiss & J. Beckwith, (1997) Domain-swapping analysis of FtsI, FtsL, and FtsQ, bitopic membrane proteins essential for cell division in Escherichia coli. *J Bacteriol* 179: 5094-5103.

Hale, C.A. & P.A. de Boer, (1997) Direct binding of FtsZ to ZipA, an essential component of the septal ring structure that mediates cell division in E. coli. *Cell* 88: 175-185.

Hale, C.A. & P.A. de Boer, (2002) ZipA is required for recruitment of FtsK, FtsQ, FtsL, and FtsN to the septal ring in Escherichia coli. *J Bacteriol* 184: 2552-2556.

Hale, C.A., A.C. Rhee & P.A. de Boer, (2000) ZipA-induced bundling of FtsZ polymers mediated by an interaction between C-terminal domains. *J Bacteriol* 182: 5153-5166.

Hale, C.A., D. Shiomi, B. Liu, T.G. Bernhardt, W. Margolin, H. Niki & P.A.J. de Boer, (2011) Identification of Escherichia coli ZapC (YcbW) as a

Component of the Division Apparatus That Binds and Bundles FtsZ Polymers. *J Bacteriol* 193: 1393-1404.

Harry, E., L. Monahan & L. Thompson, (2006) Bacterial cell division: the mechanism and its precison. *Int Rev Cytol* 253: 27-94.

Hedge, P.J. & B.G. Spratt, (1984) A gene fusion that localises the penicillin-binding domain of penicillin-binding protein 3 of Escherichia coli. *FEBS Lett* 176: 179-184.

Hell, S.W., (2009) Microscopy and its focal switch. *Nat Meth* 6: 24-32.

Hernandez-Rocamora, V.M., C. Garcia-Montanes, B. Reija, B. Monterroso, W. Margolin, C. Alfonso, S. Zorrilla & G. Rivas, (2013) MinC shortens FtsZ protofilaments by preferentially interacting with GDP-bound subunits. *The Journal of biological chemistry*.

Hirota, Y., A. Ryter & F. Jacob, (1968) Thermosensitive mutants of E. coli affected in the processes of DNA synthesis and cellular division. *Cold Spring Harb Symp Quant Biol* 33: 677-693.

Howard, M., A.D. Rutenberg & S. de Vet, (2001) Dynamic compartmentalization of bacteria: accurate division in E. coli. *Phys Rev Lett* 87: 278102.

Hu, P., S.C. Janga, M. Babu, J.J. Díaz-Mejía, G. Butland, W. Yang, O. Pogoutse, X. Guo, S. Phanse, P. Wong, S. Chandran, C. Christopoulos, A. Nazarians-Armavil, N.K. Nasseri, G. Musso, M. Ali, N. Nazemof, V. Eroukova, A. Golshani, A. Paccanaro, J.F. Greenblatt, G. Moreno-Hagelsieb & A. Emili, (2009) Global Functional Atlas of <named-content xmlns:xlink="http://www.w3.org/1999/xlink" content-type="genus-species" xlink:type="simple">Escherichia coli</named-content> Encompassing Previously Uncharacterized Proteins. *PLoS Biol* 7: e1000096.

Hu, Z. & J. Lutkenhaus, (2001) Topological regulation of cell division in E. coli. spatiotemporal oscillation of MinD requires stimulation of its ATPase by MinE and phospholipid. *Mol Cell* 7: 1337-1343.

Hu, Z., A. Mukherjee, S. Pichoff & J. Lutkenhaus, (1999) The MinC component of the division site selection system in Escherichia coli interacts with FtsZ to prevent polymerization. *Proceedings of the National Academy of Sciences of the United States of America* 96: 14819-14824.

Huecas, S., O. Llorca, J. Boskovic, J. Martín-Benito, J.M. Valpuesta & J.M. Andreu, (2008) Energetics and Geometry of FtsZ Polymers: Nucleated Self-Assembly of Single Protofilaments. *Biophysical journal* 94: 1796-1806.

Ishihama, Y., T. Schmidt, J. Rappsilber, M. Mann, F.U. Hartl, M.J. Kerner & D. Frishman, (2008) Protein abundance profiling of the Escherichia coli cytosol. *BMC genomics* 9: 102.

Ishino, F., H.K. Jung, M. Ikeda, M. Doi, M. Wachi & M. Matsuhashi, (1989) New mutations fts-36, lts-33, and ftsW clustered in the mra region of the Escherichia coli chromosome induce thermosensitive cell growth and division. *J Bacteriol* 171: 5523-5530.

Ivanov, V. & K. Mizuuchi, (2010) Multiple modes of interconverting dynamic pattern formation by bacterial cell division proteins. *Proceedings of the National Academy of Sciences* 107: 8071-8078.

Jennings, P.C., G.C. Cox, L.G. Monahan & E.J. Harry, (2011) Super-resolution imaging of the bacterial cytokinetic protein FtsZ. *Micron* 42: 336-341.
Joseleau-Petit, D., D. Vinella & R. D'Ari, (1999) Metabolic alarms and cell division in Escherichia coli. *J Bacteriol* 181: 9-14.
Kanchanawong, P., G. Shtengel, A.M. Pasapera, E.B. Ramko, M.W. Davidson, H.F. Hess & C.M. Waterman, (2010) Nanoscale architecture of integrin-based cell adhesions. *Nature* 468: 580-584.
Karimova, G., N. Dautin & D. Ladant, (2005) Interaction network among Escherichia coli membrane proteins involved in cell division as revealed by bacterial two-hybrid analysis. *J Bacteriol* 187: 2233-2243.
Kelly, A.J., M.J. Sackett, N. Din, E. Quardokus & Y.V. Brun, (1998) Cell cycle-dependent transcriptional and proteolytic regulation of FtsZ in Caulobacter. *Genes & development* 12: 880-893.
Khattar, M.M., K.J. Begg & W.D. Donachie, (1994) Identification of FtsW and characterization of a new ftsW division mutant of Escherichia coli. *J Bacteriol* 176: 7140-7147.
Khlebnikov, A., K.A. Datsenko, T. Skaug, B.L. Wanner & J.D. Keasling, (2001) Homogeneous expression of the P(BAD) promoter in Escherichia coli by constitutive expression of the low-affinity high-capacity AraE transporter. *Microbiol* 147: 3241-3247.
Kim, S.Y., Z. Gitai, A. Kinkhabwala, L. Shapiro & W.E. Moerner, (2006) Single molecules of the bacterial actin MreB undergo directed treadmilling motion in Caulobacter crescentus. *Proc Natl Acad Sci* 103: 10929-10934.
Kitagawa, M., T. Ara, M. Arifuzzaman, T. Ioka-Nakamichi, E. Inamoto, H. Toyonaga & H. Mori, (2005) Complete set of ORF clones of Escherichia coli ASKA library (A Complete Set of E. coli K-12 ORF Archive): Unique Resources for Biological Research. *DNA Res* 12: 291-299.
Lan, G., A. Dajkovic, D. Wirtz & S.X. Sun, (2008) Polymerization and bundling kinetics of FtsZ filaments. *Biophysical journal* 95: 4045-4056.
Lan, G., C.W. Wolgemuth & S.X. Sun, (2007) Z-ring force and cell shape during division in rod-like bacteria. *Proceedings of the National Academy of Sciences of the United States of America*.
Landgraf, D., B. Okumus, P. Chien, T.A. Baker & J. Paulsson, (2012) Segregation of molecules at cell division reveals native protein localization. *Nat Meth* 9: 480-482.
Lando, D., U. Endesfelder, H. Berger, L. Subramanian, P.D. Dunne, J. McColl, D. Klenerman, A.M. Carr, M. Sauer, R.C. Allshire, M. Heilemann & E.D. Laue, (2012) Quantitative single-molecule microscopy reveals that CENP-ACnp1 deposition occurs during G2 in fission yeast. *Open Biology* 2.
LaPointe, L.M., K.C. Taylor, S. Subramaniam, A. Khadria, I. Rayment & A. Senes, (2013) Structural organization of FtsB, a transmembrane protein of the bacterial divisome. *Biochemistry* 52: 2574-2585.
Lara, B. & J.A. Ayala, (2002) Topological characterization of the essential Escherichia coli cell division protein FtsW. *FEMS Microbiol Lett* 216: 23-32.

Leake, M.C., J.H. Chandler, G.H. Wadhams, F. Bai, R.M. Berry & J.P. Armitage, (2006) Stoichiometry and turnover in single, functioning membrane protein complexes. *Nature* 443: 355-358.

Levy, O., J.L. Ptacin, P.J. Pease, J. Gore, M.B. Eisen, C. Bustamante & N.R. Cozzarelli, (2005) Identification of oligonucleotide sequences that direct the movement of the Escherichia coli FtsK translocase. *Proceedings of the National Academy of Sciences of the United States of America* 102: 17618-17623.

Lewis, L.K., G.R. Harlow, L.A. Gregg-Jolly & D.W. Mount, (1994) Identification of high affinity binding sites for LexA which define new DNA damage-inducible genes in Escherichia coli. *Journal of molecular biology* 241: 507-523.

Lewis, L.K., M.E. Jenkins & D.W. Mount, (1992) Isolation of DNA damage-inducible promoters in Escherichia coli: regulation of polB (dinA), dinG, and dinH by LexA repressor. *J Bacteriol* 174: 3377-3385.

Li, Y., J. Hsin, L. Zhao, Y. Cheng, W. Shang, K.C. Huang, H.-W. Wang & S. Ye, (2013) FtsZ Protofilaments Use a Hinge-Opening Mechanism for Constrictive Force Generation. *Science* 341: 392-395.

Li, Z., M.J. Trimble, Y.V. Brun & G.J. Jensen, (2007) The structure of FtsZ filaments in vivo suggests a force-generating role in cell division. *Embo J* 26: 4694-4708.

Little, J.W., S.H. Edmiston, L.Z. Pacelli & D.W. Mount, (1980) Cleavage of the Escherichia coli lexA protein by the recA protease. *Proceedings of the National Academy of Sciences of the United States of America* 77: 3225-3229.

Liu, Z., A. Mukherjee & J. Lutkenhaus, (1999) Recruitment of ZipA to the division site by interaction with FtsZ. *Molecular microbiology* 31: 1853-1861.

Lopez-Montero, I., P. Lopez-Navajas, J. Mingorance, G. Rivas, M. Velez, M. Vicente & F. Monroy, (2013) Intrinsic disorder of the bacterial cell division protein ZipA: coil-to-brush conformational transition. *FASEB journal : official publication of the Federation of American Societies for Experimental Biology* 27: 3363-3375.

Low, H.H., M.C. Moncrieffe & J. Lowe, (2004) The crystal structure of ZapA and its modulation of FtsZ polymerisation. *Journal of molecular biology* 341: 839-852.

Lu, C. & H.P. Erickson, (1998) Purification and assembly of FtsZ. *Methods in enzymology* 298: 305-313.

Lu, C., J. Stricker & H.P. Erickson, (1998) FtsZ from Escherichia coli, Azotobacter vinelandii, and Thermotoga maritima--quantitation, GTP hydrolysis, and assembly. *Cell Motil Cytoskeleton* 40: 71-86.

Lutkenhaus, J., (2007) Assembly Dynamics of the Bacterial MinCDE System and Spatial Regulation of the Z Ring. *Annu Rev Biochem* 76: 539-562.

Lutkenhaus, J.F., B.A. Moore, M. Masters & W.D. Donachie, (1979) Individual proteins are synthesized continuously throughout the Escherichia coli cell cycle. *J Bacteriol* 138: 352-360.

Lutkenhaus, J.F., H. Wolf-Watz & W.D. Donachie, (1980) Organization of genes in the ftsA-envA region of the Escherichia coli genetic map and identification of a new fts locus (ftsZ). *Journal of Bacteriology* 142: 615-620.

Ma, L.Y., G. King & L. Rothfield, (2003) Mapping the MinE site involved in interaction with the MinD division site selection protein of Escherichia coli. *J Bacteriol* 185: 4948-4955.

Ma, X., D.W. Ehrhardt & W. Margolin, (1996) Colocalization of cell division proteins FtsZ and FtsA to cytoskeletal structures in living Escherichia coli cells by using green fluorescent protein. *Proc Natl Acad Sci* 93: 12998-13003.

Ma, X. & W. Margolin, (1999) Genetic and functional analyses of the conserved C-terminal core domain of Escherichia coli FtsZ. *J Bacteriol* 181: 7531-7544.

Maggi, S., O. Massidda, G. Luzi, D. Fadda, L. Paolozzi & P. Ghelardini, (2008) Division protein interaction web: identification of a phylogenetically conserved common interactome between Streptococcus pneumoniae and Escherichia coli. *Microbiol* 154: 3042-3052.

Männik, J., F. Wu, F.J.H. Hol, P. Bisicchia, D.J. Sherratt, J.E. Keymer & C. Dekker, (2012) Robustness and accuracy of cell division in Escherichia coli in diverse cell shapes. *Proceedings of the National Academy of Sciences*.

Margolin, W., (2005) FtsZ and the division of prokaryotic cells and organelles. *Nat Rev Mol Cell Biol* 6: 862-871.

Martos, A., C. Alfonso, P. Lopez-Navajas, R. Ahijado-Guzmn, J. Mingorance, A.P. Minton & G. Rivas, (2010) Characterization of self-association and heteroassociation of bacterial cell division proteins FtsZ and ZipA in solution by composition gradient-static light scattering. *Biochemistry* 49: 10780-10787.

Martos, A., B. Monterroso, S. Zorrilla, B. Reija, C. Alfonso, J. Mingorance, G. Rivas & M. Jiménez, (2012) Isolation, Characterization and Lipid-Binding Properties of the Recalcitrant FtsA Division Protein from <italic>Escherichia coli</italic>. *PLoS ONE* 7: e39829.

Matias, V.R., A. Al-Amoudi, J. Dubochet & T.J. Beveridge, (2003) Cryo-transmission electron microscopy of frozen-hydrated sections of Escherichia coli and Pseudomonas aeruginosa. *J Bacteriol* 185: 6112-6118.

McKinney, S.A., C.S. Murphy, K.L. Hazelwood, M.W. Davidson & L.L. Looger, (2009) A bright and photostable photoconvertible fluorescent protein. *Nat Methods* 6: 131-133.

Mercer, K.L. & D.S. Weiss, (2002) The Escherichia coli cell division protein FtsW is required to recruit its cognate transpeptidase, FtsI (PBP3), to the division site. *J Bacteriol* 184: 904-912.

Mercier, R., M.-A. Petit, S. Schbath, S. Robin, M. El Karoui, F. Boccard & O. Espéli, (2008) The MatP/matS Site-Specific System Organizes the

Terminus Region of the E. coli Chromosome into a Macrodomain. 135: 475-485.
Michie, K.A., L.G. Monahan, P.L. Beech & E.J. Harry, (2006) Trapping of a spiral-like intermediate of the bacterial cytokinetic protein FtsZ. *J Bacteriol* 188: 1680-1690.
Migocki, M.D., M.K. Freeman, R.G. Wake & E.J. Harry, (2002) The Min system is not required for precise placement of the midcell Z ring in Bacillus subtilis. *EMBO Rep* 3: 1163-1167.
Milam, Sara L., M. Osawa & Harold P. Erickson, (2012) Negative-Stain Electron Microscopy of Inside-Out FtsZ Rings Reconstituted on Artificial Membrane Tubules Show Ribbons of Protofilaments. *Biophysical journal* 103: 59-68.
Mileykovskaya, E. & W. Dowhan, (2000) Visualization of phospholipid domains in Escherichia coli by using the cardiolipin-specific fluorescent dye 10-N-nonyl acridine orange. *J Bacteriol* 182: 1172-1175.
Mileykovskaya, E. & W. Dowhan, (2005) Role of membrane lipids in bacterial division-site selection. *Curr Op Microbiol* 8: 135-142.
Mishra, M., Y. Huang, P. Srivastava, R. Srinivasan, M. Sevugan, R. Shlomovitz, N. Gov, M. Rao & M. Balasubramanian, (2012) Cylindrical cellular geometry ensures fidelity of division site placement in fission yeast. *Journal of Cell Science* 125: 3850-3857.
Modell, J.W., A.C. Hopkins & M.T. Laub, (2011) A DNA damage checkpoint in Caulobacter crescentus inhibits cell division through a direct interaction with FtsW. *Genes & development* 25: 1328-1343.
Mohammadi, T., G.E. Ploeger, J. Verheul, A.D. Comvalius, A. Martos, C. Alfonso, J. van Marle, G. Rivas & T. den Blaauwen, (2009) The GTPase activity of Escherichia coli FtsZ determines the magnitude of the FtsZ polymer bundling by ZapA in vitro. *Biochemistry* 48: 11056-11066.
Mohammadi, T., V. van Dam, R. Sijbrandi, T. Vernet, A. Zapun, A. Bouhss, M. Diepeveen-de Bruin, M. Nguyen-Disteche, B. de Kruijff & E. Breukink, (2011) Identification of FtsW as a transporter of lipid-linked cell wall precursors across the membrane. *EMBO J* 30: 1425-1432.
Möll, A., S. Schlimpert, A. Briegel, G.J. Jensen & M. Thanbichler, (2010) DipM, a new factor required for peptidoglycan remodelling during cell division in Caulobacter crescentus. *Molecular microbiology* 77: 90-107.
Moll, A. & M. Thanbichler, (2009) FtsN-like proteins are conserved components of the cell division machinery in proteobacteria. *Molecular microbiology* 72: 1037-1053.
Monahan, L.G., A. Robinson & E.J. Harry, (2009) Lateral FtsZ association and the assembly of the cytokinetic Z ring in bacteria. *Molecular microbiology* 74: 1004-1017.
Monnard, P.-A. & D.W. Deamer, (2002) Membrane self-assembly processes: Steps toward the first cellular life. *The Anatomical Record* 268: 196-207.
Mosyak, L., Y. Zhang, E. Glasfeld, S. Haney, M. Stahl, J. Seehra & W.S. Somers, (2000) The bacterial cell-division protein ZipA and its interaction with an FtsZ fragment revealed by X-ray crystallography. *Embo J* 19: 3179-3191.

Mukherjee, A. & W.D. Donachie, (1990) Differential translation of cell division proteins. *J Bacteriol* 172: 6106-6111.

Mukherjee, A. & J. Lutkenhaus, (1999) Analysis of FtsZ assembly by light scattering and determination of the role of divalent metal cations. *J Bacteriol* 181: 823-832.

Muller, P., C. Ewers, U. Bertsche, M. Anstett, T. Kallis, E. Breukink, C. Fraipont, M. Terrak, M. Nguyen-Disteche & W. Vollmer, (2007) The Essential Cell Division Protein FtsN Interacts with the Murein (Peptidoglycan) Synthase PBP1B in Escherichia coli. *The Journal of biological chemistry* 282: 36394-36402.

Mullineaux, C.W., A. Nenninger, N. Ray & C. Robinson, (2006) Diffusion of Green Fluorescent Protein in Three Cell Environments in Escherichia Coli. *J Bacteriol* 188: 3442-3448.

Nagai, T., K. Ibata, E.S. Park, M. Kubota, K. Mikoshiba & A. Miyawaki, (2002) A variant of yellow fluorescent protein with fast and efficient maturation for cell-biological applications. *Nat Biotechnol* 20: 87-90.

Navarro, F., A. Robin, R. D'Ari & D. Joseleau-Petit, (1998) Analysis of the effect of ppGpp on the ftsQAZ operon in Escherichia coli. *Molecular microbiology* 29: 815-823.

Newman, E.B., L.I. Budman, E.C. Chan, R.C. Greene, R.T. Lin, C.L. Woldringh & R. D'Ari, (1998) Lack of S-adenosylmethionine results in a cell division defect in Escherichia coli. *J Bacteriol* 180: 3614-3619.

Nguyen-Disteche, M., C. Fraipont, N. Buddelmeijer & N. Nanninga, (1998) The structure and function of Escherichia coli penicillin-binding protein 3. *Cellular and molecular life sciences : CMLS* 54: 309-316.

Niu, L. & J. Yu, (2008) Investigating intracellular dynamics of FtsZ cytoskeleton with photoactivation single-molecule tracking. *Biophysical journal* 95: 2009-2016.

Nogales, E., K.H. Downing, L.A. Amos & J. Lowe, (1998) Tubulin and FtsZ form a distinct family of GTPases. *Nat Struct Biol* 5: 451-458.

Ohashi, T., C.A. Hale, P.A. de Boer & H.P. Erickson, (2002) Structural evidence that the P/Q domain of ZipA is an unstructured, flexible tether between the membrane and the C-terminal FtsZ-binding domain. *J Bacteriol* 184: 4313-4315.

Oliva, M.A., S.C. Cordell & J. Lowe, (2004) Structural insights into FtsZ protofilament formation. *Nat Struct Mol Biol* 11: 1243-1250.

Oliva, M.A., D. Trambaiolo & J. Lowe, (2007) Structural insights into the conformational variability of FtsZ. *Journal of molecular biology* 373: 1229-1242.

Osawa, M., D.E. Anderson & H.P. Erickson, (2008) Reconstitution of contractile FtsZ rings in liposomes. *Science* 320: 792-794.

Osawa, M., D.E. Anderson & H.P. Erickson, (2009) Curved FtsZ protofilaments generate bending forces on liposome membranes. *Embo J*.

Osteryoung, K.W., K.D. Stokes, S.M. Rutherford, A.L. Percival & W.Y. Lee, (1998) Chloroplast division in higher plants requires members of two

functionally divergent gene families with homology to bacterial ftsZ. *Plant Cell* 10: 1991-2004.
Pacheco-Gómez, R., X. Cheng, M.R. Hicks, C.J.I. Smith, D.I. Roper, S. Addinall, A. Rodger & T.R. Dafforn, (2013) Tetramerization of ZapA is required for FtsZ bundling. *Biochemical Journal* 449: 795-802.
Pazos, M., P. Natale & M. Vicente, (2013) A specific role for the ZipA protein in cell division: stabilization of the FtsZ protein. *The Journal of biological chemistry* 288: 3219-3226.
Peters, N.T., T. Dinh & T.G. Bernhardt, (2011) A fail-safe mechanism in the septal ring assembly pathway generated by the sequential recruitment of cell separation amidases and their activators. *J Bacteriol* 193: 4973-4983.
Peters, P.C., M.D. Migocki, C. Thoni & E.J. Harry, (2007) A new assembly pathway for the cytokinetic Z ring from a dynamic helical structure in vegetatively growing cells of Bacillus subtilis. *Molecular microbiology* 64: 487-499.
Peters, R., (2007) Single-Molecule Fluorescence Analysis of Cellular Nanomachinery Components. *Annu Rev Biophys Biomol Struct*.
Pichoff, S. & J. Lutkenhaus, (2001) Escherichia coli division inhibitor MinCD blocks septation by preventing Z-ring formation. *J Bacteriol* 183: 6630-6635.
Pichoff, S. & J. Lutkenhaus, (2002) Unique and overlapping roles for ZipA and FtsA in septal ring assembly in Escherichia coli. *Embo J* 21: 685-693.
Pichoff, S. & J. Lutkenhaus, (2005) Tethering the Z ring to the membrane through a conserved membrane targeting sequence in FtsA. *Molecular microbiology* 55: 1722-1734.
Pichoff, S. & J. Lutkenhaus, (2007) Identification of a region of FtsA required for interaction with FtsZ. *Molecular microbiology* 64: 1129-1138.
Pichoff, S., B. Shen, B. Sullivan & J. Lutkenhaus, (2012) FtsA mutants impaired for self-interaction bypass ZipA suggesting a model in which FtsA's self-interaction competes with its ability to recruit downstream division proteins. *Molecular microbiology* 83: 151-167.
Pisabarro, A.G., R. Prats, D. Vaquez & A. Rodriguez-Tebar, (1986) Activity of penicillin-binding protein 3 from Escherichia coli. *J Bacteriol* 168: 199-206.
Pla, J., M. Sanchez, P. Palacios, M. Vicente & M. Aldea, (1991) Preferential cytoplasmic location of FtsZ, a protein essential for Escherichia coli septation. *Molecular microbiology* 5: 1681-1686.
Pogliano, J., K. Pogliano, D.S. Weiss, R. Losick & J. Beckwith, (1997) Inactivation of FtsI inhibits constriction of the FtsZ cytokinetic ring and delays the assembly of FtsZ rings at potential division sites. *Proceedings of the National Academy of Sciences of the United States of America* 94: 559-564.
Popp, D., M. Iwasa, A. Narita, H.P. Erickson & Y. Maéda, (2009) FtsZ condensates: An in vitro electron microscopy study. *Biopolymers* 91: 340-350.
Potluri, L., A. Karczmarek, J. Verheul, A. Piette, J.-M. Wilkin, N. Werth, M. Banzhaf, W. Vollmer, K.D. Young, M. Nguyen-Distèche & T. Den

Blaauwen, (2010) Septal and lateral wall localization of PBP5, the major D,D-carboxypeptidase of Escherichia coli, requires substrate recognition and membrane attachment. *Molecular microbiology* 77: 300-323.

Potluri, L.P., S. Kannan & K.D. Young, (2012) ZipA is required for FtsZ-dependent preseptal peptidoglycan synthesis prior to invagination during cell division. *J Bacteriol* 194: 5334-5342.

Quardokus, E.M., N. Din & Y.V. Brun, (2001) Cell cycle and positional constraints on FtsZ localization and the initiation of cell division in Caulobacter crescentus. *Molecular microbiology* 39: 949-959.

Raskin, D.M. & P.A. de Boer, (1997) The MinE ring: an FtsZ-independent cell structure required for selection of the correct division site in E. coli. *Cell* 91: 685-694.

Raskin, D.M. & P.A. de Boer, (1999a) MinDE-dependent pole-to-pole oscillation of division inhibitor MinC in Escherichia coli. *J Bacteriol* 181: 6419-6424.

Raskin, D.M. & P.A. de Boer, (1999b) Rapid pole-to-pole oscillation of a protein required for directing division to the middle of Escherichia coli. *Proceedings of the National Academy of Sciences of the United States of America* 96: 4971-4976.

RayChaudhuri, D. & J.T. Park, (1992) Escherichia coli cell-division gene ftsZ encodes a novel GTP-binding protein. *Nature* 359: 251-254.

Renner, L.D. & D.B. Weibel, (2012) MinD and MinE interact with anionic phospholipids and regulate division plane formation in Escherichia coli. *The Journal of biological chemistry* 287: 38835-38844.

Renz, M., B.R. Daniels, G. Vámosi, I.M. Arias & J. Lippincott-Schwartz, (2012) Plasticity of the asialoglycoprotein receptor deciphered by ensemble FRET imaging and single-molecule counting PALM imaging. *Proc Natl Acad Sci* 109: E2989–E2997.

Rivas, G., J.A. Fernandez & A.P. Minton, (2001) Direct observation of the enhancement of noncooperative protein self-assembly by macromolecular crowding: indefinite linear self-association of bacterial cell division protein FtsZ. *Proceedings of the National Academy of Sciences of the United States of America* 98: 3150-3155.

Rivas, G., A. Lopez, J. Mingorance, M.J. Ferrandiz, S. Zorrilla, A.P. Minton, M. Vicente & J.M. Andreu, (2000) Magnesium-induced linear self-association of the FtsZ bacterial cell division protein monomer. The primary steps for FtsZ assembly. *The Journal of biological chemistry* 275: 11740-11749.

Rizzo, M.A., M.W. Davidson & D.W. Piston, (2009) Fluorescent Protein Tracking and Detection: Fluorescent Protein Structure and Color Variants. *Cold Spring Harbor Protocols* 2009: pdb.top63.

Robichon, C., G.F. King, N.W. Goehring & J. Beckwith, (2008) Artificial septal targeting of Bacillus subtilis cell division proteins in Escherichia coli: an interspecies approach to the study of protein-protein interactions in multiprotein complexes. *J Bacteriol* 190: 6048-6059.

Robin, A., D. Joseleau-Petit & R. D'Ari, (1990) Transcription of the ftsZ gene and cell division in Escherichia coli. *J Bacteriol* 172: 1392-1399.

Robinson, A.C., D.J. Kenan, G.F. Hatfull, N.F. Sullivan, R. Spiegelberg & W.D. Donachie, (1984) DNA sequence and transcriptional organization of essential cell division genes ftsQ and ftsA of Escherichia coli: evidence for overlapping transcriptional units. *J Bacteriol* 160: 546-555.

Robinson, A.C., D.J. Kenan, J. Sweeney & W.D. Donachie, (1986) Further evidence for overlapping transcriptional units in an Escherichia coli cell envelope-cell division gene cluster: DNA sequence and transcriptional organization of the ddl ftsQ region. *J Bacteriol* 167: 809-817.

Rodrigues, C.D.A. & E.J. Harry, (2012) The Min System and Nucleoid Occlusion Are Not Required for Identifying the Division Site in <italic>Bacillus subtilis</italic> but Ensure Its Efficient Utilization. *PLoS Genet* 8: e1002561.

Romberg, L., M. Simon & H.P. Erickson, (2001) Polymerization of Ftsz, a bacterial homolog of tubulin. is assembly cooperative? *The Journal of biological chemistry* 276: 11743-11753.

Rueda, S., M. Vicente & J. Mingorance, (2003) Concentration and assembly of the division ring proteins FtsZ, FtsA, and ZipA during the Escherichia coli cell cycle. *J Bacteriol* 185: 3344-3351.

Rust, M.J., M. Bates & X. Zhuang, (2006) Sub-diffraction-limit imaging by stochastic optical reconstruction microscopy (STORM). *Nat Methods* 3: 793-795.

Saka, K., M. Tadenuma, S. Nakade, N. Tanaka, H. Sugawara, K. Nishikawa, N. Ichiyoshi, M. Kitagawa, H. Mori, N. Ogasawara & A. Nishimura, (2005) A complete set of Escherichia coli open reading frames in mobile plasmids facilitating genetic studies. *DNA Res* 12: 63-68.

Salis, H.M., (2011) The ribosome binding site calculator. *Methods in enzymology* 498: 19-42.

Sambrook, J. & D. Russell, (2001) *Molecular Cloning,* p. 15.57. Cold Spring Harbor Laboratory Press, Cold Spring Harbor, New York.

Sanchez, M., A. Valencia, M.J. Ferrandiz, C. Sander & M. Vicente, (1994) Correlation between the structure and biochemical activities of FtsA, an essential cell division protein of the actin family. *Embo J* 13: 4919-4925.

Scheffers, D.J., C. Robichon, G.J. Haan, T. den Blaauwen, G. Koningstein, E. van Bloois, J. Beckwith & J. Luirink, (2007) Contribution of the FtsQ Transmembrane Segment to Localization to the Cell Division Site. *J Bacteriol* 189: 7273-7280.

Schmidt, K.L., N.D. Peterson, R.J. Kustusch, M.C. Wissel, B. Graham, G.J. Phillips & D.S. Weiss, (2004) A predicted ABC transporter, FtsEX, is needed for cell division in Escherichia coli. *J Bacteriol* 186: 785-793.

Sengupta, P., T. Jovanovic-Talisman, D. Skoko, M. Renz, S.L. Veatch & J. Lippincott-Schwartz, (2011) Probing protein heterogeneity in the plasma membrane using PALM and pair correlation analysis. *Nat Meth* 8: 969-975.

Shannon, C., (1949) Communication in the presence of noise. *Proc Inst Radio Eng* 37: 10-21.

Shen, B. & J. Lutkenhaus, (2009) The conserved C-terminal tail of FtsZ is required for the septal localization and division inhibitory activity of MinC(C)/MinD. *Molecular microbiology* 72: 410-424.

Shih, Y.L., T. Le & L. Rothfield, (2003) Division site selection in Escherichia coli involves dynamic redistribution of Min proteins within coiled structures that extend between the two cell poles. *Proceedings of the National Academy of Sciences of the United States of America* 100: 7865-7870.

Shroff, H., C.G. Galbraith, J.A. Galbraith & E. Betzig, (2008a) Live-cell photoactivated localization microscopy of nanoscale adhesion dynamics. *Nat Methods* 5: 417-423.

Shroff, H., H. White & E. Betzig, (2008b) Photoactivated localization microscopy (PALM) of adhesion complexes. *Curr Protoc Cell Biol* Chapter 4: Unit 4 21.

Shtengel, G., J.A. Galbraith, C.G. Galbraith, J. Lippincott-Schwartz, J.M. Gillette, S. Manley, R. Sougrat, C.M. Waterman, P. Kanchanawong, M.W. Davidson, R.D. Fetter & H.F. Hess, (2009) Interferometric fluorescent super-resolution microscopy resolves 3D cellular ultrastructure. *Proceedings of the National Academy of Sciences of the United States of America* 106: 3125-3130.

Sitnikov, D.M., J.B. Schineller & T.O. Baldwin, (1996) Control of cell division in Escherichia coli: regulation of transcription of ftsQA involves both rpoS and SdiA-mediated autoinduction. *Proc Natl Acad Sci U S A* 93: 336-341.

Skoog, K. & D.O. Daley, (2012) The Escherichia coli cell division protein ZipA forms homodimers prior to association with FtsZ. *Biochemistry* 51: 1407-1415.

Small, E., R. Marrington, A. Rodger, D.J. Scott, K. Sloan, D. Roper, T.R. Dafforn & S.G. Addinall, (2007) FtsZ polymer-bundling by the Escherichia coli ZapA orthologue, YgfE, involves a conformational change in bound GTP. *Journal of molecular biology* 369: 210-221.

Smith, R.W., M. Masters & W.D. Donachie, (1993) Cell division and transcription of ftsZ. *J Bacteriol* 175: 2788-2791.

Spratt, B.G., (1975) Distinct penicillin binding proteins involved in the division, elongation, and shape of Escherichia coli K12. *Proceedings of the National Academy of Sciences of the United States of America* 72: 2999-3003.

Srinivasan, R., M. Mishra, L. Wu, Z. Yin & M.K. Balasubramanian, (2008) The bacterial cell division protein FtsZ assembles into cytoplasmic rings in fission yeast. *Genes & development* 22: 1741-1746.

Stenberg, F., P. Chovanec, S.L. Maslen, C.V. Robinson, L.L. Ilag, G. von Heijne & D.O. Daley, (2005) Protein complexes of the Escherichia coli cell envelope. *The Journal of biological chemistry* 280: 34409-34419.

Strauss, M.P., A.T.F. Liew, L. Turnbull, C.B. Whitchurch, L.G. Monahan & E.J. Harry, (2012) 3D-SIM Super Resolution Microscopy Reveals a Bead-Like Arrangement for FtsZ and the Division Machinery: Implications for Triggering Cytokinesis. *PLoS Biol* 10: e1001389.

Stricker, J. & H.P. Erickson, (2003) In vivo characterization of Escherichia coli ftsZ mutants: effects on Z-ring structure and function. *J Bacteriol* 185: 4796-4805.
Stricker, J., P. Maddox, E.D. Salmon & H.P. Erickson, (2002) Rapid assembly dynamics of the Escherichia coli FtsZ-ring demonstrated by fluorescence recovery after photobleaching. *Proc Natl Acad Sci* 99: 3171-3175.
Sun, Q. & W. Margolin, (1998) FtsZ dynamics during the division cycle of live Escherichia coli cells. *J Bacteriol* 180: 2050-2056.
Sun, Q. & W. Margolin, (2001) Influence of the nucleoid on placement of FtsZ and MinE rings in Escherichia coli. *J Bacteriol* 183: 1413-1422.
Sun, S.X. & H. Jiang, (2011) Physics of Bacterial Morphogenesis. *Microbiology and Molecular Biology Reviews* 75: 543-565.
Sureka, K., T. Hossain, P. Mukherjee, P. Chatterjee, P. Datta, M. Kundu & J. Basu, (2010) Novel Role of Phosphorylation-Dependent Interaction between FtsZ and FipA in Mycobacterial Cell Division. *PLoS ONE* 5: e8590.
Swords, W.E., (2003) Chemical Transformation of E. coli. In: E. coli Plasmid Vectors. N. Casali & A. Preston (eds). Humana Press, pp. 49-53.
Swulius, M.T. & G.J. Jensen, (2012) The Helical MreB Cytoskeleton in Escherichia coli MC1000/pLE7 Is an Artifact of the N-Terminal Yellow Fluorescent Protein Tag. *Journal of Bacteriology* 194: 6382-6386.
Szeto, T.H., S.L. Rowland, L.I. Rothfield & G.F. King, (2002) Membrane localization of MinD is mediated by a C-terminal motif that is conserved across eubacteria, archaea, and chloroplasts. *Proceedings of the National Academy of Sciences of the United States of America* 99: 15693-15698.
Szwedziak, P., Q. Wang, S.M. Freund & J. Lowe, (2012) FtsA forms actin-like protofilaments. *EMBO J* 31: 2249-2260.
Takada, A., K. Nagai & M. Wachi, (2005) A decreased level of FtsZ is responsible for inviability of RNase E-deficient cells. *Genes Cells* 10: 733-741.
Taniguchi, Y., P.J. Choi, G.-W. Li, H. Chen, M. Babu, J. Hearn, A. Emili & X.S. Xie, (2010) Quantifying E. coli Proteome and Transcriptome with Single-Molecule Sensitivity in Single Cells. *Science* 329: 533-538.
Thakur, M. & P.K. Chakraborti, (2006) GTPase activity of mycobacterial FtsZ is impaired due to its transphosphorylation by the eukaryotic-type Ser/Thr kinase, PknA. *The Journal of biological chemistry* 281: 40107-40113.
Thanedar, S. & W. Margolin, (2004) FtsZ exhibits rapid movement and oscillation waves in helix-like patterns in Escherichia coli. *Current biology : CB* 14: 1167-1173.
Thiel, A., M. Valens, I. Vallet-Gely, O. Espéli & F. Boccard, (2012) Long-Range Chromosome Organization in <italic>E. coli</italic>: A Site-Specific System Isolates the Ter Macrodomain. *PLoS Genet* 8: e1002672.
Thompson, R.E., D.R. Larson & W.W. Webb, (2002) Precise nanometer localization analysis for individual fluorescent probes. *Biophysical journal* 82: 2775-2783.

Tomoyasu, T., K. Yamanaka, K. Murata, T. Suzaki, P. Bouloc, A. Kato, H. Niki, S. Hiraga & T. Ogura, (1993) Topology and subcellular localization of FtsH protein in Escherichia coli. *J Bacteriol* 175: 1352-1357.

Tonthat, N.K., S.T. Arold, B.F. Pickering, M.W. Van Dyke, S. Liang, Y. Lu, T.K. Beuria, W. Margolin & M.A. Schumacher, (2011) Molecular mechanism by which the nucleoid occlusion factor, SlmA, keeps cytokinesis in check. *EMBO J* 30: 154-164.

Tonthat, N.K., S.L. Milam, N. Chinnam, T. Whitfill, W. Margolin & M.A. Schumacher, (2013) SlmA forms a higher-order structure on DNA that inhibits cytokinetic Z-ring formation over the nucleoid. *Proceedings of the National Academy of Sciences of the United States of America* 110: 10586-10591.

Touhami, A., M. Jericho & A.D. Rutenberg, (2006) Temperature Dependence of MinD Oscillation in Escherichia coli: Running Hot and Fast. *Journal of Bacteriology* 188: 7661-7667.

Trueba, F.J., (1982) On the precision and accuracy achieved by Escherichia coli cells at fission about their middle. *Arch Microbiol* 131: 55-59.

Uehara, T., H. Matsuzawa & A. Nishimura, (2001) HscA is involved in the dynamics of FtsZ-ring formation in Escherichia coli K12. *Genes Cells* 6: 803-814.

Ukai, H., H. Matsuzawa, K. Ito, M. Yamada & A. Nishimura, (1998) ftsE(Ts) Affects Translocation of K+-Pump Proteins into the Cytoplasmic Membrane ofEscherichia coli. *Journal of Bacteriology* 180: 3663-3670.

Ulbrich, M.H. & E.Y. Isacoff, (2007) Subunit counting in membrane-bound proteins. *Nat Methods* 4: 319-321.

Ursinus, A., F. van den Ent, S. Brechtel, M. de Pedro, J.V. Holtje, J. Lowe & W. Vollmer, (2004) Murein (peptidoglycan) binding property of the essential cell division protein FtsN from Escherichia coli. *J Bacteriol* 186: 6728-6737.

Van De Putte, P., J. Van Dillewijn & A. Rörsch, (1964) The selection of mutants of escherichia coli with impaired cell division at elevated temperature. *Mutation Research/Fundamental and Molecular Mechanisms of Mutagenesis* 1: 121-128.

van den Ent, F. & J. Lowe, (2000) Crystal structure of the cell division protein FtsA from Thermotoga maritima. *Embo J* 19: 5300-5307.

van Oijen, A.M., J. Köhler, J. Schmidt, M. Müller & G.J. Brakenhoff, (1998) 3-Dimensional super-resolution by spectrally selective imaging. *Chem. Phys. Lett.* 292: 183-187.

Vats, P., Y.L. Shih & L. Rothfield, (2009) Assembly of the MreB-associated cytoskeletal ring of Escherichia coli. *Molecular microbiology* 72: 170-182.

Vaughan, S., B. Wickstead, K. Gull & S.G. Addinall, (2004) Molecular evolution of FtsZ protein sequences encoded within the genomes of archaea, bacteria, and eukaryota. *J Mol Evol* 58: 19-29.

Vicente, M., M.J. Gomez & J.A. Ayala, (1998) Regulation of transcription of cell division genes in the Escherichia coli dcw cluster. *Cellular and molecular life sciences : CMLS* 54: 317-324.

Vicente, M. & J. Lowe, (2003) Ring, helix, sphere and cylinder: the basic geometry of prokaryotic cell division. *EMBO Rep* 4: 655-660.

Vicente, M., A.I. Rico, R. Martinez-Arteaga & J. Mingorance, (2006) Septum enlightenment: assembly of bacterial division proteins. *J Bacteriol* 188: 19-27.

Wang, D., D. Kong, Y. Wang, Y. Hu, Y. He & J. Sun, (2003) Isolation of two plastid division ftsZ genes from Chlamydomonas reinhardtii and its evolutionary implication for the role of FtsZ in plastid division. *J Exp Bot* 54: 1115-1116.

Wang, L., M.K. Khattar, W.D. Donachie & J. Lutkenhaus, (1998) FtsI and FtsW are localized to the septum in Escherichia coli. *J Bacteriol* 180: 2810-2816.

Wang, S., S.J. Arends, D.S. Weiss & E.B. Newman, (2005a) A deficiency in S-adenosylmethionine synthetase interrupts assembly of the septal ring in Escherichia coli K-12. *Molecular microbiology* 58: 791-799.

Wang, X., C. Possoz & D.J. Sherratt, (2005b) Dancing around the divisome: asymmetric chromosome segregation in Escherichia coli. *Genes & development* 19: 2367-2377.

Wang, X.D., P.A. de Boer & L.I. Rothfield, (1991) A factor that positively regulates cell division by activating transcription of the major cluster of essential cell division genes of Escherichia coli. *Embo J* 10: 3363-3372.

Ward, J.E., Jr. & J. Lutkenhaus, (1985) Overproduction of FtsZ induces minicell formation in E. coli. *Cell* 42: 941-949.

Weart, R.B., A.H. Lee, A.C. Chien, D.P. Haeusser, N.S. Hill & P.A. Levin, (2007) A metabolic sensor governing cell size in bacteria. *Cell* 130: 335-347.

Weiss, D.S., (2004) Bacterial cell division and the septal ring. *Molecular microbiology* 54: 588-597.

Weiss, D.S., J.C. Chen, J.M. Ghigo, D. Boyd & J. Beckwith, (1999) Localization of FtsI (PBP3) to the septal ring requires its membrane anchor, the Z ring, FtsA, FtsQ, and FtsL. *J Bacteriol* 181: 508-520.

Wiedenmann, J., S. Ivanchenko, F. Oswald, F. Schmitt, C. Rocker, A. Salih, K.D. Spindler & G.U. Nienhaus, (2004) EosFP, a fluorescent marker protein with UV-inducible green-to-red fluorescence conversion. *Proceedings of the National Academy of Sciences of the United States of America* 101: 15905-15910.

Wissel, M.C. & D.S. Weiss, (2004) Genetic analysis of the cell division protein FtsI (PBP3): amino acid substitutions that impair septal localization of FtsI and recruitment of FtsN. *J Bacteriol* 186: 490-502.

Wissel, M.C., J.L. Wendt, C.J. Mitchell & D.S. Weiss, (2005) The transmembrane helix of the Escherichia coli division protein FtsI localizes to the septal ring. *J Bacteriol* 187: 320-328.

Witken, E., (1976) Ultraviolet Mutagenesis and Inducible DNA Repair in *Escherichia coli*. *Bacteriological Reviews* 40: 869-907.

Witkin, E.M., (1946) Inherited Differences in Sensitivity to Radiation in Escherichia Coli. *Proceedings of the National Academy of Sciences of the United States of America* 32: 59-68.

Witkin, E.M. & T. Kogoma, (1984) Involvement of the activated form of RecA protein in SOS mutagenesis and stable DNA replication in Escherichia coli. *Proceedings of the National Academy of Sciences of the United States of America* 81: 7539-7543.

Woldringh, C.L., (1994) Significance of plasmolysis spaces as markers for periseptal annuli and adhesion sites. *Molecular microbiology* 14: 597-607.

Yamamoto, K. & K. Ubukata, (2001) [Beta-lactamase negative ampicillin-resistant Haemophilus influenzae(BLNAR)]. *Nippon Rinsho* 59: 688-693.

Yang, J.C., F. Van Den Ent, D. Neuhaus, J. Brevier & J. Lowe, (2004) Solution structure and domain architecture of the divisome protein FtsN. *Molecular microbiology* 52: 651-660.

Yi, Q.M., S. Rockenbach, J.E. Ward, Jr. & J. Lutkenhaus, (1985) Structure and expression of the cell division genes ftsQ, ftsA and ftsZ. *Journal of molecular biology* 184: 399-412.

Yu, X.C. & W. Margolin, (1999) FtsZ ring clusters in min and partition mutants: role of both the Min system and the nucleoid in regulating FtsZ ring localization. *Molecular microbiology* 32: 315-326.

Yu, X.C., E.K. Weihe & W. Margolin, (1998) Role of the C terminus of FtsK in Escherichia coli chromosome segregation. *J Bacteriol* 180: 6424-6428.

Zhang, M., H. Chang, Y. Zhang, J. Yu, L. Wu, W. Ji, J. Chen, B. Liu, J. Lu, Y. Liu, J. Zhang, P. Xu & T. Xu, (2012) Rational design of true monomeric and bright photoactivatable fluorescent proteins. *Nat Meth* 9: 727-729.

Appendix 1: Strains list

Strain or Plasmid	Relevant genotype	Reference/source
BL21 (DE3) pLysS	P_{Lac}::T7 RNAP, T7 Lysozyme, *cam*	Promega Inc.
B/r A	B substrain, *sulA*1	Witken *et al*. (2000)
BW25113	K-12, BD792 derivative	Datsenko *et al*. (2000)
JW2878 (Keio)	BW25113, Δ*zapA::kan*	Baba *et al*. (2006)
JW3899 (Keio)	BW25113, Δ*zapB::kan*	Baba *et al*. (2006)
BW27783	BW25113, Δ*araFGH* Δ*araEp* P_{CP8}::*araE*	Khlebnikov *et al*. (2001)
JW0939 (Keio)	BW25113, Δ*matP::kan*	Baba *et al*. (2006)
JW5641 (Keio)	BW25113, Δ*slmA::kan*	Baba *et al*. (2006)
JB566	BW25113, Δ*slmA::frt* Δ*zapA::kan*	This study
JB568	BW25113, Δ*slmA::frt* Δ*zapB::kan*	This study
MCA27	MC4100, *ftsA27*(ts), *str*	Dai *et al*. (1993)
MCZ84	MC4100, *ftsZ84*(ts), *str*	Dai *et al*. (1993)
MCI23	MC4100, *ftsI23*(ts), *str*	Dai *et al*. (1993)
MCQ1	MC4100, *ftsQ1*(ts), *str*	Dai *et al*. (1993)
PS223	W3110, *zipA1* (ts), *str*	Pichoff *et al*. (2002)
JOE565	MC4100, *ftsN*::*kan*/ pBAD33-FtsN	Chen *et al*. (2001)
CR14	MC4100, *ftsB*::*kan*/ pBAD33-FtsB	Robichon *et al*. (2008)
MDG279	MC4100, *ftsL*::*kan*/ pBAD33-FtsL	Gonzalez *et al*. (2010)
EC850	W3110, *ftsW*::*kan*/ pBAD33-FtsW	Mercer *et al*. (2002)
NB1298	MC4100, *ftsK*::*cat*/ pBAD42-FtsK	Buddelmeijer *et al*. (2004)

Appendix 2: Plasmid list

Plasmid	Relevant genotype	Reference/source
pET21b-mEos2	pUC19, P_{T7}::mEos2 *bla*	Fu *et al.* (2010)
pET28-FtsZ-mEos2	pUC19, P_{T7}::FtsZ-mEos2 *kan*	Fu *et al.* (2010)
JW0093 (ASKA+)	ColEI, $P_{T5\text{-}lac}$::6xHis-FtsZ-GFP *cat*	Kitagawa *et al*. (2005)
pJB004	ColEI, $P_{T5\text{-}lac}$::6xHis-FtsZ-mEos2 *cat*	Fu *et al*. (2010)
pJB042	ColEI, $P_{T5\text{-}lac}$::FtsZ-mEos2 *cat*	Buss *et al*. (2013)
pJB072	ColEI, $P_{T5\text{-}lac}$::6xHis-FtsZ-Dronpa *cat*	Buss *et al*. (2013)
pJB108	ColEI, $P_{T5\text{-}lac}$::FtsZ-Dronpa *cat*	Buss *et al*. (2013)
pJB106	ColEI, $P_{T5\text{-}lac}$::FtsZ-mEos3 *cat*	Buss *et al*. (2013)
pDR175	pSC101, λp_R::GFP-MinC *aadA*	Raskin *et al*. (1997)
pTH323	pSC101, P_{BAD}::*minC aadA*	Buss *et al*. (2013)
pJB095	pSC101, P_{BAD}::*sulA aadA*	Buss *et al*. (2013)
JW2878 (ASKA-)	ColEI, $P_{T5\text{-}lac}$::6xHis-ZapA *cat*	Kitagawa *et al*. (2005)
pJB056	pSC101, P_{BAD}::*zapA aadA*	Buss *et al*. (2013)
JW3899 (ASKA-)	ColEI, $P_{T5\text{-}lac}$::6xHis-ZapB *cat*	Kitagawa *et al*. (2005)
pJB065	pSC101, P_{BAD}::*zapB aadA*	Buss *et al*. (2013)
pJB139	ColEI, $P_{T5\text{-}lac}$::mEos2-SlmA *cat*	Buss *et al*. (2013)
pJB144	ColEI, $P_{T5\text{-}lac}$::GFP-SlmA *cat*	Buss *et al*. (2013)
pVS133-FtsZ	OriV, P_{Lac}::FtsZ-Venus *bla*	Buss *et al*. (2013)
pVS155-FtsA	OriV, P_{Lac}::Venus-FtsA *bla*	Buss *et al*. (2013)
pVS133-ZipA	OriV, P_{Lac}::ZipA-Venus *bla*	Buss *et al*. (2013)
pVS155-FtsK	OriV, P_{Lac}::Venus-FtsK *bla*	Buss *et al*. (2013)
pVS155-FtsQ	OriV, P_{Lac}::Venus-FtsQ *bla*	Buss *et al*. (2013)
pVS155-FtsL	OriV, P_{Lac}::FtsL-Venus *bla*	Buss *et al*. (2013)
pVS155-FtsB	OriV, P_{Lac}::Venus-FtsB *bla*	Buss *et al*. (2013)
pVS155-FtsW	OriV, P_{Lac}::FtsW-Venus *bla*	Buss *et al*. (2013)
pVS155-FtsI	OriV, P_{Lac}::Venus-FtsI *bla*	Buss *et al*. (2013)
pVS155-FtsN	OriV, P_{Lac}::Venus-FtsN *bla*	Buss *et al*. (2013)
pJB044	ColEI, $P_{T5\text{-}lac}$::*mEos2 cat*	Buss *et al*. (2013)
pXY018	ColEI, $P_{T5\text{-}lac}$::GFP-ZapA *cat*	This study
JW3899 (ASKA+)	ColEI, $P_{T5\text{-}lac}$::6xHis-ZapB-GFP, *cat*	Kitagawa *et al.* (2005)
pJB051	ColEI, $P_{T5\text{-}lac}$::mEos2-ZapA, *cat*	This study
pJB045	ColEI, $P_{T5\text{-}lac}$::ZapB-mEos2, *cat*	This study
pJB077	pSC101, P_{BAD}::mCherry-ZapA, *aadA*	This study
pJB057	ColEI, $P_{T5\text{-}lac}$::Dronpa-ZapA, *cat*	This study
pJB058	ColEI, $P_{T5\text{-}lac}$::6xHis-FtsZ-PAmCherry1, *cat*	This study
pJB066	pSC101, P_{BAD}::FtsZ-PAmCherry1, *aadA*	This study
pJB089	ColEI, $P_{T5\text{-}lac}$::Dronpa-ZapA~FtsZ-PAmCh1, *cat*	This study
pJB073	ColEI, $P_{T5\text{-}lac}$::ZapB-Dronpa, *cat*	This study

Appendix 2 - Plasmid list

Plasmid	Relevant genotype	Reference/source
pJB061	pSC101, P_{BAD}::PAmCherry1-ZapA, *aadA*	This study
pJB086	ColEI, $P_{T5\text{-}lac}$::ZapB-Dronpa~PAmCh1-ZapA, *cat*	This study
pJB090	ColEI, $P_{T5\text{-}lac}$::Dronpa-ZapA~PAmCh1-ZapA, *cat*	This study
pXY029	ColEI, $P_{T5\text{-}lac}$::mEos2-MTS, *cat*	This study
pCP20	FLP+, λ cI857^{+}, λ p_R Rep^{ts}, *bla cat*	Cherepanov *et al.* (1995)
pKD4	R6K, *frt-kan-frt*, *bla*	Datsenko *et al*. (2000)
pT7HMT	ColEI, P_{T7}::6xHis-Myc-TEV, *kan*	Geisbrecht *et al.* (2006)
pJB041	ColEI, P_{T7}::6xHis-Myc-TEV-FtsZ, *kan*	This study
pJB040	ColEI, P_{T7}::6xHis-Myc-TEV-FtsZ-mEos2, *kan*	This study

Appendix 3: Primer List

Primer #	Primer name	Sequence
1	pET21-mEos2-5F	GATCGCTAGCATGAGTGCGATTAAG
2	pET21-mEos2-3R	GATCCTCGAGTTATCGTCTGGCATTGTC
3	pET28-FtsZ-5F	ATGTCATATGTTTGAACCAATGGAACTTACC
4	pET28-FtsZ-3R	ATTAGGATCCATCAGCTTGCTTACGCAG
5	pET28-mEos2-5F	GATCGAATTCATGAGTGCGATTAAG
6	pET28-mEos2-3R	GATCCTCGAGTTATCGTCTGGCATTGTC
7	SfiI-FtsZ-5F	CTATGGCCCTGAGGGCCATGTTTGAACCAATGGAACTTACC
8	mEos2-NotI-3R	TTAAGCGGCCGCTTAATCAGCTTGCTTACGCAG
9	pCA24N/ftsZ-his-5F	ATTAACTAGTATGTTTGAACCAATGGAACTTACCAATGACGC
10	pCA24N/ftsZ-his-3R	ATTAACTAGTAGTTAATTTCTCCTCTTTAATGAATTC
11	NotI-Dronpa-5F	TTTAGCGGCCGCATGGTGAGTGTGATTAAACCAG
12	Dronpa-NotI-3R	TAATGCGGCCGCTTACTTGGCCTGCCTCGGCA
13	SpeI-FtsZ-5F	TTAACTAGTATGTTTGAACCAATGGAACTT
14	Dronpa-SalI-3R	ATATGTCGACTTACTTGGCCTGCCTCGGCA
15	mEos2-NotI-3R	AATTGCGGCCGCTTATCGTCTGGCATTGTCAG
16	SpeI-mEos2-5F	AATTACTAGTATGAGTGCGATTAAGCCAGA
17	mEos2-SalI-3R	TATATGTCGACTTAGGATCCAGAATGAGCAACAG
18	SpeI-mEos2-5F	AATTACTAGTATGAGTGCGATTAAGCCAGA
19	EcoRI-pBAD-5F	ATTAGAATTCTTATGACAACTTGACGGCTACATC
20	NheI-pBAD-3R	ATTAGCTAGCGTATATCTCCTTCTTAAAGTTAAACAAAATTATTTC
21	NheI-SulA-5F	ATATGCTAGCATGTACACTTCAGGCTATGCACAT
22	SalI-SulA-3R	TTAAGTCGACTTAATGATACAAATTAGAGTGAATTTTTAG
23	NheI-ZapA-5F	AAATGCTAGCATGTCTGCACAACCCGTCGA
24	SalI-ZapA-3R	TTAAGTCGACTCATTCAAAGTTTTGGTTAGTTTTTC
25	NheI-ZapB-5F	AAATGCTAGCATGACAATGTCATTAGAAGTGTTTGA
26	SalI-ZapB-3R	TTAAGTCGACTCAGACCTCTTCCATGCGACC
27	mEos2-NotI*-3R	ATGCGGCCGCTAGAACCAGCAGCGGAGCCAGCGCTAGCTCGTCTGGCATTGTCAGGCA
28	NotI-SlmA-5F	TAGCGGCCGCGCAGAAAAACAAACTGCGAAAAGG
29	SlmA-NotI-3R	ATGCGGCCGCTTACTGCAACTGTGCCGCAATTAG
30	SpeI-GFP-5F	ATAACTAGTATGAGTAAAGGAGAAGAACTTTTCACT
31	GFP-NheI-3R	ATAGCTAGCTTTGTATAGTTCATCCATGCCATGTGT
32	pVS-FtsZ-5F	CACCATGTTTGAACCAATGGAA
33	pVS-FtsZ-3R	ATCAGCTTGCTTACGCAG
34	pVS-FtsZ-2b-5F	CACCAAATGTTTGAACCAATGGAA
35	pVS-FtsZ-stop-3R	TTAATCAGCTTGCTTACG
36	pVS-FtsA-5F	CACCATGATCAAGGCGACGGAC
37	pVS-FtsA-3R	AAACTCTTTTCGCAGCCA
38	pVS-FtsA-2b-5F	CACCAAATGATCAAGGCGACGGAC
39	pVS-FtsA-stop-3R	TTAAAACTCTTTTCGCAGC
40	pVS-ZipA-5F	CACCATGATGCAGGATTTGCGTCTGAT
41	pVS-ZipA-3R	GGCGTTGGCGTCTTTGACT
42	pVS-ZipA-2b-5F	CACCAAATGATGCAGGATTTGCGTCTGAT
43	pVS-ZipA-stop-3R	TCAGGCGTTGGCGTCTTTGACT
44	pVS-FtsK-5F	CACCATGAGCCAGGAATACATT
45	pVS-FtsK-3R	GTCAAACGGCGGTGGGGC
46	pVS-FtsK-2b-5F	CACCAATTGAGCCAGGAATACATT
47	pVS-FtsK-stop-3R	TTAGTCAAACGGCGGTGG
48	pVS-FtsQ-5F	CACCATGTCGCAGGCTGCTCTG
49	pVS-FtsQ-3R	TTGTTGTTCTGCCTGTGC
50	pVS-FtsQ-2b-5F	CACCTTGAGCCAGGAATACATT
51	pVS-FtsQ-stop-3R	TCATTGTTGTTCTGCCTG
52	pVS-FtsL-5F	CACCATGATCAGCAGAGTGACA
53	pVS-FtsL-3R	TTTTTGCACTACGATATTT
54	pVS-FtsL-2b-5F	CACCAAATGATCAGCAGAGTGACA
55	pVS-FtsL-stop-3R	TTATTTTTGCACTACGATATT

56	pVS-FtsB-5F	CACCATGGGTAAACTAACGCTG
57	pVS-FtsB-3R	TCGATTGTT TTGCCCCGC
58	pVS-FtsB-2b-5F	CACCAAATGGGTAAACTAACGCTG
59	pVS-FtsB-stop-3R	TTATCGATTGTTTTGCCC
60	pVS-FtsI-5F	TTACGATCTGCCACCTGTCCCCTCG
61	pVS-FtsI-3R	TCGATTGTTTTGCCCCGC
62	pVS-FtsI-2b-5F	CACCAAATGGGTAAACTAACGCTG
63	pVS-FtsI-stop-3R	TTATCGATTGTTTTGCCC
64	pVS-FtsN-5F	CACCGTGGCACAACGAGATTATGTACGC
65	pVS-FtsN-3R	ACCCCCGGCGGCGAGCCG
66	pVS-FtsN-2b-5F	CACCAAGTGGCACAACGAGATTATGTACGC
67	pVS-FtsN-stop-3R	TCAACCCCCGGCGGCGAG
68	mEos2-Link-3R	AATTGAATTCGCCAGAACCAGCAGCGGAGCCAGCGGATCCTCGTCTGGCATTGTCAGG
69	EcoRI-ZapA-5f	ATATGAATTCATGAGTGCGATTAAGCCAGA
70	ZapA-NotI-3R	ATATGCGGCCGCTCATTCAAAGTTTTGGTTAGTTTTTTC
71	SpeI-ZapB-5F	ATATACTAGTATGACAATGTCATTAGAAGTGTTTGA
72	ZapB-Link-3R	TTAAGAATTCGCCAGAACCAGCAGCGGAGCCAGCGGATCCGACCTCTTCCATGCGAC
73	EcoRI-mEos2-5f	ATATGAATTCATGAGTGCGATTAAGCCAGA
74	NheI-mCherry-5f	TTAAGCTAGCATGGTGAGCAAGGGCGAGG
75	mCherry-Link-3r	TTAAGCTAGCATGAATTCGGATCCGACCCATTTGCTGTCCACCAGTCATGCTCGCCTTGTACAC
76	NheI-ZapA-5f	AAATGCTAGCATGTCTGCACAACCCGTCGA
77	SpeI-Dronpa-5F	ATATACTAGTATGGTGAGTGTGATTAAACCAGACAT
78	Dronpa-Link-3R	TATAGCTAGCGCCAGAACCAGCAGCGGAGCCAGCGGATCCCTTGGCCTGCCTCGGCAGCT
79	NotI-mCherry-5f	TTTAGCGGCCGCATGGTGAGCAAGGGCGAG
80	mCherry-NotI-3R	AAATGCGGCCGCTTACTTGTACAGCTCGTCCAT
81	SfiI-GFP-5F	AAATTTGGCCCTGAGGGCCAGTAAAGGAGAAGAACTTTTCACT
82	GFP-Link-3R	AATTAGAATTCGCCAGAACCAGCAGCGGAGCCAGCGGATCCTTTGTATAGTTCATCCATGCCA
83	FtsZ-NheI-5f	TTTAGCTAGCATGTTTGAACCAATGGAACTTA
84	mCherry-SalI-3R	AATTGTCGACTTACTTGTACAGCTCGTCCATGCCGCCG
85	HindIII-RBS-5F	AATTAAGCTTTAACTTTAAGAAGGAGATATACGCTAGCATG
86	mCherry-HindIII-3R	AATTAAGCTTTTACTTGTACAGCTCGTCCATGCCG
87	EcoRI-Dronpa-5f	TATAGAATTCATGGTGAGTGTGATTAAACCAGAC
88	Dronpa-NotI-3R	TAATGCGGCCGCTTACTTGGCCTGCCTCGGCA
89	PAmChery-Link-3R	TATAGCTAGCGCCAGAACCAGCAGCGGAGCCAGCGGATCCCTTGTACAGCTCGTCCATGC
90	SalI-RBS-5F	TTTAGTCGACAACTTTAAGAAGGAGATATACGCTAGCAT
91	ZapA-SalI-3R	TTAAGTCGACTCATTCAAAGTTTTGGTTAGTTTTTC
92	SpeI-Dronpa-5F	ATATACTAGTATGGTGAGTGTGATTAAACCAGACAT
93	MTS-3R	TTAATCTTAGCCATCATTCCTTTGTTTTGCTCTTCAAGCACTCGTCTGGCATTGTCAGGC
94	NotI-MTS-3R	ATTGCGGCCGCTTAAGATCTTACTCCGAAAAATGACTTAATCTTAGCCATCATTCCTTTGTTTTG
95	FtsZ-T7HMT-5F	AATTGTCGACAATGTTTGAACCAATGGAACTTAC
96	FtsZ-T7HMT-3R	TTAAGCGGCCGCTTAATCAGCTTGCTTACGCAG

Appendix 4: Plasmid Construction

pET21b-mEos2: To construct the pET21b-mEos2 plasmid, *mEos2* was amplified from pRSET-mEos2 plasmid (gift from SA McKinney) using primer pair 1-2, restricted with NheI and XhoI, and ligated into a similarly digested pET21b plasmid (Novagen).

pET28-FtsZ-mEos2: To construct the pET28-FtsZ-mEos2 plasmid, we first produced the pET28-FtsZ-rsFastLime plasmid using pET28-M13-rsFastLime (gift from A Egner) by swapping the coding sequence of MCP with that of FtsZ. The coding sequence of FtsZ was amplified from plasmid pJW0093 (ASKA+, FtsZ) using primer pair 3-4, digested with NdeI and BamHI, and ligated into the similarly digested pET28-M13-rsFastLime plasmid. The *ftsZ* fragment was then cut from pET28-FtsZ-rsFastLime using restriction enzymes XbaI and BamHI. The product was ligated into a similarly digested pET28-M13-mEos2 plasmid, which was constructed by swapping *rsFastlime* with *mEos2*. Specifically, *mEos2* was amplified using primer pair 5-6, restricted with EcoRI and XhoI, and ligated into a similarly digested pET28-M13-rsFastLime plasmid to replace the *rsFastLime* fragment. The linker sequence between FtsZ and mEos2 is GSAGSAAGSGEF.

pJB004: The *ftsZ-mEos2* from pET28-FtsZ-mEos2 was amplified with prime pair 7-8, digested with SfiI and NotI, and ligated into a similarly digested pJW0093 (ASKA+, FtsZ) producing $P_{T5\text{-}lac}$::6xHis-FtsZ-mEos2.

pJB042: The N-terminal His-tag and corresponding linker of FtsZ-mEos2 in pJB004 (Fu et al., 2010) was removed by inverse PCR to generate pJB042. The forward primer #9 contained a SpeI site followed by the 5' end of *ftsZ*. The reverse primer #10 was designed complementary to the sequence immediately

upstream of the His-tag start codon and also included a novel SpeI site. After PCR amplification, the reaction mixture was treated with DpnI, ligated and transformed into DH5α (Invitrogen), generating pCH027. *FtsZ-mEos2* was amplified from pET28-FtsZ-mEos2 with primers pair 13-15, restricted with SpeI and NotI, and ligated into a similarly digested pCH027, generating pJB042 ($P_{T5\text{-}lac}$::FtsZ-mEos2). The linker sequence is GSAGSAAGSGEF. Basal expression of FtsZ-mEos2 from pJB042 is significantly reduced relative to pJB004. This phenomenon is likely a result of the incorporation of the novel SpeI site in the region separating the FtsZ-mEos2 start codon from the ribosome binding site.

pJB072 and pJB108: The *dronpa* sequence from pDG1-S1 (Amalgaam) was amplified using primer pair 11-12. The fragment was then digested with NotI and ligated into a similarly digested pJW0093 (ASKA+, FtsZ), resulting in pJB072 ($P_{T5\text{-}lac}$::6xHis-FtsZ-Dronpa). The *ftsZ-dronpa* sequence was then amplified with primer pair 13-14, restricted with SpeI and SalI, and inserted into a similarly digested pJB042 producing $P_{T5\text{-}lac}$::FtsZ-Dronpa. The amino acid sequence linking FtsZ to Dronpa is GLCGR.

pJB106: The *ftsZ-mEos2* from pJB042 was amplified using primer pair 13-15. The sequence was then restricted with SpeI and HindIII, and the larger fragment, corresponding to FtsZ and an N-terminal portion of mEos2, was gel-purified. *mEos3* was amplified from pTriEX-HM-mEos3 (gift from J. Yu) using primer pair 16-17, and digested with HindIII and SalI. The 400bp fragment was combined with the *ftsZ-mEos2* fragment and inserted into a pJB042 digested with SpeI and SalI resulting in $P_{T5\text{-}lac}$::FtsZ-mEos3. The linker sequence is GSAGSAAGSGEF.

pJB095: First, the λP_R promoter from pDR175 was replaced with P_{BAD} from pBAD TOPO® (Invitrogen) using a cut-and-paste scheme involving primer pair 17-20, and restriction with EcoRI and NheI, generating pTH323. The *sulA* gene was amplified from purified *E. coli* K12 genomic DNA using primer pair 21-22 and into pTH323 similarly digested with NheI and SalI. pJB095 (P_{BAD}::*sulA*) was transformed into BW27783, a BW25113 derivative that homogenously expresses from P_{BAD} by decoupling the arabinose transporters, AraF and AraE, from induction (Khlebnikov et al., 2001).

pJB056: *zapA* was amplified from pJW2878 (ASKA+, ZapA) (Kitagawa et al., 2005) using primer pairs 23-24, restriction with NheI and SalI, and ligation with a similarly digested pTH323 creating P_{BAD}:*zapA*.

pJB065: P_{BAD}:*zapB* was constructed in the same fashion as pJB056 using primer pair 25-26 to amplify *zapB* from pJW3899 (ASKA+, ZapB) (Kitagawa et al., 2005).

pJB139: *mEos2* and *slmA* were amplified from pJB042 and genomic K12 DNA, using primer pairs 18-27 and 28-29, respectively. The fragments were digested with SpeI and NotI, gel-purified, and ligated with a similarly digested pJB042. The $P_{T5\text{-}lac}$::mEos2-SlmA containing the linker sequence ASAGSAAGSSGR.

pJB144: The GFP sequence from JW0093 (ASKA +, FtsZ) was amplified using primer pair 30-31. The fragment was digested with SpeI and NheI, and ligated with a similarly digested pJB139 creating $P_{T5\text{-}lac}$::GFP-SlmA.

pVS133 and pVS155: Construction of these plasmids utilized Gateway® Technology (Invitrogen) detailed in Chapter 5.1.8.

pJB044: *mEos2* was amplified from pJB042 using primer pair 18-15 and inserted into the backbone of pJB042, similarly digested with SpeI and NotI creating $P_{T5\text{-}lac}$::mEos2.

pXY018: *GFP* and zapA were amplified from pJW0093 (ASKA+, FtsZ) and pJW2878 (ASKA-, ZapA) with primer pairs 81-82 and 69-70, and digested with SfiI and EcoRI, or EcoRI and NotI, respecitvely. The two fragments were ligated into pJW0093 similarly digested with SfiI and NotI, generating $P_{T5\text{-}lac}$::6xHis-GFP-ZapA

pJB051: *mEos2* and *zapA* were amplified from pJB042 and pJW2878 (ASKA+, ZapA), using primer pairs 18-68 and 69-70, respectively. The fragments were digested with SpeI and EcoRI or EcoRI and NotI, gel-purified, and ligated with a pJB042 digested with SpeI and NotI. The $P_{T5\text{-}lac}$::mEos2-ZapA containing the linker sequence ASAGSAAGSSGR.

pJB045: *zapB* and *mEos2* were amplified from pJW3899 (ASKA+, ZapB) pJB042 with primer pairs 71-72 and 73-8, respectively. Fragments were cut with SpeI and EcoRI or EcoRI and NotI and ligated into pCH042 digested with SpeI and NotI creating $P_{T5\text{-}lac}$::ZapB-mEos2.

pJB077: *mCherry* and *zapA* were amplified from pZH102 (Hensel et al., 2013) and pJB056 with primer pairs 74-75 and 76-24, respectively. The fragments were cut with NheI alone, or NheI and SalI. The gel-purified *zapA* fragment was

dephosphorylated and both fragments were ligated with a similarly digested pJB056 creating P_{BAD}::mCherry-ZapA.

pJB057: *dronpa* and *zapA* were amplified from pDG1-S1 (Amalgaam) and pJW2878 (ASKA+, ZapA), using primer pairs 77-78 and 76-70, respectively. The fragments were digested with SpeI and NheI or NheI and NotI, gel-purified, and ligated with a pJB042 digested with SpeI and NotI. The $P_{T5\text{-}lac}$::Dronpa-ZapA containing the linker sequence GSAGSAAGSGEF.

pJB058 and pJB066: *PAmCherry1* (Subach et al., 2009) was amplified with primer pair 79-80, restricted with NotI and inserted into a similarly digested pJW0093 (ASKA+, FtsZ) creating pJB058 ($P_{T5\text{-}lac}$::6xHis-FtsZ-PAmCherry1). *ftsz-PAmCherry* was amplified from pJB058 with primer pair 83-84, digested with NheI and SalI, and ligated into a similarly digested pJB095, creating pJB066 (P_{BAD}::FtsZ-PAmCherry1). The linker sequence is GLCGRM.

pJB089: *ftsz-PAmCherry1* and preceding ribosome binding site (RBS) was amplified using primer pair 85-86, digested with HindIII and ligated into a similarly digested pJB057 generating $P_{T5\text{-}lac}$::Dronpa-ZapA~FtsZ-PAmCherry.

pJB073: $P_{T5\text{-}lac}$::ZapB-Dronpa was created similar to pJB045, except *Dronpa* was amplified from pDG1-S1 (Amalgaam) with primer pair 87-88.

pJB061: PAmCherry1 was amplified from pJB058 with primer pair 74-89, digested with NheI, and ligated into a similarly digested pJB056 creating P_{BAD}::PAmCherry1-ZapA.

pJB086:. *PAmcherry1-zapA* and the upstream sequence including the RBS was amplified from pJB061 with primer pair 90-91, restricted with SalI, and ligated into a similarly digested pJB073, creating $P_{T5\text{-}lac}$::ZapB-Dronpa~PAmCherry1-ZapA.

pJB090: *Dronpa-ZapA* was amplified from pJB057 with primer pair 92-70, restricted with SpeI and NotI, and ligated into a similarly digested pJB086 creating $P_{T5\text{-}lac}$::Dronpa-ZapA~PAmCherry-ZapA.

pXY029: *mEos2* was amplified with primer pair 16-93. The resulting fragment was amplified with primer pair 16-94, restricted with SpeI and NotI, and ligated into a similarly digested pJB042. The membrane targeting sequence of MinD from *Bacillus subtilis* was included in primers 93 and 94, resulting in $P_{T5\text{-}lac}$::mEos2-MTS.

pJB041: *ftsZ* was amplified from pJW0093 with primer pair 95-96, restricted with SalI and NotI and ligated with a similarly digested pT7HMT (a gift from D Leahy) (Geisbrecht *et al.*, 2005, Geisbrecht et al., 2006) creating P_{T7}::6xHis-Myc-TEV-FtsZ.

pJB040: P_{T7}::6xHis-Myc-TEV-FtsZ-mEos2 was constructed similar to pJB041, but *ftsZ-mEos2* was amplified from pJB004 with primer pairs 95-8.